Cavity-enhanced Spectroscopy of Individual Europium-doped Nanoparticles

Timon Eichhorn

Karlsruhe 2024

Cavity-enhanced Spectroscopy of Individual Europium-doped Nanoparticles

Zur Erlangung des akademischen Grades eines
DOKTORS DER NATURWISSENSCHAFTEN (Dr. rer. nat.)

von der KIT-Fakultät für Physik des
Karlsruher Instituts für Technologie (KIT)
angenommene

DISSERTATION

von

M.Sc. Timon Eichhorn

Tag der mündlichen Prüfung: 08.11.2024
Erster Gutachter: Prof. Dr. David Hunger
Zweiter Gutachter: Prof. Dr. Wolfgang Wernsdorfer

Für Anna

Zusammenfassung

Im Bereich der Quantentechnologien hat der Quantencomputer wahrscheinlich das größte Potenzial, um bahnbrechende technologische und sozio-ökonomische Fortschritte zu erzielen. Bislang ist jedoch unklar, welches Hardware-Design das Rennen um einen fehlertoleranten und skalierbaren Quantenprozessor machen wird, der in der Lage ist, praktische Probleme zu lösen. Ein vielversprechender Ansatz besteht darin, den Spin-Freiheitsgrad von Festkörperemittern als Qubits zu nutzen und Gatteroperationen über optische Übergänge mit Hilfe von Lasern durchzuführen.
In dieser Arbeit wird das Potenzial untersucht, einzelne Europiumionen, die in Yttriumoxid Nanokristalle dotiert sind, als stationäre Qubits für einen Quantencomputer zu verwenden. Europium ist ein Seltenerdmetall und zeichnet sich durch außergewöhnlich lange Kernspinkohärenzzeiten bei kryogenen Temperaturen aus, was es zu einem guten Kandidaten für die Speicherung von Quanteninformation macht. Die Kernspinzustände in Europium können durch einen optischen Übergang im sichtbaren Bereich adressiert werden, was schnelle Gatteroperationen ermöglicht. Im Gegensatz zur räumlichen Auflösung einzelner Ionen, wie es bei Ionenfallen-Quantencomputern der Fall ist, besteht hier die Idee darin, einzelne Ionen mit Hilfe von schmalbandigen Lasern spektral aufzulösen. Die Kombination von scharfen, homogenen Spektrallinien einzelner Ionen und einer breiten Verteilung der Linien verschiedenen Ionen im Frequenzraum, sollte es ermöglichen Hunderte von Emittern innerhalb eines Nanokristalls spektral aufzulösen. Dies eröffnet einen neuen Weg zu einer skalierbaren Quantenprozessorarchitektur. Der Nachteil dieses Ansatzes ist die geringe Oszillatorstärke des dipol-verbotenen Übergangs, der in Wirtskristallen mit niedriger Symmetrie nur in geringem Maße erlaubt ist. Um die niedrigen spontanen Emissionsraten zu erhöhen und Fluoreszenzsignale von einzelnen Europium-Ionen zu detektieren, werden die Nanokristalle in einen offenen, faserbasierten Fabry-Pérot-Mikroresonator integriert. Diese Bauart von optischem Resonator zeichnet sich durch ein geringes Modenvolumen von wenigen Kubikwellenlängen sowie durch hohe Gütefaktoren aus. Das ermöglicht eine starke Purcell-Verstärkung des schwachen optischen Übergangs. Darüber hinaus koppeln die Emitter im Inneren des Resonators an eine Gaußmode, die einfach durch den optischen Aufbau zu führen ist. Dies erlaubt eine hohe Wahrscheinlichkeit, ein Photon zu detektieren, das im Inneren des Resonators emittiert wurde.
Um die Europium-dotierten Nanopartikel im Inneren des Resonators zu platzie-

ren, wird ein planarer Spiegel mit einer kolloidalen Lösung, die die Nanopartikel enthält, mit einem Aerosoldruck-Verfahren bedruckt. Diese neue Methode wird in der vorliegenden Arbeit erläutert und die Druckergebnisse werden im Hinblick auf die Homogenität der räumlichen Verteilung der Partikel charakterisiert. Weiterhin wird die Ausbeute an einzelnen 60 nm Partikeln pro Fläche einer Resonatormode evaluiert. Letzteres ist eine nicht triviale Aufgabe, da Nanopartikel in Lösung die Tendenz haben Agglomerate zu bilden.
Der nächste Schritt auf dem Weg zur Resonator-verstärkten Spektroskopie von Europium-Ionen besteht darin, die Längenfluktuationen des Spiegelabstands auf wenige Pikometer zu stabilisieren, d.h. einen Bruchteil eines Atomradius. Das ist notwendig, um die hohe Finesse oder Qualitätsfaktor des Resonators zu nutzen, was zu einer schmalen Linienbreite führt, die sich mit der Linienbreite des Emitters überlappen muss. Diese hohe Anforderung wurde mit Hilfe eines selbstgebauten Aufbaus erreicht, der eine hohe mechanische Steifigkeit mit einer Grob- und Feinabstimmung aller Resonatorachsen kombiniert. Letzteres ist notwendig, um den Faserspiegel auf einem Nanopartikel zu positionieren und die Resonatorlänge auf eine gewünschte Resonanzbedingung einzustellen. Diese Resonatorplattform wurde dann in ein Durchflusskryostaten eingebaut, welcher sich durch geringere mechanische Vibrationen auszeichnet als ein zuvor verwendeter Closed-cycle Kryostat. Mit diesem Aufbau lassen sich Schwankungen des Spiegelabstands im einstelligen Pikometerbereich erzielen. Wird der Faserspiegel gegen den planaren Spiegel gepresst, entsteht ein monolithischer Fabry-Pérot-Resonator mit reduzierter Längenabstimmbarkeit, aber erhöhter Stabilität. Die Längenfluktuation liegt dann unterhalb eines Pikometers.
Schließlich wurden sechs verschiedene Nanopartikel im Resonatoraufbau bei kryogenen Temperaturen untersucht und verschiedene spektrale Eigenschaften von kleinen Europium-Ionen-Ensembles bestimmt. Die Purcell-Verstärkung der spontanen Emission konnte beobachtet werden, und es wurde eine obere Grenze der homogenen Linienbreite gemessen. Obwohl es nicht möglich war, Fluoreszenzsignale von einzelnen Ionen nachzuweisen, erlauben die bisher gemessenen Parameter eine genauere Abschätzung des von einem einzelnen Ion erwarteten Signals. Die geschätzten Photonenraten sind gering, sollten aber mit der derzeitigen Empfindlichkeit des Aufbaus nachweisbar sein, was die Fortsetzung dieser Arbeit motiviert.

Abstract

Within the field of quantum technologies, quantum computing probably has the greatest potential to generate transformative technological and socio-economical progress. However, up to now it is not clear which hardware design will win the race towards a fault-tolerant and scalable quantum processor capable of solving practical problems. One promising approach is to use the spin degree of freedom of solid-state emitters as qubits and perform gate operations via optical transitions using lasers.
In this work, the potential is investigated of using individual europium ions, doped into yttrium oxide nanocrystals, as stationary qubits for a quantum computing node. Europium is a rare-earth metal and features exceptionally long nuclear spin coherence times at cryogenic temperatures making it a good candidate to store quantum information. The nuclear spin states in europium can be addressed by an optical transition which allows for fast gate operations and facilitates a spin-photon interface. In contrast to spatially resolving individual ions, as it is done in ion trap quantum computers, the idea here is to spectrally resolve single ions using narrowband lasers. Due to a broad distribution of the narrow homogeneous lines of single ions in frequency space, it becomes feasible to spectrally resolve hundreds of emitters within one nanocrystal and opening up a way for a scalable quantum computing platform. The downside of this approach is a low oscillator strength of the dipole-forbidden transition which is only weakly allowed in low symmetry host crystals. In order to enhance the low spontaneous emission rates and make it feasible to obtain fluorescence signals from single europium ions, I incorporate the nanocrystals into an open-access, fiber-based Fabry-Pérot microcavity. This type of cavity features a low mode volume of a few cubic wavelengths as well as high quality factors. Therefore, I can make use of a strong Purcell enhancement of the weak optical transition. In addition, the emitters inside the cavity couple to a well-collectable Gaussian cavity mode leading to a high probability of a photon counting event of the detector from a photon emitted inside the cavity.
In order to incorporate the europium-doped nanoparticles into the cavity, a planar mirror is aerosol-printed with a colloidal solution containing the nanoparticles. This new aerosolprinting method is explained and the printing results are characterized in terms of the homogeneity of the spatial distribution of particles as well as efficiency to obtain single 60 nm nanoparticles within the area of a cavity mode. The latter is a non-trivial task since nanoparticles in solution have the tendency

to form agglomerations.
The next step towards cavity-enhanced spectroscopy of europium ions is to stabilize the cavity length jitter to a few picometer i.e. a fraction of an atomic radius. This is necessary to make use of the high finesse or quality factor of the cavity, resulting in a narrow cavity linewidth which has to overlap with the emitter linewidth. This demanding requirement was achieved using a home-built scanning cavity stage which combines high mechanical stiffness with a coarse and fine tunability of all axes, necessary to laterally position the fiber mirror onto a nanoparticle and set the cavity length to a desired resonance condition. The cavity stage was then mounted into a flow cryostat system which features lower mechanical noise than a previously used closed-cycle cryostat. With this setup it is reliably possible to achieve single-digit picometer cavity length fluctuations with an open cavity. Pressing the fiber mirror against its planar opponent, creates a monolithic Fabry-Pérot cavity with limited length tunability but increased stability below a length fluctuation of a picometer.
Finally, six different nanoparticles were investigated in the cavity at cryogenic temperatures and different spectral properties of small europium-ion ensembles could be determined. The Purcell enhancement of the spontaneous emission could be observed and an upper bound of the homogeneous linewidth was measured. Although, it was not possible to detect fluorescence signals from single ions, the parameters measured so far permit a more precise estimation of the photon flux expected from a single ion. The estimated signal strengths are low but should be detectable with the current performance of the setup, motivating to carry on this work.

Contents

1. Introduction

The Second Quantum Revolution At the beginning of the 20th century, it was almost unimaginable for the fathers of quantum mechanics that it would be possible to isolate and control a single quantum object like an atom or electron. Half a century later, technological applications were invented that are based on the understanding of quantum mechanics. The most prominent examples are the transistor, enabling digital electronics, solar cells and the laser. These new technologies created new economic sectors and boosted economical growth and wealth of humankind. This is now called the first quantum revolution. However, these devices are still macroscopic and only harness the quantum effects of bulk materials. In 1995 it was then achieved for the first time to manipulate the internal states of a single ion trapped inside a vacuum chamber by means of laser radiation [1], [2]. This major achievement let the vision of a second quantum revolution become realistic, where individual quantum systems are employed for technical applications. In particular, the second quantum revolution is about harnessing quantum effects like superposition or entanglement. It soon became apparent that these properties can be used for quantum information processing (QIP), which has become a large field of research in physics within the past thirty years.

The development of new technologies is often linked to economical and military power which attracts the attention of those in charge of governments and large companies. This also applies to the new quantum technologies that are currently being developed. In 2016 the European Union published a Quantum Manifesto[1] which called for a joined initiative of the countries of the EU to launch a large-scale research funding program for future quantum technologies. In 2018 the Quantum Technology (QT) Flagship program started[2], which funds ambitious projects within the field of QIP with a sum of 1 billion euros spent over ten years. The aim of this flagship program is to promote innovation in the four major areas of quantum technologies, namely communication, computing, simulation and sensing and metrology. It also supports European companies in this field to bring quantum research from the laboratory to commercial applications. Other nations like the United States of America, the United Kingdom and China have launched similar programs [3], which highlights the importance and expectations that governments

[1] Quantum Manifesto
[2] `https://qt.eu/`

have. Roberto Viola, Director General of the Communications Networks, Content and Technology at the European Commission in 2020, emphasized that "Quantum is a highly strategic area for Europe. We must master it, [...] to secure our technological sovereignty in a competitive field." [4].

Quantum Computing Within the four major areas funded by the flagship program, building a universal quantum computer capable of solving practical problems is expected to be the hardest task to achieve. Therefore, the Quantum Manifesto lists quantum computing as a long-term goal which will be reached on a timescale of several decades. A universal quantum computer is understood to be capable of running arbitrary quantum algorithms defined by a sequence of single- and two-qubit gate operations [5]. It can be shown that an arbitrary single qubit rotation together with an entangling gate between two qubits (e.g. CNOT-gate) is sufficient to build a universal quantum computer [6]. Furthermore, the hardware platform has to fulfill a few more requirements, known as DiVincenzo's criteria [7]:

1. A scalable physical system with well characterized qubits.
2. The ability to initialize the state of the qubits to a simple fiducial state.
3. Long relevant decoherence times, much longer than the gate operation time.
4. A "universal" set of quantum gates.
5. A qubit-specific measurement capability.
6. The ability to interconvert stationary and flying qubits.
7. The ability to faithfully transmit flying qubits between specified locations.

The last two points become only necessary when quantum communication channels are involved in the QIP ecosystem. However, since it will be hard to realize millions of interacting qubits within a single processor node, there are ideas of entangling several smaller nodes by using photons as flying qubits transmitted via quantum channels and therefore perform a distributed quantum computation. This finally will lead to the establishment of the so-called quantum internet [8]. To build up such an infrastructure, the European Union launched the European Quantum Communication Infrastructure (EuroQCI) program in 2019, where all member state now take part [9].

The power of quantum computation also strongly relies on the type of quantum algorithm run on the machine. So far it doesn't appear that a quantum computer will outperform its classical counterpart in all tasks. Only in specific cases quantum algorithms exist that can solve a certain problem at all or provide a speedup.

A list of currently available quantum algorithms can be found on the "Quantum Algorithm Zoo" webpage [3]. Among these algorithms there are a few prominent examples, like Shor's [10] or Grover's algorithm [11], which might turn a future quantum computer into such a powerful tool that the prospect of reaching this goal was sufficient to convince many governments and companies to heavily invest into this endeavor.

For the classical computer it became clear quite quickly that silicon-based transistor technology will be the best choice to build the hardware from. Contrarily, there are many approaches out now how to build a quantum processor node. A short overview over the most promising platforms can be found in the appendix of [12]. Historically, the first approach was to use trapped ions, where local gate operations are done using lasers which address spatially-separated individual ions [1]. Two-qubit gate operations to create entanglement are achieved via common vibrational modes of the ion chain inside the trap [13], [14]. The other early stage platform used nuclear magnetic resonance (NMR) techniques in ensembles of atoms [15]. The most mature computing platform to date are probably superconducting quantum circuits [16]. Here, artificial atoms are created using superconducting electrical circuits at millikelvin temperatures. Another approach which provides a favorable scaling behaviour in terms of number of qubits per node are arrays of neutral atoms trapped in optical lattices [17], [18]. Purely photonic circuits also provide an interesting platform since they don't require a cryogenic environment or ultra-high vacuum chambers [19], [20]. In the past decade, quantum emitters in the solid-state became another promising approach to build a quantum processor [21], [22]. In this field, a great variety of emitters and solid-state host materials can be employed. To name just a few, donors in silicon [23], [24], color centers in diamond [25]–[27], molecular spins [28], [29], quantum dots [30], [31] and last but not least rare-earth ions (REI) [32]–[36] are currently investigated.

The SQUARE Project The work presented in this thesis was part of the SQUARE project within the QT flagship program. SQUARE is the acronym for "Scalable Rare-Earth Ion Quantum Computing Nodes" and the project consortium consisted of six university research groups and two companies. The goal of this project was to establish a new type of quantum computing hardware using individual rare-earth ions doped into solid-state hosts as qubits. REIs randomly doped into crystalline hosts feature several aspects that meet DiVincenzo's criteria:

- Scalability in the number of qubits due to a large ratio ($\sim 10^4 - 10^5$) of the inhomogeneous broadening of spectral lines to the homogeneous linewidth of a single rare-earth ion.

[3] `https://quantumalgorithmzoo.org/`

- Qubit encoding in the nuclear spin degree of freedom which possesses outstanding coherence times ranging from milliseconds to hours.
- Spin-photon interface due to an optical transition coupling to the qubit states.
- Fast single-qubit gate operations via driving the optical transition by strong laser pulses.
- Two-qubit gates via a magnetic or electric dipole blockade mechanism (see Section 2.6).
- State-selective readout of the qubit state due to narrowband optical transitions at cryogenic temperatures.
- Quantum communication spin-photon interface with an optical transition in the telecom band at 1.5 µm in erbium.

These different aspects are not realized in every species of the REIs but it would be possible in the future to co-dope multiple species into the same host crystal and thus assign specialized tasks to certain species. Further details on how a quantum processor node based on rare-earth ions could look like are sketched in the "Roadmap for Rare-Earth Quantum Computing" which was published by the SQUARE consortium [37]. It should be noted that there is also an ensemble-based approach towards quantum computing with REIs using stoichiometric crystals lightly doped with another REI species to create clusters of spectral satellite lines [36]. Those satellite lines are then ensembles of optically addressable spin qubits. Several detuned satellite lines emerge from the crystal lattice mismatch around a dopant ion creating a handful individually addressable qubits. However, it is not straightforward how it will be possible to scale up the number of qubits in this approach. Whereas the single-instance approach we are following here, could provide hundreds to thousands of qubits per node with a good interconnectivity between the qubits, as simulations have shown [38]. The ensemble approach, on the contrary, circumvents another issue of the rare-earths: the long lifetimes of the optically excited states ($\sim 0.1 - 10\,\mathrm{ms}$) and thus low spontaneous emission rates. This is due to the dipole-forbidden 4f-4f transitions, which we would like to harness, that are only weakly allowed in low symmetry hosts.

In order to still be able to detect fluorescence signals from single ions one can make use of the Purcell-effect (Chapter 3) in optical cavities to boost the spontaneous emission rate. Using different types of micro-and nanoscale cavity designs, it was possible in the recent years to detect most of the REI species promising for QIP [39]–[51]. Within the SQUARE consortium we investigated various interesting species like cerium, europium, neodymium, ytterbium and erbium in the different

research teams participating in the project. Therein, my task was to detect single Europium ions inside yttrium oxide nanocrystals for the first time. Europium features a particularly low branching ratio of less than one percent (Section 2.4) together with a long excited state lifetime of 2 ms in the nanocrystals used here. To detect single ions it is necessary to incorporate them into an optical cavity with high Purcell-factor. To do so, we built an open-access, fiber-based Fabry-Pérot microcavity stage (Chapter 5), dispersed the europium-doped yttria nanocrystals onto the planar mirror (Chapter 4) and performed cavity-enhanced spectroscopy at cryogenic temperatures (Chapter 6). So far, it was not possible to detect single ions but we characterized the optical and spin properties of small ion ensembles at cryogenic temperatures and obtained a clearer picture of limiting factors for the single ion detection.

Outline of this Thesis In Chapter 2 I explain the level scheme of europium ions inside a low-symmetry yttrium oxide host crystal and summarize how the nanoparticles I am using in this work are fabricated. We determined the branching ratio of the two relevant optical transitions, since it is a critical parameter for the estimation of the Purcell enhancement and single ion countrates later. The second chapter closes with a summary of the findings of a master project that I supervised. Therein, we simulated the expected single- and two-qubit gate fidelities, respectively, for a quantum processor node based on europium ions. As already briefly motivated, optical cavities are necessary to enhance the spontaneous emission rate of the weak transition of europium. I will explain the basics of Fabry-Pérot-type cavities in Chapter 3 as well as the theoretical framework, the Jaynes-Cummings model, of light-matter interactions inside a resonator. The chapter thereafter is denoted to the new method of aerosolprinting nanoparticles on cavity mirrors and the characterization of the printing results. Open-access Fabry-Pérot cavities require careful stabilization of the mirror distance in order to maintain the resonance condition. For the cavity design used here, root-mean-square (RMS) cavity length jitter of only a few picometers are necessary to achieve the designed Purcell enhancement. This stability has to be maintained also at cryogenic temperatures inside a flow cryostat. I will explain the principles of the cavity stage design, the required optics and electronics to stabilize the cavity to 2.5 pm RMS at 10 K. Finally, I investigate the spectral properties of small europium ion ensembles in six different nanoparticles at cryogenic temperatures. The inhomogeneous linewidths are measured as well as the lifetime reduction and the resulting Purcell factors. Furthermore, I performed high-resolution laser scans to resolve a statistical fine structure within the inhomogeneous line and refined the search for spectral lines of single ions. Using small ensembles, an upper bound on the homogeneous linewidth is measured such that the complete set of cavity quantum electrodynamics (QED) parameters describing the system could be evaluated. Finally, I present an estimation of the countrate from a single ion under realistic circumstances. The

thesis concludes with a summary of the results and an outlook on how to improve different aspects of the experiment in the future.

2. Europium-doped Yttria Nanocrystals for Quantum Information Processing

The element europium belongs to the group of rare-earth metals. These comprise the elements scandium and yttrium as well as the group of the lanthanides in the periodic table. Although the name suggests a scarce occurrence in the Earth's crust, this is actually not the case, and the total amount of metals like copper and gold is estimated to be lower than that of the rare-earth metals [52]. But the rare-earth atoms, often bound in oxides, appear spatially distributed in lower densities and thus are harder to extract in large amounts, hence the name. The different atom species were mostly discovered during the 18th and 19th centuries with europium being one of the latest, as it was discovered not before 1901 [53].

The advent of modern technologies in the second half of the 20th century created a boost for the applications of rare-earth metals. To name just a few, manufacturing strong permanent magnets is achieved using neodymium. Europium is used to generate red colors in LCD displays or fluorescent lamps, and almost all species can be used to build lasers for different colors. However, as showcased in the introduction chapter, rare-earths feature interesting properties not only for many classical technologies but also for future quantum technologies. Their unique electronic level structure makes them promising candidates for an efficient spin-photon interface [54].

In this chapter, I will briefly explain the level scheme of europium ions doped into an yttrium oxide host matrix. Scaling down the host crystal size from bulk to nanoscales was an important step to incorporate rare-earth ions in microcavities. I will summarize how it was possible to reduce the crystal size without loosing the good coherence properties of the rare-earths. An important parameter for the estimation of the Purcell factor is the branching ratio of the excited state into the desired, Purcell-enhanced, transition. We therefore determined this parameter for the nanoparticle (NP) batch used for cavity-enhanced spectroscopy. Then, I will summarize the properties of the $^5D_0 \rightarrow {}^7F_0$ and $^5D_0 \rightarrow {}^7F_2$ transitions, which are the optical transitions that we are able to Purcell-enhance in the cavity. The chap-

ter closes with an outline how single europium ions can be harnessed as qubits for a quantum computer node and I will present simulations on the gate performance that I did together with the master student Christian Rentschler.

2.1. Level Scheme

This section summarizes the relevant level scheme of europium inside low symmetry hosts. Further information can be found in the paper of Binnemanns [55] and in [54]. Europium belongs to the lanthanide series which are the elements with proton numbers 57-71 in the periodic table. They share similiar chemical properties since they all exhibit completely filled outer lying $5s$, $5p$ and $6s$ orbitals. The electronic configuration of the lanthanides is $[Xe]6s^2 4f^n$, where the 4f shell is filled up with electrons with rising proton number. Here, I use yttrium oxide (Y_2O_3), also called yttria, as a host crystal. The lanthanide doping atoms randomly replace the yttrium atoms in the host matrix. They form coordinate bonds, which, in yttria, leads to a trivalent ionic charge state, La^{3+}, hence the name rare-earth ions (REI).

The electronic configuration of europium doped into an yttria host crystal is therefore $[Xe]4f^6$. Six electrons partially fill the $4f$ orbitals, which feature smaller radii than the filled $5s^2$ and $5p^6$ orbitals. This leads to an effective shielding of the $4f$ orbitals from electro-magnetic pertubations of the environment, giving rise to the exceptionally good coherence times of the optical $4f$ transitions, as will be shown later. The downside of the transitions within the $4f$ shell is their dipole-forbidden nature, leading to weak oscillator strengths and thus long optical lifetimes. To observe these forbidden transition at all, the europium atoms have to be doped into a host crystal with low symmetry to weakly allow transitions within the $4f$ orbitals by admixing other orbitals.

The electron repulsion and spin-orbit coupling already gives rise to 295 $^{2S+1}L(\tau)_J$ non-degenerate levels. Here, τ is a quantum number to differentiate between levels with identical S and L. The pertubation caused by the crystal-field further splits these levels by lifting the $J = |L - S|, \ldots, L + S$ degeneracy, dependent on the point group symmetry of the host crystal (see Table 4 in [55]). The europium ions inside an yttria host matrix can replace the yttrium ions at the monoclinic C_2 and trigonal C_{3i} (S_6) symmetry sites. At the C_2 site they feature a fully-lifted degeneracy i.e. all spectral lines can be observed. The C_{3i} site is centrosymmetric and thus no electric dipole transitions are allowed and the J-degeneracy is not fully lifted.

For this work, I am only interested in the optical transitions between the ground

state manifold ^7F_J and the next higher lying term ^5D_J. The transition between the lowest lying levels is $^5D_0 \rightarrow {}^7F_0$ at 580.6-580.8 nm in yttria, which is only weakly allowed at the C_2 symmetry. Another transition of interest for the experiments presented here is the $^5D_0 \rightarrow {}^7F_2$ transition at 611 nm. This transition is called a hypersensitive transition since it's oscillator strength strongly depends on the host crystal symmetry. It has the largest branching ratio of all transitions of the considered manifold (details see Section 2.4). The only transitions between the considered levels which is present for ions at the C_{3i} symmetry, are the two magnetic dipole transitions $^5D_0 \rightarrow {}^7F_1$. Since I don't address these transitions, the spectroscopy results presented in the following chapters always refer to europium ions at the C_2 site.

Eu^{3+} is a non-Kramer's ion hence no net electron spin is present. However, both the $^{151}Eu^{3+}$ and $^{153}Eu^{3+}$ europium isotopes, being equally abundant, feature a nuclear spin of $I = 5/2$. Due to the hyperfine splitting in the ground and excited state a single europium ion exhibits nine ground state transitions at zero magnetic field. As will be explained in detail later, the hyperfine states posses an outstanding coherence time and thus a suited for quantum information storage. Since they can be addressed directly via an optical transition the level scheme of europium provides a good candidate for a spin-photon interface for quantum technologies. The level scheme of the transitions relevant for this work is shown in Fig. 2.1. A room-temperature spectrum of europium-doped yttria nanoparticles was measured in a confocal microscope setup, by exciting the ions off-resonantly via the phonon-broadened $^7F_1 \rightarrow {}^5D_1$ transition using a 532 nm laser. The spectrum together with an assignment of the transitions is shown in Fig. 2.4.

2.2. Nanoparticle Fabrication and Characterization

Rare-earth ions doped into bulk solids can feature among the best optical and nuclear spin coherence times for any solid-state emitters. For example, sub-kilohertz optical homogeneous linewidths have been measured for europium doped into Y_2SiO_5 crystals at cryogenic temperatures [54]. Using dynamical decoupling techniques and high magnetic fields, Zhong et al. [57] could show a record nuclear spin coherence time of over six hours. However, bulk crystals are not suitable for integration into Fabry-Pérot microcavities. One approach is to thin down the bulk crystal to form a micrometer thick membrane which can be bonded onto the planar cavity mirror [58]. However, using a membrane is not suitable to obtain a high spatial density of ions, needed for strong dipole interactions to implement two-qubit gate operations (see Section 2.6), but at the same time coupling only a

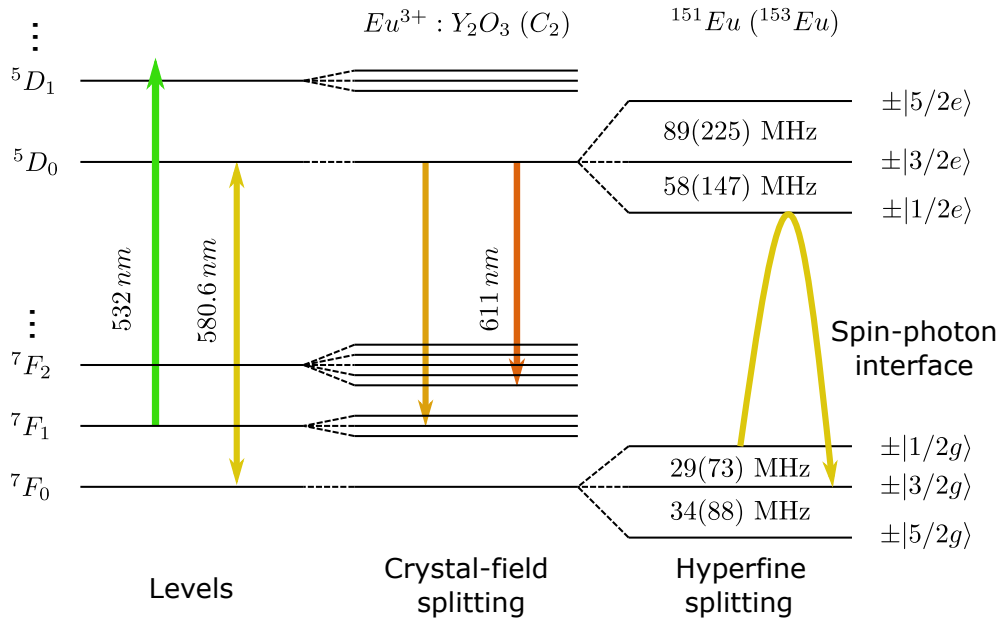

Figure 2.1: Level scheme of the relevant transitions of europium in an yttria host matrix replacing the yttrium atoms at the C_2 symmetry site adapted from [56]. The colored arrows mark laser excitation paths (green: off-resonant excitation at room-temperature, yellow: resonant excitation in cavity experiments) as well as optical decay paths which can be detected in the confocal microscope and cavity setups. The curved yellow arrow marks the transition between two possible qubit states in the hyperfine levels which can be driven and read out by the resonant optical transition (see Section 2.6) and establishes a spin-photon interface.

limited number of $10^3 - 10^4$ ions to the cavity field in order to spectrally resolve individual ions. These requirements can only be fulfilled in nanocrystals. In order to minimize the scattering losses inside the cavity (see Section 3.5), nanoparticle diameters below 100 nm are necessary. It is a non-trivial task to scale down the crystal sizes while maintaining the good coherence properties of the rare-earth ions. The group of Dr. Philippe Goldner at Chimie ParisTech in Paris, has researched the mechanisms leading to a linewidth broadening in Eu:Y_2O_3 nanoscale crystals for over a decade now [59]–[64]. They are able to produce nanoparticles down to 60 nm diameter with homogeneous linewidths as narrow as 56 kHz, which are about two orders of magnitude larger than the best bulk values. The nuclear spin coherence times of several milliseconds are only about a factor of ten less than the bulk values (14-16 ms [65]).

The nanoparticle batch used for the experiments in this thesis were synthesized by Dr. Shuping Liu in the group of Dr. Philippe Goldner using homogeneous precipitation. A high content of 5 mol/l urea is added in the initial aqueous solution to control the size of the nanoparticles. Afterwards the amorphous Eu^{3+}:YCO

nanocrystals are annealed for 18 h at 800 °C where they form polycrystalline yttria nanoparticles of an average size of 60 nm with a doping concentration of 0.3% in our case [63]. The exact size distribution of this batch is not known but 100 nm particles produced in a similar manner showed a width of the size distribution of about 30 nm [63]. It was found that a high-power oxygen plasma annealing (2 x 3 min at 900 W power using a 2.45 GHz microwave source) can heal oxygen-related defects in the crystal lattice and increases the optical coherence by a factor of three to 5.68 ± 0.21 µs in comparison to the untreated particles [64], [66].

They also measured the temperature dependence of the homogeneous linewidth in photon echo (PE) as well as spectral hole burning (SHB) measurements. The main difference between the two spectroscopy techniques is the timescale over which the linewidth is averaged. Thus, also the laser linewidth over the respective timescale becomes important. In their case, SHB measurements average over about one millisecond leading to much broader linewidths than for the PE measurements, since at these timescales spectral diffusion becomes visible. The temperature dependence for both measurement types is linear for temperatures below 10 K due to broadening caused by tunneling two-level systems (TLS). For higher temperatures the two-phonon Raman process (TPR) leads to a strong T^7 temperature dependent increase of the linewidth [60]. The fits to the temperature dependence for both measurement techniques obtained in [64] are plotted in Fig. 2.2.

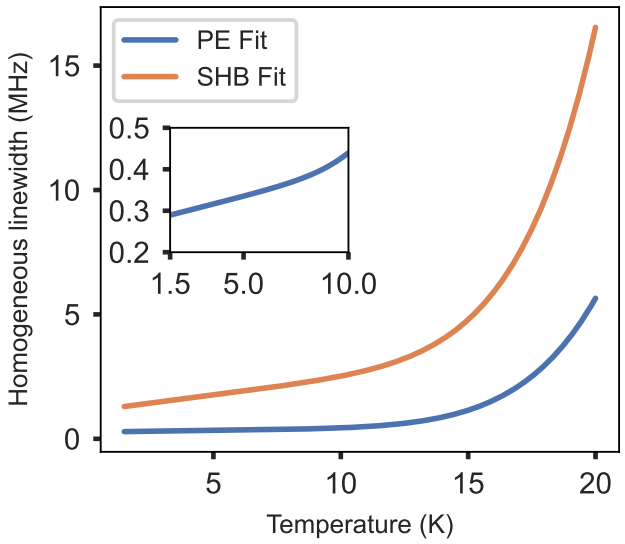

Figure 2.2: Temperature dependence of the homogeneous linewidth of the ${}^5D_0 \rightarrow {}^7F_0$ ground state transition. The curves are fit functions to data taken by [64] in a photon-echo (PE, blue) and a spectral-hole-burning (SHB, orange) measurement, respectively.

In my attempts of resolving spectral lines of individual europium ions presented in Chapter 6, I have to average the countrates over several seconds. Therefore, I expect to see homogeneous linewidths which are limited by spectral diffusion and thus are about 1-2 MHz broad.

2.3. Number of Ions in a Single Nanoparticle

In order to estimate the number of europium ions within a nanoparticle, I use the concentration of yttrium atoms occupying the C_2 symmetry site per volume $c_Y = 1.6 \cdot 10^{22}\,\mathrm{cm}^{-3}$ [67], calculate the volume of a spherical nanoparticle of given diameter and replace the fraction of yttrium atoms by europium atoms, given by the doping concentration of $c_{Eu} = 0.003$:

$$N(d_{NP}) = c_{Eu}\, c_Y\, \frac{4}{3}\pi \left(\frac{d_{NP}}{2}\right)^3 . \tag{2.3.1}$$

The average number of ions per nanoparticle for a range of diameters is plotted in Fig. 2.3.

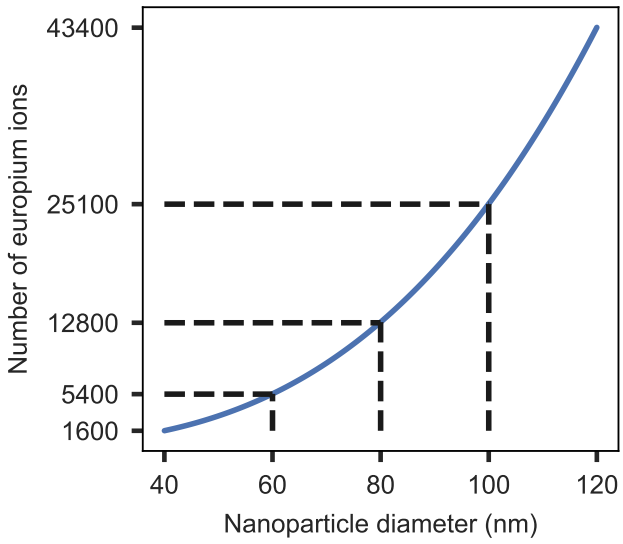

Figure 2.3: Average number of europium ions inside an yttria nanoparticle dependent on its diameter.

2.4. Determination of Branching Ratios

The branching ratios of the $^5D_0 \rightarrow {}^7F_0$ and $^5D_0 \rightarrow {}^7F_2$ transitions are important parameters for a precise determination of the expected Purcell enhancement and the single ion countrate estimations presented in Chapter 6. Therefore, the master student Xiaoyu Yang, under my supervision, determined the branching ratios of those transitions for the same batch of nanoparticles that I also used in the cavity experiments. The procedure to measure a europium spectrum with good signal-to-noise ratio (SNR) in a confocal microscope setup was the following:

- Spin-coat aquaeous nanoparticle solution onto a glass substrate[4].
- Search for a large agglomeration of nanoparticles with good SNR in the scanning confocal microscope setup.
- Excite the ions off-resonantly and cw with a 532 nm laser[5] at a power of 6 mW in front of the objective.
- Take a europium spectrum with a wavelength and intensity calibrated grating spectrometer[6].
- Record a background spectrum by moving the laser focus about 5 µm away from the agglomerate to obtain the spectrum of the bare glass substrate.
- The Europium spectrum is background corrected, normalized and the intensity calibration is applied.

The resulting spectrum of the $^5D_0 \rightarrow {}^7F_J$ transitions can be seen in Fig. 2.4. All decay channels of the $^5D_0$ excited state can be identified except of the $^7F_6$ manifold. However, the latter is reported to have a vanishing contribution to the overall intensity [68]. Looking at the inset in Fig. 2.4, which shows the spectral window from 578 nm to 605 nm, a few additional peaks can be seen. The C_{3i} site is centrosymmetric and thus no electric dipole transitions are allowed and only the $^5D_0 \rightarrow {}^7F_1$ magnetic dipole transitions are observed [68]. According to Table 4 of [55], the trigonal symmetry class of the C_{3i} point group results in two sublevels i.e. the spectrum should reveal two additional transitions of the $^7F_1$ multiplet. Forest and Ban pinned down the two C_{3i} transitions in yttria at 582.2 nm and 592.5 nm by lifetime measurements of the different lines [68]. This reveals much longer lifetimes of the C_{3i} lines compared to the C_2 lines (5 ms vs. 1 ms). Furthermore, Forest and Ban assign the weak lines in the 580-600 nm spectral window to emission from the $^5D_1$ excited state.

[4] Laseroptik GmbH, Hannover
[5] *Cobolt Samba*, Hübner Photonics
[6] *Shamrock 500i with iVAC316 LDC-DD camera* and 150 l/mm grating, Andor Technologies

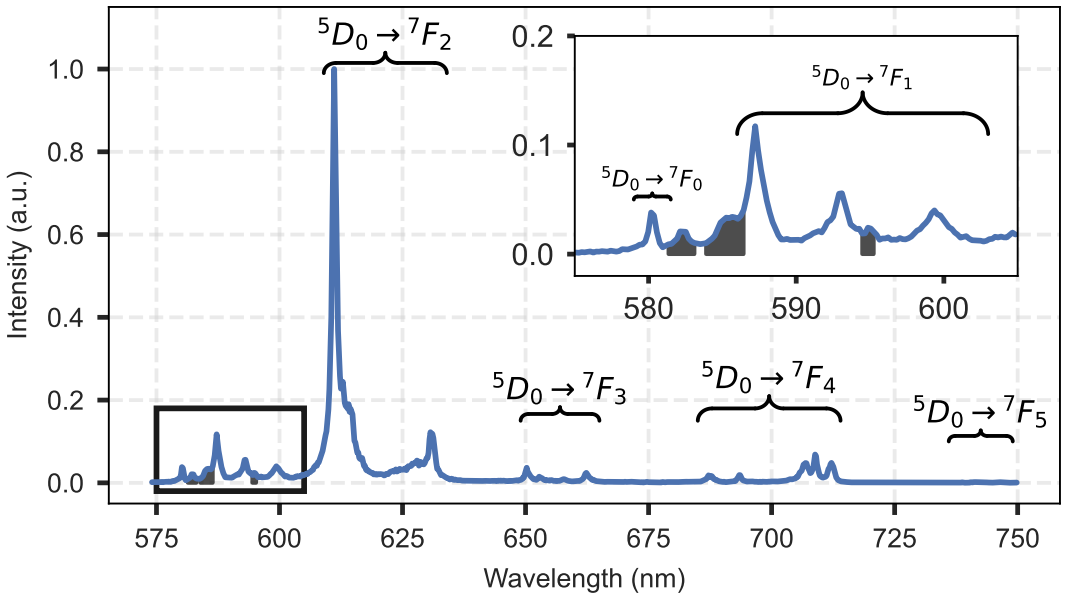

Figure 2.4: Spectrum of the $^5D_0 \rightarrow {}^7F_J$ transitions of europium-doped yttria nanocrystals adapted from [56]. The inlet shows a zoom into the spectral region from 578 nm to 605 nm and the grey areas are subtracted from the total area beneath the spectrum for the calculation of the branching ratios.

We are only interested in the branching ratio of ions at C_2 symmetry site, which in the cavity experiments will be excited resonantly on the $^7F_0 \rightarrow {}^5D_0$ transition. However, it is known that an energy transfer mechanism between the $^5D_0$ levels of the C_2 and C_{3i} exists. Since the $^5D_0$ (C_2) has a lower energy than the $^5D_0$ (C_{3i}) level, the transfer of energy from the C_2 site ions is mediated by a phonon absorption and thus has a vanishing contribution at cryogenic temperatures [69]. Therefore, the spectrum of the Europium ions at the C_{3i} symmetry and lines from the $^5D_1$ emission are subtracted from the total area of the spectrum (grey areas in Fig. 2.4). To extract the branching ratio of the $^5D_0 \rightarrow {}^7F_0$ transition, which is limited by the spectrometer resolution, a Gaussian function is fit to the peak and a wavelength range of eight sigma around the peak center is considered as the spectral area of the peak $I_{J=0}$. The data points as well as the considered red peak area are shown in Fig. 2.5a). The branching ratio is determined by the division to the integral over the whole spectrum I_{tot} corrected by the grey areas:

$$\zeta_{J=0} = \frac{I_{J=0}}{I_{tot}} = 0.007 \pm 0.001. \tag{2.4.1}$$

The error is estimated from changing the integration limits and the background subtraction value. This result is within the range of values that Tobias Krom

has already measured for a different sample [70] and about half of the previously assumed ratio of $1/62 = 0.016$ by [67].

Since I am able to collect also the emission from the ${}^5D_0 \rightarrow {}^7F_2$ transition in the cavity experiments, we also calculated the respective branching ratio $\zeta_{J=2}$. In the following, by refering to this branching ratio, I mean just the emission into the strongest transition of the $J = 2$ multiplet at 611 nm. In the cavity experiments, the narrow cavity line will just partially overlap with this transition and thus the others are not relevant to us. The branching ratio is determined in the same way as before, but a Lorentzian line is fitted to the data since the spectrometer resolution is not limiting here. The integral is then taken over a wavelength range of eight full width at half maximum (FWHM) around the highest peak as depicted in Fig. 2.5b). This results in a branching ratio of:

$$\zeta_{J=2} = \frac{I_{J=2}}{I_{tot}} = 0.36 \pm 0.03 \tag{2.4.2}$$

The error was estimated by using different sizes of the integration window since this has the largest influence.

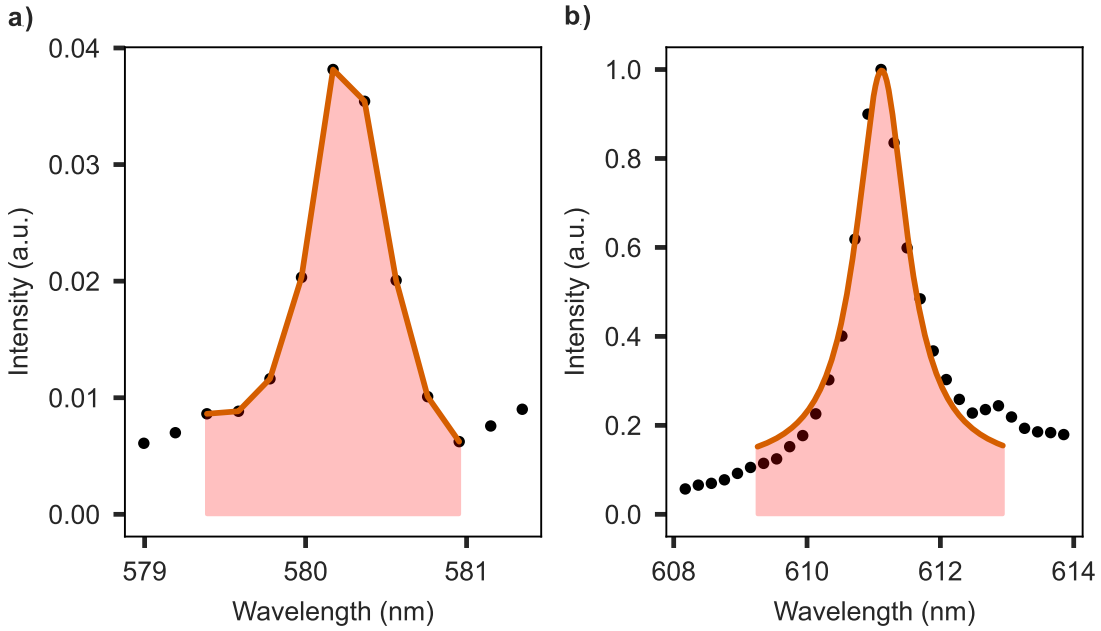

Figure 2.5: Cuts of the spectrum shown in Fig. 2.4 (black points) around the $J = 0$ (a) and the $J = 2$ (b) transitions. The branching ratios are extracted using the red areas under the fitted curves. In (a) the area is spanned by straight connections between the datapoints since the spectrometer resolution is limiting here. For the spectral line in (b) a Lorentzian fit is done to determine the area under the peak.

2.5. Properties of the $^5D_0 \rightarrow {}^7F_0$ and $^5D_0 \rightarrow {}^7F_2$ transitions

Finally, I summarize the most important properties of the two optical transitions of europium-doped yttria nanoparticles at cryogenic temperatures in Table 2.1. The values without reference were measured by people in the group. Furthermore, I give

Parameter	$^5D_0 \rightarrow {}^7F_0$ **transition**	$^5D_0 \rightarrow {}^7F_2$ **transition**
λ_{center}	580.86 nm	611.7 nm
ζ_J	0.007 ± 0.001	0.36 ± 0.03
γ_{inh}	27 GHz [64]	-
γ_h	56 kHz (PE) / 1.1 MHz (SHB) [64]	680 ± 20 GHz
T_2/T_2^*	5.67 ± 0.21 µs / 0.29 µs [64]	-
T_1	2.0 ± 0.1 ms	2.0 ± 0.1 ms

Table 2.1: Summary of the properties of the two optical transitions relevant for this thesis. The parameters are determined in 0.3%Eu:Y_2O_3 nanoparticles of 100 nm and 60 nm average diameters at cryogenic temperatures. The homogeneous linewidths and coherence times measured by [64] were measured at 1.5 K. γ_{inh} (γ_h) denotes the inhomogeneous (homogeneous) linewidth, T_2 (T_2^*) the coherence (pure dephasing) time and T_1 the optical lifetime.

an overview of the properties of the hyperfine transitions in yttria nanoparticles at liquid helium temperatures in Table 2.2. The values taken from [61] were measured for nanoparticles of 400 nm diameter composed of 130 nm crystallites and a doping concentration of 0.5%. The parameters listed here are the relevant qubit properties for a future quantum processor node based on europium ions.

2.6. Europium Qubits for Quantum Information Processing

In order to establish a quantum computer processor node inside a europium-doped nanoparticle, we first need to define the qubit states and how they can be controlled and read out. Since the ground state hyperfine levels of both europium isotopes feature long coherence times, they are well-suited for qubit encoding. Thus, two of the three ground state HF levels are defined as logical qubit and the resonant optical transition at 580 nm is used as a spin-photon interface to perform fast

Parameter	Value
$\gamma_{inh,spin}$	$107 \pm 8\,\mathrm{kHz}$ [61]
$\gamma_{h,spin}$	$250 \pm 38\,\mathrm{Hz}$ (SE) / $39 \pm 3\,\mathrm{Hz}$ (DD) [61]
$T_{2,spin}$	$1.3 \pm 0.2\,\mathrm{ms}$ (SE) / $8.1 \pm 0.6\,\mathrm{ms}$ (DD) [61]
$T_{1,spin}$	$2.7 \pm 1.5\,\mathrm{s}$ (short) / $32 \pm 13\,\mathrm{s}$ (long)

Table 2.2: Summary of the properties of the ground state hyperfine transitions of europium-doped yttria nanoparticles. SE abbreviates spin-echo and DD stands for a dynamical decoupling sequence being used to extend the coherence time. $\gamma_{inh,spin}$ ($\gamma_{h,spin}$) symbolizes the inhomogeneous (homogeneous) linewidth of the hyperfine transitions and $T_{1,spin}$ ($T_{2,spin}$) the spin (coherence) lifetime.

control operations on the qubit and to read out its state. DiVincenzo has shown that an arbitrary rotation on the Bloch sphere of the qubit (single qubit gate (SQG)) together with a two-qubit gate to entangle different qubits is sufficient to implement an arbitrary unitary operation on a number of qubits and hence to build a universal quantum computer [6]. An introduction to quantum computing and gates can be found in the book of Nielson and Chuang [5] . The two ground hyperfine states defined as the qubit states together with the optically excited state make up a Λ-level scheme in europium. This can be used to implement single-qubit rotations in various ways. For example a two-photon resonant Raman process [71] can be used, the dark state scheme (DSS) proposed by Roos and Mølmer [72] or a fractional-STIRAP [73]. Due to a different permanent electric dipole moment in the ground and excited state manifold of the optical transition in europium [74], [75], a dipole-blockade mechanism, similiar to the scheme proposed for Rydberg atoms [76], can be used to entangle two europium ions. A scheme to realize a two-qubit CNOT gate via this mechanism was proposed already in 2002 by Ohlsson et al. [32]. Figure 2.6 shows the relevant level scheme and sequence of optical π-pulses to perform such a gate operation.

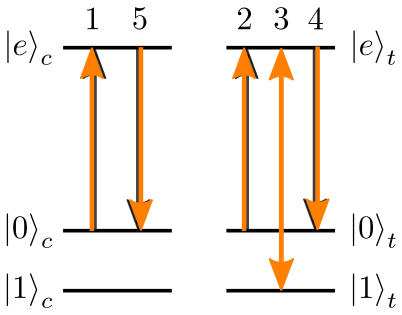

Figure 2.6: CNOT-gate operation using the electric dipole blockade between a control (c) and target (t) ion as proposed by [32]. All arrows denote optical π-pulses to transfer the population between the respective levels. The first pulse excites the population in the $|0\rangle$ state of the control ion. The next three pulses on the target ion implement a NOT operation i.e. a swap of the population between the qubit states. Finally, the last pulse deexcites the control population in the optically excited state. The sketch is taken from [77].

The first pulse excites the control ion if the qubit was in state $|0\rangle$ thereby changing the electric field in its environment. The optical transition of the target ion experiences a frequency shift. Due to the dipolar nature of the interaction, the strength of the shift falls off with the cube of the distance between both ions, $\Delta\mu \propto 1/r^3$. Afterwards three π-pulses are applied at the frequency of the initial target transition to swap the population of the target qubit (NOT operation). However, this NOT operation is only successfull if the target ion is still on resonance with the driving laser frequency. If it was shifted out of resonance by the excited control ion, nothing happens to the target qubit state. Finally, the last π-pulse on the control ion brings back the population from the excited state to the qubit manifold.

Within the master project of Christian Rentschler, under my supervision, we investigated the expected performance of such gate operations in a europium-doped yttria nanocrystal. Therefore, he set up a simulation software, carefully tested it and ran parameter sweeps for different types of single- and two-qubit gate operations. The details can be found in his masterthesis [77] and I will just give a summary and present the most important plots of his thesis in the following.

A single europium ion is represented by its six HF states in the ground and excited state manifold. We want to simulate the evolution of its density matrix in an open quantum system approach including population decay and decoherence. The theoretical framework of open quantum systems can be studied in textbooks such as [78]. The dynamics of such a system is described by the Lindblad master equation:

$$\dot{\rho}_S(t) = \mathcal{L}\,\rho_S(t), \tag{2.6.1}$$

with the Lindblad-Liouville superoperator $\mathcal{L}$ incorporating the Hamiltonian of the europium atom, the electro-magnetic driving field and a dipol interaction term representing the coupling of the atomic transitions to the driving field. Furthermore, $\mathcal{L}$ incorporates the Lindblad operators generating population decay and decoherence. The driving fields are strong coherent light pulses. We describe them as classical fields satisfying Maxwell's equations since in the full quantum mechanical picture the photon Hilbert space would become too large and solving the problem intractable.

Christian Rentschler then wrote a Python program called Cavity-Light-Matter-Simulator (CALM) which uses numerical methods to solve the time-dependent Lindblad equation for each given time step and thus the evolution of the qubit state vector on the Bloch sphere. CALM is based on the open-source Python package QuTIP (Quantum Toolbox in Python) which provides master equation solvers. Although the name suggests it, for the results presented here, no cavity effects are taken into account since we assumed the situation of the bad cavity regime $\kappa \gg \gamma$ such that the light fields inside the cavity appears to build up and decay instantaneous. CALM was then used to calculate the fidelity of a gate operation, defined as:

$$\mathcal{F}_{gate}(\rho_{in}, \rho_{out}) = \left(Tr\sqrt{\sqrt{\rho_{in}}\rho_{out}\sqrt{\rho_{in}}} \right)^2 . \tag{2.6.2}$$

It describes the overlap between the qubit state before (ρ_{in}) and after (ρ_{out}) the gate operation. Sometimes also the infidelity, $p = 1 - \mathcal{F}_{gate}$, is calculated, which expresses the probability that a gate operation failed.

The parameters entering the simulation such as population decay and decoherence rates as well as HF splittings were taken for europium-doped yttria nanocrystals. Since the HF oscillator strengths are not known for yttria, we took the numbers for Eu:Y_2SiO_5 given in [79]. As the decoherence rate or coherence time T_2 limits the fidelity for longer pulses and thus longer gate durations, a realistic value of $T_2 = 5\,\mu s$ was taken. The simulation revealed that we also cannot make the pulses arbitrarily short and strong and thus the Rabi frequency high, since AC Stark shifts are detoriating the gate operation. These AC Stark shift emerge from the multilevel structure of europium since off-resonantly driven neighboring HF-levels shift the transition frequency out of resonance. We found that it is therefore most beneficial to use the lowest lying $|0\rangle := |3/2g\rangle$ and $|1\rangle := |5/2g\rangle$ states as qubit and consider only the ^{153}Eu isotope due to the larger splitting. The optical transitions to the $|1/2e\rangle$ state are used to coherently drive the gate operations. The qubit coherence time was assumed to be $T_{2,spin} = 1\,ms$.

The different types of single qubit gates as described above were simulated and the dependencies on different pulse shapes (Gaussian, sechyp, square) and their

parameters such as the duration and detuning were plotted. We evaluated the infidelity averaged over the six different axial pure states on the Bloch sphere used as input states of the gate operation. Minimum infidelities for NOT-operations of $1.6 \cdot 10^{-2}$ were obtained for square pulses using the DSS scheme. In the initial proposal by Roos and Mølmer they used sechyp pulses to drive the optical transition which are more robust against detunings. For the single instance approach simulated here, we found that truncated Gaussian-shaped or square pulses perform better. The trajectory of the qubit Bloch vector on the Bloch sphere during a single qubit NOT gate operation using the DSS scheme with Gaussian pulses is depicted in Fig. 2.7a). Even lower infidelities of $2.4 \cdot 10^{-3}$ were found for the NOT-gate using Raman pulses with a detuning of -2 GHz. However, the Raman pulses might be impractical to realize with spectrally dense ion lines. A summary of the best infidelities for the different types of single-qubit gates can be seen in Fig. 2.8. Looking at the duration of a gate operation, we obtain values of only a few hundred nanoseconds. Thus, clock frequencies of a future quantum processor node in the few megahertz regime seem possible. This feature is certainly a big advantage of the spin-photon interface realized in europium ions.

We also simulated the performance of a CNOT-gate between two europium ions. When using the DSS to perform the NOT-operation on the target qubit, we could identify parameter regions where the infidelity is below $4.0 \cdot 10^{-2}$ marked as the area inside the black lines in Fig. 2.7.

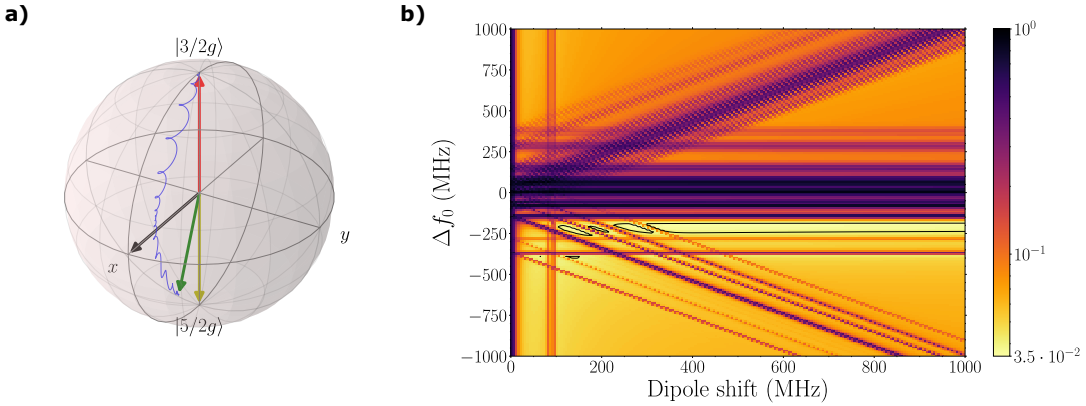

Figure 2.7: a): Evolution of the qubit Bloch vector during a single qubit NOT gate operation using the DSS scheme with Gaussian pulses. The qubit is initially in the $|3/2\,g\rangle$ state (red arrow) and its Bloch vector is rotated along the blue trace to the final state (green arrow) within a duration of 290 ns. The target state is the $|5/2\,g\rangle$ state (yellow arrow) which is reached with an infidelity of 2.5%. The black arrow depicts the dark state. b): Colormap of the infidelity of a CNOT-gate operation using the DSS for the NOT-gate on the target qubit. The infidelity was simulated varying the strength of the dipole shift between both ions as well as the detuning of the optical transitions $\Delta f_0 = f_c - f_t$ of the control and target ions. The black line encloses areas with an infidelity below $4.0 \cdot 10^{-2}$. Both plots are taken from [77].

The total gate time of such a CNOT-gate is about $T_{CNOT} = T_{NOT} + 2T_{c,\pi} \approx 370\,\text{ns}$ and thus not much longer than a single qubit gate. The sweep of the strength of the dipole shift as well as the detuning between the optical transitions of control and target ions Δf_0 reveals large differences in the infidelity. The purple lines with infidelities close to unity stem from the overlap with one of the other hyperfine transitions of this multi-level structure. In general negative detunings are more favorable since the direction of the dipole shift simulated here then shifts all the target lines away from the addressed target transition frequency. Christian Rentschler also calculated the CNOT-gate infidelities for longer optical coherence times, which could be reached by material improvements in the future. Scaling up to $T_2 = 100\,\mu\text{s}$ could result in fidelities of 99%, however at the cost of a longer gate duration of 850 ns. When using only π-pulses to accomplish the CNOT-gate operation the simulation reveals a factor of two higher infidelities and gate durations compared to using the DSS for the NOT-operation as can be seen in the summary of the gates performances depicted in Fig. 2.8.

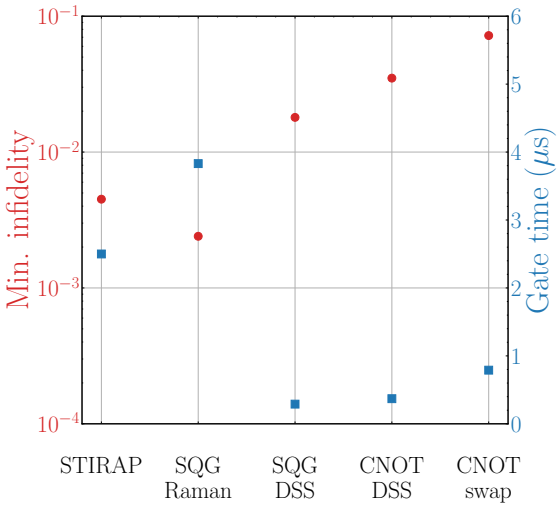

Figure 2.8: Summary of the simulation results for different types of single qubit gates (SQG) as well as CNOT gates using the dipole blockade mechanism and either the DSS or three π-pulses to perform the NOT-operation on the target ion. The red dots show the minimum, averaged infidelities whereas the blue squares depict the total duration of the gate operation. The graph is taken from [77].

During this master project, Adam Kinos in the group of Prof. Stefan Kröll at Lund University also performed a detailed analysis of gate operations using europium qubits in a YSO host material [38], [80], [81]. It should be noted that they also considered another type of two-qubit gate, which is a controlled-phase gate, which they called interaction gate. For this type of gate operation, both qubits are excited simultaneously and the dipole shift imprints a phase shift between both transitions which is mapped onto the qubit by deexciting both ions on the same pathway. This gate requires less strong dipole interactions thus increasing the connectivity and thus number of ions that can be entangled.

3. Fiber Fabry-Pérot Microcavities

In this chapter, I will briefly introduce the theoretical concepts to understand the experimental setup and measurements presented in the following chapters. I will start with a brief motivation why to use fiber-based microcavities for quantum optics experiments. Afterwards, the parameters to describe a Fabry-Pérot type cavity are summarized. The fabrication of microscale cavity mirrors on the end-facet of a single-mode optical fiber will be explained and how the high reflectivity of the mirror coating is achieved. Subsequently, the Jaynes-Cummings model to describe light-matter interactions inside an optical resonator will be briefly introduced and the Purcell factor is derived. Furthermore, a generalization of the Purcell enhancement of two optical transitions within the same cavity is presented. The chapter closes with a calculation of different cavity parameters to estimate the cavity performance.

3.1. Motivation

At the advent of the 20th century two french physicists, Charles Fabry and Alfred Pérot, reported about a new type of interferometer consisting of two planar, silver-coated plates [82], [83]. Their apparatus featured screws to carefully align the plates such that they observed interference fringes when the plates became parallel. This simple experimental setup became known as Fabry-Pérot interferometer (FPI) and is nowadays a standard type of optical resonator used in many applications ranging from laser resonators to gravitational wave detectors.

Although Fabry and Pérot already anticipated that their new type of interferometer might be used for various purposes, it took about fifty years until Edward Purcell theoretically described the enhancement of the spontaneous emission rate of a nuclear spin transition when coupled to a microwave resonator. As will be derived later in 3.6.3, the ratio of the spontaneous emission rate with (γ) and

without (γ_0) the resonator, called Purcell factor F_P, is given as [84]:

$$F_P = \frac{\gamma}{\gamma_0} = \frac{3}{4\pi^2}\lambda^3\frac{Q}{V}. \tag{3.1.1}$$

The Purcell factor is dependent on the quality factor of the resonator $Q = \nu/\delta\nu$ and the mode volume V of the electro-magnetic (EM) field. Here, the frequency of the EM-field is denoted as ν and the linewdith of the resonator as $\delta\nu$. In order to gain a high Purcell factor one therefore has to increase the quality factor and decrease the mode volume as far as possible.

The first experimental observation of the Purcell-effect was achieved by Haroche in 1983 [85] using a superconducting millimeter-wave Fabry-Pérot resonator. In order to see a decrease in the spontaneous emission lifetime they had to reach a high Q factor in the order of 10^6. Also the first approaches in the optical domain made use of a large quality factor since their macroscopic FPIs had large mode volumes $V_m \sim 10^4 - 10^6\lambda^3$ resulting in Purcell factors in the order of $\sim 10^2$ [86], [87].

However, for emitters with linewidths broader than the cavity linewidth, as often encountered in solid state systems, the effective quality factor,

$$Q_{eff} = (Q_c^{-1} + Q_e^{-1})^{-1}, \tag{3.1.2}$$

of cavity and emitter has to be taken into account. A broad emitter therefore limits the Purcell enhancement. In order to still increase the emission rate for such a system, the only way is to reduce the mode volume of the cavity. This can be achieved in micro- or nanocavities, which feature mode volumes down to below λ^3. In the past decade advancements in fabrication techniques such as direct laser writing [88], focused ion beam milling [89]–[91], CO_2 laser ablation [92], [93] or chemical etching techniques [94]–[96] made it possible to produce a great variety of micro-and nanoscale cavity designs. The most prominent cavity designs are micropillars, microdisks or whispering gallery mode (WGM) resonators, photonic crystals and fiber-based FPIs as used for the experiments described here. In combination with high-reflectivity distributed Bragg reflector (DBR) mirrors, which will be explained in Section 3.4, it was possible to also maintain a high Q factor while scaling down the mode volume. A more detailed classification of cavity designs and their achieved performance can be found in [97].

Fiber-based Fabry-Pérot microcavities (FFPC) [92], [98], as used for the experiments presented in this thesis, feature one or both mirrors on the end-facet of an optical fiber. Usually, a single-mode fiber with a concave depression is used as the incoupling mirror. The second mirror can either be realized on a macroscopic planar mirror [99], [100] as sketched in Fig. 3.1a) or another single- or multi-mode fiber [101]–[103] as drawn in Fig. 3.1b). The fiber-fiber design allows just for one-dimensional tuning of the cavity length but has the advantage of a smaller footprint

and an efficient collection of the cavity mode into an optical fiber. This might be advantageous to connect multiple cavities in a low-loss fiber network. Using a macroscopic planar mirror on one side opens up the possibility to investigate a great variety of samples inside the cavity. Furthermore, the open-access design makes it possible to move the fiber also laterally across the mirror which is suitable for spatially inhomogeneous samples. Last but not least, different sample mirrors can be quickly swapped which facilitates the sample characterization.

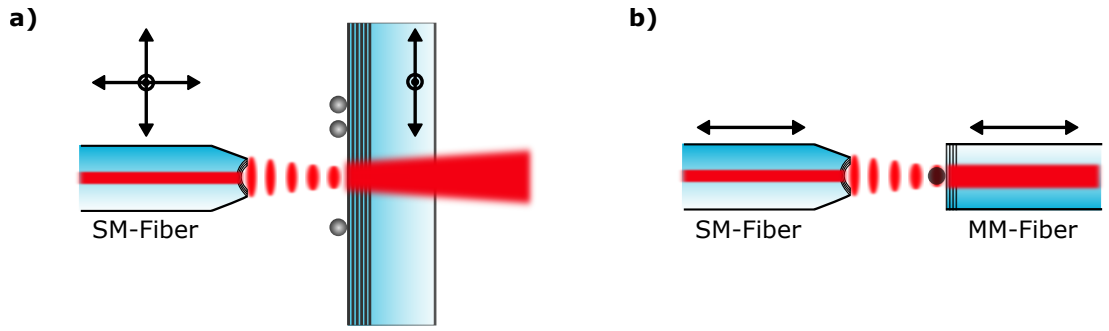

Figure 3.1: a): Sketch of a fiber-based Fabry-Pérot microcavity consisting of a concave mirror on the endfacet of a single mode (SM) fiber and a second planar mirror carrying the sample (grey spheres) adapted from [56]. The latter can be moved laterally to move the sample in and out of the cavity mode (red) and the fiber can be scanned in all three directions. This type of cavity is used for the work presented here. In sketch b) a fiber-fiber design is shown consisting of a single mode fiber with concave depression and a flat multi mode (MM) fiber which carries the sample. Both fibers can be moved in the longitudinal direction to adjust the cavity length.

All FFPC designs feature a small mode volume and high Q factors. For example, mode volumes down to $\sim \lambda^3$ were achieved and it was possible to reach the first longitudinal mode order, hence a cavity length of $\lambda/2$, using a plano-concave cavity with silver coated mirrors [104]. When using DBR mirror coatings the reflectivity can be increased to near unity and quality factors of up to 10^7 with a record finesse of 195,000 have been measured with such a cavity design [105]. A review on FFPCs presenting the achievements made in various research fields and the perspectives for their applications in the future can be found in [106].

3.2. Parameters of a Fabry-Pérot Cavity

The simplest type of Fabry-Pérot cavity consists of two opposing planar mirrors, where a standing wave field is created as soon as the mirror distance reaches an integer multiple of half the wavelength $d = q\lambda/2$, $q \in \mathbb{N}$. Here, the injected light

field is thought of as a plane, monochromatic wave of wavelength (frequency) $\lambda(\nu)$. The figures of merit describing a Fabry-Pérot type cavity, that I will use throughout this thesis, are summarized in Table 3.1. Whenever an approximate sign appears, the expression is only valid for cavities with low losses and high reflectances of the cavity mirrors. A careful derivation of these expressions can be found in the appendix of [107]. For further details conduct [92], [108] or the book of Saleh and Teich [109].

Parameter	**Formula**	**Explanation**
Free spectral range (FSR)	$\Delta\nu = \frac{c}{2nd}$	Spectral distance between neighboring resonances, with the cavity length d, refractive index of the medium inside the cavity n and speed of light c.
FSR in cavity length	$\Delta d = \frac{\lambda}{2}$	The cavity length distance between adjacent modes Δd is always given by half of the wavelength.
Linewidth (FWHM)	$\delta\nu \approx \Delta\nu \cdot \frac{T_1+T_2+\mathcal{L}}{2\pi}$, $\kappa = 2\pi\delta\nu$	Linewidth of the Lorentzian-shaped cavity resonances, where $T_1(T_2)$ denote the transmission of the first (second) mirror and $\mathcal{L}$ the sum of all losses inside the cavity.
Finesse	$\mathcal{F} \approx \frac{\Delta\nu}{\delta\nu} \approx \frac{2\pi}{T_1+T_2+\mathcal{L}}$	Number of round-trips the light wave takes on average until it leaves the cavity.
Cavity transmission	$T_{cav}(\nu) \approx T_{max} \cdot \frac{(\delta\nu)^2}{(\delta\nu)^2+(\nu-q\Delta\nu)^2}$	Lorentzian-shaped cavity transmission as a function of the frequency ν of the light wave; $q \in \mathbb{N}$ denotes the longitudinal mode order.
Maximum transmission	$T_{max} \approx \frac{4T_1T_2}{(T_1+T_2+\mathcal{L})^2}$	Maximal transmission on the peak of the resonance.
Quality factor	$Q = \frac{\nu_0}{\delta\nu} = q\mathcal{F}$	Figure of merit of resonators describing the amount of energy stored in the cavity in terms of the energy loss per round-trip.
Intra-cavity power	$P_{peak} \approx 4T_1 \cdot \left(\frac{\mathcal{F}}{\pi}\right)^2 P_{in}$, $P_{peak} \approx \frac{4\,P_{out}}{T_2}$, $\bar{P}_{peak} \approx \frac{P_{peak}}{2}$	Peak intra-cavity power at an antinode of the standing wave field and its temporal average. The first expression describes the peak power if the power P_{in} in front of the incoupling mirror of transmission T_1 is known, whereas the second expression can be used if the outcoupled power P_{out} and the transmission T_2 of the second mirror is known.
Outcoupling efficiency	$\eta_{out} \approx \frac{T_2}{T_1+T_2+\mathcal{L}}$	Fraction of light leaving the cavity through the outcoupling mirror of transmission T_2.

Table 3.1: Summary of the most important parameters to describe a Fabry-Pérot cavity.

3.3. Parameters of the Spatial Mode of the Cavity

So far, I have only considered the discretized longitudinal eigenmodes of a Fabry-Pérot resonator. However, a realistic cavity also poses boundary conditions to the electro-magnetic field in the transveral directions. To obtain the mode functions $u(x, y, z)$ of the three-dimensional cavity eigenmodes, the scalar Helmholtz equation for a monochromatic wave must be solved. Simplifying the latter using the paraxial approximation [110],

$$\left|\frac{\partial^2 u}{\partial z^2}\right| \ll \left|2k\frac{\partial u}{\partial z}\right|, \qquad \left|\frac{\partial^2 u}{\partial x^2}\right|, \qquad \left|\frac{\partial^2 u}{\partial y^2}\right|, \tag{3.3.1}$$

which can be applied as long as the variation of the mode function along the z-axis is small on the scale of the wavelength and compared to the changes in the transverse directions. The resulting paraxial wave equation, among other solutions, can then be solved by the so-called Hermite-Gaussian (HG) modes, also known as Transverse-Electro-Magnetic (TEM) modes, of order (n, m):

$$\begin{aligned} u_{n,m}(x,y,z) = \left(\frac{2}{\pi}\right)^{\frac{1}{2}} \left(\frac{1}{2^{n+m}\, n!\, m!}\right)^{\frac{1}{2}} \frac{1}{w(z)} H_n\left(\frac{\sqrt{2}x}{w(z)}\right) H_m\left(\frac{\sqrt{2}y}{w(z)}\right) \\ \times e^{-\frac{\left(x^2+y^2\right)}{w(z)^2}} e^{-\frac{ik\left(x^2+y^2\right)}{2R(z)}} e^{i(n+m+1)\Phi(z)}\,. \end{aligned} \tag{3.3.2}$$

The function $H_n(x)$ denotes the Hermite polynomial of order n:

$$\begin{aligned} H_n(x) &= 2^{-\frac{n}{2}} (n!)^{-\frac{1}{2}} \pi^{-\frac{1}{2}} (-1)^n e^{x^2} \frac{\mathrm{d}^n e^{-x^2}}{\mathrm{d}x^n}\,, \\ \text{e.g.,}\ \ H_0(x) &= 1,\ H_1(x) = 2x,\ H_2(x) = 4x^2 - 2, \ldots\,. \end{aligned} \tag{3.3.3}$$

Further details on higher-order transverse modes in fiber-based microcavities, such as their spectrum, increased diffraction losses and mode coupling due to imperfect mirror profiles can be found in [97], [111].

The TEM_{00} mode, called Gaussian mode, is of special importance since it is the fundamental mode of Fabry-Pérot resonators and describes the beam profile emitted by free-space lasers:

$$u_{0,0}(x,y,z) = \left(\frac{2}{\pi}\right)^{\frac{1}{2}} \frac{1}{w(z)} e^{-\frac{\left(x^2+y^2\right)}{w(z)^2}} e^{-\frac{ik\left(x^2+y^2\right)}{2R(z)}} e^{i\Phi(z)}\,. \tag{3.3.4}$$

The parameters defining the TEM-modes are the following:

- w_0 denotes the beam waist, i.e., the minimal (transverse) radius at which the amplitude has dropped by e^{-1} with respect to its maximum value.

- $w(z) = w_0\sqrt{\left(1 + \left(\frac{z}{z_R}\right)^2\right)}$ is the beam radius at position z.
- $z_R = \frac{\pi w_0^2}{\lambda}$ is called the Rayleigh range, which determines the region $-z_R < z < z_R$ where the beam is strongly focused. At the Rayleigh range the beam radius has increased to $\sqrt{2}w_0$.
- $R(z) = z\left(1 + \left(\frac{z_R}{z}\right)^2\right)$ represents the phase front's radius of curvature. $R(z) \to \infty$ within the Rayleigh range and $R(z) \to z$ in the far field ($z \gg z_R$). Therefore, the phase front has the shape of a plane wave at $z = 0$ and tends to the one of a spherical wave in the far field.
- $\Phi(z) = tan^{-1}(z/z_R)$ is the Gouy phase, which is an additional phase shift occuring in focused beams [110]. It adds up to π for a propagating beam from $-\infty$ to ∞.

The mode parameters explained above, except of the Gouy phase, are pictured in the sketch of a Gaussian mode in Fig. 3.2.

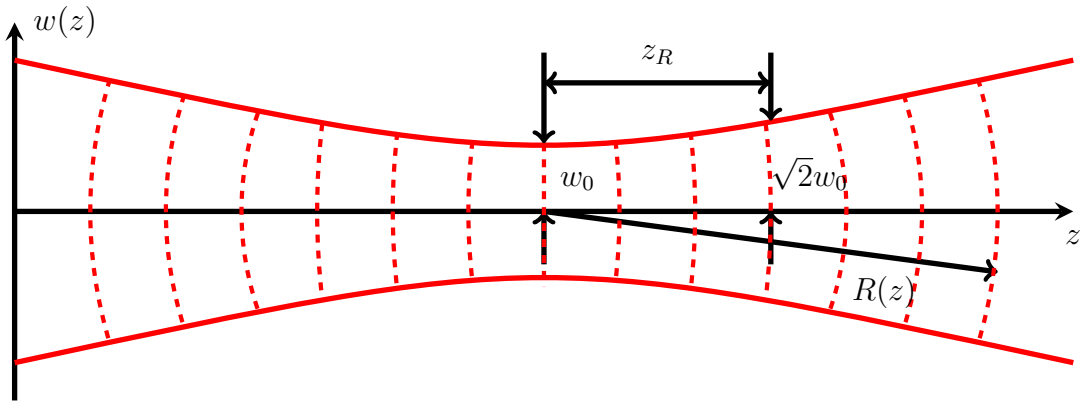

Figure 3.2: Sketch of a Gaussian mode to visualize the parameters defining it.

The two mirrors of a Fabry-Pérot resonator pose two boundary conditions to the TEM modes. The phase front's radius of curvature has to match the radius of curvature (ROC) of each mirror profile i.e. $R(d) = r_{C,1}$ and $R(0) = r_{C,2}$. Using these conditions together with a given wavelength λ fixes all open parameters of the TEM mode and thus defines the mode geometry inside the resonator. A summary of formulas describing the geometrical parameters of the cavity mode used throughout this thesis is shown in Table 3.2.

Parameter	Formula	Explanation
Resonance condition	$\nu_{qmn} = \Delta\nu \left(q + \frac{\theta_{m,x}}{\pi} + \frac{\theta_{n,y}}{\pi}\right),$ $\theta_{k,i} = \left(\frac{1}{2} + k\right) \Phi(z)$	Frequency of a cavity resonance for a HG-mode of longitudinal mode order q and transveral mode order m, n. Higher order modes feature a higher resonance frequency and appear at longer cavity lengths.
Stability range	$0 < \left(1 - \frac{d}{r_{C,1}}\right)\left(1 - \frac{d}{r_{C,2}}\right) < 1$	Criterion for a stable resonator i.e. its beam doesn't diverge in consective round-trips.
Stability range (planar-concave FPI)	$r_C > d$	Stability range if one mirror is planar i.e. $r_{C,2} = \infty$. However, for our mirror profiles a drop in finesse is observed for $d > r_C/2$ [111].
Mode waist	$w_0 = \sqrt{\frac{\lambda}{\pi n}} \sqrt[4]{r_C d - d^2}$	Waist of the cavity mode at the planar mirror.
Mode radius	$w_C = \sqrt{\frac{\lambda}{\pi n}} \sqrt[4]{\frac{r_C^2 d}{r_C - d}}$	Radius of the cavity mode at the fiber mirror.
Cavity length	$d = \frac{\lambda_q \lambda_{q\pm1}}{2n\lvert\lambda_{q\pm1} - \lambda_q\rvert}$	Determination of the optical cavity length by measuring a cavity spectrum with wavelengths spaced by one FSR.
Mode volume	$V_m = \frac{\int \lvert\mathbf{E}(\mathbf{r})\rvert^2 \, \mathrm{d}^3 r}{max(\lvert\mathbf{E}(\mathbf{r})\rvert^2)}$ $= \frac{\pi w_0^2 \, d}{4}$	General definition of the mode volume and the specific expression for FPIs assuming a Gaussian mode.

Table 3.2: Summary of the most important geometrical parameters of a TEM cavity mode.

It should be noted that the vectorial nature of the light field has been omitted so far. However, due to non-rotationally symmetrical mirror profiles, shown in

the next Section 3.4, the two polarization eigenmodes are not degenerate anymore and differ in their resonance frequency. The polarization mode splitting can be approximated in first order to [112]:

$$\nu_\perp - \nu_\parallel \approx \frac{\Delta\nu\lambda}{(2\pi)^2} \frac{r_C^\perp - r_C^\parallel}{r_C^\perp r_C^\parallel}. \tag{3.3.5}$$

For the cavity measurements presented in this thesis, the input polarization is always aligned such that only one mode is excited and the splitting becomes irrelevant.

3.4. High-reflectivity Cavity Mirrors

3.4.1. Fabrication of Mirror Profiles

There are mainly two techniques how to machine a micrometer-scale concave depression on the end-facet of a cleaved optical fiber: focused ion beam milling and laser ablation. David Hunger and Jakob Reichel were the first using a CO_2-laser, emitting at 10.6 µm, to shoot concave depressions centered at the core of a single-mode fiber [92], [93]. In comparison to focused ion beam milling, this technique creates very smooth surfaces of about 0.15 nm RMS surface roughness [104] rendering it possible to build high-finesse cavities. The laser pulse of several Watts power is focused onto the silica glass of the fiber tip and evaporates some material at the surface due to the strong absorption of silica in the mid-infrared. The molten glass then leads to an atomically smooth surface due to surface tension. The laser shot leaves a nearly Gaussian-shaped depression, which can be approximated by a parabola around the center. The power of the laser pulse as well as the number of pulses influences the depth of the profile while the radius of curvature can be adjusted by the beam waist.

Our fiber machining setup also features a microscope and white light interferometer (WLI) to characterize the profiles (see [104] for details). The most important parameters, which we measure for each fiber, are the depth of the profile t, the $1/e$ radius of the Gaussian profile a and ellipticity $\epsilon = \sqrt{1 - r_C^{(x)}/r_C^{(y)}}$. The radius of curvature at the center can then be calculated as $r_C = a^2/2t$. Using single- or multi-shot ablation, a variety of profiles can be machined with ROCs ranging from 5-500 µm. The fibers used for the experiments presented in this thesis were fabricated by the master student Tobias Krom and details about the fiber machining setup, the settings used and the fiber parameters can be found in his thesis [113]. The ROCs for this fiber machining run were between 10 µm to 50 µm with profile

depths around 1 µm.

Pictures of a machined fiber-tip can be seen in Fig. 3.3a) and b) (taken by Hanno Kaupp). Since the profiles are sometimes tilted with respect to the fiber end-facet, angular alignment of the cavity is required and the optimal cavity performance often coincides with a slightly tilted fiber with respect to the planar mirror. In order to achieve shortest possible cavity lengths the rim of the fiber-tip around the profile is cropped by laser ablation using a mulit-shot pattern. This allows for larger tilting angles of the fiber without increasing the cavity length. In Fig. 3.3c) a WLI interference pattern of a mirror profile with cropped rim can be seen. The height difference between neighboring bright fringes correspond to about 240 nm.

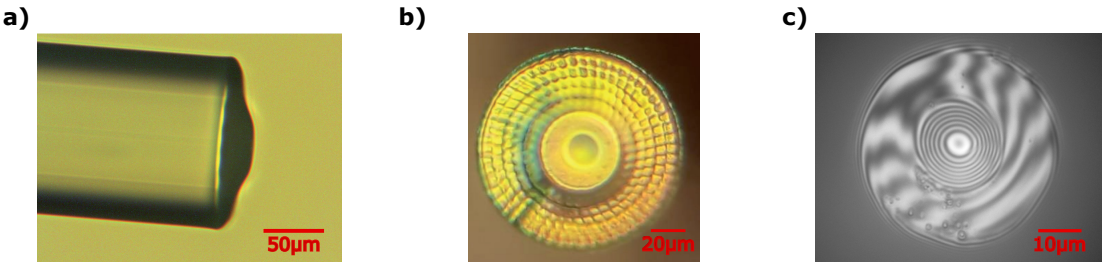

Figure 3.3: a) and b): Pictures of a fiber profile machined by CO_2-laser ablation (taken by Hanno Kaupp). The cropping of a rim around the profile by multi-shot ablation is visible in both pictures. Picture c) is a WLI image of a fiber profile of about 20 µm ROC. Each fringe of the interference pattern corresponds to a height difference of about 240 nm.

3.4.2. Distributed Bragg Reflector Coatings

DBRs consists of alternating layers of high (n_H) and low (n_L) refractive index materials with optical thickness of $\lambda/4$. The partial reflections at each refractive index jump interfere constructively in reflection leading to a high reflectivity of the coating stack. In order to simulate the EM-response of a DBR coating or even the entire cavity when a light wave impinges from one direction, the transfer matrix method can be employed. Thereby, the system under investigation is modeled by a series complex transfer matrices $M = M_N \cdot M_{N-1} \cdot ... \cdot M_1$. Each matrix describes the change in the EM-field when propagated through a stack based on Fresnel's formulas:

$$\begin{pmatrix} E_{out} \\ H_{out} \end{pmatrix} = M \cdot \begin{pmatrix} E_{in} \\ H_{in} \end{pmatrix} . \tag{3.4.1}$$

The derivation of the transfer matrix method and further details can be found in the book of Furman and Tikhonravov [114]. The transfer matrix method can then

be used to simulate the mirror or cavity parameters such as reflectivity, transmission, absorption losses and longitudinal electric field distribution.

The reflectivity of a DBR stack for the design wavelength can be approximated as [115]:

$$R = \left(\frac{n_0 n_L^N - n_S n_H^N}{n_0 n_L^N + n_S n_H^N} \right)^2 , \tag{3.4.2}$$

where N denotes the number of layers and $n_{0/S}$ denote the refractive indices of the medium in front of the mirror and the mirror substrate, respectively. The reflectivity is maximal at the designed wavelength but extends over a certain wavelength range, called the stop band. The width of the stop band solely depends on the refractive index contrast of the two materials used in the layer stack. Regarding the electric field distribution, we have to ensure that the nanoparticles residing on the planar mirror surface are located at the maximum i.e. an antinode of the standing wave. A high refractive index material as final layer creates a field node at the surface such that one has to add a spacer layer of low refractive index material to correctly position the nanoparticles.

Finalising a DBR stack with a high refractive index layer has the advantage of a lower vulnerability to scattering losses from surface roughness due to a vanishing electric field at the surface. Furthermore, it reduces the penetration depth of the field inside the coating stack. One disadvantage of DBR mirror coatings in comparison e.g. to silver-coated mirrors is their large penetration depth in the order of several hundred nanometers, which considerably increases the mode volume in the case of microcavities. The penetration depth is the distance from the surface of the DBR stack to the virtual position of a hard mirror where the impinging light would be reflected. However, the definition of the penetration depth depends on the context whether one looks at the reflection phase, the time delay upon reflection or the imaging behaviour of a focused beam. Therefore, Koks et al. [116] define a phase, frequency and modal penetration depth. Since the effects on the Purcell factor are minor in the case of the cavity described here, I relegate to their paper for the definition of the penetration depths and its implication to other cavity parameters.

The coatings of the fibers and planar mirror used for the experiments described in this thesis were designed by the master student Tobias Krom and the coating simulations as well as further details can be found in his thesis [113]. He optimized the coating parameters for a maximal single ion countrate in a fiber-fiber cavity setup which are not exactly the optimal parameters for the cavity used here. We use a coating of 14 layer pairs of Ta_2O_5 ($n_H = 2.13$) and SiO_2 ($n_L = 1.48$) (given by the manufacturer Laseroptik GmbH) for the planar mirror. The last layer only has an optical thickness of $0.81\,\lambda/4$ and acts as spacer layer. This DBR then results in

a transmission of 200 ppm at a center wavelength of 585 nm. Since the geometrical thickness of the stack is contracting upon cooldown, the center wavelength is shifting about 5 nm towards smaller wavelengths when cooling down to 4 K. The fiber mirrors I use have a lower transmission of 25 ppm at 585 nm, achieved by a stack of 15 layer pairs with an additional high refractive index layer on top of the coating.

3.5. Losses inside a Cavity

So far the losses per roundtrip inside the resonator where summarized in the single parameter $\mathcal{L}$. Since the scanning cavity microscopy technique (see Sec. 6.2) basically images the spatial variations of losses, a closer look into different loss mechanisms is necessary to understand this imaging technique. Since I aim for operating a high-finesse cavity which is sensitive to losses on the level of parts per million (ppm), quantifying the different loss channels becomes important.

Losses of an Empty Cavity Except of the mirror transmission losses given by $T_{1/2}$ the DBR mirror stacks also feature absorption losses, denoted by $A_{1/2}$. The fiber mirror with 25 ppm transmission has about $A_1 \approx 60$ ppm absorption loss according to the manufacturer. The planar mirror features a reduced absorption since it was annealed at 400 °C for three hours. However, since the exact absorption of the planar mirror is not known, I assume a value of $A_2 \approx 40$ ppm to match the measured finesse. Additionally, scattering losses, denoted by $S_{1/2}$, due to the roughness of the mirror surface detoriate the cavity performance. The root mean square (RMS) surface roughness of the planar mirror is given by the surface roughness of the substrate[7]. The manufacturer guarantees a surface roughness of $\sigma_{sc} < 0.2$ nm, which was confirmed by atomic force microscopy (AFM) measurements in the group. The losses per roundtrip can then be calculated as [117]:

$$S_i = \left(\frac{4\pi\sigma_{sc}}{\lambda}\right)^2. \tag{3.5.1}$$

Using the above equation, one obtains scattering losses for each mirror surface of about $S_{1/2} \approx 20$ ppm.

In summary, the total losses per roundtrip of an empty cavity can be summed up to,

$$\mathcal{L}_0 = A_1 + A_2 + S_1 + S_2. \tag{3.5.2}$$

[7] 12.7x3.0 mm, plane substrate, Laseroptik GmbH

Scattering Losses of a Nanoparticle If a nanoparticle, residing on the planar mirror, is brought into the cavity, this leads to an increased extinction of the light field. In the following it is assumed that the NP is located in the field maximum of an antinode. To quantify this effect, the extinction cross-section $\sigma_{ex} = \sigma_{abs} + \sigma_{sc}$ describes the effective area blocking a beam incident on the object. It divides into the absorption σ_{abs} and scattering σ_{sc} cross-section, respectively. It should be noted that this quantity is not related to the geometrical size of the object. For the yttria NPs used in the experiments presented here, the absorption cross-section is negligible and only scattering of the light field is relevant. Thus, the extinction simplifies to $\sigma_{ex} \approx \sigma_{sc}$. The scattering effects inside a light field are treated by the theory of Mie [118]. A summary of it can be found in the PhD-thesis of Matthias Mader [108] and a detailed treatment can be found in the book of Quinten [119].

Here, I make use of the Rayleigh approximation,

$$\frac{n_{NP}}{n_{medium}} \frac{2\pi r}{\lambda} \ll 1, \tag{3.5.3}$$

which is valid as long as the geometrical size of the scatterer is much smaller than the wavelength, although we are close to that limit. The Mie theory describes the problem more exactly and would give slightly different cross-sections but is much more complex to treat.

The scattering losses from a nanoparticle can be calculated as,

$$S_{NP} = \frac{4\sigma_{NP}}{\pi w_0^2}, \tag{3.5.4}$$

with the scattering cross-section given by [99],

$$\sigma_{NP} = \frac{1}{6\pi\epsilon_0^2} \left(\frac{2\pi}{\lambda}\right)^4 |\alpha|^2. \tag{3.5.5}$$

The polarizability of a sphere of refractive index n_{NP} and volume

$$V_{NP} = 4/3\pi \left(d_{NP}/2\right)^3, \tag{3.5.6}$$

lying on a dielectric surface being surrounded by a medium of n_{medium}, is derived in [120] as:

$$\alpha_{||} = \epsilon_0 V_{NP} \frac{n_{medium}^2 \left(n_{NP}^2 - n_{medium}^2\right)}{n_{medium}^2 + \frac{5}{16}(n_{NP}^2 - n_{medium}^2)}. \tag{3.5.7}$$

Here, an orientation of the induced dipole parallel to the surface is assumed. This results in a scattering loss scaling with the sixth power of the nanoparticle diameter

making the cavity a suitable tool to optically detect nanoparticles down to sizes of a few tens of nanometers:

$$S_{NP} = \frac{8\pi^4}{3^3}\frac{d_{NP}^6}{\lambda^4 w_0^2}\left(\frac{n_{medium}^2\,(n_{NP}^2 - n_{medium}^2)}{n_{medium}^2 + \frac{5}{16}(n_{NP}^2 - n_{medium}^2)}\right)^2. \tag{3.5.8}$$

The total losses per rountrip inside a cavity with a nanoparticle residing at the field antinode are then given by:

$$\mathcal{L} = A_1 + A_2 + S_1 + S_2 + 2S_{NP} = \mathcal{L}_0 + 2S_{NP}. \tag{3.5.9}$$

The above expression enters the different cavity parameters given in Table 3.1 and a plot of the normalized maximum cavity transmission as well as the finesse, dependent on the diameter of the nanoparticle inside the cavity, is shown in Fig. 3.4.

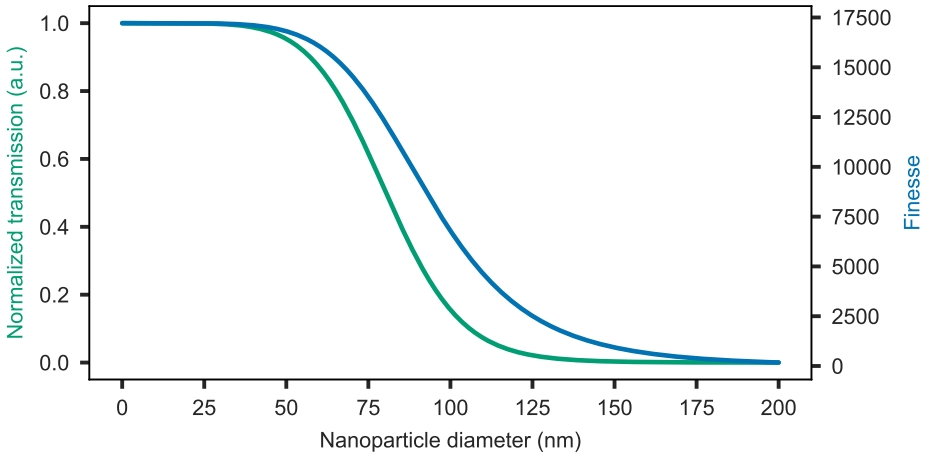

Figure 3.4: Normalized maximum cavity transmission (green) and finesse (blue) dependent on the scattering losses induced by a nanoparticle of the given diameter. The mirror parameters are those of the coatings used for the measurements presented in this thesis: $T_1 = 25\,\text{ppm}$, $T_2 = 200\,\text{ppm}$, $A_1 = 60\,\text{ppm}$, $A_2 = 40\,\text{ppm}$, $S_{1/2} = 20\,\text{ppm}$.

A nanoparticle of 60 nm diameter, which is the average diameter of the sample batch, that I use for the measurement of this thesis, causes about 13 ppm scattering losses and leads to a normalized transmission of 87%, thus a reduction of already 13%. The finesse should only be slightly reduced to 16,000 from 17,200 for a bare cavity.

Characterizing the distribution of nanoparticles on the cavity mirror (see Sec. 4.4), I find that also more than one can lie within the area of the cavity mode. Therefore, I consider also the case of the scattering losses stemming from multiple particles

of the same size. Assuming that the cavity mode is then scattered by a single spherical particle of an effective polarizability,

$$\alpha_{eff} \propto V_{eff} = \frac{4}{3}\pi \left(\frac{\sqrt[3]{N} d_{NP}}{2} \right)^3 . \tag{3.5.10}$$

The maximum transmission dependent on the diameter for the case of a single, two or three nanoparticles of the same size is plotted in Fig. 3.5. It shows that for example a reduction to 36% of the clean mirror transmission could hint to a single NP of about 87 nm diameter, but also two particles of 69 nm or three 60 nm particles are possible. Since all three diameters are within the width of the size distribution of the nanoparticle batch, scanning cavity microscopy images can't reveal the true number of particles. Only if the size distribution of the particles would have a width of a few nanometers, the number of particles within the cavity mode diameter could be resolved.

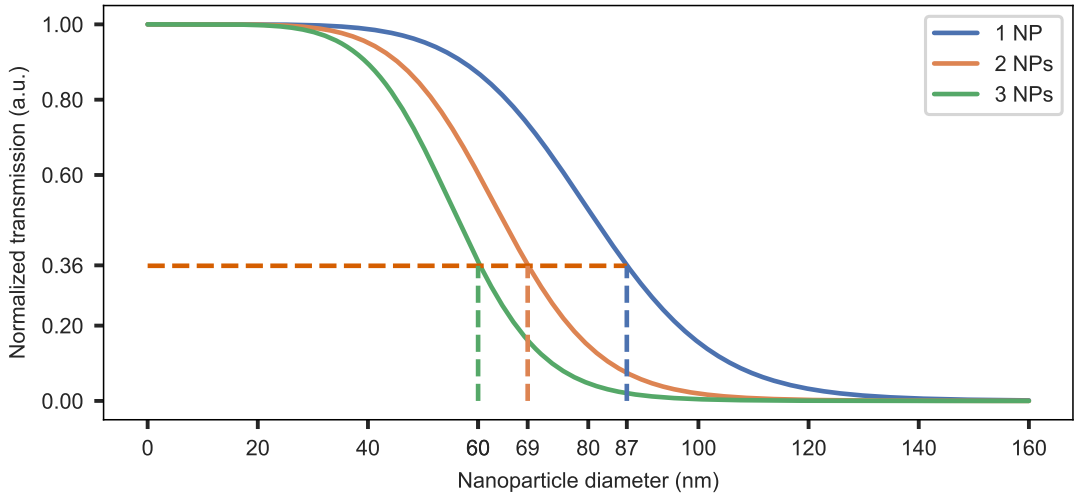

Figure 3.5: Normalized maximum cavity transmission dependent on the single particle diameter for one, two or three NPs of the same size lying within the area of the cavity mode.

3.6. Light-Matter Interactions in a Cavity

3.6.1. Jaynes-Cummings Model

The quantum mechanical description of an emitter coupling to a single mode of the electromagnetic field was first derived by Jaynes and Cummings in 1963 [121].

This model lays the foundation for the field of cavity quantum electrodynamics (cQED) showing a plethora of quantum optics phenomena and applications. The Hamiltonian of the system can be separated in three terms,

$$\hat{H}_{JC} = \hat{H}_c + \hat{H}_{em} + \hat{H}_{int} = \hbar\omega_c \hat{a}^\dagger \hat{a} + \hbar\omega_0 \hat{\sigma}^+ \hat{\sigma}^- + \hbar g_0 (\hat{a}^\dagger \hat{\sigma}^- + \hat{\sigma}^+ \hat{a}). \tag{3.6.1}$$

The first terms describes the single mode of the electromagnetic field realized inside a cavity with the field creation (annihilation) operator $\hat{a}^\dagger$ ($\hat{a}$) and angular frequency ω_c. The emitter is considered simplified as a two-level system (TLS) with transition frequency ω_0 between ground and excited state and its creation (annihilation) operator $\hat{\sigma}^+$ ($\hat{\sigma}^-$). The last term mediates the interaction between the cavity mode and the emitter in the dipole and rotating wave approximation (RWA). In the RWA terms are neglected which oscillate around zero much faster than the interaction time scale. The strength of interaction is expressed in the coupling rate

$$g_0 = \sqrt{\frac{\omega_0 \mu_0^2}{2\epsilon_0 \hbar V_c}} \xi^2. \tag{3.6.2}$$

Here, $\mu_0 = -e\langle e|x|g\rangle$ denotes the transition dipole matrix element between the ground and excited state $|g\rangle$ and $|e\rangle$, respectively. The factor $\xi = \frac{|\vec{\mu_0} \cdot \vec{E}|}{|\vec{\mu_0}||\vec{E}|}$ takes into account the overlap between the emitter's dipole orientation and the polarization of the cavity field. In the following, I will assume a perfect overlap and thus set $\xi^2 = 1$. The coupling rate is inversely proportional to the cavity mode volume $g_0 \propto 1/\sqrt{V_c}$, which demands for smallest possible mode volumes to obtain a high coupling rate.

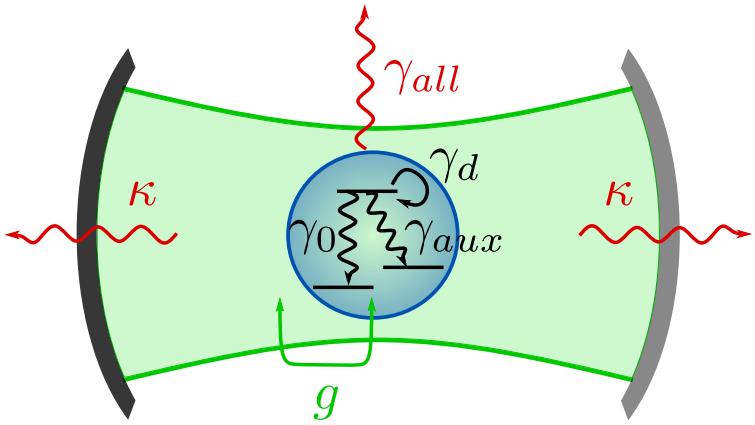

Figure 3.6: Sketch of an emitter with three-level scheme (black) inside a cavity mode (green) to examplify the cQED parameters used to describe the system dynamics. Red arrows and letters assign loss rates out of the cavity. The green arrow shows the coherent coupling between the emitter and cavity field at rate g, whereas the black arrows and rates describe the internal dynamics of the emitter.

To study the dynamics of the emitter-cavity system including losses and decoherence, one has to consider the following Lindblad master equation, which describes the time-evolution of the emitter's density matrix ρ,

$$\dot{\rho} = i[\rho, \hat{H}] + \mathcal{L}^{c}_{damp} + \mathcal{L}^{em}_{damp} + \mathcal{L}_{deph}. \tag{3.6.3}$$

The Lindblad superoperators $\mathcal{L}$ are defined as

$$\mathcal{L}^{c}_{damp} = \frac{\kappa}{2}(2\hat{a}\rho\hat{a}^{\dagger} - \hat{a}^{\dagger}\hat{a}\rho - \rho\hat{a}^{\dagger}\hat{a}) \tag{3.6.4}$$

$$\mathcal{L}^{em}_{damp} = \frac{\gamma_0}{2}(2\hat{\sigma}_{-}\rho\hat{\sigma}_{+} - \hat{\sigma}_{+}\hat{\sigma}_{-}\rho - \rho\hat{\sigma}_{+}\hat{\sigma}_{-}) \tag{3.6.5}$$

$$\mathcal{L}_{deph} = \frac{\gamma_d}{4}(\hat{\sigma}_z\rho\hat{\sigma}_z - \rho), \tag{3.6.6}$$

with σ_z being the third Pauli matrix.

The first superoperator defines the photon loss rate of the cavity κ and the second one the emitter population decay rate γ_0 from the excited state into the desired ground state. The last superoperator describes the pure dephasing of the considered dipole moment at a rate γ_d. In the spectral domain, the corresponding linewidths of these rates are full widths at half maximum (FWHM). These different rates are visualized in the sketch of Fig. 3.6. From the master equation 3.6.3 one can derive the equations of motion of the emitter and cavity mode populations, respectively, as well as the evolution of the emitter's coherence. Details can be found in [122], [123] and in the textbooks [78], [124].

The figure of merit to characterize the coupled cavity-emitter system is the cooperativity C, which the ratio of the effective coupling rate between the emitter and the cavity R, to all dephasing mechanisms [122],

$$C = \frac{R}{\gamma} = \frac{4g^2}{(\kappa + \gamma)\,\gamma}, \tag{3.6.7}$$

with the total dephasing rate $\gamma = \gamma_0 + \gamma_{aux} + \gamma_d$. Here, I have taken into account the decay channel to other auxiliary levels with the rate γ_{aux}, as shown in Fig. 3.6. This results in a modified coupling coupling rate $g = \sqrt{\zeta}\, g_0$, which takes into account the fraction of photons emitted into the desired transition, denoted as branching ratio ζ:

$$\zeta = \frac{\gamma_0}{\gamma_{all}} = \frac{\gamma_0}{\gamma_0 + \gamma_{aux}}. \tag{3.6.8}$$

The cooperativity can be used to discriminate between three different regimes:

- coherent regime: $C \gg 1$ and $2g > |\kappa + \gamma|$

- strong coupling regime: $C > 1$ and $2g > \kappa, \gamma$
- weak coupling regime: $C < 1$

The coherent regime allows for a deterministic coupling between the photonic and emitter quantum states, which opens up the possibility for various quantum information operations [125]–[128]. It was first demonstrated experimentally using superconducting microwave cavities and Rydberg atoms [129], [130]. The first realization with optical photons were achieved just a few years later in the group of Kimble [86], [131].
Until now, the strong coupling regime has been demonstrated with various emitter systems such as trapped atoms [132], single molecules [133], quantum dots (QD) [134] and other emitters in the solid state [135]–[137] to name just a few.

The cavity-emitter system with Europium ions considered in this work only shows a weak coupling due to a low g value as will be shown later. This implies that photons cannot be reabsorbed by the emitter before they get lost via the cavity or into free-space. The cavity just enhances the emitter decay rate into the well-collectable cavity mode. The figure of merit in this regime is the Purcell factor, expressing the ratio of the emission rate into the cavity mode compared to the free-space emission rate.

3.6.2. Free-space Emission

To start with, the emission rate in free-space is defined as the inverse lifetime of the excited state T_1,

$$\gamma_{all} = \frac{1}{T_1} = \gamma_0 + \gamma_{aux} = \frac{\omega_0^3 \mu_0^3 + \sum_i \omega_i^3 \mu_i^3}{3\pi\epsilon_0 \hbar c^3}. \tag{3.6.9}$$

Here, I have taken into account the more realistic situation of a multi-level scheme with the emission rate into the desired transition γ_0 and the emission into all other possible (auxiliary) levels γ_{aux}.

3.6.3. Purcell factor

The Purcell factor describes ratio of radiation losses via the cavity to the spontaneous emission rate in free-space,

$$F_P = \frac{\gamma_c}{\gamma_0}. \tag{3.6.10}$$

It can be derived by solving the Lindblad master equation 3.6.3 as sketched in Section 3.6.1 or the book of Walls and Milburn [138]. Another route is to start with Fermi's golden rule [139] as done in [124]. However, it should be noted that there is also a purely classical description of the Purcell enhancement as shown in [140].

In the following, I will derive a generalized Purcell factor by calculating the emission rate into the cavity mode γ_c with Fermi's golden rule and assuming a Lorentzian shaped cavity and emitter density of states, $\rho(\omega)$ and $\Lambda(\omega)$, respectively [141]:

$$F_P^* = \frac{1}{\gamma_0}\frac{2\pi}{\hbar^2}\int_0^\infty M_0^2(\omega)\Lambda(\omega)\rho(\omega)d\omega. \tag{3.6.11}$$

The normalized densities of states are given in terms of their FWHM linewidths κ, γ and central frequencies ω_c, ω_0, respectively:

$$\rho(\omega) = \frac{2}{\pi}\frac{\kappa}{4(\omega-\omega_c)^2+\kappa^2}, \tag{3.6.12}$$

$$\Lambda(\omega) = \frac{2}{\pi}\frac{\gamma}{4(\omega-\omega_0)^2+\gamma^2}. \tag{3.6.13}$$

The dipole transition matrix element is given as

$$M_0^2 = \frac{\hbar\omega_0\mu_0^2}{2\epsilon_0 V_c}\xi^2. \tag{3.6.14}$$

The integral 3.6.11 can be solved analytically using partial fractions and a contour integration in the complex plane [141]. The resulting expression can be further simplified by the realistic assumptions $\kappa \ll \omega_c$ and $\gamma \ll \omega_0$ to give

$$F_P^* = \frac{3}{4\pi^2}\left(\frac{\lambda}{n}\right)^3\frac{\omega_0}{V_c}\frac{(\kappa+\gamma)}{4(\omega_0-\omega_c)^2+(\kappa+\gamma)^2} \tag{3.6.15}$$

$$= \frac{3}{4\pi^2}\left(\frac{\lambda}{n}\right)^3\frac{Q_c}{V_c}\frac{\kappa(\kappa+\gamma)}{4\delta^2+(\kappa+\gamma)^2}. \tag{3.6.16}$$

In the last step, I further assumed that $\kappa \ll \omega_c \approx \omega_0$ to introduce the cavity quality factor $Q_c = \kappa/\omega_c$. Here, I consider again the case of a perfect dipole-field overlap $\xi^2 = 1$ and n denotes the refractive index of the medium inside the cavity. To calculate the generalized Purcell factor for our Fabry-Pérot type microcavities, it is more convenient to express it in terms of the cavity finesse $\mathcal{F}$ and mode waist w_0:

$$F_P^* = \frac{6}{\pi^3}\left(\frac{\lambda}{n}\right)^2\frac{\mathcal{F}}{w_0^2}\frac{\kappa(\kappa+\gamma)}{4\delta^2+(\kappa+\gamma)^2}. \tag{3.6.17}$$

Note, that I started the derivation with an emitter density of states of linewidth γ which can be expressed as the sum of all emitter loss and decoherence rates as in

section 3.6.1, $\gamma = \gamma_0 + \gamma_{aux} + \gamma_d$. Therefore, the above derivation gives a generalized Purcell factor that takes into account emitter dephasing. The ideal Purcell factor F_P as originally published by E. M. Purcell in 1946 [84] can be restored in the so-called bad cavity regime, where $\kappa \gg \gamma$ and the cavity-emitter detuning $\delta = 0$ is vanishing,

$$F_P = \frac{6}{\pi^3}\left(\frac{\lambda}{n}\right)^2 \frac{\mathcal{F}}{w_0^2}. \tag{3.6.18}$$

Take a note, that in this limit the Purcell enhancement solely depends on the cavity parameters.

If the emitter linewidth exceeds the cavity linewidth $\gamma \gg \kappa$, called the bad emitter regime, the expression 3.6.17 can be simplified to

$$F_P^* = \frac{6}{\pi^3}\left(\frac{\lambda}{n}\right)^2 \frac{\mathcal{F}}{w_0^2}\frac{\kappa}{\gamma}. \tag{3.6.19}$$

To complete my nomenclature, I finally introduce the effective Purcell factor

$$F_P^{eff} = \zeta F_P, \tag{3.6.20}$$

which takes into account the branching ratio of the Purcell-enhanced transition. This quantity can be determined experimentally as the measured lifetime shortening compared to the emitter in free space.

The Purcell factor can also be linked to the cooperativity and can be expressed in terms of the cQED parameters introduced before [142]:

$$F_P^{eff} = \frac{R}{\gamma_0} = C\frac{\gamma}{\gamma_0} \tag{3.6.21}$$

In the case of a lifetime-limited emitter linewidth ($\gamma = \gamma_0$), the cooperativity and Purcell factor are equal $F_P^{eff} = C$. In the bad cavity limit, which historically was considered first, $R \approx 4g^2/\kappa$, the effective Purcell factor reduces to,

$$F_P^{eff} = \frac{4g^2}{\kappa\,\gamma_0}. \tag{3.6.22}$$

3.6.4. Lifetime Reduction

After having formally derived the Purcell factor it remains to show how it can be measured in an experiment. Since the precise measurement of the free-space emission rate into the full solid-angle is not feasible, it is more practiable to measure

the excited state lifetime once in free-space and in the cavity. From these two quantities the effective Purcell factor can then be determined as

$$F_P^{eff} = \zeta \frac{\gamma_c}{\gamma_0} = \frac{\gamma_c + \gamma_{all}}{\gamma_{all}} - 1 = \frac{T_1}{T_{1,c}} - 1. \tag{3.6.23}$$

Knowing the branching ratio of the enhanced transition one can then calculate back the ideal Purcell factor $F_P = F_P^{eff}/\zeta$.

It should be noted that the cavity mode can in principle have a significant spatial overlap with the free-space emission γ_{fs}, which requires a modification of the above formula. However, for the cavity geometries considered in this work ($w_c/L_{cav} \approx 0.2$), this fraction is negligible [97]:

$$\gamma_{fs} = \gamma_0 \left(1 - \frac{3\Delta\Omega}{8\pi}\right) \tag{3.6.24}$$

$$\text{with} \quad \frac{\Delta\Omega}{4\pi} = \sin^2\left(\frac{1}{2}\arctan\frac{w_c}{L_{cav}}\right) \approx 1.7\%. \tag{3.6.25}$$

3.6.5. Enhanced Branching Ratio and Collection Efficiency

Besides the shortening of the excited state lifetime the cavity has another advantageous effect, namely the enhancement of the branching ratio

$$\zeta_c = \frac{(F_P+1)\gamma_0}{(F_P+1)\gamma_0 + \gamma_{aux}} = \frac{F_P+1}{F_P + \frac{\gamma_0+\gamma_{aux}}{\gamma_0}} = \frac{F_P+1}{F_P+1/\zeta}. \tag{3.6.26}$$

The intuitive picture behind this larger branching ratio is that the cavity leads to additional photons being scattered only into this particular transition in addition to the unaltered free-space emission. Therefore, the cavity enhancement can induce a cycling transition with near unity branching ratio which is desirable for the optical readout of quantum states [143].

Furthermore, the photons scattered into the cavity mode can be collected much more efficient by optical fiber or low-loss free-space transmission optics compared to capturing a dipole emission with an objective. The fraction of light emitted into the cavity mode compared to the overall emission rate $\gamma_{tot} = \gamma_c + \gamma_{all}$ is denoted as cavity collection efficiency

$$\beta = \frac{\gamma_c}{\gamma_{tot}} = \frac{F_P\gamma_0}{(F_P+1)\gamma_0 + \gamma_{aux}} = \frac{F_P^{eff}}{F_P^{eff}+1}. \tag{3.6.27}$$

3.6.6. Cavity-enhancement of Two Transitions

An excited state of real emitters can often decay into multiple final states as it is the case also for the Europium ions investigated in this thesis. If more than one of the emitter's optical transitions lie within the stop band of the cavity mirrors, it can be possible to Purcell-enhance those transitions simultaneously. The Fabry-Pérot type cavities used in this work can be tuned to a cavity length where two Europium transitions spectrally overlap with two cavity modes separated by one FSR. This has two advantages that will be used in the experiment. First of all it further enhances the overall fluorescence of the Europium ions and secondly the twofold Purcell enhancement can be used to determine the free-space lifetime. Therefore, I will derive a formula for the total Purcell factor when two transitions are enhanced.

I assume a cavity and emitter spectral density consisting of two Lorentzians being far-detuned with $|\omega_1 - \omega_2| \gg \gamma_i, \kappa_i, i \in \{1, 2\}$:

$$\Lambda(\omega) = M_1^2(\omega_1)\Lambda_1(\omega, \omega_1, \gamma_1) + M_2^2(\omega_2)\Lambda_2(\omega, \omega_2, \gamma_2) \tag{3.6.28}$$

$$\rho(\omega) = \rho_1(\omega, \omega_1, \kappa_1) + \rho_2(\omega, \omega_2, \kappa_2). \tag{3.6.29}$$

Here, the transition dipole matrix element $M_i^2(\omega_i)$ is assigned as the weighting factor of each Lorentzian line. Inserting these functions into eq. 3.6.11, the result is simply the sum of both individual generalized Purcell factors,

$$F^*_{P,both} = F^*_{P,1} + F^*_{P,2}, \tag{3.6.30}$$

as long as the assumption holds that all cross-terms are negligible small:

$$\int_0^\infty M_1^2(\omega_1)\Lambda_1(\omega)\rho_2(\omega)d\omega = \int_0^\infty M_2^2(\omega_2)\Lambda_2(\omega)\rho_1(\omega)d\omega \approx 0. \tag{3.6.31}$$

The spectral tunablility of the cavity resonances permits to measure three different Purcell-enhanced lifetimes, namely the lifetime where just transition 1(2) is on resonance with the cavity $T_{1,1,c}(T_{1,2,c})$ and the lifetime where the double resonance condition is met and both transitions are simultaneoulsy Purcell-enhanced $T_{1,both,c}$. Having determined these three lifetimes one can calculate the free-space lifetime using the following relation:

$$F^*_{P,both} = F^*_{P,1} + F^*_{P,2} = \frac{T_1}{T_{1,1,c}} - 1 + \frac{T_1}{T_{1,2,c}} - 1 = \frac{T_1}{T_{1,both,c}} - 1 \tag{3.6.32}$$

$$\Leftrightarrow T_1 = \left(\frac{1}{T_{1,1,c}} + \frac{1}{T_{1,2,c}} - \frac{1}{T_{1,both,c}}\right)^{-1}. \tag{3.6.33}$$

Thus, the spectral tunability of our cavity system opens up a new way to determine the free-space lifetime solely from measurements with the emitter being inside the cavity.

3.7. Expected Cavity Performance

As already discussed in Sec. 3.4, the mirror transmissions as well as the radius of curvature of the fiber profile are crucial parameters for the cavity performance and hence their values should be optimised for the respective measurements. Since the 60 nm nanoparticles residing on the planar mirror will introduce scattering losses, the finesse cannot be increased arbitrarily by decreasing the mirror transmissions. Therefore, I plot the finesse of a cavity incorporating a 60 nm yttria nanoparticle in Fig. 3.7a) dependent on the transmissions of the planar mirror T_2 for a fiber mirror transmission T_1 in the range from 10 ppm to 100 ppm, respectively.

However, the Purcell factor of an FPI cavity is proportional to the ratio between finesse and mode waist of the cavity $F_P \propto F/w_0^2$ as shown in Sect. 3.6.3. Therefore, a high Purcell enhancement is reached when both quantities are optimized. Minimal mode waists of about 0.5 µm are feasible as can be seen in Fig. 3.7b). Therefore, fiber profiles of a radius of curvature of 5 µm have to be fabricated, which is at the limit of our fiber-machining setup, and the shortest possible cavity length, including the penetration depths into the DBR stack, of about 2.5 µm has to be reached.

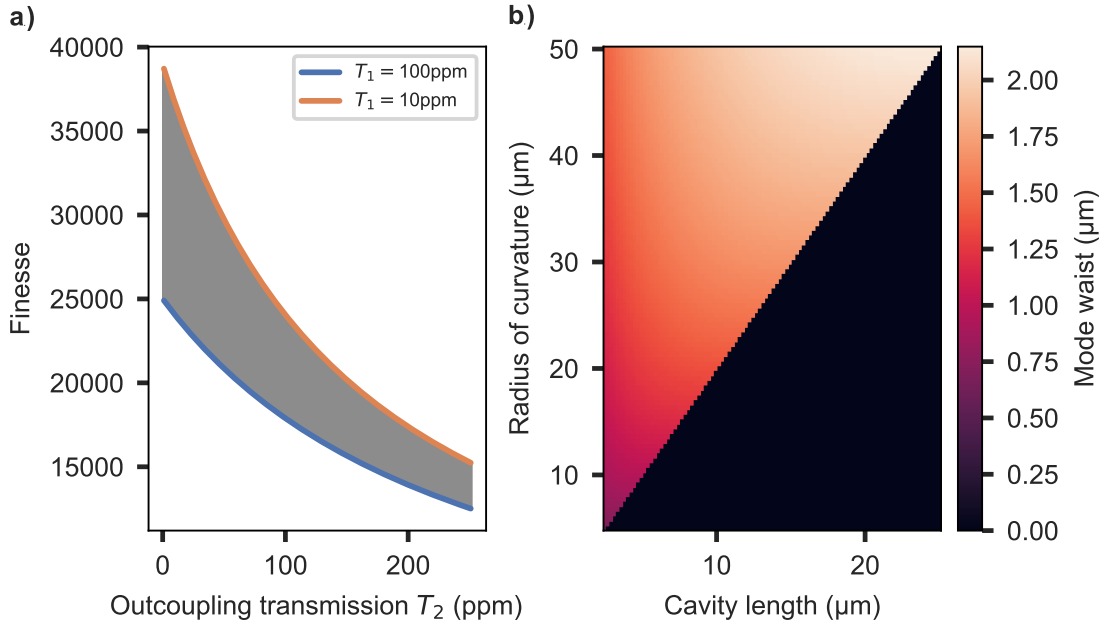

Figure 3.7: a): Cavity finesse as a function of the transmission of the planar mirror T_2 for a range of transmission values of the fiber mirror coating T_1 (grey area) between $T_1 = 100\,\text{ppm}$ (blue) and $T_1 = 10\,\text{ppm}$ (orange). The scattering losses introduced by a 60 nm yttria nanoparticle are incorporated. b): Cavity mode waist dependent on the cavity length and radius of curvature. For the cavities considered here losses due to mode mixing increase strongly for $d \geq r_c/2$ [111], which is why only mode waists for $d \leq r_c/2$ are calculated.

The aim of this work is to detect the fluorescence signal from a single europium ion. Therefore, it is not sufficient to maximize the Purcell factor but rather the fluorescence countrate of photons coupled out of the cavity has to be as high as possible. For a pulsed experiment under resonant excitation, the latter can be calculated as:

$$R_{pulsed} = p_{ex} \cdot f_{rep} \cdot \frac{F_P^{eff}}{F_P^{eff}+1} \cdot \left(1 - e^{-\frac{F_P^{eff}+1}{T_1} t_{det}}\right) \eta_{out}, \tag{3.7.1}$$

with the excitation probability $p_{ex} = 0.5$ for incoherent driving, the repetition rate $f_{rep} \approx 1/t_{det}$ and the detection time window of length t_{det}. The above equation also includes the outcoupling efficiency η_{out} defined in Tab. 3.1, which is also dependent on the mirror transmission values. Therefore, the highest countrate is achieved for a balance between faster decay of the emitter due to the Purcell effect and a high transmission of the outcoupling mirror to be able to collect the photons. In Fig. 3.8a) one can see the (effective) Purcell factors defined in Eq. 3.6.18 (Eq. 3.6.20) which can be reached with the finesses and mode waists discussed before. However, the estimation of the single ion countrate coupled out of the cavity

in Fig. 3.8 dependent on the transmission values of both mirrors shows that the highest countrate (marked by the black cross) is achieved with a moderate effective Purcell factor of 8.3 at a finesse of 18,000 and mode waist of 1.0 µm.

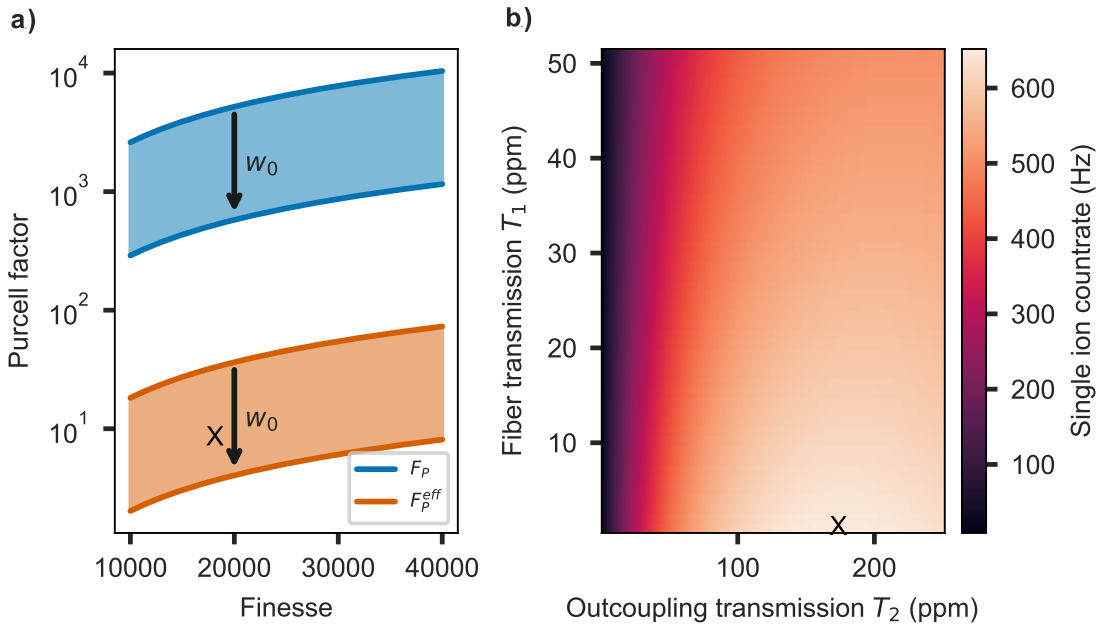

Figure 3.8: a): Estimation of the ideal (F_P, blue) and effective (F_P^{eff}, orange) Purcell factors defined in Eq. 3.6.18 and Eq. 3.6.20 dependent on the cavity finesse for a cavity mode waist ranging from 0.5 µm to 1.5 µm (black arrow). b) The estimated rate of photons coupled out at the planar cavity mirror for a single europium ion inside a 60 nm nanoparticle dependent on the transmission of the fiber mirror T_1 and the planar mirror T_2. The black cross indicates the mirror transmissions needed for a maximal single ion countrate which is achieved with a moderate Purcell factor of 8.3 (black cross in a)).

4. Aerosol Jet Printing Nanoparticles on Cavity Mirrors

The next step towards cavity-enhanced spectroscopy of europium-doped nanoparticles is to distribute individual nanoparticles on the surface of the planar cavity mirror. Therefore, the powder of yttria nanoparticles, that we obtain from the group of Philippe Goldner at the Institut de Recherche de Chimie Paris, has to be dissolved in a solution for one of the deposition techniques presented in this chapter. Forming a stable colloidal solution of nanoparticles in a liquid is a non-trivial task and the research field of colloidal chemistry investigates the fundamental principles. I will give a short introduction into this field in the first section 4.1 and summarize the most important phenomena. Section 4.2 is devoted to the different methods that have been tested to homogeneously distribute the colloidal suspension on the mirror surface. Due to difficulties with the existing techniques such as dropcasting and spin-coating, I established a new method by aerosol-jet-printing the solution onto the cavity mirrors. The working principle of an aerosol jet printer as well as the procedure to print diluted nanoparticle dispersions is explained in Section 4.3. As a last step, in Section 4.4, the printed mirrors are characterized with respect to the amount of individual nanoparticles in comparison to agglomerations of many particles and their spatial distribution on the mirror surface.

4.1. Basic Principles of Colloidal Solutions and Surface Effects

In the following, I will give an introduction to the main aspects of colloid chemistry and physical effects that should be considered at the interface between a dielectric medium and a liquid. A more detailed description can be found in the book of Cosgroves [144] or the review article of Wang and Zhou [145].

The term *colloid* means glue-like and was first introduced by Thomas Graham in 1861 [146] describing the inability of a fluid to pass through a fine membrane.

Colloids are materials composed of at least two phases, where one is dispersed in the other. The medium as well as the dispersed phase can be gaseous, fluid or solid. In the following, I will stick to the case of a dispersion of solid particles in a liquid, hence a colloidal solution. The colloidal domain is defined by a particle size between a few nanometers to tens of micrometers.

4.1.1. Electrostatics of a Charged Particle in an Electrolyte

In the 1930s, Hamaker [147] was the first to quantitatively describe the tendency of the colloid particles to aggregate due to an attractive van der Waals force between two particles in close proximity. The attractive van der Waals force can be counteracted by a repulsive electrostatic force. Therefore, the particles have to be charged by one of the following mechanisms:

- Ionisation of surface groups
- Ion adsorption
- Non-symmetric ion dissolution
- Isomorphous ion substitution (e.g. exchange of Al^{3+} with Si^{4+} ions between different layers of clay).

This creates a charged atmosphere of electrolyte around the particles which counterbalances the surface charge, described by the electrochemical double layer model (Stern-Gouy-Chapman model) which is sketched in Fig. 4.1. The inner layer, also called Helmholtz layer, extends from the particle surface up to the outer Helmholtz plane (OHP) in which ions are stuck to the surface and not considered to be in thermal motion. Increasing the distance from the OHP, the diffusive layer, also called Gouy-Chapman layer, starts. Within that layer there is a dynamic ionic atmosphere under Brownian motion. The electrostatic potential $\phi(x)$ falls off linearly within the inner layer and can be approximated by an exponential decay within the diffusive layer:

$$\phi(x) = (\phi(OHP) - \phi(aq))\ e^{-\kappa x} = \Delta_{aq}^{OHP}\phi\, e^{-\kappa x}. \tag{4.1.1}$$

Here, $\phi(aq)$ refers to the potential in the bulk solution. The distribution of ions in the diffusive layer is described by the reciprocal of the Debye length,

$$\kappa = \sqrt{\frac{2z^2e^2N_A\,c(aq)}{\epsilon\,\epsilon_0\,k_B\,T}}. \tag{4.1.2}$$

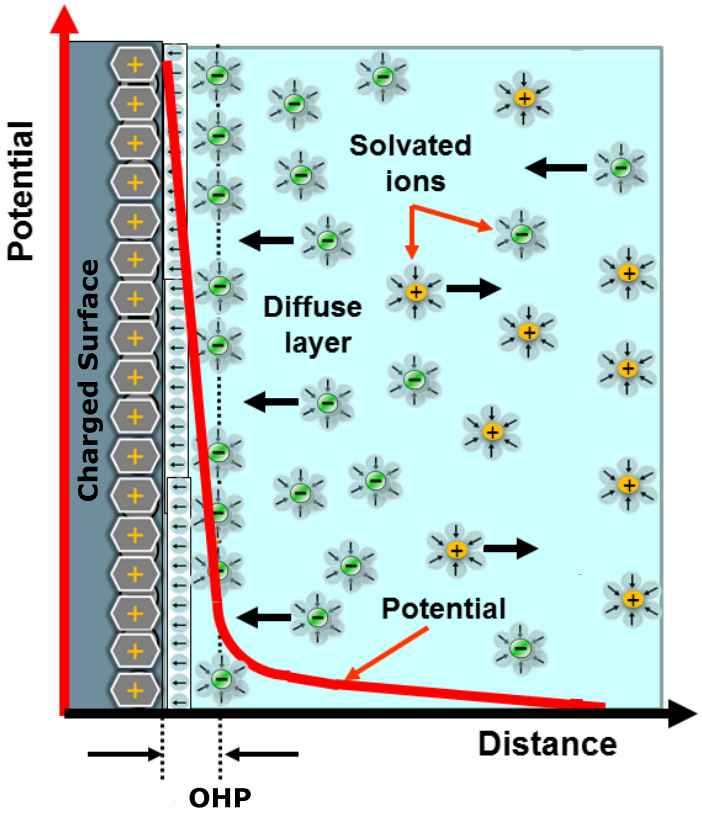

Figure 4.1: Sketch of the double layer model describing the electric charge distribution and electrostatic potential (red curve) at an interface of a charged solid surface and a liquid electrolyte (picture adapted from [148]). The outer Helmholtz plane (OHP) denotes the maximum distance from the surface where electrolyte ions are stuck to the surface and not in thermal motion in comparison to the ions in the diffusive layer.

Important factors are the ion valency z, the ionic concentration of the bare electrolyte $c(aq)$ and the temperature T. The second factor determining the potential in the diffusive layer is its difference between the outer Helmholtz plane and the bare electrolyte potential, which is often equated with the zeta potential ζ and has to be measured.

For the definition of the zeta potential, one considers a relative motion between both phases. Then a shear plane can be assumed which is the effective location of the solid-liquid interface. The zeta potential is defined as the electrostatic potential at this shear plane. There are different methods to measure the zeta potential based on whether the solid or electrolyte or both are in motion. Since this work is in the field of quantum optics, I will exemplarily explain the laser Doppler electrophoresis (LDE) method. The colloid particles are brought into motion by an

electric field between two electrodes and the electrolyte is considered to be stationary. Laser light of wavelength λ_0 is shone through the solution with refractive index n under and angle φ with respect to the direction of the electric field and the scattered light is detected under an angle θ. Now, the particle velocity v_p can be measured via the Doppler shift of the scattered laser light:

$$\delta\nu = \frac{2n\,v_p}{\lambda_0}\,sin\left(\frac{\theta}{2}\right)\,\cos(\varphi). \tag{4.1.3}$$

Since the magnitude of the Doppler shift is typically small (order of a few tens of Hertz), a heterodyne detection scheme is employed. For the usual case of $\kappa\,r_{NP} > 1$, the zeta potential can be finally attained by the Smoluchowski equation [149]:

$$\zeta = \frac{v_p}{E}\frac{\eta}{\epsilon\,\epsilon_0}, \tag{4.1.4}$$

with the electric field strength E and the viscosity of the colloid solution η.

4.1.2. Stability of a Colloidal Solution

As soon as the diffusive layers of two particles start to overlap, the repulsive electrostatic force comes into play. However, if it cannot counteract the attractive van der Waals force, the particles can stick together and aggregate, also called coagulation. Over time such a solution forms agglomerates of many primary particles with sizes of up to more than ten times the size of the primary particles [150]. Colloidal stability describes the tendency of the particles to aggregate and became an intense research field in colloidal chemistry.

The physical model behind the coagulation dynamics is described by the DLVO theory (named after Boris Derjaguin, Lew Landau, Evert Verwey, Theodoor Overbeek) [151], [152]. It assumes the total colloidal pair potential to be a sum of the attractive V_A and repulsive V_R potentials, respectively:

$$V_{tot} = V_A + V_R = -\frac{A\,r_{NP}}{12h} + 2\pi\epsilon\,r_{NP}\,\zeta^2\,e^{-\kappa\,h}. \tag{4.1.5}$$

In the above expression, A denotes the Hamaker constant and r_{NP} the particle radius. It is valid as long as the particle separation $h \ll 2\,r_{NP}$ and $\kappa\,r_{NP} < 3$. I have replaced the surface potential of the original expression of V_R [153] by the zeta potential which is a reasonable assumption in many cases. The total potential is proportional to the radius of the particle, $V_{tot} \propto r_{NP}$, which leads to the fact that agglomeration dynamics depend also on the size of the primary particles. The summation of the attractive and repulsive potentials leads to a primary maximum V_{max} in the total potential as depicted in Fig. 4.2. This poses an energy barrier for the aggregation of two particles.

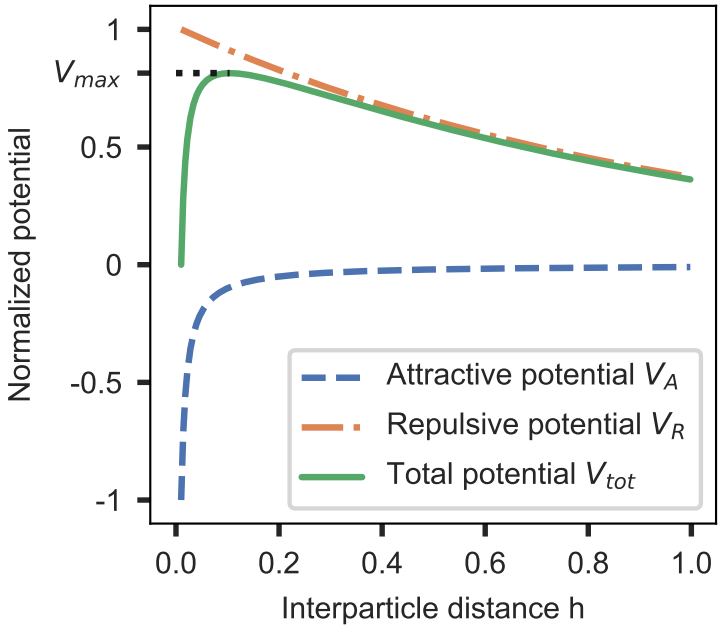

Figure 4.2: Plot of the normalized attractive van der Waals potential (blue), the normalized repulsive potential (orange) and the sum of both potentials (green) between two charged particles in an electrolyte in close proximity. The height of the potential barrier V_{max} determines the likelihood of an aggregation of the two particles at a collision event.

A rule of thumb states that a solution is stable for a reasonable amount of time as long as $V_{max} > 20 k_B T$, since the relative number of collisions that lead to a coagulation of two particles can be estimated as:

$$n \approx e^{-\frac{V_R}{k_B T}}. \tag{4.1.6}$$

This results in $n \approx 2 \cdot 10^{-9}$ for $V_R = 20\, k_B T$.

4.1.3. Surfactants

To form a stable colloidal solution, the repulsive interaction between the particles has to be known and controlled. This can be done by adjusting the zeta potential and the ionic concentration $c(aq)$ with the use of surfactants.

Classification Surfactants, short for surface-active agents, are organic molecules that have the ability to adsorb at interfaces and alter their physical properties. The first natural surfactants used by humankind are soaps. Since this class of

molecules has a broad range of applications, a great variety of surfactants exists and research on new types is ongoing. One can classify surfactants into four types:

- Anionics and cationics are dissolved into oppositely charged surfactant ions and counter-ions
- Non-ionics possess a highly polar but non-charged part
- Zwitterionics combine a posititve and negative group within the same molecule.

The performance of a surfactant to stabilize a certain colloidal solution can be expressed in its efficiency i.e. the concentration needed to reach a certain reduction in surface tension and its effectiveness meaning the maximum reduction in surface tension regardless of the concentration. An important parameter for the use of surfactants is their critical micelle concentration (CMC). Above this concentration of surfactant in the solution, the molecules start to aggregate in structured supramolecules called micelles instead of adsorbing at the desired surface. The Krafft temperature T_K denotes the crossing point of the temperature curves of solubility and CMC. Above T_K the solubility strongly rises due to micelle formation. Below the Krafft temperature crystallization of the surfactant happens. To obtain well-dispersed surfactant monomers and hence an efficient surfactant, it is crucial to stay above the Krafft temperature and below the CMC.

Sodium Dodecyl Sulfate (SDS) In the following description of the preparation of cavity mirrors with yttria nanoparticles, I used sodium dodecyl sulfate (SDS) as a surfactant solved in bidestilled water as it was done by my predecessor [97]. The CMC of SDS at 25°C is 8.2 mmol/l, which corresponds to 2.4 mg/ml and its Krafft temperature is about 15°C [154]. The SDS molecule features a hydrophilic end which binds to the water molecules whereas it is assumed that the other hydrophobic end adsorbs at the surface of the yttria nanoparticles leading to a shell of SDS molecules covering the nanoparticle surface and improving the dispersion in water.

For future work, a more quantitative approach would be to first determine the zeta potential of the yttria nanoparticles in water and based on this, search for a suitable surfactant. The effectiveness of different surfactants and their right concentration could be checked by dynamic light scattering (DLS) measurements which reveal the distribution of particles sizes in the solution. Therefore, the amount of primary particles can already be optimized in the solution which should simplify the sample preparation methods discussed in the next section.

4.2. Overview of Sample Preparation Methods

Having dissolved the yttria nanoparticle powder and SDS in water, the next step is to distribute the solution on the surface of the cavity mirror. Different preparation techniques are available to achieve this and a discussion of various methods can be found in [145]. I tried out dropcasting, spin-coating and aerosol-jet-printing. The respective results are discussed in the following. A successfull sample preparation should fulfill the following objectives:

- Distribute well-isolated primary nanoparticles on the cavity mirror with inter-particle distances of about 5 - 10 µm to be resolvable by scanning cavity microscopy
- Establish reproducible recipes
- Find characterization methods for a reliable discrimination between individual nanoparticles and agglomerations.

Common to all sample preparation methods is the surface activation before deposition and a post-deposition cleaning by two minutes of oxygen plasma treatment each. Furthermore, the nanoparticle solution is sonicated with a sonotrode tip[8]. The tip is directly held into the solution to maximize the power of the ultrasound waves dissipated in the solution. I tried out different sonication time spans from a few minutes up to 30 min. It seems that longer times lead to a smaller amount of huge agglomerates but it still seems to be inefficient to break up the agglomerates into their primary particles. All equipment that comes in contact with the NP powder or solution like vials, beakers and spatula were cleaned for five minutes in an ultrasonic bath using an isopropanol solution and were dried with pressurized air.

Dropcasting Dropcasting is the easiest and fastest method since only a pipette is needed to place a droplet of few µl on the activated mirror surface. To check whether primary particles can be found, a droplet was placed on a scanning electron microscopy (SEM) net and SEM[9] images where taken by Patrice Brenner (Center for Functional Nanostructures, KIT). An image with a large field of view including the rim of the droplet can be seen in Fig. 4.3a). Investigating different areas within the droplet with a higher resolution reveals only big agglomerations of many primary nanoparticles as is depicted in Fig. 4.3b). Therefore, dropcasting proved to be not successfull since no well-separated single NPs could be found. Additionally, the size distribution of the agglomerates appears to be very broad.

[8] *Sonopuls Mini20 with MS1.5 tip*, Bandelin electronic Gmbh
[9] *Crossbeam 1540EsB*, Carl Zeiss AG

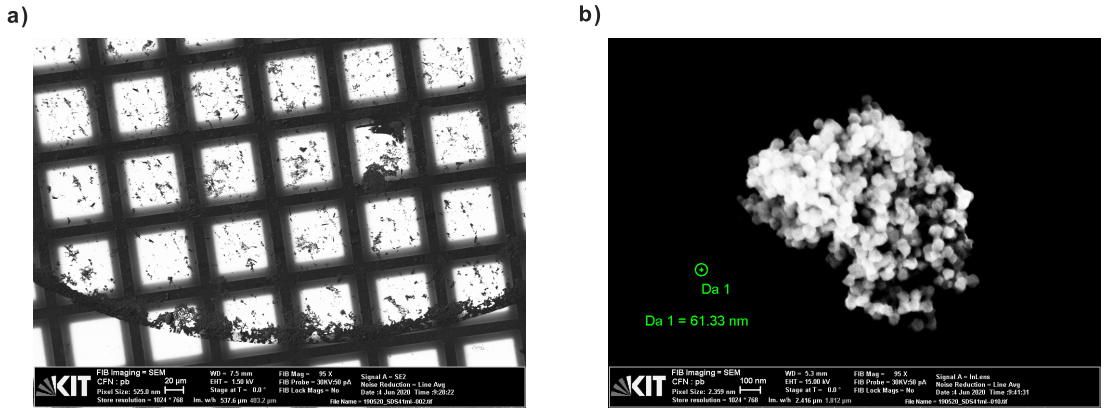

Figure 4.3: Scanning electron microscopy (SEM) images of a droplet of yttria nanoparticles dissolved in water. Image a) includes the rim of the droplet with a large field of view (WD=working distance, EHT=10 kV e-beam acceleration voltage) and a lot of big agglomerations can be seen. The right image b) depicts such an agglomeration of many primary nanoparticles in a high resolution scan.

Spin-coating My predecessor Julia Benedikter successfully spin-coated individual yttria NPs from a different batch using a dispersion of nanoparticle powder in water with SDS in a volume ratio of 1:200:1000. Spin-coating erbium-doped yttria NPs onto a DBR cavity mirror using ethanol as a solvant proved also to be successfull [155]. However, Julia Benedikter already tried out ethanol solutions and found a higher background fluorescence in confocal microscope scans in comparison to the SDS and water solution. This might be due to the excitation wavelengths in the visible domain, whereas for erbium a lower background fluorescence can be expected since the 1535 nm transition in the near-infrared domain is addressed. I tried to reproduce the results from my predecessor using the same recipe as well as slight variations of it regarding the spin-coater[10] parameters and powder and SDS concentrations. I was not successfull in coating the mirror surface with a high amount of well-dispersed, individual nanoparticles using the spin-coating technique. Reasons for the limited reproducibility of the recipe, could lie in the fact that we used a new batch of nanoparticles which had a smaller diameter of 60 nm instead of 100 nm. As discussed before in Section 4.1, the colloidal pair potential is linearly dependent on the particle diameter and thus could be very different for the 60 nm particles. It is known that the tendency of colloidal solutions to form agglomerates also depends on the storage time and drying process [150] leading to unreproducible results even for the same batch of particles.

[10] *SPIN150 Wafer Spinner*, APT GmbH

Yttria Thin Film Embedding For the sake of reducing the scattering losses of the nanoparticles even further, it is advantageous to embed them by a thin film with a smooth surface with root-mean-square (RMS) roughness $\sigma_{surface} \leq 0.2\,\text{nm}$. As described in detail in [97], covering the nanoparticles with a PMMA layer was proven successfull. To match the refractive indices it would be desirable to embed the yttria nanoparticles by an yttria thin film. Simulations have shown that not only a higher cavity finesse can be gained and thus a higher Purcell factor, but also an additional lifetime reduction of about 2.4 due to a resonant yttria thin film etalon.

In collaboration with the group of Philippe Goldner at Chimie ParisTech in Paris, we tried to embed nanoparticles on top of a cavity mirror by deposition of a 160 nm yttria layer using chemical vapour deposition (CVD). However, since the DBR mirror coating can only be heated to about 450°C, we had to restrict the deposition temperature to 500°C. This led to an amorphous yttria thin film of low surface roughness of $\sigma_{surface} \approx 0.2\,\text{nm}$ averaged over an area of $4 \times 4\,\mu\text{m}^2$. However, the thin film showed very strong background fluorescence and a low cavity finesse of only up to 5,000. According to our collaborators the deposition should take place at least at 650°C to get a polycrystalline film which should have properties more similar to the bulk material. However, a polycrystalline film is expected to have a higher surface roughness due to nanopillars sticking out of the surface. We could reduce the high background fluorescence by high power oxygen plasma annealing, but the cavity performance of the mirror still remains too bad to be useful. Therefore, this project was not pursued any further.

4.3. Aerosol Jet Printing Method

During discussions with Robert Huber (Lichttechnisches Institut (LTI), KIT), who was using an aerosol jet printer for his PhD-project [156], the idea came up to use the aerosol-jet-printing as a new method for preparing our samples. The aerosol-jet-printing of the colloidal yttria nanoparticle solution was done together with Robert Huber at the LTI cleanroom. Robert Huber operated the aerosol jet printer[11] during the four printing runs. A detailed description of the printer setup can be found in his thesis as well as in the manufacturer's manual [157]. I will summarize it in the following.

[11] *Aerosol Jet 5X*, Optomec Inc.

4.3.1. Aerosol Jet Printer Setup

The printer consists of a two-axis linear positioning stage, sketched in Fig. 4.4a), which bears the cartridge and printing head (nozzle). The stage allows for a 10 µm positioning precision of the nozzle. The substrate is placed below the printing head on a moveable plate. The latter is patterned with boreholes to hold the substrate on the plate using vacuum. The plate can be heated up to 120°C to accelerate the drying process of the aerosol droplets.

The cartridge is filled with a liquid, also denoted as the printing ink, and creates the aerosol stream which is guided to the nozzle. A drawing of the working principle of the cartridge is shown in Fig. 4.4b). Ultrasound waves of several megahertz frequency are transmitted via a water basin and diaphragm to the ink. The high ultrasound frequency leads to a standing wave inside the cartridge and the aerosol droplets of 1 to 5 µm diameter are created at the crest [158]. The ultrasound (atomizer) power influences the droplet size and amount of liquid that is vaporized. The optimal value of this parameter depends on the viscosity of the ink. The droplets are then dragged away by a stream of nitrogen gas. This aerosol or atomizer stream is then guided through a reception tube out of the cartridge and into the printer nozzle. The incoming nitrogen gas can be wettened in order to prevent the aerosol droplets drying out before they reach the sample. The whole cartridge can be heated such that the ink and aerosol droplets can be kept at an elevated temperature if needed.

The aerosol stream leaves the cartridge through a flexible tube and is guided into the printer head carrying the nozzle. In order to get a well-focused beam, a nitrogen sheath gas stream is injected into the nozzle (see Fig. 4.4c)). The design of the nozzle together with the enclosing sheath gas stream compresses the aerosol stream and leads to an aerodynamic focusing. Focus diameters between 10 µm and 600 µm can be reached, dependent on the chosen nozzle diameter between 100 µm and 1 mm. The atomizer and sheath streams can be adjusted in the printer control software to obtain the desired focus. The printing process can be quickly interrupted by either a mechanical or aerodynamical shutter within a few milliseconds.

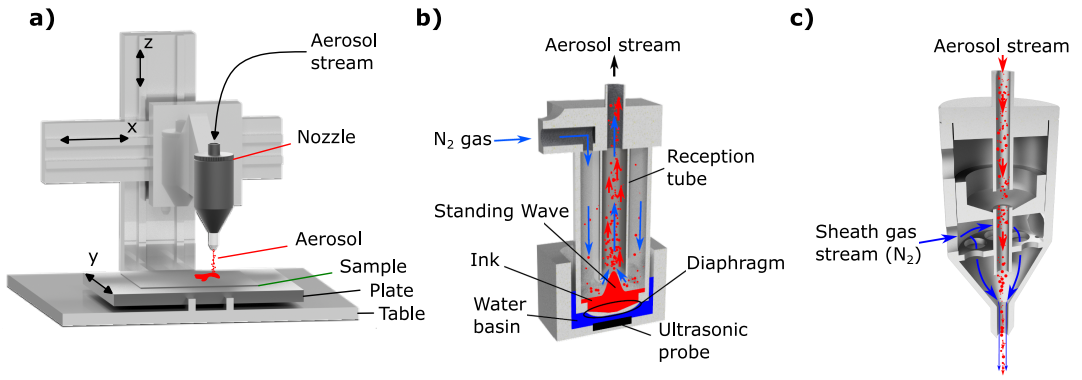

Figure 4.4: Setup of the aerosol jet printer consisting of a moveable plate which carrys the sample and a two-axis linear positioning stage (a), carrying the cartrigde (b) and printer head (nozzle) (c). Inside the cartridge an ultrasonic probe generates a standing wave of the ink and aerosol droplets are carried away at its crest. The aerosol stream is guided into the nozzle where a sheath gas stream is added for aerodynamical focusing (pictures are adapted from [156]).

4.3.2. Printing Recipe

For printing yttria nanoparticles on our cavity mirrors, we used a dispersion of roughly 0.6 mg: 0.5 mg : 3 ml (NP powder : SDS : water) of the 0.3 % Eu-doped 60 nm yttria nanoparticles. The cartridge needs at least 3 ml of ink, so most of the solution is left afterwards and can be reused. We faced problems with contamination of the solution with silver ink from previous printing runs causing strong background fluorescence. Therefore, we decided to use a second cartridge which was not used for silver ink before. We cleaned all parts of the printer that get in contact with the nanoparticle solution with isopropanol in an ultrasonic bath and dried them with pressurized air. Before filling the cartridge with the yttria solution, we did some test printing runs on a glass substrate with water. If no printing patterns are visible under the microscope, the printer was considered to be clean. After filling the cartridge with the nanoparticle solution, the atomizer was switched on and ran for about 15 min to sonicate the solution and potentially break up agglomerations.

The most challenging part is to find out a good set of printer parameters to get well-dispersed individual nanoparticles. To quickly iterate through the various parameters, we printed a meander-shaped $1 \times 1\,\mathrm{mm}^2$ square on a glass substrate and checked the result with a microscope inside the cleanroom. Since there are

still agglomerates printed, the scattered light of those can be seen, especially when using darkfield microscopy. Thereby, one can get a coarse estimate of the spatial homogeneity of the printing pattern. The following printer parameters gave good results according to the characterization described in the next section:

- 300 µm diameter nozzle operated in a defocused position (focus spot approximately 1 mm above the sample to get less serpentine structures in the printing pattern)
- 50 µm pitch between each line
- Wettened aerosol stream by filling purified water into the bubbler which is kept at 25°C
- 80 % atomizer power to get less aerosol particles in the stream
- 16 - 18 SCCM (standard cubic centimeters per minute) atomizer stream (relates to the volume stream of solution that is deposited)
- 40 SCCM sheath stream (influences the focusing behaviour)
- 2 - 15 mm/s printing velocity (of importance for the desired printing structure and amount of deposited solution)
- 80°C plate temperature (could influence the evaporation dynamics of the droplets on the substrate, but no influence was seen so far).

If the wrong parameters are chosen one can clearly see the serpentine printing pattern in the microscope image as depicted in Fig. 4.5a). This image was taken in one of the early printing attempts with a low printing speed of 2.5 mm/s, 100 % atomizer power and 20 (40) SCCM atomizer (sheath) stream.

Figure 4.5a) also shows the checkerboard pattern that was shot into the mirror surface by the CO_2 laser used for fiber machining. The detailed sketch of the mirror pattern is shown in Fig. 4.5b). In total, each mirror was patterned with four 2 mm × 2 mm large, numbered crosses. These shots were done with high laser power such that the crosses are visible by bare-eye for effortless coarse alignment inside the cavity. In each quadrant of a cross, there is a labeled checkerboard pattern with shot distances of 10 µm and 50 × 50 µm fields. The latter corresponds to the scanning range of the cavity at room temperature as will be discussed in the next chapter. These shots were manufactured with lower CO_2 laser power and only have a height of a few 100 nm such that the cavity fiber doesn't get stuck during a scan. These patterns proved to be helpful in localizing a certain nanoparticle across different measurement setups in order to compare e.g. confocal

microscope and scanning cavity images of the same particle. Dividing the mirror surface into different areas has the advantage that different printing parameter regimes can be tested on the same mirror. Even different nanoparticle solutions could be printed on the same surface. This speeds up not only the fabrication but also the characterization of the samples.

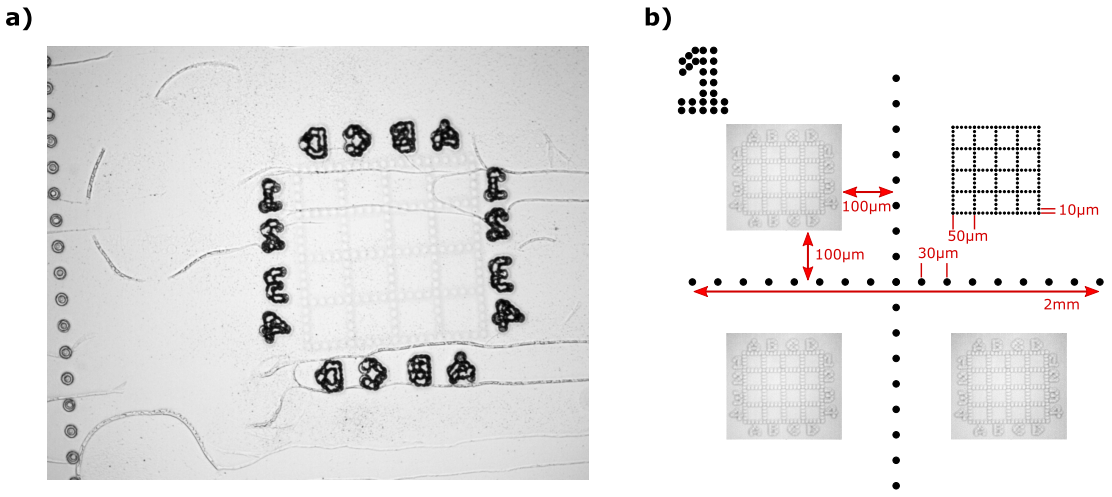

Figure 4.5: a): Microscope image of the serpentine printing structure if the wrong printing parameters are chosen. The picture also shows the checkerboard structure in one edge of the cross which is shot into the mirror surface by the CO_2 laser. b): sketch of the checkerboard pattern positions within one labeled cross (not to scale).

4.4. Characterization of Printed Mirrors

In the following, I will present the characterization of cavity mirrors with respect to the nanoparticle distribution by aerosol-jet-printing as described in the latter section. The characterization focuses on four main aspects:

1. Amount of single, primary nanoparticles with minimum inter-particle distance of 600 nm (point spread function (PSF) of our confocal microscope)
2. Homogeneous spatial distribution of particles across the printed area
3. Unchanged optical properties (europium spectrum)
4. Background fluorescence countrate and spectrum.

To verify the first point, SEM images were taken by Patrice Brenner to confirm the existence of primary nanoparticles. But also atomic force microscopy (AFM) and white light interferometer (WLI) images were taken to confirm single particles

by their height. Furthermore, a confocal microscope was used to characterize the spatial distribution and verify that the optical properties, such as the spectrum and lifetime of europium ions, are preserverd after the printing process. Additionally, the strength of the background fluorescence and its spectrum can be checked in the confocal microscope setup. Lastly, scanning cavity images are recorded (see Section 5.2 for details) to check whether single particles can be resolved by the larger cavity PSF of about 3 µm diameter. The spatial homogeneity of the printing pattern can also be evaluated by scanning cavity images. Finally, the performance of the cavity in terms of its finesse is characterized.

4.4.1. Scanning Electron Microscopy

A SEM-net was aerosol-jet-printed with optimized printer parameters which are the same as for the cavity mirrors. Figure 4.6a) shows an SEM image with large field of view where droplet structures are visible. These are most likely the aerosol droplets contaminated by some residuals of ink in the cartridge. The SDS in the printed solution should have been removed by oxygen plasma cleaning. Zooming into a black square on the net, one can identify well-dispersed primary nanoparticles with diameters below 100 nm in Fig. 4.6b). However, the exact size determination is not reliable at this resolution and is more sophisticated in general. Therefore, we resign from evaluating the size distribution of the nanoparticles here.

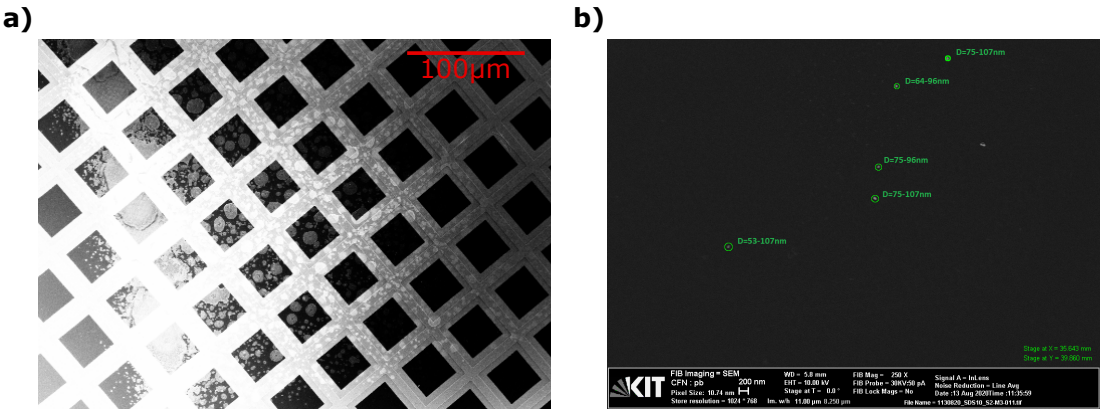

Figure 4.6: a): SEM image with a large field of view reveals residuals of the aerosol droplets on the net. b): Zooming into a black square on the net, shows well-dispersed primary nanoparticles with an inter-particle distance of more than 400 nm labeled in green.

SEM images with high resolution as in Fig. 4.6b) of ten $50 \times 50\,\mu m^2$ fields of the net were taken to quantify the number of single, primary particles (monomers) and

agglomerates. The latter are divided into dimers, when two nanoparticles have a distance of less than 600 nm, or trimers, when three nanoparticles lie within that diameter. Four or more primary particles are denoted as agglomerates. The sample was printed two times with a speed of 10 mm/s, 80 % atomizer power and 18 (40) SCCM atomizer (sheath) stream. The histogram of relative occurrence of monomers, dimers, trimers and agglomerates is shown in Fig. 4.7. About one quarter of all printed particles are monomers giving are reasonable number of primary particles. Since I didn't observe such a high amount of primary particles when dropcasting or spin-coating the SDS solution, I expect that already the nanoparticle dispersion contains mostly agglomerates. Hence, the aerosol jet printer is able to break those up into primary particles. Since the solution was also sonicated before dropcasting and spin-coating, it is not clear why there are much less and smaller agglomerates after printing. One reason could be the higher ultrasound frequency of several megahertz of the printer cartridge in comparison to only 20 kHz frequency of the sonotrode. According to the sonotrode manufacturer Bandelin GmbH, the ultrasound frequency influences the size of the gas cavities formed in the solution during sonication. A higher frequency produces smaller cavity sizes which could be more efficient to brake up small agglomerates into primary particles. However, the implosion of the gas cavities has less force if they are smaller.

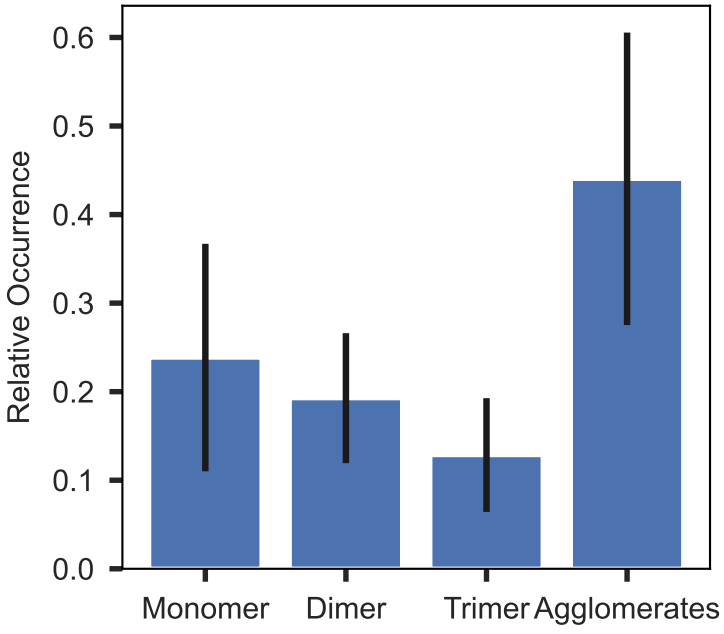

Figure 4.7: Histogram of relative occurrence of nanoparticle monomers, dimers, trimers and agglomerates over an area of $500 \times 500\,\mu m^2$ on a SEM-net. The sample was printed two times with a speed of 10 mm/s, 80 % atomizer power and 18 (40) SCCM atomizer (sheath) stream.

4.4.2. Atomic Force Microscopy

Atomic force microscopy measurements allow the determination of a precise height profile of the mirror surface. We typically use AFM[12] images as a method to confirm the low surface roughness of our cavity mirrors. Additionally, single nanoparticles can be confirmed by their measured height which should be equal to the diameters of the particles as can be seen in Fig. 4.8b). However, the lateral profile is limited by the AFM cantilever[13] point spread function and strongly depends on the AFM settings. This method therefore is not very accurate in discriminating between monomers and small agglomerations. Additionally, large agglomerations cause image artifacts or even a damage of the cantilever due to their heights of up to several microns (see Fig. 4.8a)). The advantage of AFM measurements is that they can be done on the final sample mirror in contrast to SEM images. Furthermore, it was possible to pick up a single nanoparticle by the cantilever using the contact mode and place it again on a desired location on the mirror surface. Three AFM images confirming this pick and place procedure are shown in Fig. A.1 in the Appendix A.

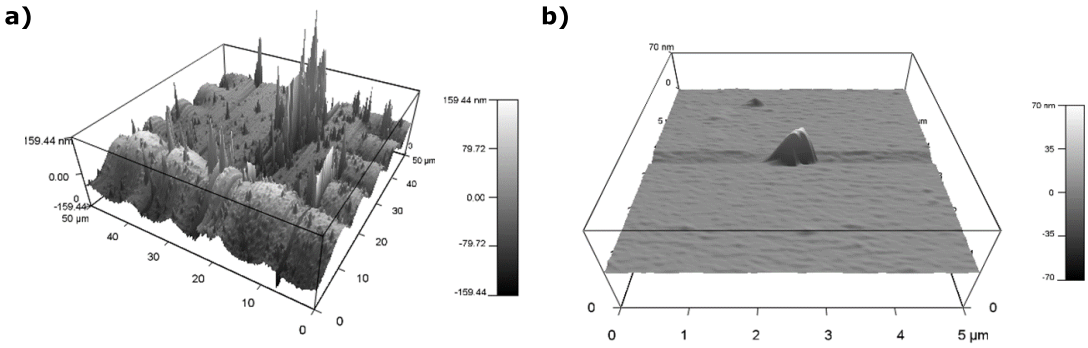

Figure 4.8: Atomic force microscopy images of a spin-coated cavity mirror. Image a) shows a $50 \times 50\,\mu m^2$ field of a checkerboard containing lots of large agglomerates where the measured height steeply increases and the cantilever might crash into the particle. Image b) shows a smaller region of $5 \times 5\,\mu m^2$ where the measured height of approximately 70 nm matches the one of a single primary particle.

4.4.3. Confocal Microscopy

Almost all of the four aspects for the mirror characterization stated at the beginning of this section can be checked by confocal microscopy scans. A sketch of the confocal microscope as well as a list of components of the setup can be found

[12] *MFP-3D origin*, Asylum Research
[13] *OMCL 160AC-NA*, $Q = 520$, $f_0 = 267\,kHz$, Olympus Cooperation

in the masterthesis of Jonas Grammel [159]. The only feature which is difficult to prove reliably is the existence of primary nanoparticles. Since the PSF of the confocal microscope is about 600 nm in diameter and thus much larger than the particle diameters, one can only confirm the existence of a single, primary particle by its fluorescence countrate. An estimation of this countrate dependent on the nanoparticle diameter is plotted in Fig. 4.9. The blue curve shows the countrate if the full visible spectrum is detected, whereas the orange curve assumes a collection of only the ${}^5D_0 \rightarrow {}^7F_2$ transition. The countrates in Fig. 4.9 are calculated assum-

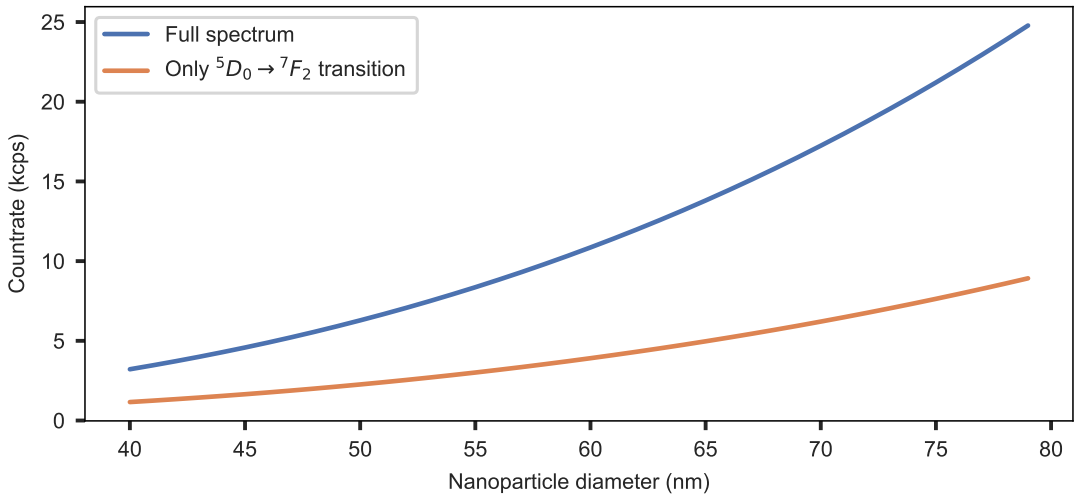

Figure 4.9: Estimation of the fluorescence countrate of a single, primary nanoparticle dependent on its diameter in the confocal microscope setup. The blue curve shows the countrate if the whole visible europium spectrum is detected, wherease the orange curve depicts only the countrate expected from the 611 nm transition using a 610/5 nm band-pass filter.

ing an off-resonant excitation at 532 nm with only about 20 % excitation efficiency resulting in approximately 2 cps/ion overall detection efficiency as determined by [67] in a similar setup. This amounts to countrates of about 4 (10) kcps for a 60 nm particle using a 610/5 nm band-pass filter (full spectrum).

Based on this, I set the following criteria for detecting a single, primary nanoparticle in a confocal microscope scan:

- Search for a PSF-limited spot
- Check whether the background-corrected countrate is within the range as estimated in Fig. 4.9
- Confirm the europium spectrum.

However, it should be noted that these criteria are just a coarse guideline to find single nanoparticles and their existence can only be checked with certainty in SEM-images.

For the measurement shown in the following, I excited the ions with laser light at 532 nm[14] and 1.0 mW excitation power in front of the objective. When focusing the laser on a clean spot on the mirror, a background fluorescence countrate of 1-2 (10-20) kcps is observed with (without) inserting a 610/5 nm band-pass filter. The detector dark countrate is about 0.5 kcps. Some spots on the mirror show a much higher fluorescence rate when the laser is pointed there for the first time. A bleaching of the fluorescence is visible over a timescale of several seconds. Sometimes also a blinking i.e. sudden jumps in the countrate trace are visible. It is not clear where this comes from but most likely there are still residuals from other ink used in the same cartridge which fluoresce. The background spectrum shows no distinct features and appears rather constant over the whole visible range. Positioning the laser on a PSF-limited spot with lowest observed signals gives a fluorescence countrate of about 3.5 (23) kcps and hence we get a signal-to-noise ratio of only $SNR \approx 1.3\,(0.5)$ for the smallest particles. Therefore, the smallest particles measured here could be around 50 nm which is reasonable.

The confocal microscope images constitute a good method in terms of characterizing the homogeneity of the printing pattern and density of particles. In Fig. 4.10 a comparison between an aerosol printed (a) and spin-coated (b) mirror can be seen. The color scale for the countrates is different for both scans since in image b) the sample seems to be slightly defocused because the PSF appears larger. However, one can clearly see the differences in the size and amount of agglomerations. The aerosol-printed mirror shows no huge agglomerations which size exceeds more than a few PSFs. The spin-coated sample features several agglomerations that are of a size of several tens of microns which could damage the cavity fiber during a cavity scan. The aerosol-printed mirror also reveals a more homogeneous distribution of particles with a high amount of faint, PSF-limited spots.

[14] *Cobolt Samba*, Hübner Photonics GmbH

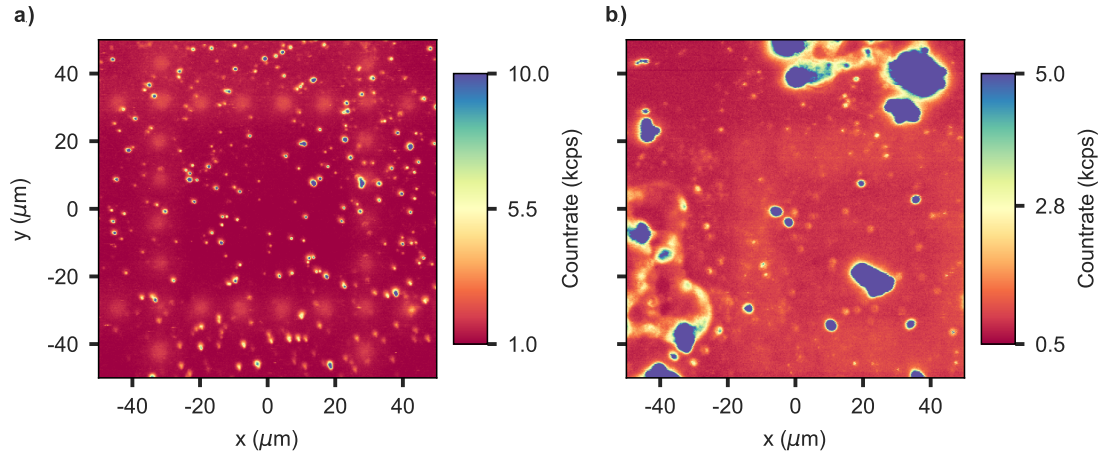

Figure 4.10: Confocal microscope scans of a $100 \times 100\,\mu m^2$ area of an aerosol-printed mirror (a) in comparison to a spin-coated sample (b). Image a) shows a much more homogeneous distribution of small particles and almost no big agglomerations.

A further advantage of the aerosol jet printing method is the better control over the spatial density of particles, controlled by the printing speed and atomizer stream. Varying the latter between 16 SCCM and 18 SCCM results in a different number of particles distributed over an area of the same size as shown in Fig. 4.11. The histogram of the number of pixels with a certain countrate in Fig. 4.11c) shows a higher amount of pixels with countrates between 1.5 to 4 kcps for the region printed with 18 SCCM which constitutes a higher amount of small particles than for the 16 SCCM printing region.

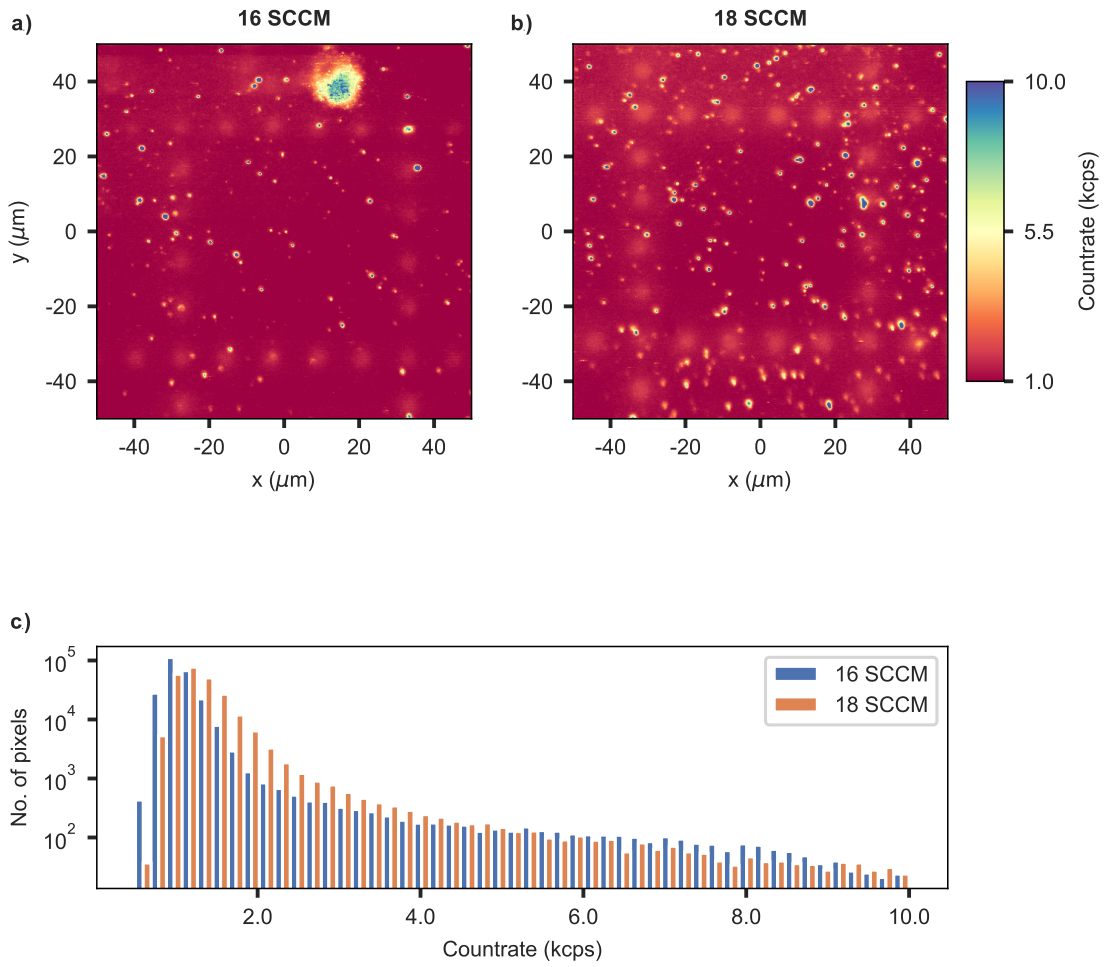

Figure 4.11: Confocal microscope scan of the printing pattern for an atomizer stream of 16 SCCM (a) in comparison to 18 SCCM (b). A lower atomizer stream leads to a lower number of particles within the same area as expected. The histogram in c) visualizes the number of pixels with a given countrate for both images a) and b), respectively.

4.4.4. White Light Interferometry

Mareike Dortmund and Bhavesh Kharbanda investigated the detection of single nanoparticles using the white light interferometer (WLI) of our fiber machining setup in their bachelor's [160] and internship projects, respectively. They found out that it is possible to detect nanoparticles down to a diameter of about 50 nm. However, such small particles just give a height difference of about 0.5 nm in

the WLI image after averaging for 2000-3000 times per image as can be seen in Fig. 4.12. This method therefore adds a quick measurement technique to our repertoire of characterization methods, provided that the surface roughness of the sample is below 0.5 nm. I did not conduct any WLI measurements for the characterization of the aerosol-printed mirrors since the sample preparation was already finished when we investigated this method in more detail.

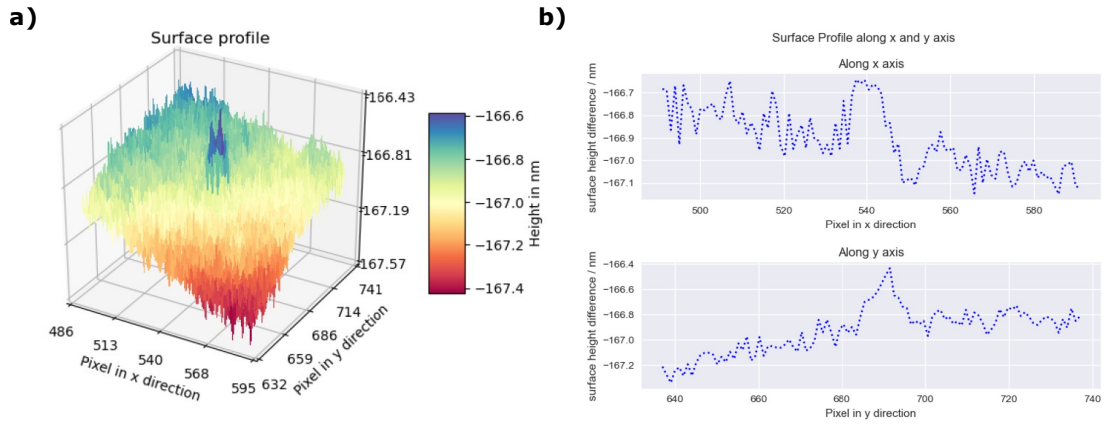

Figure 4.12: White light interferometry image of a single nanoparticle taken from [160]. Image a) shows a color-coded height profile of a single 61 ± 9 nm diameter NP giving rise to a deviation in the surface height of 0.3 nm measured by the WLI. Two cuts through the height profile in a) in the x-and y-direction, respectively, are shown in b).

4.4.5. Scanning Cavity Microscopy

The final characterization step is to perform scanning cavity microscopy (see Section 5.2 for details) to see whether individual nanoparticles can be resolved in the cavity with its larger PSF of approximately 3 µm. A scan of the 580 nm laser cavity transmission of a checkerboard field is depicted in Fig. 4.13. This field was printed with 80 % atomizer power and 18 (40) SCCM atomizer (sheath) stream at a speed of 10 mm/s. Well-dispersed PSF-limited spots can be observed in the transmission scan suitable for cavity spectroscopy. Some faint spots show a reduction in the cavity transmission of about 30-40 % resulting in nanoparticle diameters of about 80-90 nm according to Eq. 6.2.2. Of course for some spots it could also be the case that a small cluster of more than one NP lies within the cavity PSF as depicted in Fig. 3.5.

However, it should be noted that not all of the dark spots show Europium fluorescence and the high fraction of larger agglomerates (black spots) is not suitable for cavity spectroscopy because of the high scattering losses. It was observed that the finesse only slightly reduced from 15,000-17,000 on a clean mirror without

sample to about 14,000-16,000 on a spot on the printed mirror where no distinct feature can be seen (referred to as "clean" spot on the sample mirror in the following). Therefore, the aerosol-printing sample preparation method is suitable for cavity mirror preparation. Further details on the characterization of individual nanoparticles can be found in Section 6.2.

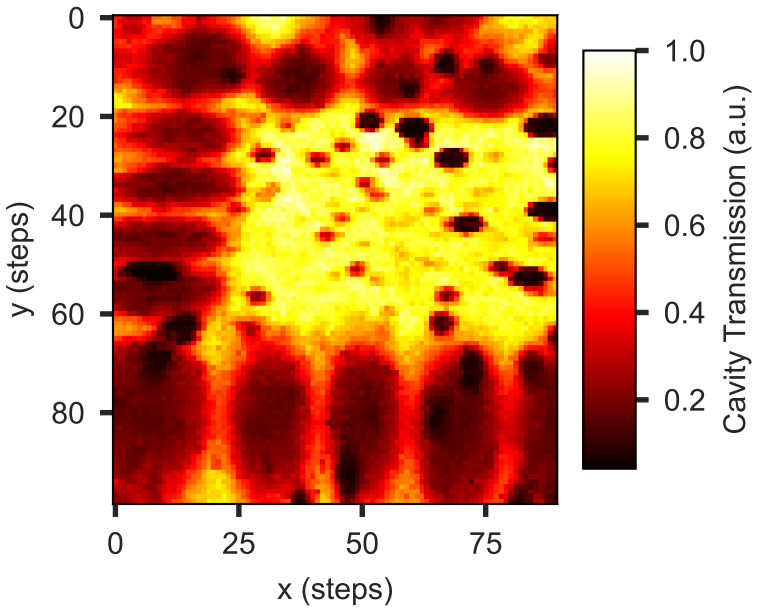

Figure 4.13: Scanning cavity microscopy image of the 580 nm laser transmission of an aerosol-printed mirror. The field of view is approximately $50 \times 50\,\mu m^2$ as can be seen by the checkerboard field markers. The mirror was printed with 80 % atomizer power, 18 (40) SCCM atomizer (sheath) stream at a speed of 10 mm/s. Well-dispersed, PSF-limited features can be seen with a reduction in cavity transmission of about 30-40 % indicating single nanoparticles of sizes between 80-90 nm (for further details consult Sec. 3.5 and Sec. 6.2).

For the master project of Tobias Krom, who picked up individual nanoparticles at the core of a single mode fiber to incorporate a single nanoparticle into a fiber-fiber Fabry-Pérot microcavity [113], we produced glass substrates with a lower density of particles to reach an average inter-particle distance of about 10 - 15 µm. Therefore, those substrates were printed with the same settings listed in 4.3.2, but at the highest speed of 15 mm/s.

4.4.6. Summary

In summary, the three main goals were achieved, namely the preparation of cavity mirrors with well-dispersed single nanoparticles using a reproducible aerosol-jet-printing method and the foundation of methods to reliably characterize the results. The new printing method was the only one that could break up agglomerations into primary nanoparticles. Further advantages of the method are that several mirror regions can be printed with different nanoparticles or solutions, and thus, the mirror surface can be used efficiently in comparison to spin-coating. There are many parameters that can be varied to get the desired printing result. However, the ratio of primary particles to agglomerations of about 25 % needs to be improved by a more detailed analysis of the zeta potential of the colloidal solution and the right choice of surfactant. Although the spectral properties of the Eu-doped yttria nanoparticles are not changed during the mirror preparation process, there are still residuals or contamination particles on the mirror surface which show a PSF-limited spot size in the scanning cavity images and a strong and broadband fluorescence. These features sometimes make it tedious to find a good nanoparticle inside the cavity and should be removed in future preparation processes.

5. Ultrastable Cryogenic Scanning Cavity

Having successfully prepared a cavity mirror, another crucial aspect to perform cavity experiments with open-access Fabry-Pérot cavities is to keep the cavity length at a fixed position on the desired resonance. Especially at cryogenic temperatures this challenge is even more demanding since the running cryostat poses a strong source of mechanical noise and the higher stiffness of materials improves the coupling of the latter to the cavity mechanics. In the first Section 5.1, I will calculate the required cavity length stability for the cavity parameters in this experiment. The following Section 5.2 then explains the design principles of the cavity stage which combine full tunability of all axes to perform scanning cavity measurements with a high longitudinal stability. The latter is improved by an active stabilization using digital feedback controllers as described in Section 5.3. Afterwards, I will present the flow cryostat setup as well as its operation and performance in Section 5.4 and close the chapter with the measurement results of the cavity stability at cryogenic temperatures in Section 5.5.

5.1. Requirements on Longitudinal Stability

Before going into the details of how the length of a fiber-based microcavity can be stabilized, I will estimate the level of fluctuation of the mirror separation required to avoid deterioration of the cavity performance. Therefore, one can calculate the reduced Purcell factor under Gaussian-type length fluctuations as

$$F_P^\star = \frac{\gamma_c}{\gamma_0} = \frac{1}{\gamma_0}\frac{2\pi}{\hbar^2}\int_0^\infty M_0^2(\omega)\,\Lambda(\omega)\int_{-\infty}^{\infty}\rho(\zeta)\,\sigma(\omega-\zeta)\,d\zeta d\omega. \tag{5.1.1}$$

In the above expression, the functions are defined as follows:

$$M_0^2(\omega) = \chi^2 \mu_0^2 E_{vac}^2 = \chi^2 \frac{\mu_0^2 \hbar \omega_0}{2\epsilon_0 V_c}, \tag{5.1.2}$$

$$\Lambda(\omega) = \frac{2}{\pi} \frac{\gamma}{4(\omega - \omega_0)^2 + \gamma^2}, \tag{5.1.3}$$

$$\rho(\omega) = \frac{2}{\pi} \frac{\kappa}{4(\omega - \omega_c)^2 + \kappa^2}, \tag{5.1.4}$$

$$\sigma(\omega) = \frac{1}{\sqrt{2\pi}\sigma_z} e^{-\frac{(\omega-\omega_c)^2}{2\sigma_z^2}}. \tag{5.1.5}$$

The parameters κ, γ denote the FWHM linewidth of the cavity and emitter, respectively, and σ_z the standard deviation of the cavity length jitter. Replacing the functions defined above in Eq. 5.1.1 and evaluating the integrals, gives the following expression for the Purcell factor including Gaussian cavity length jitter [161]:

$$F_P^\star = F_P \sqrt{\frac{\pi}{8}} \frac{\kappa}{\sigma_z} e^{\frac{(\kappa+\gamma)^2}{8\sigma_z^2}} erfc\left(\frac{\kappa+\gamma}{2\sqrt{2}\sigma_z}\right). \tag{5.1.6}$$

Here, F_P is the bare Purcell factor as defined in Eq. 3.6.16. Considering the 580 nm transition at cryogenic temperatures, the emitter linewidth γ is orders of magnitude smaller than the cavity linewidth $\kappa \gg \gamma$, such that one can neglect the emitter linewidth and the modification of the bare Purcell factor in Eq. 5.1.6 solely depends on the ratio of cavity linewidth to length jitter.

For the measurements presented in this thesis the cavity finesse lies in the range between 10,000 and 20,000 at a wavelength of 580.8 nm. The resulting reduction of the bare Purcell factor for these cavity parameters dependent on the RMS cavity length jitter is plotted in Fig. 5.1. In order to achieve a nearly finesse-limited Purcell factor, a cavity stability in the single-digit picometer range has to be reached. Note that the $^5D_0 \rightarrow {}^7F_2$ transition of europium at 611 nm constitutes the opposite case, because the emitter linewidth of this transition is much broader than the cavity linewidth, $\gamma \gg \kappa$ (see Fig. 2.5). Therefore, the Purcell factor of this transition is not affected by the cavity stability. However, since the europium ions will be excited with the 580 nm laser, the cavity stability affects the fluctuations of the excitation power also for measurements where only the 611 nm fluorescence is collected.

In the recent past, lots of progress has been made in stabilizing high-finesse, open-access microcavities to sub-nanometer cavity length fluctuations in a cryogenic environment [50], [58], [134], [161]–[165]. The lowest RMS cavity length jitter of 0.5 pm was achieved by [134] with a plano-concave microcavity when both mirrors are brought into contact and using a wet cryostat. Running an open microcavity inside a closed-cycle cryostat poses an even greater challenge due to a

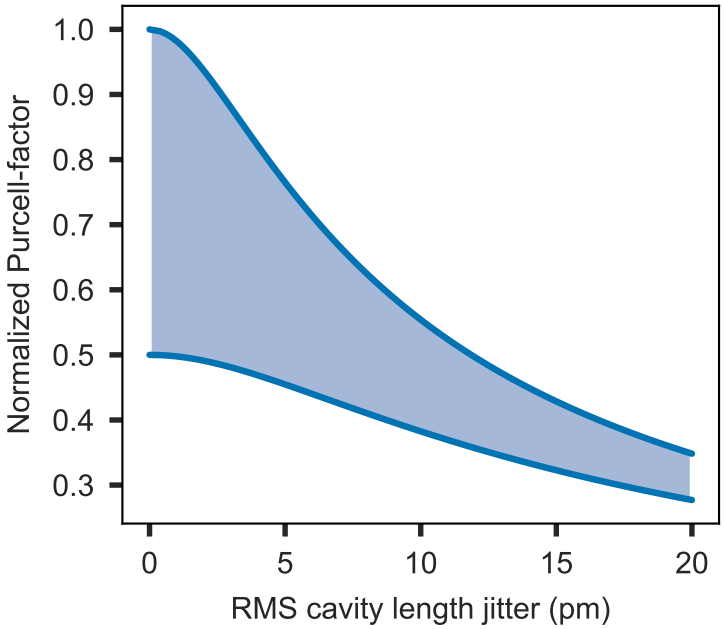

Figure 5.1: Normalized Purcell factor dependent on the RMS cavity length jitter for a cavity finesse between 10,000 and 20,000 (blue area) at a wavelength of 580 nm.

higher noise level of the cold plate in such cryostats. To my knowledge, the best stability was achieved by [58] with 2-3 pm. However, their cavity design has no fibe-mirror but two coated macroscopic plates with concave depressions. Cavities including at least one fiber-mirror have been stabilized to 14 pm RMS length jitter during the quiet phase of a closed-cycle cryostat at 11 K [161] and down to 5 pm at 4 K in a bath cryostat [165].

5.2. Scanning Cavity Design

This section summarizes the design ideas and the assembly of the cavity stage for the flow cryostat used for the measurements presented in this thesis. In the following, I will just give a brief summary of the stage design and relegate to the theses of my predecessors Thomas Hümmer [107], who invented the room-temperature design and co-founded the company Qlibri GmbH to commercialize the idea, and Julia Benedikter [97], who modified the design for a cryogenic environment. Further details can also be found in our paper on the stability of the microcavity platform at cryogenic temperatures [166] and in the thesis of Maximilian Pallmann [167]. Furthermore, I explain the optical setup required to record scanning cavity microscopy images and demonstrate the tracking of a particular nanoparticle

during a cooldown of the cryostat.

5.2.1. Design Principles

The main aspect of the cavity stage design is to reach a high longitudinal stability in combination with a full tunability of all three cavity axes for temperatures ranging from room temperature down to a few Kelvin. Therefore, a high passive stability in combination with a closed-loop feedback mechanism to stabilize the cavity length is employed. The bandwidth of the closed-loop control is limited to below the first mechanical eigenfrequency of the system since the feedback signal would otherwise excite this resonance. Hence, one goal of the mechanical design is to increase the system's eigenfrequencies as high as possible. The acoustic noise in the lab was measured to be dominant up to a few kilohertz [107]. Therefore, eigenfrequencies above this value won't be excited by these noise sources.

The resonance frequency of a spring-mass system is given by $f = \sqrt{k/m}$ with the spring constant k and mass m. Thus, a high stiffness (high k) together with a small mass increases the eigenfrequency. For the stage design this was achieved using flexure-mechanical elements made out of stiff metals like titanium. Micro- to femto-scale movements are realized by bending motions using piezo stacks. The length of the piezo-steered cavity must cover a dynamic range of 10^7 ranging from several microns, to be able to scan over several FSRs, down to a few hundred femtometers during active stabilization (see Section 5.5). It is not possible to cover such a dynamic range with a single piezo stack, because on the one hand no appropriate voltage source is available and on the other hand a large piezo travelling range comes with a higher capacitance which creates a low-pass filter limiting the bandwidth of the active feedback. Therefore, the piezo control of the longitudinal cavity axis is physically separated into a long piezo stack (coarse piezo) for fine tuning over several microns and a thin piezo plate (fine piezo) for ultra-fine tuning with sub-picometer precision up to about 100 nm tuning range at cryogenic temperatures. The coarse tuning up to millimeter ranges is achieved by electrical motors turning micrometer screws.

Measuring the amplitude and phase of the cavity's transfer function at cryogenic temperatures proves the accomplishment of the design goals as can be seen in Fig. 5.2. Here, the cavity length is modulated by a small sinusoidal voltage on the fine piezo stack to excite mechanical resonances along the longitudinal cavity axis. The modulation frequency is then swept from 100 Hz to 100 kHz and the laser transmission signal is measured while the cavity length resides on the side-of-fringe of a resonance. Mixing the cavity transmission signal with the driving voltage of the piezo gives the amplitude and phase response of the system.

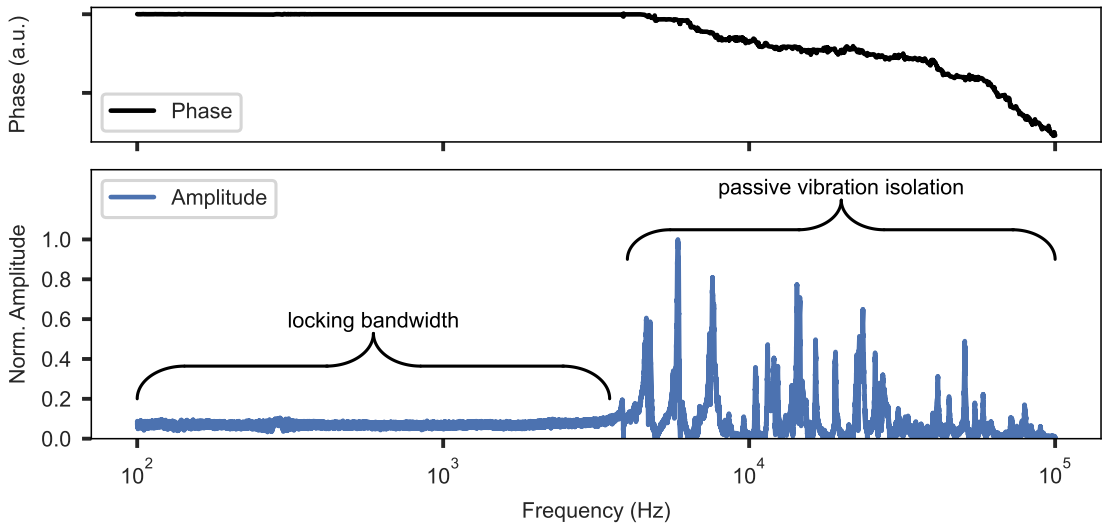

Figure 5.2: Amplitude (bottom) and phase (top) of the mechanical transfer function of the cavity at 10 K (plot adapted from [166]). The transfer function was recorded by homodyne detection of the laser cavity transmission signal while sweeping the modulation frequency for the longitudinal cavity axis. The braces mark the frequency intervals where active cavity length stabilization (locking) is possible and where a vibration isolation has to minimize the coupling to noise sources.

No mechanical resonances occur up to frequencies of about 4.5 kHz opening up a high bandwidth for active cavity length stabilization, called locking (see Section 5.3). In order to avoid excitation of the resonances appearing above 4.5 kHz one has to minimize the coupling of noise sources by a passive vibration isolation. In another experiment, where we operate a similar cavity stage inside a more noisy closed-cycle cryostat, steel-springs are used as vibration isolation against noise stemming from the cryostat cold plate [166]. For the stage used here, I waived a vibration isolation because the flow cryostat provides an environment, which is quiet enough to reach a reasonable cavity stability, as will be shown later.

5.2.2. Cryogenic Nanopositioning Stage

Following the design principles discussed before, I will now show how we translated them into a cryogenic nanopositioning cavity stage mounted in the flow cryostat's sample chamber. All parts of the cavity mechanics are assembled on the main frame, a titanium block, which resides on three posts to match the heigth of the free-space cavity mode with the cryostat windows. A sketch of the piezo-steered scanning cavity principle can be seen in Fig. 5.3a). A top-view picture of the main frame is shown in Fig. 5.3b), where the most important parts are labeled by the numbers.

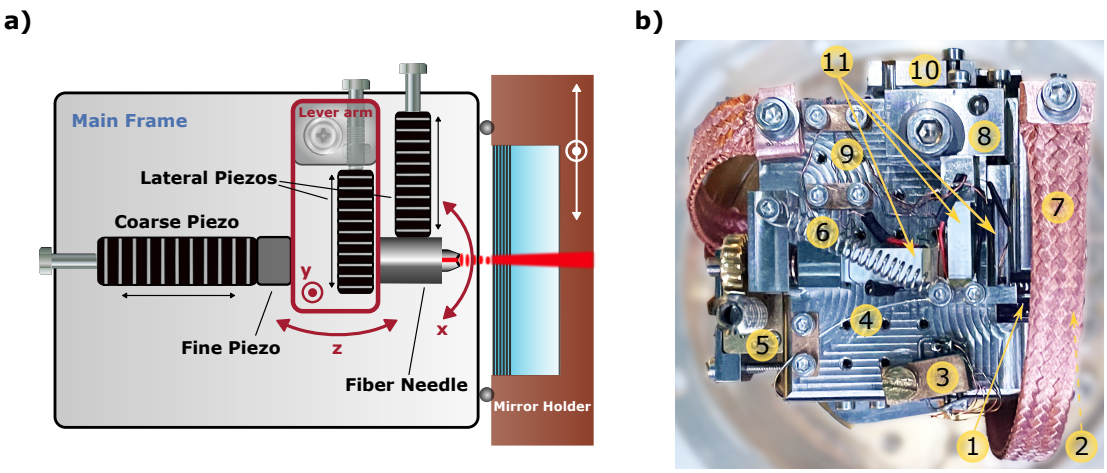

Figure 5.3: a): Schematic drawing of the scanning cavity principle (adapted from [166]): the central element is a titanium lever arm which holds the needle with the cavity fiber. The fiber tip can be moved in all directions by bending motions of the lever arm (y,z) or needle (x) using piezo stack actuators. Each piezo stack can be preloaded by a screw. Electrical motors are used to turn micrometer screws which can coarse tune the cavity length by moving the coarse and fine piezos and shift the mirror holder in the x-y plane. b): Top view picture of the main frame of the nanopositioning stage: (1) the fiber inside the needle as well as (2) the planar mirror are hidden behind a thermal link to the cold plate (7); (3) main frame thermometer; (4) cavity fiber; (5) z-motor with gearwork; (6) steel spring to create restoring force; (8) titanium lever arm; (9) piezo cables with copper-beryllium clamps; (10) x-motor; (11) coarse & fine, x- and y-piezos.

Lever Arm Mechanics The central element is a titanium lever arm (8), which bears the cavity fiber (4) glued into a syringe needle (1) using two-component epoxy glue[15]. The coarse[16] and fine[17] piezos (11) lead to a rotation of the lever arm resulting in a linear shift of the cavity length for small elongations. A spring (6) is used to create a restoring force for the rotation of the lever arm. The tightness of the screw (with plate springs underneath) next to the lever arm bearing strongly influences the cavity length stability. A tight screw clamps down the lever arm and reduces its mechanical vibrations. However, it also increases the required force of the coarse and fine piezos to move the lever arm and thus reduces the cavity length tuning range. Therefore, a good compromise between both features has to be chosen.

The y-piezo[18] (11) is clamped into a groove on top of the lever arm. It creates

[15] *UHU Endfest*, UHU Holding GmbH
[16] *PSt 150/5x5/20*, Piezomechanik GmbH
[17] *PA4FEW*, Thorlabs GmbH
[18] *PSt 150/3.5x3.5/20*, Piezomechanik GmbH

a downwards bending motion of the arm and it thereby moves the fiber in the y-direction. The x-piezo[19] directly touches the metal needle carrying the fiber and thus induces a bending motion along the x-axis. All piezos can be preloaded by screws.

In order to minimize the transmission of vibrations from the cold plate to the piezos, their cables are exchanged by 0.5 mm thin copper wires which are clamped down on the heavy main frame using copper-beryllium clamps (9).

Motorized Coarse Tuning As will be shown later in Subsection 5.2.3, the piezo-steered bending motions only allow for a fiber movement of a few microns at cryogenic temperatures. In order to extend the length tuning range of the cavity to hundreds of microns, needed to compensate thermal contractions during the cooldown, an electrical DC motor[20] together with a gearwork (5) is used. The worm gear turns a micrometer screw that preloads and shifts the z-axis piezos. The planar cavity mirror is clamped into a copper mirror holder (2), which is pulled against the main frame by a steel spring. The spring is hidden inside the main frame and oriented such that it creates a restoring force for the x- and y-movement of the mirror holder. Three glass spheres of 1 mm diameter are inserted into little pockets on the mirror holder and serve as slide bearing to reduce the friction of the mirror holder on the titanium block. Two more of the DC motors and gearworks are used to turn micrometer screws that can shift the holder in the x- and y-direction over a range of several millimeters.

The motors and gearworks are not designed for cryogenic operation and often get stuck upon cooldown. A careful investigation of the motor behaviour when dipping it into an open, liquid nitrogen dewar provided insights on the origins of failure. The following preparation procedure for the motor and gearwork proved to make most of them work properly at all temperatures during a cooldown without heating the motors by applying high currents:

1. Open up the motor by taking off the rear plastic cap.
2. Widen the inner diameter of the rear bearing using a 1.03 mm reamer.
3. Grind off the motor axis a few hundred micrometers.
4. Remove grease and oil from the motor parts and gearwork by putting them into an ultrasonic bath for 10 min in warm soap water.
5. Rinse the parts with water.

[19] *PSt 150/2x3/20*, Piezomechanik GmbH
[20] *V-TEC 6V Micro 10x12 mm, 54 rpm*, Eckstein GmbH

6. Put them again into the ultrasonic bath for 10 min in isopropanol.
7. Air-dry the motor and gearwork.
8. Check if gear wheels are free from grease using a microscope.

Thermalization The sample chamber of the cryostat can be filled with helium exchange gas (see Section 5.4 for details) in order to guarantee a proper thermalization of the nanoparticles residing on the planar mirror surface. The disadvantage of exchange gas cooling is that the entire cavity platform is also cooled down to a few Kelvin, including the piezo actuators and motors. Thus, all parts must withstand and be operational at liquid helium temperatures. Additionally, a minimal relative length change is desired between different parts to avoid tensions and drifts of the cavity mechanics. The piezo stack actuators have a negative coefficient of thermal expansion of $\alpha = -5 \cdot 10^{-6}\, 1/K$ [168] in axial direction i.e. they are expanding upon cooldown. Since there is no material with a similar, negative thermal expansion from which the main frame of the cavity stage could be build from, we decided to use titanium, which has a small coefficient of thermal expansion. The integrated, relative thermal contraction when titanium is cooled from 293 K down to 4 K is about $15 \cdot 10^{-4}$ [169]. However, this comes at the cost of a low thermal conductivity of $\lambda = 0.1 - 6.0\, W/mK$ (4 K to 300 K)[170] and high specific heat capacity of $c_p = 0.52\, J/gK$ (at 298 K) [170] in comparison to other metals. This makes it more challenging to thermalize the stage. Therefore, I added two thermal links made from flexible copper braid (7) thermally connecting the top part of the main frame to the cryostat cold plate. A more careful discussion of cryo-compatible materials and thermalization can be found in [97].

5.2.3. Scanning Cavity Microscopy

In order to find suitable nanoparticles on the planar cavity mirror and locating the fiber position onto it to perform cavity-enhanced spectroscopy, I make use of the piezo-steered scanning of the fiber mirror as explained above. The idea is to record the cavity transmission signal of a narrowband laser (linewidth smaller than the cavity linewidth) coupled into the cavity fiber while sweeping the cavity length over a few FSR to always capture a fundamental mode. This cavity transmission signal is saved at each pixel of an image. The peak cavity transmission T_{max}, as given in Table 3.1, is then extracted and set as the value of that pixel. We denote such an image as cavity transmission scan. More information on this technique as well as the technical details to acquire fast cavity scans can be found in [107].

The lateral resolution of this type of microscopy is limited by the cavity mode

waist diameter, which is about 3 µm for the measurements presented in this thesis. Cavity transmission scans are imaging the maximum cavity transmission normalized to the empty cavity transmission,

$$T_{max,n} = \frac{T_{max,S}}{T_{max,0}} = \frac{\mathcal{L}_0^2}{\left(\mathcal{L}_0 + 2S(\sigma_{ex})\right)^2}, \tag{5.2.1}$$

where I used the expression given in Tab. 3.1 for $T_{max,0}$. Since the bare cavity losses $\mathcal{L}_0$ are constant at each pixel, this results in imaging the additional losses per roundtrip inside the cavity $S = S(\sigma_{ex})$. The latter depend on the extinction cross-section σ_{ex} of scatterers or absorbers residing on the mirror surface. The extinction resolution is hence limited by the bare cavity losses or finesse and the signal-to-noise ratio in order to detect a change in the normalized transmission:

$$S_{ex} = \frac{\pi}{\mathcal{F}_0}\left(T_n^{-\frac{1}{2}} - 1\right). \tag{5.2.2}$$

For example, for an empty cavity finesse of 20,000 and a decrease of the transmission on the scatterer by 10%, one obtains additional losses of about $S_{ex} \approx 40\,\text{ppm}$. The gain in sensitivity using the cavity instead of just a single-pass transmission, like for a conventional microscope, is proportional to the finesse [107]. Taking into account a 3-5 times smaller PSF of an optical microscope in comparison to the cavity mode waist, this constitutes an increase in sensitivity of three orders of magnitude.

Optical Setup The optical setup for scanning cavity microscopy measurements is shown in Fig. 5.4.

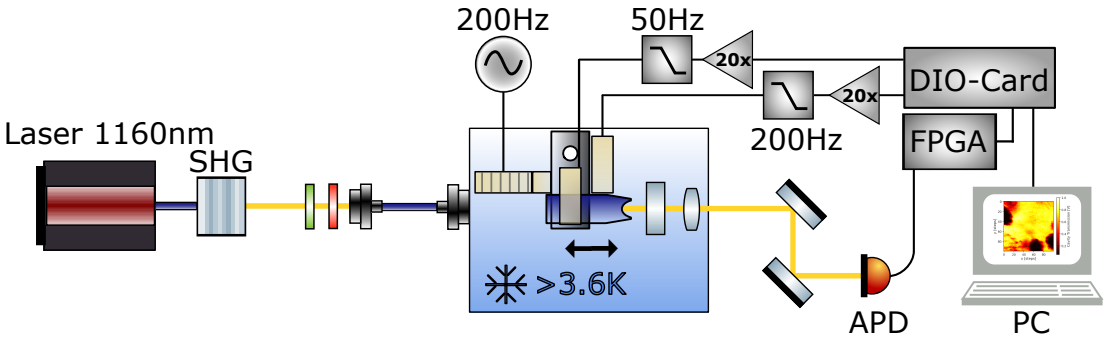

Figure 5.4: Sketch of the optical setup used for scanning cavity microscopy measurements. Green and red plates symbolize quarter- and half-waveplates, respectively. SHG: second harmonic generation crystal, DIO-card: digital input-output card, FPGA: field programmable gate array, APD: avalanche photodiode, PC: lab computer.

For high resolution cavity scans, the 580 nm europium spectroscopy laser is used.

The laser system consists of a 1160 nm external cavity diode laser (ECDL)[21] tuned by a digital laser controller[22]. The fiber-coupled laser output is guided into a temperature-stabilised[23] second-harmonic-generation (SHG) stage[24] which outputs the frequency-doubled 580 nm laser light. The polarisation of the latter can be controlled by a quarter- and half-waveplate, respectively, before it is coupled into a single-mode optical fiber. The fiber enters the cryostat via a vacuum-tight fiber feedthrough and is spliced to the cavity fiber[25] inside the cryostat.

The free-space transmission of the cavity mode is collimated and coupled out of the cryostat through its optical window. An avalanche photodiode (APD)[26] with 50 MHz bandwidth is used to measure the cavity transmission signal during the scan. In order to perform fast cavity scans a detector with at least this bandwidth has to be used to properly sample the sharp resonances.

During a scan the coarse piezo length is modulated with a 200 Hz triangular-shaped voltage signal where the amplitude is chosen such that the longitudinal scanning range covers 2-3 FSR. A digital input-output-card (DIO-card)[27] generates waveforms to control the x- and y-piezo movements, respectively, during the scan. The outputs of the DIO-card are amplified[28] and low-pass filtered[29]. The filtering becomes relevant for the cavity length stability measurements in Section 5.5 to reduce the electrical noise on the x(y)-piezo.

A field programmable gate array (FPGA) hardware[30] receives the cavity transmission signal from the APD and detects the peak position. It outputs a widened, rectangular-shaped signal of the same height as the cavity transmission peaks such that the DIO-card with a lower sampling rate can capture the correct peak height of the resonances. The latter digitizes the measurement signal and sends it to the computer.

[21] *DLpro*, Toptica Photonics AG
[22] *DLCpro*, Toptica Photonics AG
[23] *TEC-1091 controller*, Meerstetter Engineering GmbH
[24] *WH-0580-000-A-B-C*, NTT Electronics, periodically poled lithium niobade (PPLN) waveguide
[25] *SM530-125-160AL pure silica core*, ART Photonics GmbH
[26] *APD120A/M*, Thorlabs GmbH
[27] *NI 6323 with breakout box BNC 2110*, National Instruments Corp.
[28] x-piezo: *WMA-200 Low Noise*, y-piezo: *WMA-02*, both from Falco Systems B.V. used for the measurements of the cavity length stability in this chapter and where changed later on to *PDm200*, PiezoDrive amplifiers for both piezos which are used for most measurements presented in Chapter 6
[29] homebuilt 1st order low-pass filters with cutoff frequencies 200 Hz (x-piezo) and 50 Hz(y-piezo)
[30] *STEMlab 125-14*, Red Pitaya

Tracking a Nanoparticle during the Cooldown I close this section with a series of scanning cavity images, shown in Fig. 5.5, where I tracked a preselected nanoparticle (green circles) during a cooldown of the cryostat from room temperature down to 20 K. At a temperature of 265 K it seems that some condensation on the mirror surface is present which vanishes again but left a dirty spot in the lower half of the scanning image at 235 K.

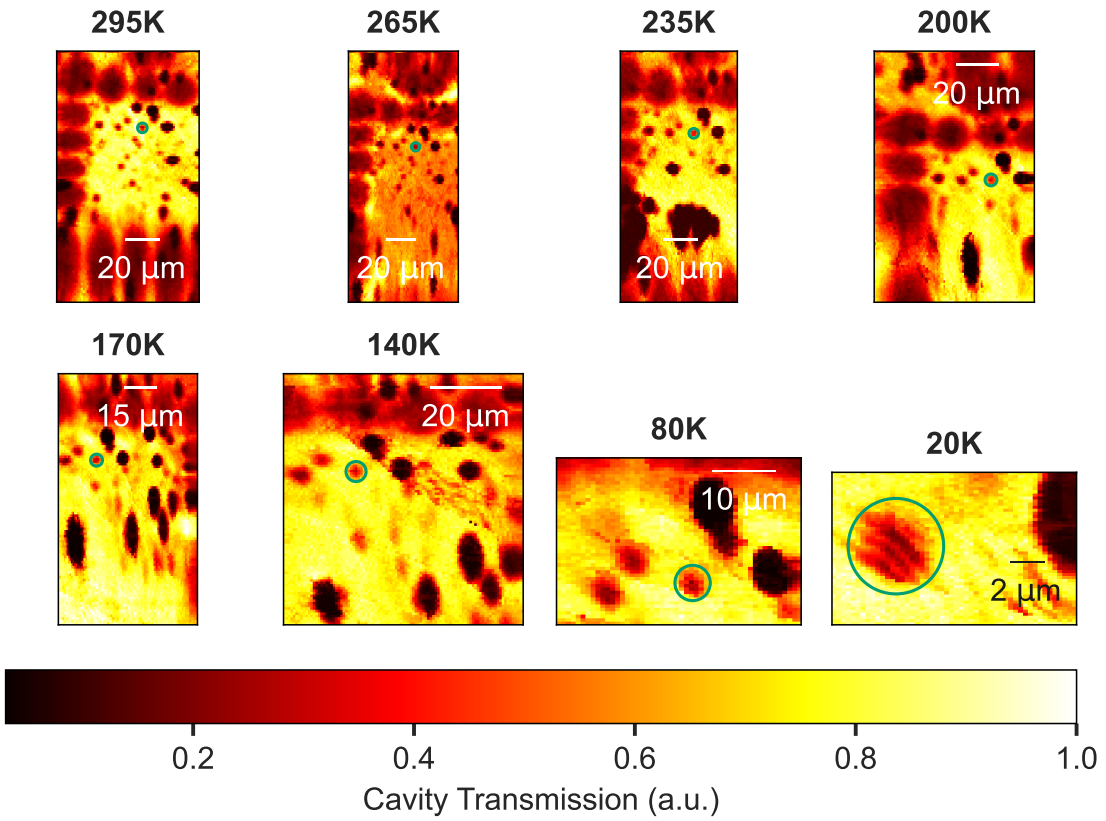

Figure 5.5: Scanning cavity images during a cooldown from room temperature to 20 K following nanoparticle 5 (green circle). The grid structure, which was shot into the mirror (see Fig. 4.5), can be seen (dark red circles) and help to track the particle. The aspect ratios of the scanning images change with temperature due to a reduced maximum elongation of the piezo stacks.

For better orientation on the mirror surface, a checkerboard grid structure was shot into the DBR coating by a CO_2-laser as shown in Fig. 4.5. The pitch of the shots is 10 µm.

As discussed before, the piezo stacks expand upon cooldown whereas all other materials of the cavity stage contract. This leads to a drift of the fiber position to the lower-right over several tens of micrometers, as shown in [166]. Additionally,

the longitudinal cavity axis also shrinks by several tens of micrometers which is beyond the travel range of the z-piezos. Therefore, the three-axis coarse tunability by the electrical motors must be used to compensate those drifts. The selected nanoparticle can be seen in every temperature step which proves the reliable functioning of the modified DC motors.

The total field of view as well as the aspect ratio changes significantly during the cooldown. This depends on the piezo prestress and the different thermal contraction of each axis. The full x,y,z-scanning range at room temperature amounts to about $40 \times 60 \times 10\,\mu m^3$ and reduces to about $5 \times 5 \times 2\,\mu m^3$ at the lowest possible temperature of 3.4 K. The scanning range is therefore only slightly larger than the cavity mode PSF although making use of a bipolar piezo driving with $\pm 200\,V$ as soon as reaching temperatures below 100 K.

5.3. Active Cavity Length Stabilization

In order to stabilize the cavity length to a desired resonance condition, one can use a closed-loop feedback mechanism. Therefore, an error signal containing information about the relative cavity detuning with respect to a given setpoint is fed into a proportional-integral-derivative (PID) controller and the output of the latter is connected to a controlling element. A general introduction to closed-loop control mechanism can be found in [171] and Chapter 6 of [172].

5.3.1. Side-of-Fringe Locking

There are different ways to generate the error signal, e.g. using a laser phase modulation as done in the Pound-Drever-Hall (PDH) locking scheme [173], [174], which was used by my predecessor [97] and which I use to lock the spectroscopy laser to the reference cavity as shown in Section 6.1. For locking the microcavity, I follow the simplest approach of generating an error signal, which is to measure the laser transmission intensity behind the cavity. At the fringe of the Lorentzian cavity resonance, a change in the cavity length of Δz translates into an intensity fluctuation ΔI on the detector as depicted in Fig. 5.6a). As long as the cavity length stays within the left (right) fringe of the cavity resonance, also called the capture range, the slope does not change its sign, and e.g. a reduction of the cavity length with respect to the setpoint can be detected by an increase of the transmission intensity and vice versa. This kind of scheme is called side-of-fringe (SOF) locking. In comparison to the PDH locking scheme, it features a lower capture range and is subsecptible to laser intensity fluctuations. As will be shown

later, the latter can also be an advantage since the SOF method simultaneously stabilizes the intracavity power if the same laser is used for excitation of the emitters. Furthermore, it requires less technical overhead.

To estimate the sensitivity of the error signal and later calculate the root-mean-square (RMS) length jitter, one linearizes the Lorentzian line in a narrow interval around the setpoint and uses the slope of the curve K at that point to convert the intensity to length fluctuations:

$$K = \frac{4\,I_{stp}^2}{\delta d\,I_0}\sqrt{\frac{I_0}{I_{stp}} - 1} = \frac{8\,\mathcal{F}\,I_{stp}^2}{\lambda\,I_0}\sqrt{\frac{I_0}{I_{stp}} - 1}, \tag{5.3.1}$$

with $\delta d = \lambda/(2\,\mathcal{F})$ and $I_{stp}(I_0)$ being the transmission intensity at the setpoint (peak). The slope factor dependent on the setpoint in terms of the normalized height on the resonance is shown in Fig. 5.6b).

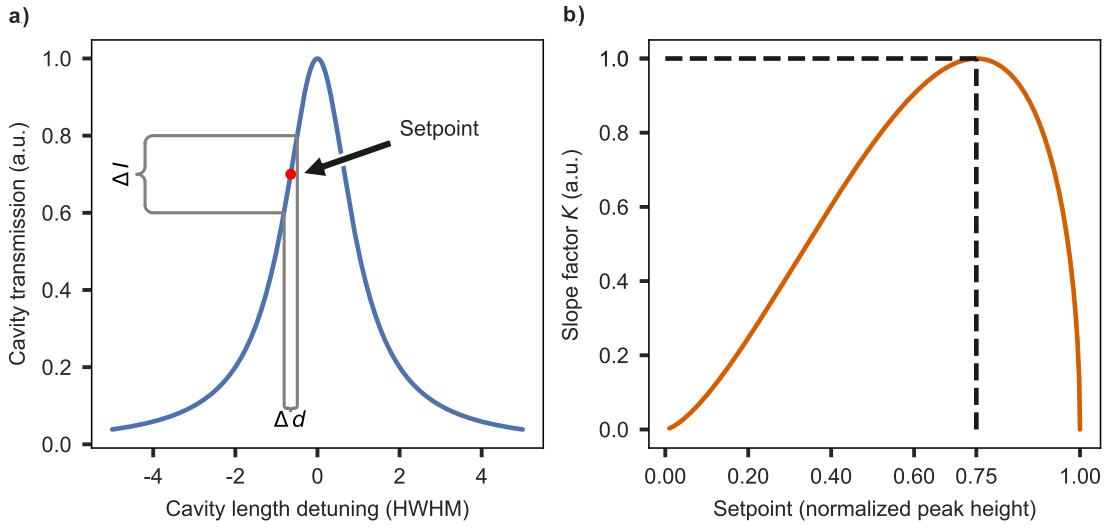

Figure 5.6: a): Visualization of the side-of-fringe locking technique where a relative cavity length change $\Delta\,d$ translates into an intensity fluctuation $\Delta\,I$ in the cavity transmission of the locking laser. The locking setpoint (red dot) denotes the intensity or cavity detuning at which the cavity length is stabilized. b): Normalized slope of the Lorentzian cavity line as a function of the locking setpoint in units of the normalized peak height of the cavity transmission. The highest sensitivity is obtained if the setpoint is located at 75% of the peak transmission where the steepest slope occurs.

The SOF locking setpoint giving the best SNR is at 75% of the resonance peak height due to the steepest slope. The slope factor is proportional to the finesse of the cavity and thus the latter has to be chosen such that a desired sensitivity of the SOF lock can be reached. For example, a finesse of 1200 at a wavelength of 640 nm,

as used in this experiment, leads to a maximum slope factor of $K \approx 5\,\mathrm{mV/pm}$ assuming 1 V peak intensity. Since typical detector noise levels for avalanche photodetectors (APD) are in the order of a few hundred microvolts RMS, the cavity stability would be limited to about a hundred femtometer by the detector noise level.

5.3.2. Optical Setup for Locking

For the measurements of the cavity length stability in Section 5.5, a second locking laser at 640 nm[31] is added to the optical setup as shown in Fig. 5.7. A pellicle couples out 4% of the laser intensity to a photodiode (PD)[32] for power monitoring. The red locking laser is fiber coupled into one port of a wavelength division multiplexer (WDM)[33], which combines the 580 nm spectroscopy laser and the 640 nm locking laser into the same cavity fiber. Furthermore, the WDM features a second output port where 10% of the combined light intensity is coupled out for monitoring (not shown here). An acousto-optic modulator (AOM) is used to pulse the spectroscopy laser.

Both laser wavelengths are split again behind the cryostat by a dichroic mirror[34] and guided onto different APDs[35]. The cavity transmission signal of the 640 nm laser is used as error signal for SOF-locking. Therefore, the APD signal is fed into the fast PID (digital PID controllers realized on FPGA hardware[36]). The output of the latter is split and on the one hand connected to a slow PID for drift compensation internally on the same FPGA board. On the other hand its analog output port is low-pass filtered at 1 kHz[37] and connected to the fine piezo of the cavity stage. The analog output port of the slow PID is amplified[38] and low-pass filtered by a homebuilt 3rd-order low-pass filter at about 10 Hz before it connects to the coarse pizeo of the cavity stage.

[31] homebuilt ECDL with *HL63142DG* diode, Ushio and *DC100 laser controller*, TUIOptics
[32] *PDA36A-EC*, Thorlabs GmbH
[33] *customized 2x2 90:10 WDM*, Thorlabs GmbH
[34] *Semrock FF635-Di01-25x35*, IDEX Health & Science LLC
[35] lock (580 nm) APD: *APD120A/M* (*APD410A/M*), both Thorlabs GmbH
[36] *STEMlab 125-14*, Red Pitaya
[37] *EF110*, Thorlabs GmbH
[38] *SR560* low noise preamplifier with 5x gain, 1 kHz low-pass filter with 6 dB/oct roll-off, Stanford Research Systems and *WMA200*, Falco Systems

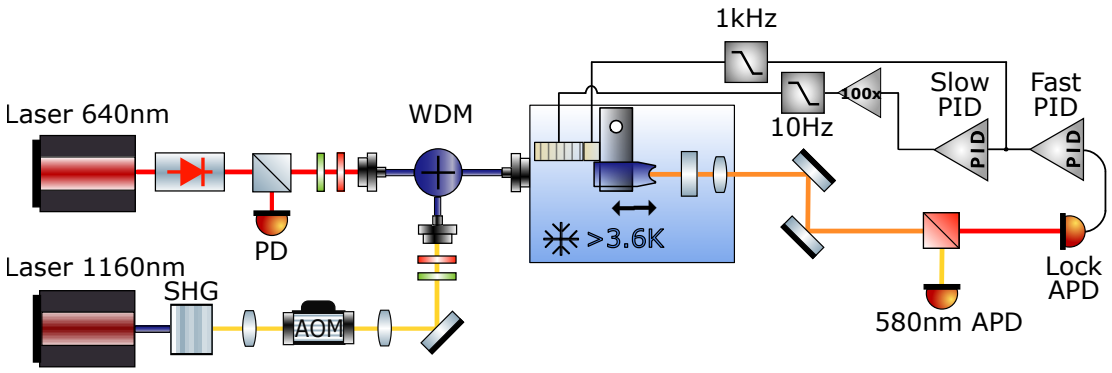

Figure 5.7: Sketch of the optical setup used for characterizing the cavity length stability. SHG: second harmonic generation crystal, AOM: acousto-optic modulator, PD: photodiode, APD: avalanche photodiode, WDM: wavelength division multiplexer, PID: proportional-integral-derivative controller.

5.3.3. Locking Sequences

The feedback loop for active stabilization consists of the detector recording the error signal, which is fed into the fast PID controller sending the control signal onto the fine piezo. Since the FPGA output voltage range is only 0-2 V and the fine piezo signal is not amplified to reduce electrical noise, the travel range of this piezo is limited to a few tens of picometers below 10 K. Since there are two piezo stacks available to control the cavity z-axis, both piezos are used in a cascaded lock. Thereby, the slow PID is used to keep the output voltage of the fast PID within the center of its dynamic range (0-2 V). The control signal of the slow PID is amplified by a factor of hundred and strongly low-pass filtered to reduce electrical noise. The slow PID signal applied to the coarse piezo is therefore capable of compensating cavity length drifts of several nanometers stemming e.g. from piezo creep.

The settings of both PID controllers can be changed by a Python-based graphical user interface (GUI) named PyRPL (Python RedPitaya Lockbox) [175], [176]. PyRPL is a software package, specialized on digital feedback control for quantum optics experiments. It provides a simple front end to make use of the various digital signal processing (DSP) functionalities of the STEMlab FPGA hardware. For example, it can be used as oscilloscope, signal generator, trigger, digital filter or PID module. Further details on the software architecture and available DSP modules can be found in the thesis of the developer Leonhard Neuhaus [172].

In cooperation with him, I customized the Lockbox module of PyRPL to provide two internally connected PID controllers with two separate outputs, which

we called Duallockbox. The Lockbox module is a higher-level software module developed for active stabilization of Fabry-Pérot interferometers. The Duallockbox combines two PID controllers with oscilloscope, signal generator and digital filter modules to perform a calibration of the error signal and a sequenced lock. The latter means that different locking stages with different gain and setpoint settings as well as custom functions can be called. In the following, I will explain three algorithms that I implemented to automatize the setpoint calibration and sequenced locking for different scenarios.

Duallockbox Sequence The first sequence describes the standard locking scenario using the Duallockbox. In order to perform a SOF-lock on a desired cavity resonance, the Lockbox module needs to calibrate the cavity transmission signal in order to calculate the voltage of the given locking setpoint. This is done in the first step of the sequence shown in Fig. 5.8.

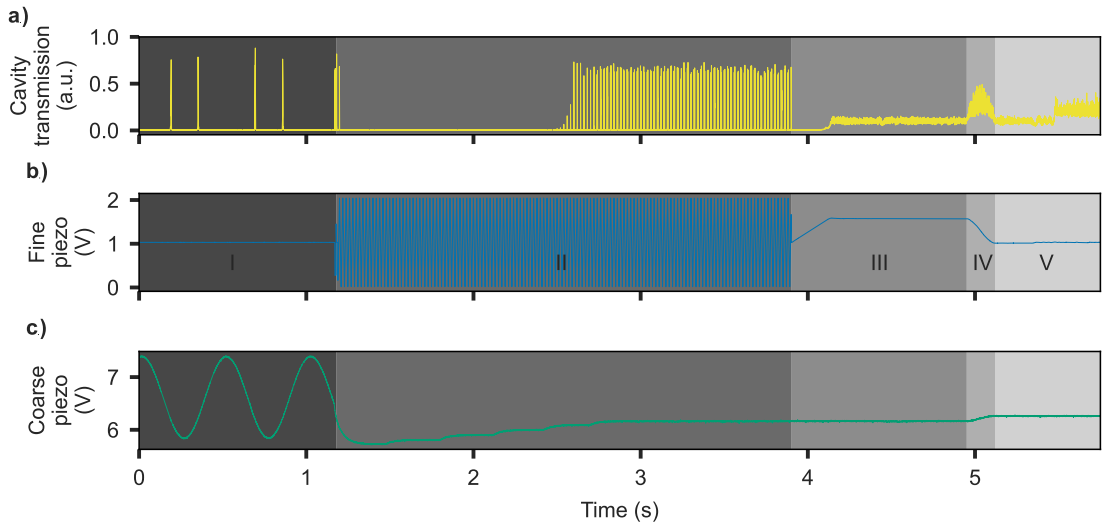

Figure 5.8: Oscilloscope time traces of the cavity transmission signal (a) as well as the voltages applied on the fine (b) and coarse (c) piezos. In the first step (I) the resonance is calibrated. In phase (II) the resonance is approached slowly until it enters the capture range of the lock. Thereafter, the fine piezo PID controller is switched on to catch the resonance in step (III). The drift compensation of the coarse piezo is switched on in phase (IV) and locking on the desired final setpoint is accomplished in the last step (V).

A 2 Hz sinusoidal waveform is applied to the coarse piezo (Fig. 5.8c)) and its offset is adjusted such that the desired cavity resonance is centered in the sweep range. The oscilloscope module of PyRPL simultaneously records the cavity transmission signal (Fig. 5.8a)) as well as the coarse piezo output channel. The transmission peak voltage is obtained to calibrate the amplitude of a Lorentzian function used

as model for the error signal. From now on the locking setpoint for the fast lock can be entered in units of HWHM of the cavity resonance and is converted into the setpoint voltage for the PID using the calibrated Lorentzian function. Simultaneously, the coarse piezo voltage at the peak transmission is calculated in order to know the resonance position in units of the coarse piezo voltage.

The second step, realized in a custom function called by the locking stage, is used to gradually shift the cavity length into the capture range of the fast lock. Therefore, the sinusoidal sweep is switched off and the coarse piezo voltage is set to a constant value slightly below the resonance position. A loop is switched on which increases the output voltage in every iteration. In parallel, a 50 Hz triangular waveform is applied to the fine piezo output (Fig. 5.8b)), and an oscilloscope trace of the cavity transmission as well as fine piezo output voltage is taken at each coarse piezo voltage step. As soon as the cavity transmission exceeds 90% of the peak height measured in the first step and is located within 1.1 V and 1.9 V of the fine piezo voltage, the loop stops and the coarse piezo voltage is kept constant. This can be seen in the second half of step two in Fig. 5.8. The cavity resonance is now positioned inside the capture range of the fast lock for a positive PID setpoint and gain setting.

The third step accomplishes the capturing and locking onto the side-of-fringe of the resonance. The fine piezo output is switched from the signal generator to the fast PID, which captures the resonance on a low setpoint of typically 3 HWHM with a low gain. In the next step, the slow PID is enabled at a setpoint of 1 V output signal of the fast PID i.e. in the center of its dynamic range. Therefore, the coarse piezo shifts the cavity length accordingly as seen in step four in Fig. 5.8c).

The last step typically consists of two Lockbox stages. In one stage, the fast PID gain is increased to its final value which gives the best locking performance. In the final stage the fast PID setpoint is shifted to its desired final value depending on the type of measurement performed. This accomplishes the locking sequence of the Duallockbox and a software trigger to start a spectroscopy measurement can be given by PyRPL. Furthermore, the module provides an automated relocking functionality, which detects when a certain locking threshold is exceeded and triggers the locking sequence again.

Dual-Input-Dual-Output Sequence To use the 640 nm laser for locking the cavity onto a double-resonance (DR) condition with the 580 nm spectroscopy laser, I modified the Duallockbox sequence described above to a dual-input-dual-output (DIDO) sequence. The main difference constitutes in the 640 nm laser transmission being used as error signal for the lock for which the setpoint has to be adjusted such that the spectroscopy laser is also on resonance. In Fig. 5.9 the oscilloscope

traces of the cavity transmission of the 580 nm/640 nm laser (a)/(b) as well as the outputs for the fine (c) and coarse (d) piezos, respectively, are shown.

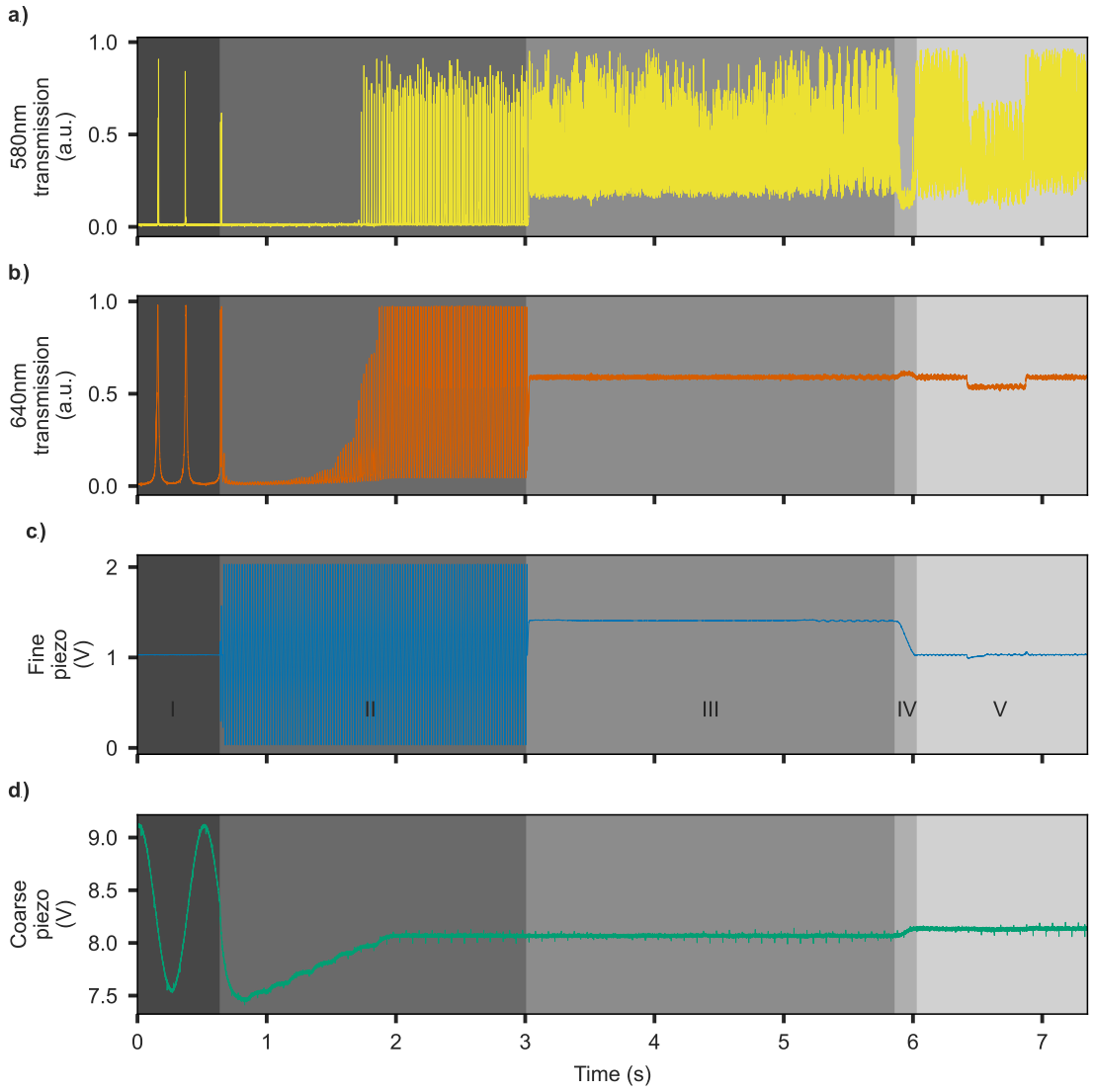

Figure 5.9: Oscilloscope time traces of the cavity transmission signals of the 580 nm spectroscopy laser (a) and 640 nm locking laser (b), as well as the voltages applied on the fine (c) and coarse (d) piezos, respectively. In the first step (I) both resonance are calibrated. In phase (II) the locking resonance is approached slowly until it enters the capture range of the lock. In the third part of the sequence (III) the fine piezo PID controller is switched on to lock on the calibrated setpoint of the 640 nm transmission. Afterwards, in (IV), the drift compensation of the coarse piezo is switched on. In the last step (V) the locking setpoint is readjusted to match the desired setpoint on the spectroscopy resonance.

The first step starts with a measurement of both laser transmission channels in order to determine the locking setpoint on the 640 nm resonance which corresponds to the given setpoint on the 580 nm resonance. Usually, one locks the cavity with zero cavity-laser detuning i.e. at a setpoint of 0 HWHM. But this sequence also features locking on arbitrary setpoints which result in a cavity being detuned from the spectroscopy laser. The first step of the sequence also calibrates the 640 nm laser signal in the same manner as described in the first step of the Duallockbox sequence above.

In the second step, the coarse piezo is used to shift the cavity into the capture range of the fast PID as described in the Duallockbox sequence.

The following stage of the sequence accomplishes SOF-locking on the 640 nm resonance using only the fast PID. As can be seen in the yellow trace in Fig. 5.9a) the locking setpoint doesn't correspond to the 580 nm laser being fully on resonance. This mismatch between the locking setpoint calculated in step one and the actual setpoint is attributed to a low timing resolution of the oscilloscope traces of both transmission signals recorded in the first step.

After the activation of the slow drift compensation on the coarse piezo in step four, I call a custom function to adjust the locking setpoint to match the desired setpoint of the spectroscopy resonance. This is achieved by a gradient-descent algorithm measuring the mean cavity transmission of the 580 nm laser and comparing it to the desired setpoint. In the fifth step in Fig. 5.9, three loop cycles of this algorithm can be seen. In the final step in trace a), a slightly higher mean transmission signal and smaller peak-to-peak amplitude can be observed. This corresponds to a cavity position on resonance with the 580 nm laser as it was given for this sequence.

In order to compensate for drifts in the detuning between the 580 nm and 640 nm cavity resonances, a setpoint-adjustment loop function can be started in the final stage of the DIDO-sequence. It basically repeats the gradient-descent algorithm described above after a given time interval and readjusts the locking setpoint. The drifts in the detuning are mainly caused by piezo creep of the x-and y-piezos moving the lateral fiber position. Due to different cavity dispersions of both lasers their resonance conditions therefore shifts differently. In the long term, laser frequency drifts could also lead to drifts in the detuning.

5.3.4. Pulsed Locking

The DIDO-locking scheme gives the best cavity length stability as shown in Section 5.5. However, it requires the cavity to be operated under the DR-condition

of both lasers. This is not always guaranteed due to the limited wavelength tunability of the 640 nm locking laser. To be independent of a separate locking laser and to be able to perform measurements at every longitudinal mode order, I implemented a pulsed locking scheme. It requires only the spectroscopy laser and a pulse module[39] to play transistor-transistor-logic (TTL) pulse sequences. The STEMlab FPGA board features digital input-output channels which can be used to switch on and off the PID modules or trigger a waveform on the signal generator module by TTL-pulses. The cavity is locked on a low setpoint of 3 HWHM of the spectroscopy resonance using the Duallockbox sequence. After the sequence has finished successfully, the TTL-pulse sequence shown in Fig. 5.10 is started. For the optical setup used for such a measurement, see Fig. 6.1 in Chapter 6.

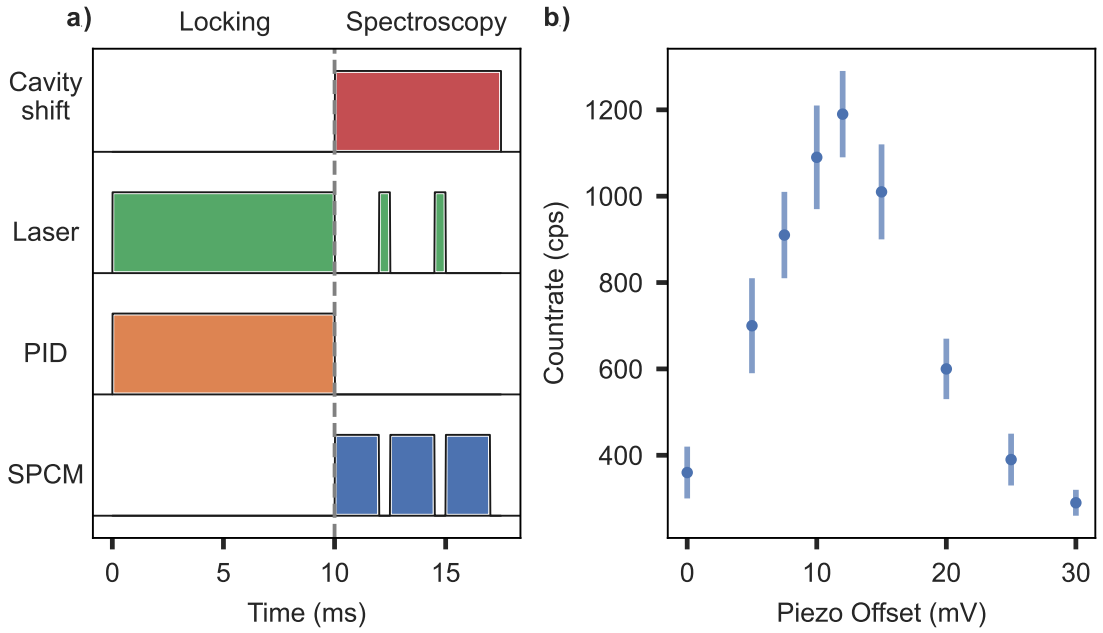

Figure 5.10: a): Pulse sequence diagram for the pulsed locking scheme. A colored rectangle in the row of the respective device symbolizes that the latter is switched on for the depicted time interval. Cavity shift: shifting the cavity length by an fine piezo offset voltage, PID: proportional-integral-derivative controller (lock), SPCM: single photon counting module. b): PLE countrate measured for different fine piezo offset voltages to perform the cavity shift during the spectroscopy phase as shown in a).

The pulse sequence consists of a time window of 10 ms were the laser (via an acousto-optic modulator (AOM)) and both PIDs are switched on to stabilize the cavity. Afterwards, the PIDs are switched off and keep their output value for the time span of the spectroscopy measurement, which is typically a few milliseconds. Within the spectroscopy time window an arbitrary pulse sequence for the laser

[39] *Pulse Streamer 8/2*, Swabian Instruments GmbH

and single photon counting module (SPCM) to detect the fluorescence photons can be played, e.g. to record a lifetime histogram.

Since the cavity length resides at the SOF locking setpoint and thus is detuned to the spectroscopy wavelength, it is desirable to shift the cavity on resonance during the spectroscopy measurement. To achieve this, I trigger the signal generator module to output a single square waveform of given amplitude on the fine piezo output channel. This deterministically shifts the cavity to a certain length without active feedback. By monitoring the fluorescence countrate dependent on the offset voltage applied to the fine piezo, one can determine the amplitude of the square wave, which maximizes the countrate and thus shifts the cavity on the peak of the resonance. Such a measurement is depicted in Fig. 5.10b). In this case, an offset voltage of 12 mV leads to a threefold higher fluorescence countrate as compared to the cavity staying at the locking setpoint.

The disadvantage of this method is the reduced cavity length stability which is given by the passive stability without active feedback (see Sec. 5.5). The interleaved locking phase can only compensate for slow drifts up to a few Hertz bandwidth.

5.3.5. Software Architecture for Measurement Automation

Finally, I would like to highlight some further advantages of the software-controlled FPGA hardware, as described before, in comparison to the analog PID controllers used in the group before. For example, different Lockbox parameter settings can be stored and recalled, which allow for fast switching between different locking procedures. Furthermore, I use this functionality to switch between settings for scanning cavity measurements and performing spectroscopy with a locked cavity. Cavity-enhanced spectroscopy requires the monitoring and control of the cavity locking status during sophisticated and long-term measurements. To further automate the cavity control and start and stop measurements depending on the locking status, I implemented software-based connections between PyRPL and other measurement control GUIs using the Python library RPyC (Remote Python Call [177]). Since a plethora of Python GUIs to control the various devices in the group's labs already existed, these software connections open up a simple way of connecting the required GUIs for a certain measurement with just a few lines of code.

Software Architecture Except of the PyRPL Lockbox, the main components of the software architecture to control the lifetime, high-resolution laser scans and

(transient) spectral hole burning measurements presented in Chapter 6 are the:

- "MeasurementControl GUI" to conduct the overall measurement, initialize it and collect the data.
- "Pulse GUI" to load and play digital pulse sequences on the *PulseStreamer* which is also used to trigger other devices if needed.
- "TimeTagger GUI" to communicate with the *TimeTagger*[40], which records the timestamps of the photon counting events and calculates countrates or histograms.
- "KeysightAWG GUI" to load, queue and play waveforms on the arbitrary waveform generator (AWG)[41], which is driving an AOM or EOM controlling the laser power or frequency, respectively.

A schematic drawing of the software and hardware connections between the different GUIs and devices is shown in Fig. 5.11.

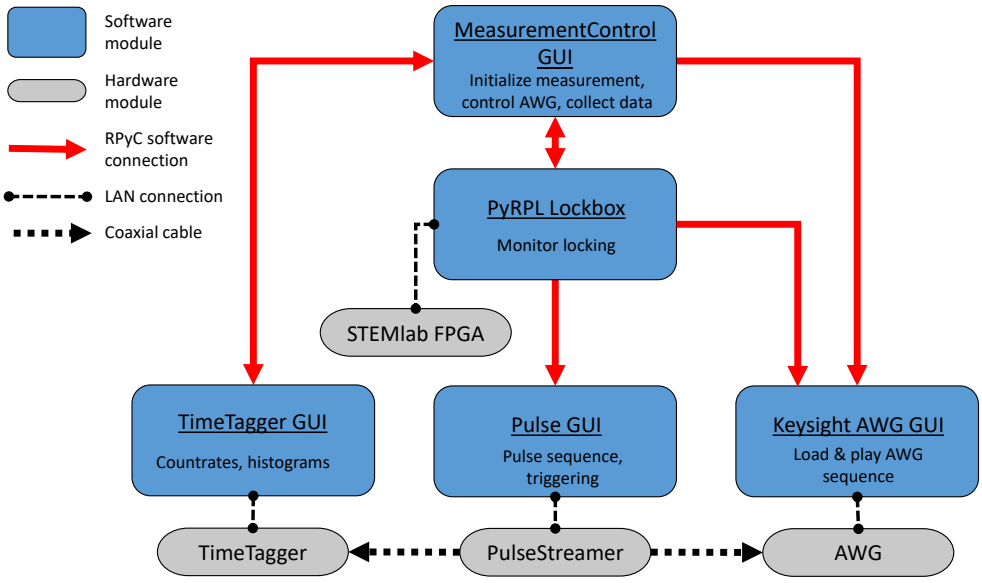

Figure 5.11: Component diagram of the software architecture to realize an automation of cavity-enhanced spectroscopy measurements. A single headed red arrow represents a function call in the remote GUI. Double-headed red arrows symbolize a bidirectional communication between two GUIs in order to exchange data sets or remotely call functions of the other GUI.

[40] *Time Tagger 20*, Swabian Instruments GmbH
[41] *M3300A module*, Keysight Technologies

The main aspect behind this particular software architecture is the interaction of different asynchronous loops running in every GUI. However, remotely calling a PyRPL function in another GUI's asynchronous loop can crash PyRPL. Therefore, the PyRPL Lockbox serves as a master loop, which remotely calls functions in other slave GUIs involved in the measurement. Measurements can therefore be interrupted by PyRPL whenever a relocking or readjustment of the locking setpoint is needed. For locking, the power of the spectroscopy laser usually has to be much higher compared to the power levels used for single europium ion spectroscopy. The laser power can be controlled via the carrier amplitude of the AWG driving an AOM. Hence, a software connection between the PyRPL Lockbox and the "KeysightAWG GUI" is needed. Additionally, the spectroscopy laser has to run cw for successfull operation of the PyRPL Lockbox sequences. This is achieved by interrupting the pulse sequence via the software connection to the "Pulse GUI", which switches on and off the AOM and triggers measurements of the TimeTagger.

In order to achieve a callback to the PyRPL Lockbox, e.g. when the relocking attempt should be triggered by the "MeasurementControl GUI" or the measurement has finished, I make use of flags which are read out by PyRPL at a time defined by its asynchronous loop cycle. This is indicated by the double-headed arrow in Fig. 5.11.

In the future, the frequency stabilization of the spectroscopy laser and a drift compensation of the lateral fiber position could be included in the measurement routine. If one aims to perform temperature dependent measurements, it is also straight forward to include the cryostat's temperature controller GUI into the software architecture.

Sequence Diagram Having discussed the component diagram of the software architecture in Fig. 5.11, I close the section with a sequence diagram of a fully automated high-resolution laser scan measurement (see Fig. 6.9) in Fig. 5.12. Here, the spectroscopy laser is scanned over several megahertz with a high resolution using the AWG. The cavity is actively stabilized on the spectroscopy laser resonance and the cw countrate of the 611 nm fluorescence is measured. The "Pulse GUI" is used to start a pulse sequence e.g. to trigger the AWG and gate the single photon detector. The "TimeTagger GUI" collects the countrate data from the detector events.

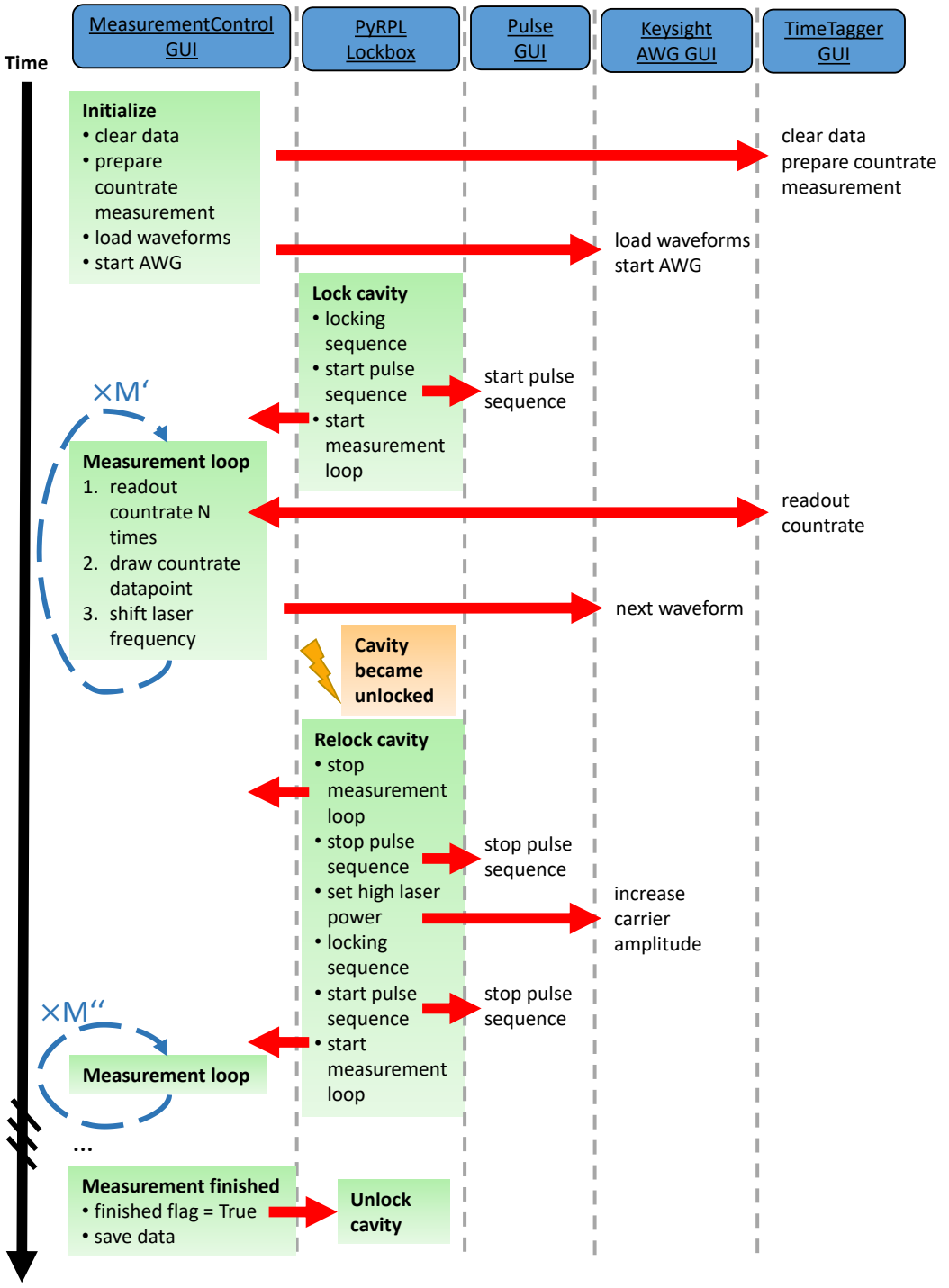

Figure 5.12: Sequence diagram of an automated high-resolution laser scan measurement as done in Sec. 6.4. Each column represents the actions of that particular GUI and the chronological order is downwards. The red arrows denote a remote function call or data transfer via a Remote Python Call (RPyC) software connection.

First of all, the "MeasurementControl GUI" initializes the measurement, which includes data clearance, setting parameters for the countrate measurement and loading waveforms into the AWG queue and starting it. Afterwards, the cavity is locked using one of the locking sequences explained in Subsection 5.3.3. If the cavity was locked successfully, the pulse sequence in the "Pulse GUI" as well as the central measurement loop of the "MeasurementControl GUI" is remotely started by the PyRPL Lockbox. I modified the automated relock functionality so that PyRPL first interrupts the measurement loop, pulse sequence, as well as increases the laser power, if necessary, before it starts the locking sequence. The central measurement loop running in the "MeasurementControl GUI" controls the laser frequency and reads out the desired number of countrate datapoints at the respective frequency. When the given number of frequency scans have been acquired and thus the whole measurement is finished, the "MeasurementControl GUI" saves the data and sets a finished flag. The latter triggers the PyRPL Lockbox to unlock the cavity.

The high-resolution laser scan measurement sequence as explained above can take up to several hours in total if averaging of several seconds per datapoint is needed. Since the microcavity inside the cryostat is susceptible to slow drifts of the cavity length or can suddenly be kicked out of lock by mechanical disturbances in the lab, a careful and reliable monitoring of its locking status is necessary. Having automated the spectroscopy routine by the shown sequence therefore facilitates the work of the researcher.

5.4. Helium Flow Cryostat Operation

Despite the careful design and choice of materials of the cavity stage, reaching the stability level of a few picometers at cryogenic temperatures, required for this experiment, also strongly depends on the cryostat to be used. My predecessor incorporated the cavity stage into a closed-cycle cryostat [97], which features the advantage of being cryogen-free and requires low maintenance. Although, we managed to operate the nanopositioning stage inside this closed-cycle cryostat [166], [167] with a decent stability of 15 pm RMS at 10 K, the mechanical noise level of the cold plate is much higher compared to wet cryostats. With the prospect of reaching even lower cavity length jitter, we decided to use a liquid helium (LHe) continous flow cryostat for this experiment. In the following, I will describe the cryostat assembly, how to operate it and its performance.

Cryostat Setup The cryostat is a customized version of a *Konti Micro* continous flow cryostat from the company CryoVac. The cryostat diameter was enlarged to

meet two requirements: the cavity stage needs to fit in the sample chamber and there must be space between the sample chamber and radiation shield windows to place a lens mount. Furthermore, the sample chamber can be sealed with indium to be used with helium exchange gas for a better thermalization of the nanoparticles than in previous experiments [67], [97]. A picture of the main cryostat chamber (9) with the pipes to the vacuum- and helium-systems, respectively, as well as electrical and fiber feedthroughs is shown in Fig. 5.13a). Removing the lid of the vacuum recipient opens up the view on the radiation shield (11) and indium-sealed sample chamber (14) as can be seen on the picture in Fig. 5.13b).

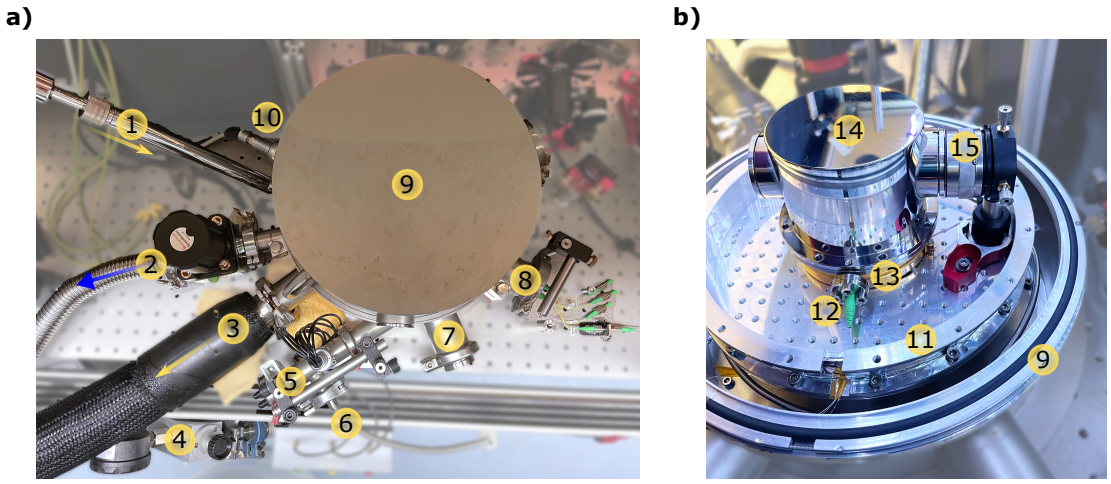

Figure 5.13: a): Top view on the flow cryostat assembly: (1) liquid helium transfer line and inlet; (2) vacuum tube connecting the vacuum recipient to the turbo pump; (3) heated hose for cold helium exhaust gas connecting the heat exchanger with the helium pump (not shown here); (4) three-way valve with pressure gauge to evacuate the sample chamber and fill it with helium exchange gas; (5) electrical connections for sample chamber; (6) sample chamber connection to three-way valve; (7) overpressure valve for the vacuum recipient; (8) fiber feedthrough to vacuum recipient; (9) cryostat chamber (details see b)); (10) thermometer and heater connection to temperature controller (not shown here). b): Picture of the open cryostat chamber: (11) radiation shield with superinsulation foil; (12) fiber feedthrough for sample chamber; (13) cold plate with heat exchanger beneath; (14) sample chamber lid with two optical windows; (15) collimation lens for free-space cavity transmission inside x,y,z-mount.

The working principle of this cryostat is to let liquid helium (LHe) flow through a heat exchanger to cool a cold plate attached to it. The liquid helium is provided by a dewar, which is connected by a transfer line to the cryostat inlet (1). The evaporated helium gas is sucked away into a heated hose (3) by a rotary vane pump[42] standing in a pump room outside the lab to reduce acoustic noise (not

[42] *V-VC 50*, Elmo Rietschle by Gardner Denver GmbH

shown here). The exhaust gas is then guided through a gas meter to monitor the helium consumption and returned into the helium system of the building to be reliquified. To evacuate the whole cryostat chamber, a combined membrane roughing and turbomolecular pump[43] (not shown here) is connected to the vacuum recipient (2) as well as the separate inlet for the sample chamber (6). The latter is also used to fill the sample chamber with helium gas using the three-way valve incorporating a pressure gauge (4). The vacuum-tight fiber-feedthrough to the cryostat (8) is realized by 1 mm holes drilled into a blind flange and sealed by two-component epoxy glue[44]. The second fiber-feedthrough from the vacuum to the sample chamber (12) is made in the same manner. The cryostat provides 18 pins for the electrical connections to the sample chamber (5) used for the piezos, motors and stage thermometer[45] as well as two coaxial cables for future RF-connections. Additionally there is a connector (10) for the thermometer[46] installed below the cold plate as well as the resistive heater wire. These are connected to a temperature controller[47] (not shown here). In order to reduce the coupling of acoustic noise from the lab into the sample chamber, all cables and pipes are clamped to the optical table whenever possible. Between the windows of the sample chamber and radiation shield, a three-axis lens[48] mount (15) is placed to collimate the free-space mode coupled out of the cavity. Placing the lens inside the sample chamber directly behind the cavity mirror would be advantageous to get a smaller mode diameter, but was not possible due to constraints in the size of the sample chamber. The current position is about 4 cm away from the cavity mode waist and results in a collimated beam diameter of about 1 cm. This is the largest diameter that can be accepted to avoid mode clipping at windows and mirrors further down the beam path.

Operation Before starting a cooldown, the sample chamber has to be properly sealed using an indium wire. Since helium gas leaking out of the exchange gas chamber will not freeze out at cold parts of the cryostat, in comparison to all other gases (so-called cryo pump), it will break the isolation vacuum and thus lead to an inefficient cooling. Therefore, careful leak testing of the indium seal as well as the fiber-feedthrough to the sample chamber is necessary before every cooldown. Leakage rates up to 10^{-7} mbar l/s are acceptable. If this value cannot be reached, most probable leakages occur at the fiber-feedthrough since the glue usually withstands just a few cooldown cycles. Such a leak can be sealed by

[43] *T-Station85*, Edwards GmbH
[44] *UHU Plus Schnellfest*, UHU Holding GmbH
[45] thermistor ranging from 0.6K to 200K
[46] *DT-670-CU-1.4L*, Lake Shore Cryotronics Inc., silicon diode thermometer ranging from 1.4K to 500K
[47] *TIC500*, CryoVac GmbH
[48] *LA1422-AB*, f=39 mm, Thorlabs GmbH

putting some new glue on the outside of the feedthrough while the sample chamber is under vacuum to suck in the glue into the molecular holes. Another probable location of a leakage is the connection of both ends of the indium wire. Although low leakage rates can be reached, the turbomolecular pump must be permanently running during the cryostat operation to maintain an isolation vacuum of about 10^{-6} mbar at cryogenic temperatures.

After successfull leak testing, the radiation shield can be attached and the vacuum recipient can be closed. Now another method of leak testing the sample chamber can be applied: the exchange gas chamber is filled with helium gas to about 500 mbar and the leak testing device is connected to the cryostat's vacuum system. This setting constitutes the situation during the cryostat operation, where an overpressure inside the sample chamber leads to a diffusion of helium into the vacuum chamber.

Before starting the cooldown, the exchange gas chamber should also be evacuated once to sub-millibar levels to remove the residual air and reduce adsorptions on the surfaces. Afterwards, the chamber can be flushed a few times with helium gas before filling again about 500 mbar exchange gas into it. The helium pressure will then decrease to about 50 mbar at 20K during the cooldown. The helium exchange gas can also be refilled when the cryostat is cold and having the chamber filled with a few hundreds millibar at cold temperatures has been found to give a good thermalization.

A needle valve (NV) on the transfer line from the dewar to the cryostat regulates the flow of LHe into the heatexchanger. Furthermore, a proportional magnetic valve (PMV) in a bypass of the exhaust gas pipe can be used to regulate the gas flow in combination with the NV when the main pipe is closed by a butterfly valve. This regulates the helium gas pressure inside the heat exchanger, which has a great influence on the mechanical vibrations of the cold plate as will be shown in the next Section 5.5. To regulate the cryostat's temperature, one can use one of the two thermometers as input signal for a PID controller which stabilizes the temperature by regulating either the electrical power supplied to the heater wire or the opening of the PMV, hence controlling the helium flow through the heat exchanger. I solely used the regulation by the heater power since it reacts faster. The temperature controller also provides programming of temperature ramps and features digital inputs and outputs to trigger measurements. As will be shown in the next paragraph this cryostat is especially suited for fast cooldowns and temperature dependent measurements due to its low latency of the temperature control.

Cooldown Performance When the NV is opened by several turns to reach a high LHe flow rate, a cooldown with an empty sample chamber can be achieved in less than an hour. The temperature curve during such a cooldown is depicted in Fig. 5.14a) and a zoom to the low temperature range can be seen in Fig. 5.14b). The minimum temperature of the cold plate is 2.4 K i.e. below the LHe temperature of 4.2 K, which is possible due to a reduced partial pressure inside the heat exchanger. This principle can be further used in a single-shot cooldown to 1.7 K. Therefore, one closes needle valve completely while the return line to the helium pump is still open. Thereby, the remaining helium gas is sucked away, thus reducing the pressure inside the heat exchanger and cooling it further down. However, this temperature only holds on for about 15 seconds until the cold plate quickly heats up due to a lack of LHe. The temperature curve of such a single shot cooldown can also be seen in Fig. 5.14b).

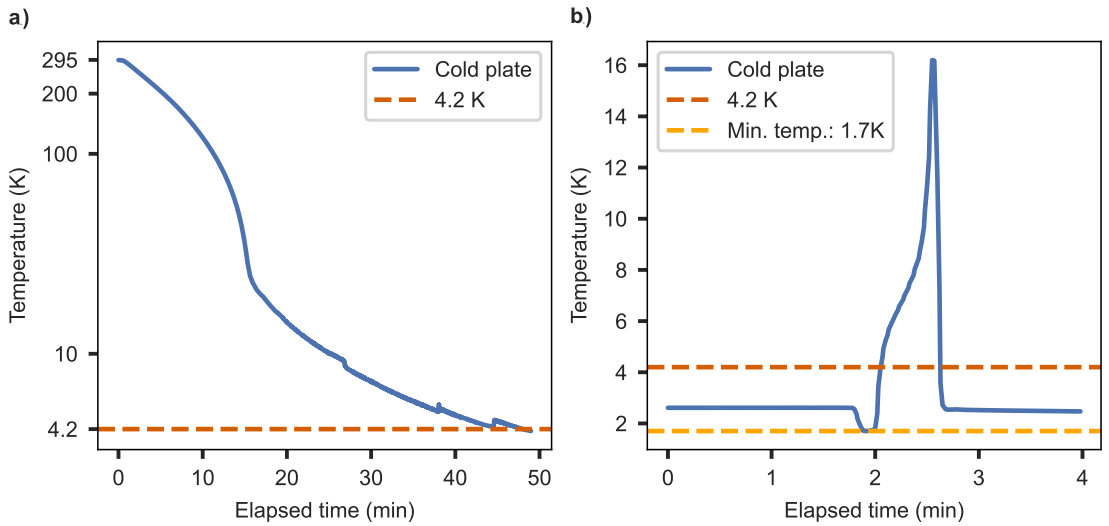

Figure 5.14: a): Time trace of the temperature of the cold plate during a cooldown of the cryostat with an empty sample chamber. b): Minimum temperatures of the cryostat cold plate with an empty sample chamber. The continous minimum temperature is about 2.4 K and decreases to 1.7 K for a few seconds in the single-shot mode.

If the cavity stage is mounted inside the sample chamber, a cooldown takes slightly longer due to the high heat capacity of the titanium main frame. However, the speed of the cooldown is not limited by the cooling power of the cryostat but one rather aims for a slow cooldown over hours or days in order to avoid strong temperature gradients causing mechanical stress in the cavity mechanics. A minimum temperature of 3.4 K on the main frame thermometer can be reached.

The liquid helium consumption of the flow cryostat strongly depends on the temperature the cold plate is kept at. It is monitored via the gas meter measuring the

volume of the exhaust gas which can be converted to the LHe volume by,

$$V_{LHe}[l] = 1.336\, V_{gas}[m^3]. \tag{5.4.1}$$

It can be as low as 0.35 l/h for temperatures above 20 K such that a full 100 l dewar can keep the cryostat cold for 6-7 days. However, at the minimum temperature of 2.4 K the consumption is about 2.4 l/h and the dewar needs to be refilled or exchanged after 1,5 days.

5.5. Cavity Stability in a Flow Cryostat

Finally, I present the measurements of the cavity length stability when the cryostat is operated at 10 K. The data presented here is partially taken from our publication [166]. In order to perform the stability measurements, the cavity is kept on the side-of-fringe of the 640 nm locking laser resonance. The finesse of that resonance is about 1200 resulting in a FWHM of 260 pm. The stability is then characterized in three different ways:

- Passive stability (blue trace in Fig. 5.15) refers to applying just a drift compensation of a few Hertz bandwidth to the coarse piezo to compensate for piezo creep
- Active stability (orange) measurements additionally make use of the fast feedback controller on the fine piezo with 800 Hz bandwidth
- Contact stability (green) means that the fiber tip, or some protruding part of it, physically touches the planar mirror, leading to a reduced relative motion between both mirrors.

For each of these settings, a time trace of the cavity transmission signal is recorded and its fast Fourier Transform (FFT) is calculated by the oscilloscope[49], which outputs a power spectrum (PS). The PS is then averaged a hundred times. Each dataset therefore shows the average cavity length fluctuations over several seconds time span. Finally, the PS is converted to an amplitude spectral density (ASD). Therefore, the PS in units dBm is first converted into volts using the oscilloscope impedance of 50 Ohm:

$$U = \sqrt{50\,\Omega \cdot 1\,mW \cdot 10^{\frac{PS}{10}}}. \tag{5.5.1}$$

The slope factor K of the Lorentzian cavity resonance, given by Eq. 5.3.1, and the spectrum's frequency bin $\Delta\nu$ is used to convert the voltage spectrum into the ASD:

$$ASD = \frac{U}{K\sqrt{\Delta\nu}}. \tag{5.5.2}$$

[49] *Waverunner HRO 64Zi* 400 MHz 12-bit 2GS/s, Teledyne LeCroy

The ASDs measured for the passive and active scenario are depicted in Fig. 5.15a).

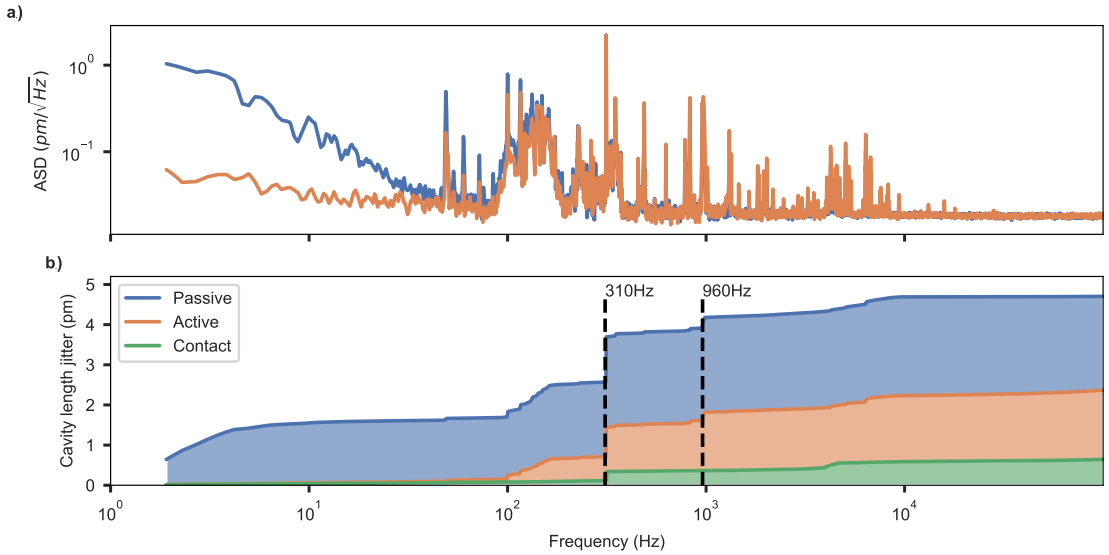

Figure 5.15: a): Amplitude spectral density (ASD) of the cavity length jitter for a passive (blue) and actively stabilized (orange) cavity at 10 K. b): Cumulative root-mean-square (RMS) cavity length jitter as a function of the frequency for a passive (blue) and actively stabilized (orange) cavity as well as the fiber being in physical contact with the planar mirror (green). Both figures are adapted from [166].

The largest difference between both spectra can be seen in the frequency range up to 100 Hz, where the active feedback has a strong effect and considerably reduces the cavity length jitter. Above 10 kHz one observes a flat noise floor indicating that electronic or laser noise is limiting here.

In order to visualize the cavity length jitter in units of picometer, I calculate the cumulative RMS cavity length jitter as a function of the frequency,

$$RMS(\nu) = \sqrt{\int_0^{\nu} ASD(\nu')^2 \, \mathrm{d}\nu'}, \tag{5.5.3}$$

and plot it for all three stability configurations in Fig. 5.15b). Here, the noise floor above 9 kHz was subtracted due to the aforementioned reason. The cumulative RMS plot reveals that also the mechanical resonances around 150 Hz and 310 Hz are damped by the active stabilization, since the step height at these frequencies is smaller for the active mode (orange). It should be noted that the RMS values add up non-linearly in this cumulative plot. This implies that the same step height at a higher base level (passive trace, blue) stem from a higher length jitter at that frequency. In contact mode (green) the step at 310 Hz and around 8 kHz are still

visible, but the mechanical noise over the entire bandwidth of the spectrum is strongly damped.

The cumulative RMS values over the entire spectrum show a passive stability of below 5 pm, whereas active feedback can half this value to 2.5 pm. With these values the requirement on the longitudinal stability as estimated in Subsection 5.1 was met and a cavity of up to 20,000 finesse can be operated at cryogenic temperatures not being limited by mechanical vibrations. Bringing the fiber into contact with the planar mirror strongly reduces the longitudinal tunability of the cavity, but comes at the benefit of a highly stable cavity of 0.7/0.8 pm (active/passive) RMS length jitter.

Since the passive stability in contact is almost as good as with active feedback, I resign from locking the cavity and keep it passively on resonance. To exemplify the high stability, a cavity spectroscopy measurement of the 11th longitudinal mode order of the 580 nm laser is recorded. Therefore, the laser frequency is swept over 12 GHz to cover several linewidths (2.5 GHz or 18 pm) at a finesse of 16,000. The laser is scanned in a triangular shape at a slow speed of 0.5 Hz, thus being susceptible also to low frequency noise. Figure 5.16 shows the cavity transmission time trace over ten averages (blue) together with fits of a Lorentzian (light red, dashed-dotted) and Gaussian (dark red, dotted) function, respectively. The cumulative root mean square error (RMSE) of the fits are depicted below.

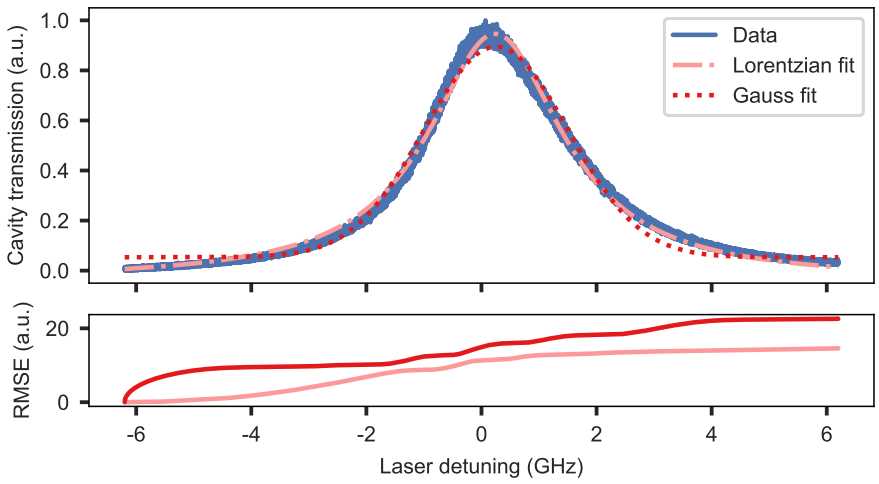

Figure 5.16: Cavity spectroscopy measurement of the 11th mode order of the 580 nm spectroscopy laser together with Lorentzian (light red, dashed-dotted) and Gaussian (dark red, dotted) function fits. The fiber was in physical contact with the planar mirror and passively stable at a temperature of 10 K. The data trace (blue) shows the average of ten laser scans over 12 GHz bandwidth with a scanning frequency of 0.5 Hz. The figure is adapted from [166].

The Lorentzian fit shows a lower residuum which highlights that the Gaussian-type mechanical noise is not dominant and a finesse-limited cavity performance is achieved.

I observed that besides clamping all cables and the cavity fiber on the main frame of the stage, the cavity stability is strongly dependent on the helium pressure inside the heat exchanger (measured at the PMV in the helium gas return line). Closing the butterfly valve of the main return line, the PMV in the bypass can be used to control the flow rate through the heat exchanger. When gradually closing this valve the helium pressure inside the heat exchanger rises from about 20 mbar when fully open to about 800 mbar. The latter is the maximum pressure where the cooling power is still sufficient to keep the temperature at about 10 K. Figure 5.17 shows the decrease in cavity length jitter of an actively stabilized cavity over an order of magnitude when the pressure is rising. The measurement implies that the vibrations on the cryostat cold plate are reduced by a higher pressure inside the heat exchanger. However, the exact mechanism is not fully understood. It could be attributed to a reduced helium flow rate which calms down the noise. Another mechanism could be the shift in the position of the boiling point, where the liquid helium from the dewar becomes gaseous. Dependent on this position inside the transfer line or heat exchanger the coupling of the boiling noise to the cold plate might be different.

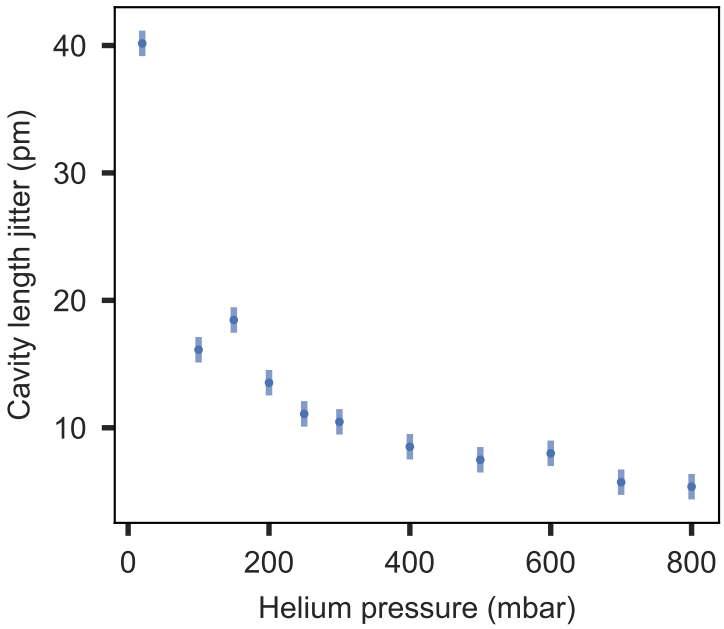

Figure 5.17: The RMS cavity length jitter of an actively stabilized, open cavity is plotted against the helium pressure inside the cryostat heat exchanger at 10 K.

6. Cavity-enhanced Spectroscopy of Individual Nanoparticles

After successfully distributing well-dispersed nanoparticles on the cavity mirror and optimizing the stability of the cavity and the scanning functionality at cryogenic temperatures, I am now able to perform cavity-enhanced spectroscopy of europium ions. Firstly, I will explain the optical setup used for the measurements presented in this chapter. Thereafter, scanning cavity microscopy measurements reveal the size of the six nanoparticles investigated throughout the chapter. Following this, the linewidths and center positions of the inhomogeneous distribution of ion ensembles are measured by coarse-resolution laser scans, and fine-resolution scans are conducted to resolve the statistical fine structure. To quantify the performance of the cavity, I determine the lifetime shortening and Purcell factors of the optical transitions. Due to long-lived nuclear spin states at cryogenic temperatures, I show the ability to optically address individual hyperfine (HF) states and to repump a spectral hole. I close the characterization of small ensembles of europium ions by measuring the saturation behaviour and homogeneous linewidth. Finally, an overview of the cavity QED parameters of the current setup and an estimation of the countrate that can be expected from a single europium ion are presented.

6.1. Optical Setup

I extend the optical setup used for scanning cavity microscopy and the characterization of the cavity stability presented in Chapter 5, in order to perform lifetime measurements and high resolution laser scans of small europium ion ensembles inside the cavity. The setup used for the measurements presented in this chapter is depicted in Fig. 6.1.

Preparation Optics In order to perform spectroscopy of europium ions, I need to monitor the wavelength of our 580 nm laser module so some laser power is branched

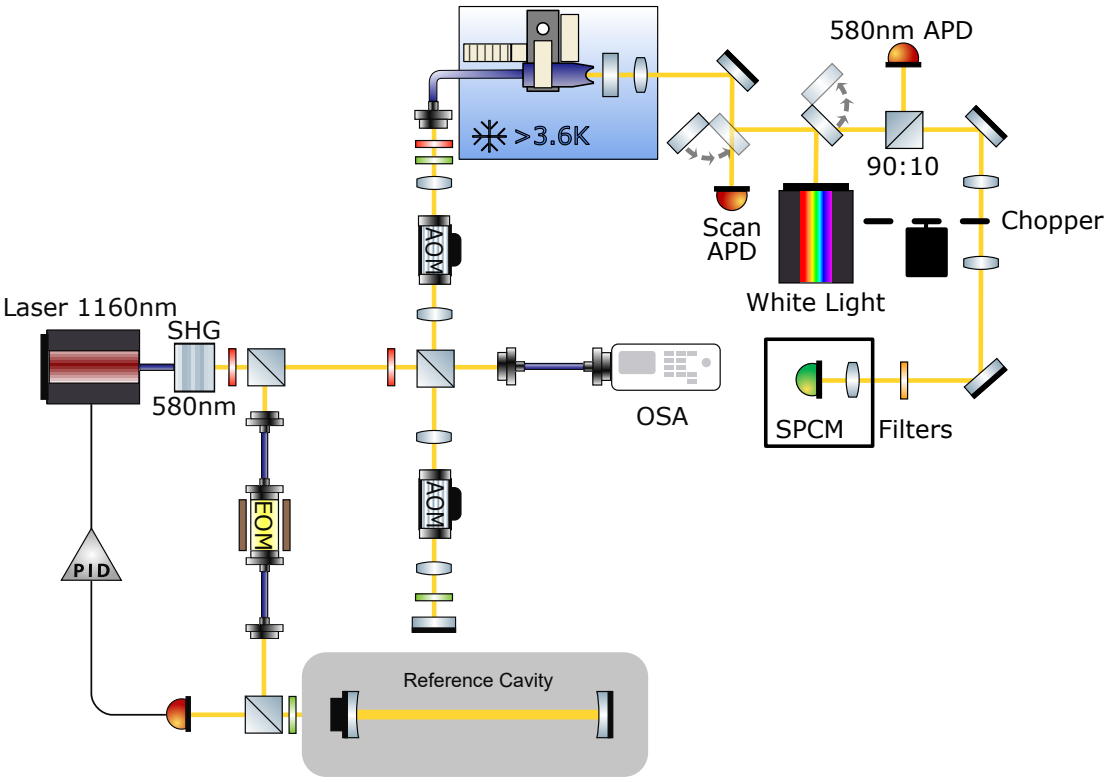

Figure 6.1: Schematic drawing of the optical setup used for cavity-enhanced spectroscopy of europium ions adapted from [56]. PD: photodiode, SHG: second harmonic generation crystal, PID: PID-controller, EOM: electro-optic modulator, AOM: acousto-optic modulator, OSA: optical spectrum analyzer, APD: avalanche photodiode, SPCM: single photon counting module.

off into an optical spectrum analyzer (OSA)[50]. This device has a frequency resolution of 2 GHz and ±100 MHz accuracy in the visible domain. The remaining laser power is guided into a 50 MHz-bandwidth acousto-optic modulator (AOM)[51] in double-pass configuration in order to reach a six orders of magnitude suppression of the laser power for pulsed, resonant spectroscopy measurements. The light then passes another acousto-optic modulator[52] with a higher bandwidth of 150 MHz in order to perform high resolution sweeps of the laser frequency. In addition, this AOM is also used to create a two- or three-tone pattern to address the europium HF levels as presented in Section 6.6. Finally, a quarter- and half-waveplate is placed in front of the fiber coupler to control the polarization of the excitation light.

[50] *771A Laser Spectrum Analyzer*, Bristol Instruments
[51] *AOMO 3200-121*, Gooch&Housego
[52] *AOMO 3350-199*, Gooch&Housego

Reference Cavity The 1160 nm diode laser can be frequency stabilized to an external reference cavity to obtain a narrow laser linewidth for high resolution laser scans and to avoid frequency drifts over the long measurement times of several hours. The reference cavity setup was assembled by my colleague Sören Bieling, who also optimized and characterized it. The core component is a cylindrical ultra low expansion (ULE) spacer[53] of length 64.6 mm. On both ends of the spacer, highly reflective, concave DBR mirrors[54] are mounted to make up the Fabry-Pérot cavity. The mirrors have a radius of curvature of 150 mm and a transmittance of 70 ppm. A finesse of about 10,200(800) was measured by my colleague, which results in a cavity linewidth of 240(20) kHz with a free-spectral range of 2.45(0.06) GHz. We use the standard Pound-Drever-Hall stabilization technique [173] to lock the laser frequency to the narrow resonance of the reference cavity. A fiber-coupled electro-optic phase modulator[55] is used to modulate sidebands with a 20 MHz frequency detuning. The cavity reflection signal is detected with a 50 MHz bandwidth APD[56]. The demodulated, low pass filtered signal is fed into an FPGA-based feedback controller[57] which is connected to the laser piezo and current control to close the feedback loop. A laser frequency stability of about 20 kHz was measured when averaged over several minutes timescale. A 13 h-long measurement was recorded to monitor the long-term stability and drift of the laser frequency. The results are depicted in Fig. 6.2. Each datapoint in Fig. 6.2a) represents the standard deviation of the PDH error signal converted to frequency and averaged over one second. It shows that our laser can be stabilized to below 20 kHz over a timespan of several hours which is necessary for the long measurement times for the high resolution laser scans presented in Section 6.4. The plot in Fig. 6.2b) depicts the absolute laser frequency measured by the OSA. It can be seen, that the drift of the frequency is limited by the device accuracy of ±100 MHz.

[53] *Zerodur*, Schott
[54] *HR580nm/0°*, Laseroptik
[55] *PM594*, Jenoptik
[56] *APD120A/M*, Thorlabs GmbH
[57] *Digilock 110*, Toptica

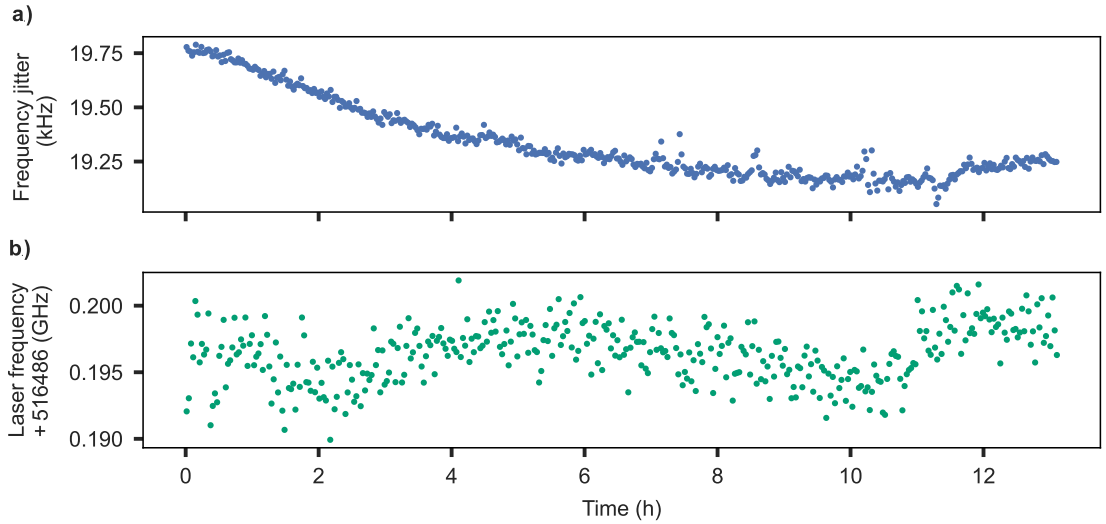

Figure 6.2: Monitoring of the long-term laser frequency stability (a) and absolute laser frequency (b). Each datapoint in (a) represents the standard deviation of the frequency jitter averaged over one second using the PDH error signal. Datapoints in (b) are frequencies measured by the OSA with an accuracy of ±100 MHz.

Collection Optics For the measurements of this chapter I have also extended the optical setup which collects the light coupled out at the free-space side of the cavity. I installed a motorized flip mirror[58] to either guide the cavity transmission onto an APD[59] with 50 MHz bandwidth for cavity scans, or reflect the fluorescence light towards the single photon detector. In order to stabilize the length of the microcavity to a particular resonance of the 580 nm laser, 10% of the power are coupled out onto another APD[60] which has a variable gain, a lower bandwidth of 10-100 kHz, but a higher sensitivity in order to achieve low intracavity power levels. Whenever just the 611 nm fluorescence of europium is detected, I can exchange the 90:10 beam splitter with a dichroic mirror[61] to fully reflect the 580 nm transmission. The latter then serves as excitation and locking light simultaneously. The next element in the propagation direction is an optical chopper[62] where the chopper wheel is placed at the focus of a 4f-setup with focal length of 75 mm in order to minimize the transient time between the open and closed chopper windows. At a chopper frequency of 330 Hz, this results in a transient time of about 30 μs. The chopper is needed for pulsed measurements in order to block the excitation pulse, while the 580 nm fluorescence should be detected. I observed a higher dark countrate which exponentially decays over several milliseconds when the detector

[58] *MFF101/M*, Thorlabs GmbH
[59] *APD120A/M*, Thorlabs GmbH
[60] *APD440A/M*, Thorlabs GmbH
[61] *MD588*, Thorlabs GmbH
[62] *MC2000B-EC*, Thorlabs GmbH

is gated on after an excitation pulse of a few nanowatts if no chopper is blocking the excitation pulse. I attribute this behaviour to heating of the sensor of the single photon counting module (SPCM)[63]. The SPCM is protected from ambient light with a light-tight box to reach the dark countrate of 20 cps. Additionally, I placed a motorized filter positioner[64] directly at the entrance hole of the box. Depending on the wavelength of the fluorescence light that I want to detect, it can be switched between a 580 nm band pass filter[65], a combination of 610 nm band pass[66] and 594 nm long pass[67] filters or a 600 nm band pass filter[68] with a 50 nm broad spectral window covering both fluorescence channels.

Lastly, it is also possible to insert a mirror on a magnetic mount into the collection optics beam path in order to shine in white light from a thermal lamp[69] through the planar mirror and collect the cavity transmission through the fiber. The light filtered by the cavity is then guided to a Czerny-Turner spectrograph[70] via a fiber link and a spectrum of the white light cavity transmission can be taken. This is used to determine the cavity length from two resonances at wavelengths $\lambda_{1,2}$ differing by one FSR according to:

$$d_c = \frac{\lambda_1 \lambda_2}{2(\lambda_1 - \lambda_2)}. \tag{6.1.1}$$

6.2. Scanning Cavity Microscopy of Single Nanoparticles

The first step towards cavity-enhanced spectroscopy is to locate a suitable nanoparticle within the cavity. The easiest way is to search for a nanoparticle at room temperature, due to a larger scanning range of the piezos, and keep track of its position during the cooldown. However, even at room temperature it turned out to be challenging to find a small nanoparticle on the aerosol-printed cavity mirror since many features on the surface show strong scattering or absorption or turn out to be unwanted remnants of ink jet printing or dirt, as can be seen in the scanning cavity image in Fig. 4.13. Unfortunately, many of the scatterers on the mirror also show a significant fluorescence signal when excited with the 580 nm

[63] *COUNT-100C*, LaserComponents
[64] *ELL9*, Thorlabs GmbH
[65] *FF01-580/14-25*, Semrock
[66] *FF01-610/5-25*, Semrock
[67] *BLP01-594R-25*, Semrock
[68] *84-785 BP 600/50*, Edmund Optics
[69] *SLS201L/M*, Thorlabs GmbH
[70] *Shamrock 500i with iVAC316 LDC-DD camera*, Andor Technologies

laser, so I developed a strategy to discriminate between europium and other fluorescing particles.

After having recorded a transmission scan of a certain area within the checkerboard grid, I place the cursor on a spot with a decrease in transmission between 10 % to 80 % resulting in a modest reduction of the finesse. I start with pulsed, resonant excitation and collection of the 580 nm transition, which is the simplest spectroscopy method because, in comparison to the double-resonance technique explained below, I can use any fundamental cavity mode order. I use a battery with tunable voltage connected to the coarse piezo to passively stay on the resonance for a few seconds. The laser is tuned to the center of the $^7F_0 \rightarrow {}^5D_0$ transition at 580.6 nm. Using a pulse sequence of a 1.5 ms excitation pulse followed by 40 μs pause to wait for the chopper transient and a 1.5 ms detection window, I should observe a histogram with a 1-2 ms decay time constant if the investigated spot contains europium-doped nanoparticles. If this is not the case, one typically observes shorter time constants which range from a few tens to hundreds of microseconds.

The latter cases sometimes make it difficult to be sure to observe fluorescence coming from europium ions. Therefore, a second spectroscopy technique was established using a double-resonance (DR) scheme, where the ions are excited via the $^7F_0 \rightarrow {}^5D_0$ transition and only collect the $^5D_0 \rightarrow {}^7F_2$ fluorescence by choosing the appropriate band pass filter. The cavity spectrum overlaps with these two transitions at the 20^{th} longitudinal mode order of the 580 nm resonance, which can be found if the optical cavity length, measured by the white light transmission spectrum, is around 5.8 μm. At this cavity length the two cavity modes overlapping with both europium transitions are split by one FSR and hence this is the shortest cavity length for the DR scheme. Since the fluorescence of the 580 nm transition is not collected, I use the transmission of the excitation light as error signal for a side-of-fringe locking of the cavity and perform a continuous wave (CW) measurement. The increase in the photoluminescence excitation (PLE) countrate, when the cavity is locked on the DR mode order, can be seen in Fig. 6.3. However, it should be noted that it is also possible that two mode orders around the 20th feature a higher countrate or the difference in countrates is much less than depicted in Fig. 6.3, since the overlap of the narrow cavity linewidth (few GHz) with the much broader $^7F_2$ transition (680 GHz) depends on the local cavity dispersion.

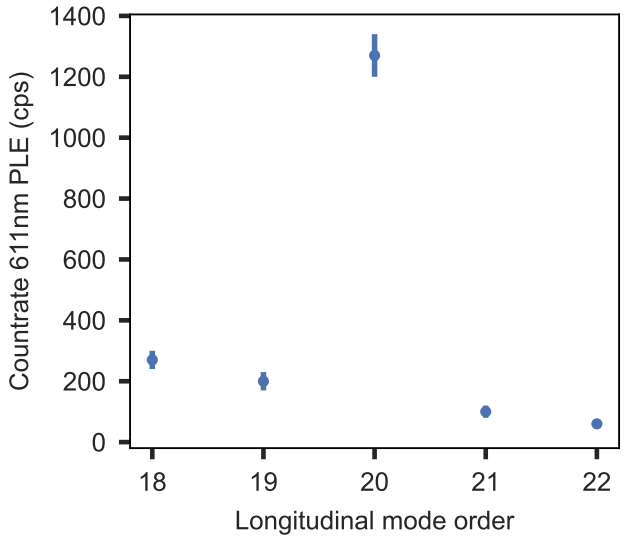

Figure 6.3: Fluorescence countrate of the ${}^5D_0 \rightarrow {}^7F_2$ transition as a function of the 580 nm longitudinal mode order of the cavity for a CW measurement. The measurement was performed on nanoparticle 3 at a temperature of 25 K.

A last check to confirm europium fluorescence is to tune the laser wavelength off resonant from the ${}^7F_0 \rightarrow {}^5D_0$ transition and perform the previously mentioned spectroscopy techniques again. To detune the laser cavity by several angstrom a screw has to be manually turned and the temperature of the SHG stage has to be adjusted. Therefore, this background measurement requires more effort and is usually done as a last check if both of the other methods were already successful.

In the course of this thesis, I found six nanoparticles in total, labeled NP1 - 6, suitable for cavity-enhanced spectroscopy which I will characterize in the following sections. The first important parameter is the size of the particle, which can be determined with a high precision by the transmission losses of a scanning cavity microscopy image (see [99], [107], [108]). Measuring the cavity transmission of the bare cavity on a clean spot on the mirror, T_0, and the cavity transmission when being centered on the nanoparticle, T_{NP}, lets one determine the scattering loss due to the nanoparticle:

$$S_{NP} = \frac{1}{2}(T_1 + T_2 + \mathcal{L}_0)\left(\sqrt{\frac{T_0}{T_{NP}}} - 1\right) = \frac{\pi}{\mathcal{F}_0}\left(\sqrt{\frac{T_0}{T_{NP}}} - 1\right), \tag{6.2.1}$$

with the finesse of the empty cavity $\mathcal{F}_0$. Using Eq. 3.5.8, the diameter of the

nanoparticle can then be calculated as,

$$d_{NP} = \sqrt[6]{\frac{3^3}{8\pi^4} w_0^2 \lambda^4 \left(\frac{\pi}{\mathcal{F}_0} \left(\sqrt{\frac{T_0}{T_{NP}}} - 1 \right) \right) \frac{n_{medium}^2 \left(n_{NP}^2 - n_{medium}^2\right)}{n_{medium}^2 + \frac{5}{16}\left(n_{NP}^2 - n_{medium}^2\right)}}. \quad (6.2.2)$$

I calculated the diameters of all six nanoparticles using the refractive indices $n_{NP} = n_{yttria} = 1.93$ [178], $n_{medium} = n_{air} = 1$ and a finesse of $\mathcal{F}_0 = 16,000 \pm 1,600$. The wavelength used for the transmission scans is 580.8 nm and the mode waist is calculated from the curvature of the fiber mirror $ROC = 25 \pm 3\,\mu$m and cavity length using the formula given in Tab. 3.1 to be $w_0 = 1.40 \pm 0.06\,\mu$m. The transmission values are obtained by fitting a 2D Gaussian function on the cavity mode PSF and using its constant background fit parameter as value for T_0 and the peak height as T_{NP}. The scanning cavity images of the nanoparticles can be seen in Fig. 6.4 and the resulting diameters are summarized in Tab. 6.1.

NP	**1**	**2**	**3**	**4**	**5**	**6**
d_{NP}(nm)	88 ± 2	90 ± 2	89 ± 2	69 ± 1	95 ± 2	84 ± 2

Table 6.1: Diameters of the six nanoparticles investigated in this thesis. The uncertainties are given by $\sigma_{d_{NP}} = 0.02\, d_{NP}$ and are limited by the error of the transmission losses.

The uncertainties of the diameters are estimated as $\sigma_{d_{NP}} = 0.02\, d_{NP}$, being limited by the estimated relative error of 10% on the finesse (3(4)% relative error of the beam waist (transmission loss)). It should be noted that I assumed to have measured single nanoparticles here, but the transmission losses of e.g. three nanoparticles of 55 nm diameter would be the same as for one 80 nm particle. Thus, I can't exclude that some of the nanoparticles NP1 - 6 are actually small agglomerations of two or three particles (see also Fig. 3.5).

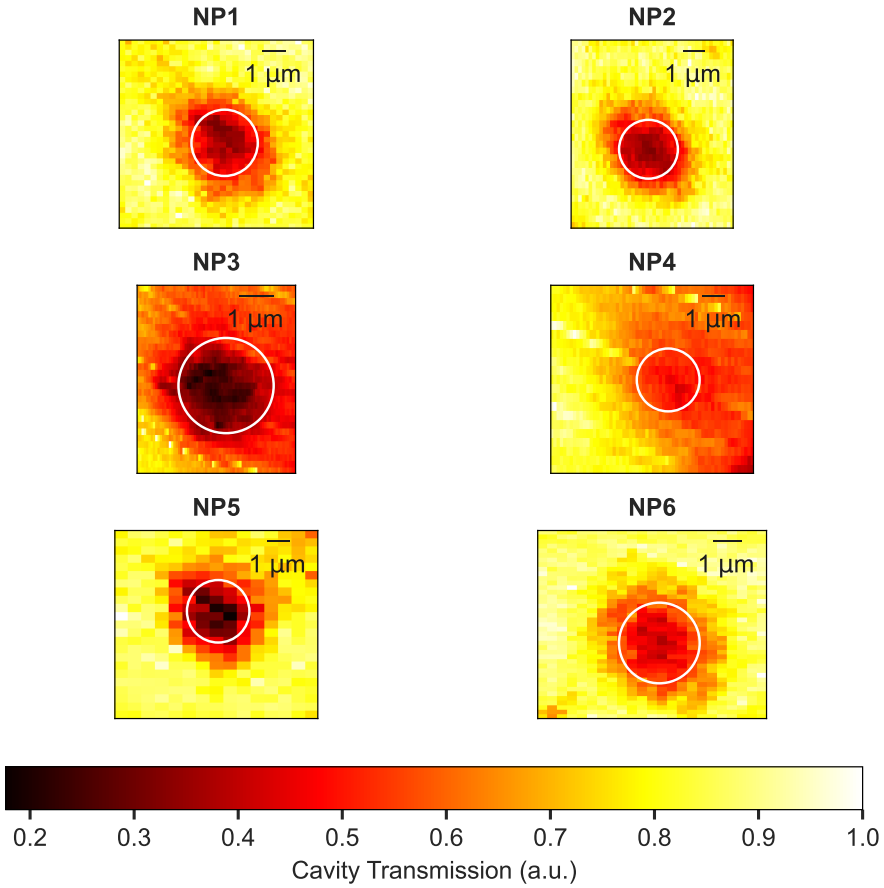

Figure 6.4: Scanning cavity microscopy images of the six nanoparticles investigated throughout this thesis. The white circles around the center of the cavity mode point spread function have a radius of one standard deviation resulting from the 2D Gaussian fit. The scale bar is calculated from this radius assuming a cavity mode waist of $w_0 = 1.4\,\mu$m.

6.3. Inhomogeneous Lines

Having found a suitable nanoparticle at room temperature, I slowly cool down the cryostat in temperature steps of 35 K. At each step I wait for the cavity stage to thermalize, record cavity scans and compensate the drift of the fiber position to stay at the nanoparticle position. During one cooldown I also measured the inhomogeneous line of NP5 for each temperature step using the pulsed, resonant excitation scheme and manually tuning the laser frequency in coarse steps over the inhomogeneous line. The PLE measurements of the lines together with a Lorentzian fit can be seen in Fig. B.2 in the appendix. The inhomogeneous broadening is caused mainly by point defects in the crystal lattice and thus should have the shape of a Lorentzian function [179], [180]. The FWHM and center wavelength

of the lines are extracted from the Lorentzian fits and plotted as a function of the cavity temperature in Fig. 6.5.

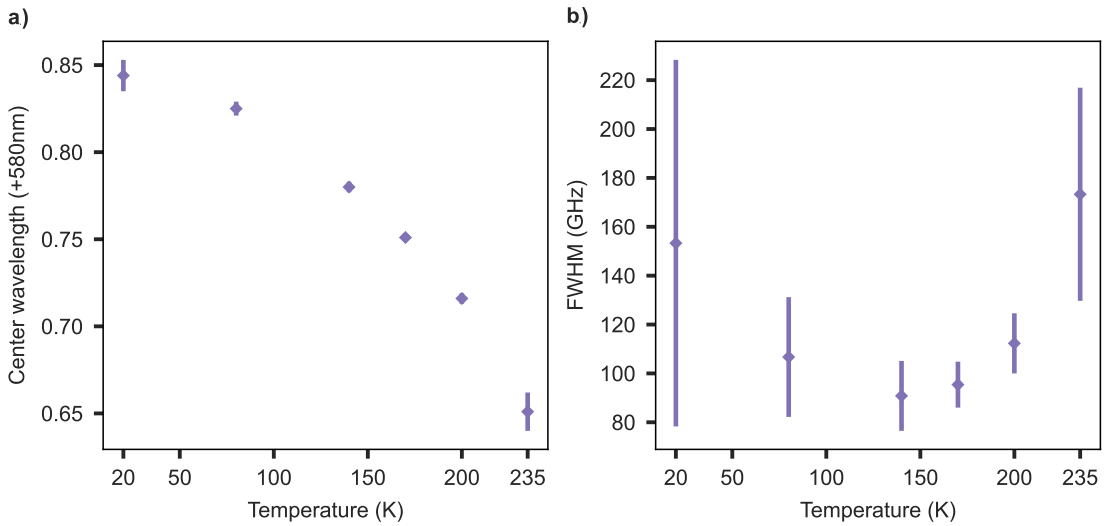

Figure 6.5: The center wavelength (a) and FWHM (b) of the Lorentzian fit to the inhomogeneous line of NP5 are plotted against the cavity temperature during a cooldown.

In Fig. 6.5a) a blue shift of the inhomogeneous line center with increasing temperature can be observed from 580.85 nm at cryogenic temperatures to 580.65 nm close to room temperature. A shift of the line center with temperature in lanthanide-doped solids is well known and was first described by Kushida et al. [181] for Nd:YAG crystals. They explain the lineshift by the dynamical strain of a two-phonon Raman process which shifts the energy levels with temperature. Usually, a red shift is observed for most transitions, however certain circumstances in the level structure can lead to the blue shift as observed here.

Looking at the temperature dependence of the linewidth in Fig. 6.5b), a narrowing of the line with decreasing temperature can be seen as expected. The large uncertainty of the datapoint at 20 K is attributed to a low signal-to-noise ratio of this measurement (see Fig. B.2f)). Also the datapoint at 80 K doesn't match the trend but also has a quite large uncertainty. Above 100 K the homogeneous linewidth should be approximately $\gamma_h(100\,\mathrm{K}) \approx 100\,\mathrm{GHz}$, according to [60], and thus exceeds the inhomogeneous broadening due to the $\gamma_h \propto T^7$ temperature dependence. However, measurements on a powder of nanoparticles of the same batch done by Xiaoyu Cheng in our group resulted in a linewidth of $110 \pm 3\,\mathrm{GHz}$ at room temperature, which indicates that NP5 shows a broader linewidth than the nanoparticle ensemble average. The broad room-temperature linewidth could also come from the convolution of a broad inhomogeneous distribution, visible at cryogenic temperatures, with the 110 GHz homogeneous line resulting in the ob-

served room temperature linewidth of about 200 GHz.

Finally, I evaluate the inhomogeneous lines of all six nanoparticles at cryogenic temperatures of 20 K. The measured PLE fluorescence countrates, dependent on the laser wavelength are depicted in Fig. 6.6. The datasets for NPs 1, 5 and 6 (plots a), e) and f)) were taken using the pulsed, resonant spectroscopy scheme and manually tuning the diode laser wavelength. For NPs 2, 3 and 4 the DR scheme was used, where the wavelength of a dye laser[71] is continously scanned and the 611 nm CW fluorescence is recorded. If the linewidth exceeded the mode-hop free tuning range of the dye laser, a total of up to three scans were stitched together. This spectroscopy technique has the advantage of a fast data acquisition combined with a higher wavelength resolution of the datapoints compared to manually tuning the diode laser. A single dye laser scan with reasonable exposure time per datapoint over 60 GHz only takes about a minute. Since the fiber cavity is locked to the dye laser transmission, the feedback loop automatically shifts the cavity length according to the laser wavelength and guarantees a stable intracavity power level of $\pm 10\%$ over the whole scan.

[71] *Matisse 2 DX*, Sirah Lasertechnik

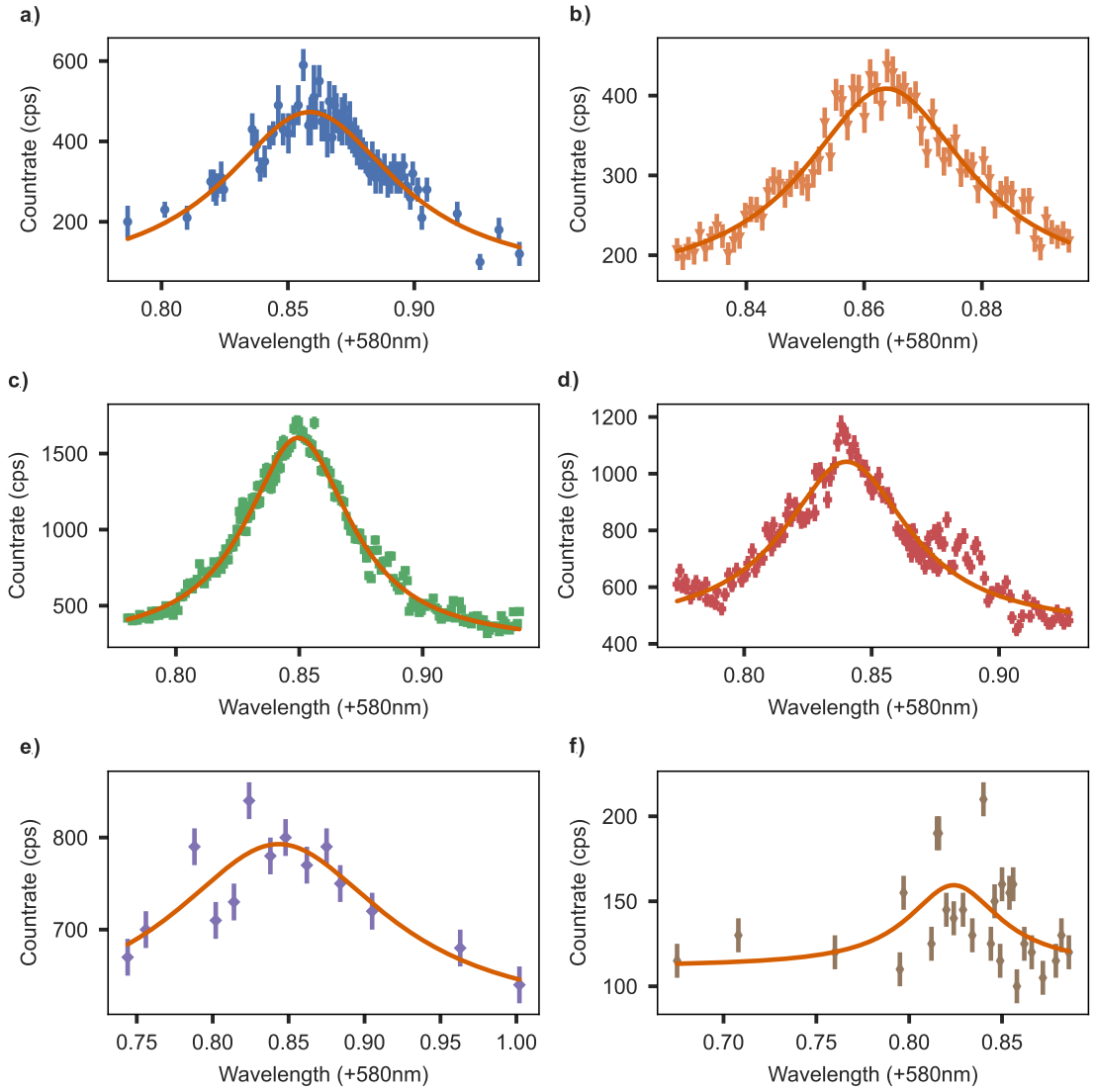

Figure 6.6: PLE fluorescence laser scans at 20 K for NP1(a) to NP6(f) together with a Lorentzian fit adapted from [56]. Data for NP1,5 and 6 (plots a), e) and f)) were taken by the pulsed, resonant scheme and manually tuning the diode laser wavelength. Data for NP2,3 and 4 (plots b),c) and d)) were recorded using CW excitation with a continuously scanned dye laser and collection of the 611 nm fluorescence.

I summarized the properties of the six nanoparticles found so far in Fig. 6.7. All measured inhomogeneous linewidths are much broader than the previously reported value of 22 GHz from a single nanoparticle [67] and lie between 33 GHz to 150 GHz. However, the yttria nanoparticles used here, additionally have been annealed in an oxygen plasma under high RF power, which seems to cause a broadening of the inhomogeneous line by about a factor of three [66]. One cannot observe any correlation between the linewidth and center wavelength or size of the

nanoparticle. But despite the fact that six samples are not enough for statistical significance, I see a distribution of the center positions over 40 GHz and different signal to noise ratios between the different particles.

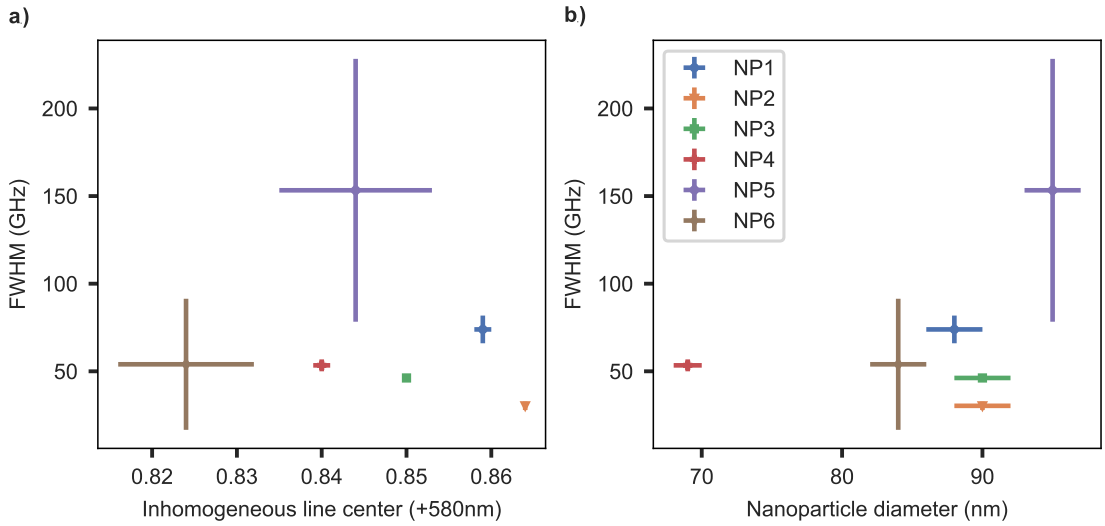

Figure 6.7: Inhomogeneous linewidths (FWHM) versus the respective center wavelength of the line (a) and versus the nanoparticle diameter obtained in Section 6.2 (b) adapted from [56].

6.4. High Resolution Laser Scans

Statistical Fine Structure The next goal is to refine the laser scans described in the previous section in order to observe signatures of the statistical fine structure within an inhomogeneous line. The total number of europium ions replacing yttrium ions at the C_2 lattice site can be estimated to approximately 8,000 to 18,000 ions for the nanoparticle diameters between 70 nm and 90 nm and a doping concentration of 0.3% as investigated here. Simulating the distribution of ions over the broad inhomogeneous line, including the full level structure, gives about ten to twenty ions within a power-broadened linewidth of 10 MHz in the center of the inhomogeneous line. Low power laser scans therefore should reveal the non-uniform distribution of the ions over a small spectral domain of a few gigahertz, denoted as statistical fine structure. Assuming a Poissonian distribution of ten to twenty ions within a 10 MHz frequency bin, results in a relative deviation of $\sqrt{N_{ions}}/N_{ions} \approx 20 - 30\,\%$ of the signal strengths matching the results of the simulation in Fig. 6.8b).

I have been attempting many approaches e.g. performing scans at elevated temper-

atures around 20 K to avoid optical pumping into other HF levels (see Section 6.6 for details) or pursuing measurements down to 4.3 Kto reduce the homogeneous linewidth of the emitters. I also scanned with varying laser powers ranging over two orders of magnitude since the single ion saturation power is yet unknown. Different spectral regions on the fringes and in the center of the inhomogeneous lines of NP3 and NP4 were investigated. The single-pass AOM was used to create three-tone pulses of equal power with frequency spacings matching the HF splitting of either the ^{151}Eu or ^{153}Eu isotope. The three-tone excitation was tested with alternating frequencies as well as creating all three tones simultaneously. As I will showcase in the following, spectral features in the CW 611 nm PLE fluorescence can be observed using the double-resonance scheme. However, in summary I have to assert that none of these features is fully reproducible over several scans.

In Fig. 6.8 a high-resolution laser scan was performed in the center of the inhomogeneous line of NP4 at 10K. The scan direction was the same for both traces, but the second trace (orange) has an y-axis offset of 100 cps to be distinguishable from the first scan. The frequency was scanned with the grating piezo of the 1160 nm diode laser over $\Delta\nu \approx 1.8$ GHz, while the laser was free-running since it was not possible to lock it to the reference cavity for such wide scan ranges. Due to the low countrate, the signal was averaged for one second per frequency, which led to long measurement times of about half an hour per scan. I observed that the free-running laser is drifting in frequency over several megahertz up to tens of megahertz depending mainly on the previous voltages applied to the scanning piezo (piezo creep). The overall trend in the countrate of both curves is similar with some matching features. However, they show different strengths and other features can not be reproduced. The 580 nm transmission light simultaneously serves as CW excitation and locking signal for the fiber cavity. From the transmitted light behind the cavity, one can calculate the mean intracavity power at the field antinode to be:

$$P_c = \frac{2\,P_{out}}{T_{DBR,2}} = \frac{2\,P_{APD}}{T_{path}\,T_{DBR,2}}. \tag{6.4.1}$$

Here, the path transmission value is used to calculate back the power P_{out}, coupled out from the cavity, from the measured power on the APD $P_{APD} = T_{path}\,P_{out}$. Using $P_c \approx 10\,\mu$W $\approx 10^3\,P_{sat}$ gives a small signal but avoids too strong power broadening which would smear out the statistical fine structure.

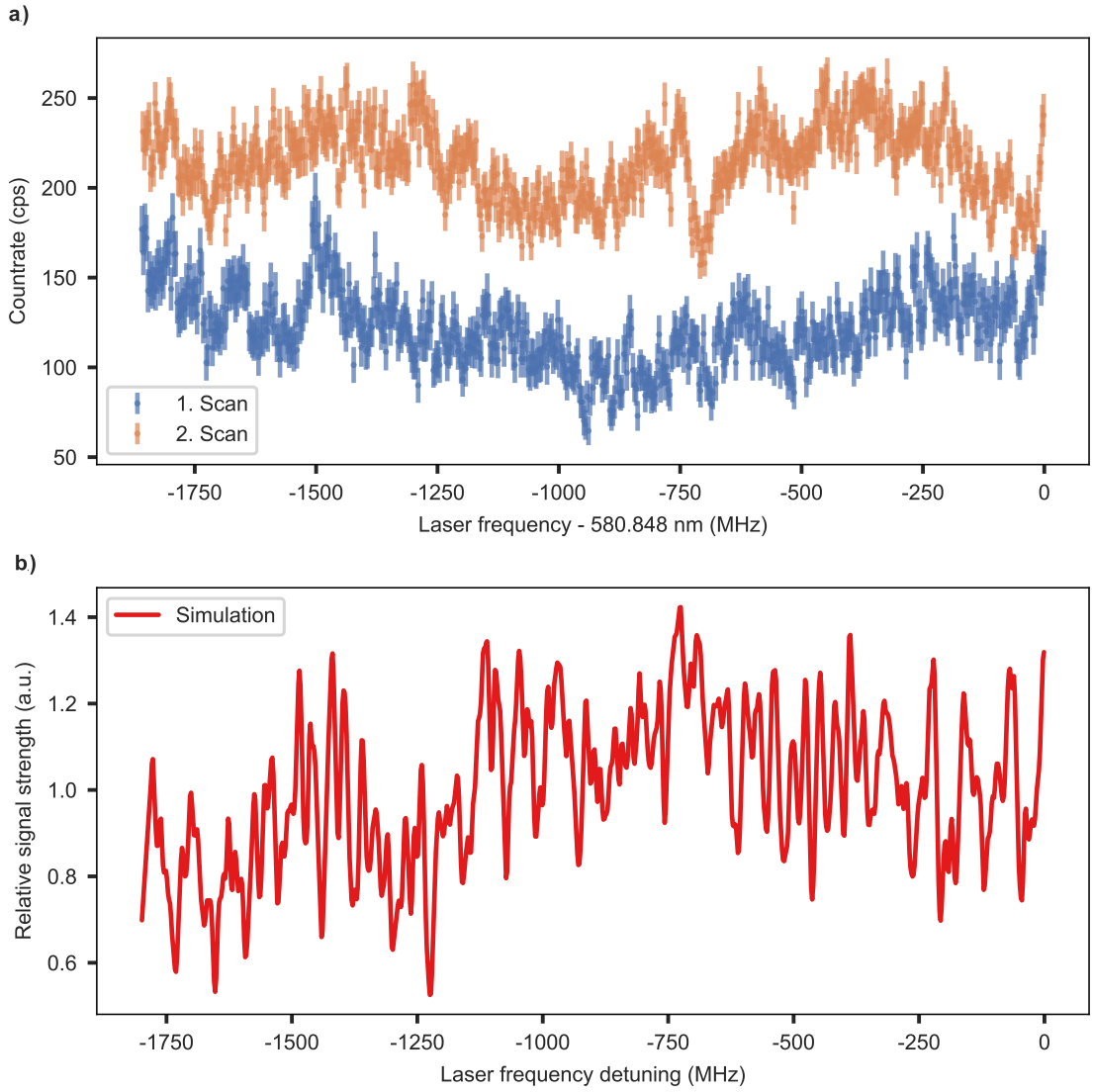

Figure 6.8: High resolution laser scans in the center of the inhomogeneous line of NP4 at 10 K (a). The diode laser grating voltage was slowly scanned in a sawtooth shape to get a frequency resolution of 1 MHz and some statistical fine structure can be observed in the countrate. The second scan (orange) has an offset of 100 cps for better visibility. In (b) a simulation of the relative signal strength is shown for a laser scan with 2 MHz laser linewidth, 10 MHz power-broadened homogeneous emitter linewidth and a distribution of 8,000 ions over a 60 GHz inhomogeneous linewidth.

Search for Single Europium Ions In a next step, the intracavity power is reduced even further to about 1 μW to reduce the power broadening. The 611 nm CW fluorescence countrates are then slightly above the dark count level of our detector of $R_{dark} \approx 20 \pm 5$ cps which requires even longer signal averaging. Typi-

cally, I used 5 s per frequency leading to a total time of 20 min per scan over just a scan range of 25 MHz. The laser is locked to the reference cavity to obtain a 20 kHz narrow laser linewidth. Scanning the locked laser with a sub-megahertz precision can be done using an AOM. This has the disadvantage of a strong variation of the diffraction efficiency over the scanning bandwidth. I chose a different route and implemented an electronic sideband (ESB) PDH locking scheme [182]. The ESB scheme is a modification of the PDH locking technique, whereby the RF signal to generate the optical sidebands already contains electronic sidebands at frequencies $\pm\Omega_1$. The optical signal at the phase modulator output then shows two main sidebands at detunings $\pm\Omega_2$, where each possesses again two sidebands detuned by $\pm\Omega_1$. The advantage of the ESB locking scheme lies in the fact that one is able to lock the laser to the reference cavity line with the standard PDH setup with (de-)modulation frequency Ω_1 and simultaneously shift the laser frequency by varying Ω_2, which shifts the detuning of the main sidebands. The ESB RF signal is generated by an AWG and thus the laser frequency can be adjusted with a precision below its linewidth. The cryostat is operated at its minimum temperature of 4.3 K to decrease the homogeneous linewidths. In order to avoid permanent spectral hole burning, which is observed for temperatures below 10 K (see Section 6.6), the single-pass AOM is used to create a three-tone matching the HF splitting of the ^{151}Eu isotope. Two scans with a frequency stepsize of 100 kHz in the center of the inhomogeneous line of NP4 can be seen in Fig. 6.9a). Although the fluctuations in the countrate are exceeding one standard deviation and spectral features can be observed, the second scan reveals that these features do not reproduce in general. A simulation of the spectrum over the same bandwidth is shown in Fig. 6.9b). The simulation randomly distributes the spectra of 8000 europium ions over the inhomogeneous linewidth of 60 GHz taking into account the full hyperfine level structure (i.e. 9 transitions per ion) for both isotopes. The homogeneous linewidth was assumed to be 500 kHz at an excitation power level of one saturation power P_{sat} (light red curve) and a factor of ten broader, i.e. 5 MHz, for a power level of 100 saturation powers (dark red curve). One can clearly see how a high excitation power smears out the sharp spectral lines. To match the countrate level of the measurement, I assumed a single ion countrate of 1 cps per ion and offset the curves by the dark countrate of 20 Hz. Comparing the measured spectra with the simulation suggests that the excitation power level of 1 μW in the measurement should be close to one saturation power since rather narrow features can be observed. However, in similar experiments, where single rare earth ions could be detected, saturation powers of below one photon per cavity lifetime have been measured [44], [50]. In this setup, one photon per cavity lifetime would amount to $P_c \approx 5$ nW i.e. the measurement presented here was performed rather at $P \approx 200\, P_{sat}$. Interestingly, a similarly high resolution laser spectra as depicted in Fig. 6.9a) was measured when using a single tone excitation, which should lead to optical pumping into an off-resonant HF state. The fact that no strong optical pumping at a temperature of 4.3 K is observed, could also be explained by the

high excitation power.

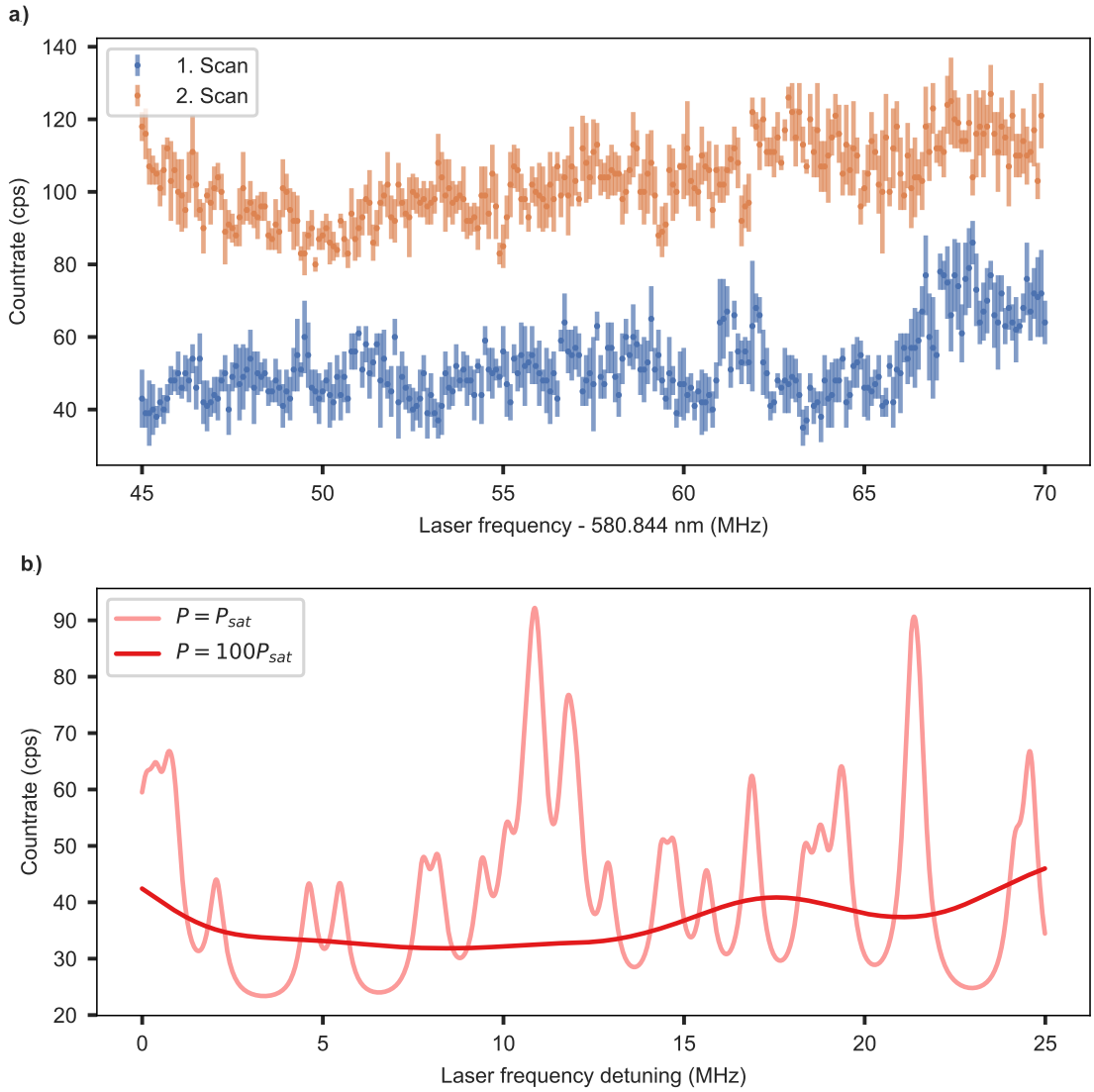

Figure 6.9: a): High resolution laser scans in the center of the inhomogeneous line of NP4 at 4.3 K. A frequency resolution of 100 kHz was achieved in the measurement by locking the laser to the reference cavity. The second scan (orange) has an offset of 50 cps for better visibility. b): Simulations of the spectrum for power-broadened linewidths at one saturation power P_{sat} (light red) and a power of hundred saturation powers (dark red). For the simulation data a countrate of 1 cps per ion was assumed and the data was offset by the dark countrate of 20 cps to match the measured countrate level.

Zooming into two narrow spectral windows of the first scan around 49.5 MHz and 62 MHz and fitting Lorentzian lines to these features, narrow linewidths of 0.2 MHz to 0.6 MHz are obtained. These narrow lines seem to fit quite well to the expected

homogeneous linewidth of a single europium ion of 0.6 MHz at 4 K as reported by [60]. Unfortunately, due to a lack of reproducibility of these signals, I was unable to conduct further measurements like recording a second-order correlation function to check the single emitter nature of these features.

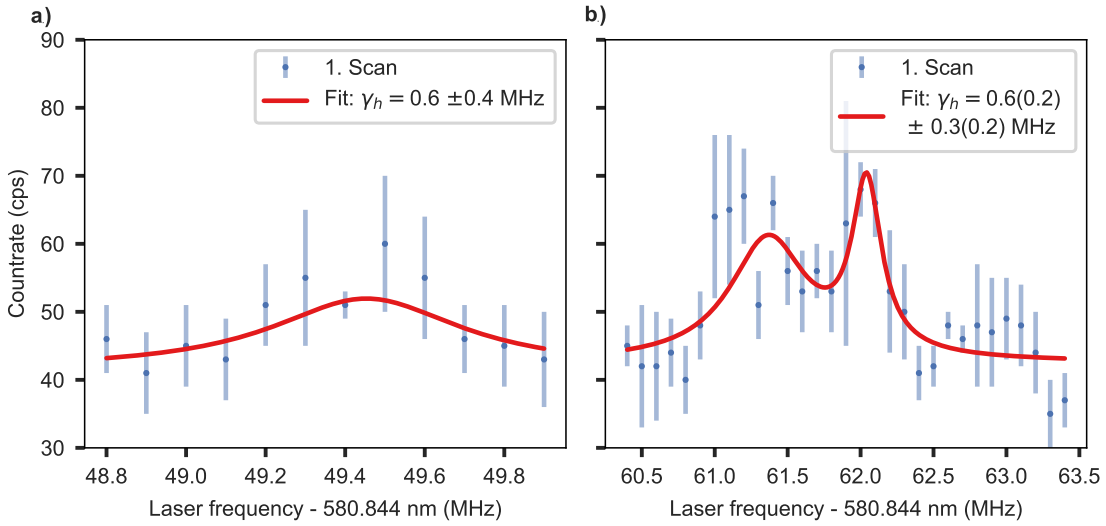

Figure 6.10: Fits of Lorentzian lines to the spectral features at 49.5 MHz (a) and 62 MHz (b) laser detuning of the 1st high resolution laser scan in Fig. 6.9a). The FWHM of the fitted curves reveal sub-megahertz structures of potential homogeneous lines of single europium ions.

In the following, I would like to discuss several aspects that could lead to the observed fluctuations in the countrate and could explain why they don't reproduce in each scan. A drift of the laser frequency during the scan could prevent the replication of the latter. However, the laser is locked to a reference cavity which is designed to have only low frequency drifts of the order of 50 Hz per second [183], which would amount to a few tens of kilohertz over the course of one scan. I monitored the absolute frequency of cavity resonance over 32 days and could observe drifts less than 200 MHz in agreement with the 50 Hz per second drift rate measured by [183]. Although it requires a high drift stability of various experimental parameters to resolve sub-megahertz linewidths at such low countrate levels, the laser stability should not be limiting.

The polarization of the excitation light is another parameter that might drift over time and could cause spectral features to disappear in the next scan due to a smaller or even vanishing overlap between the polarization of the electric field and the emitter's transition dipole orientation. To test this hypothesis, I monitored the polarization angle over a time span of five hours, which can be seen in Fig. 6.11. The light enters the cavity fiber with a linear polarization and the cavity transmis-

sion spectrum is monitored while sweeping the cavity length over a resonance. The polarization mode splitting of the cavity can be seen in Fig. 6.11 b). Here, the polarization is initially rotated such that one can resolve both polarization eigenmodes of the cavity with roughly equal intensity, which is referred to as 45° polarization. Fitting a sum of two Lorentzian lines to the data reveals the heights of both peaks from which a polarization visiblity, $V = (I_1 - I_2)/(I_1 + I_2)$, can be calculated. This value is then converted to an angle by mapping $V = [-1, 1] \rightarrow \phi = [0°, 90°]$. Monitoring the cavity transmission signal over five hours, only a small drift of the polarization of about 10° is observed, as depicted in Fig. 6.11 a). This result rules out the hypothesis that the limited reproducibility of the high resolution laser scans comes from a drift in the polarization of the excitation light. On the contrary, the polarization is stable over the course of several high-resolution laser scans which takes about one to two hours. This indicates that another important parameter of the experiment is stable enough to perform such challenging measurements.

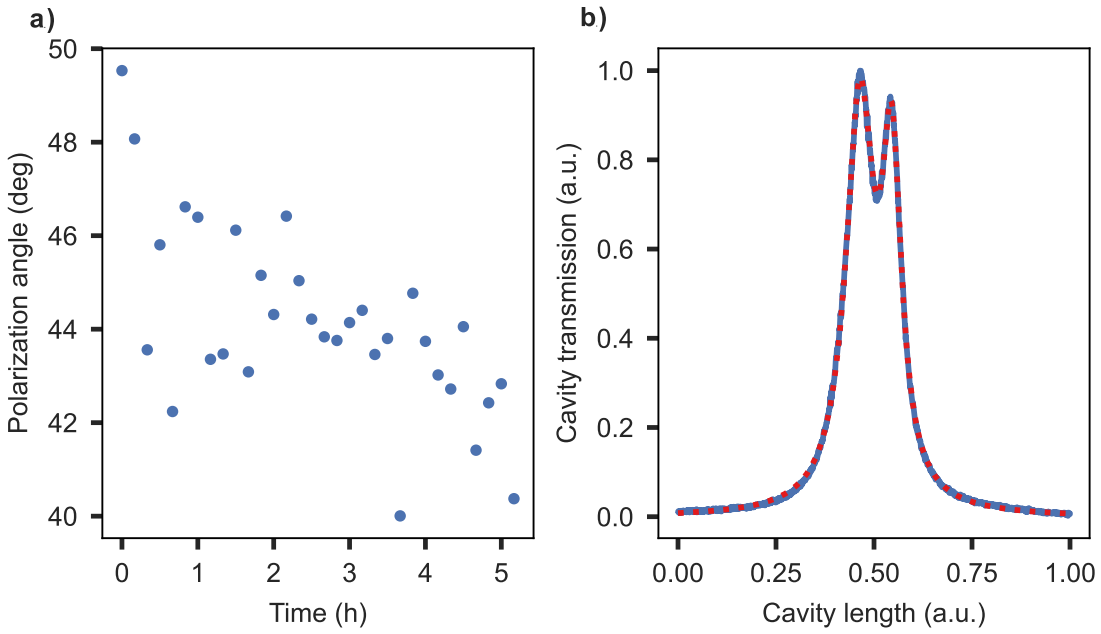

Figure 6.11: Monitoring of the polarization angle of the excitation light in transmission of the cavity over 5 h (a). A cavity transmission spectrum is taken every 10 min where the cavity length is swept over a resonance and the polarization angle is calculated from the peak heights of the polarization mode splitting of the cavity mode (b).

Collaborators from Lund University (Adam Kinos and Andreas Walther) investigated the effects of instantaneous spectral diffusion (ISD) [184], [185] and mentioned that this could be an issue for our experiments. ISD describes the stochastic frequency shift of a transition induced by the (off-resonant) excitation of an ion in close proximity. The electric dipole blockade mechanism, which we

would like to harness for two-qubit gate operations could lead to ISD in this case. Analyzing the sources of errors for single qubit gate fidelities they concluded that it becomes necessary to deplete the population in a certain spectral window around a targeted ion by optical pumping in order to avoid ISD errors [81]. Since I can not identify any other mechanism which changes the result of each laser scan, it is likely that this complex system of many emitters being in spatial and spectral proximity demands for a more sophisticated measurement scheme. It should also be noted that so far all successfull detections of single rare-earth ions were achieved using samples with much lower dopant densities than in our case, which reduces ISD effects.

Fluorescence Lifetime Spectroscopy Since I was not able to identify the source of irreproducibility in our measurements, I conclude that the CW laser scan method conducted here, is not suitable to detect single europium ion signals. The group of Hugues de Riedmatten at ICFO in Barcelona has detected single erbium ions in a similar cavity experiment by performing a pulsed, resonant excitation and detection measurement [50], [155]. They recorded a histogram for each frequency and calculated a histogram asymmetry by dividing the counts in the first half of the histogram by the counts detected in the second half. Thereby, they calculate a kind of derivative of the histogram which should be insensitive to background fluctuations or other sources of slow drifts. Combining this method with a randomized frequency scan instead of the linear sweep that I have done so far, should further rule out correlations between (instantaneous) spectral diffusion of the ions and the direction of the frequency scan. I have yet not done such measurements, since it requires more technical overhead because a second laser to lock the fiber cavity has to be used which has to be frequency stable with respect to the 580 nm spectroscopy laser over the long measurement times of several hours. In addition, taking a histogram with reasonable statistics at every laser frequency results in even longer measurement times.

6.5. Purcell Enhancement

The following section presents lifetime measurements of ensembles of ions, addressed by a power-broadened linewidth, of all six nanoparticles from which the Purcell enhancement and thus the cavity performance is deduced. To start with, an estimation of the maximum and ensemble averaged Purcell factors is calculated using an analytic approach to model the different detrimental effects as discussed below. Furthermore, numerical simulations of the decay dynamics of emitters in a real cavity are performed. The findings are used to finally evaluate the data of cavity-enhanced and free-space lifetime measurements and calculate the respective

Purcell enhancement.

Estimation of Purcell Factors The effective Purcell factor F_P^{eff}, given by Eq. 3.6.20, is reduced by three main correction factors in a realistic Fabry-Pérot cavity, namely:

1. The cavity length jitter correction $\xi_{vibrations}$.
2. The dipole orientation correction ξ_{dipole}.
3. The electric field correction ξ_{field}.

The maximum and ensemble averaged effective Purcell factors can thus be described as

$$F_P^\star(d_{NP}) = \xi_{field}(d_{NP})\,\xi_{vibrations}\,F_P^{eff}(d_{NP}), \tag{6.5.1}$$

$$\langle F_P^\star(d_{NP})\rangle = \langle\xi_{field}(d_{NP})\rangle\,\langle\xi_{dipole}\rangle\,\xi_{vibrations}\,F_P^{eff}(d_{NP}). \tag{6.5.2}$$

The dependency on the nanoparticle diameter d_{NP} is written explicitely, since it has a strong influence on the cavity finesse (see Fig. 3.4), which enters the Purcell factor according to Eq. 3.6.18. I will always plot the Purcell factor as a function of the diameter in the following, because this parameter has the largest influence. Quantities in angled brackets denote an average value for a large ensemble of ions inside a nanoparticle.

First of all the cavity length jitter around the peak of the resonance, as analyzed in Chapter 5, leads to a correction factor [161],

$$\xi_{vibrations} = \sqrt{\frac{\pi}{8}}\frac{\delta d}{\sigma_z}e^{\frac{\delta d^2}{8\sigma_z^2}}\left(1-\mathrm{erf}\left(\frac{\delta d}{2\sqrt{2}\sigma_z}\right)\right) = 0.63, \tag{6.5.3}$$

which is the same for every emitter inside the nanoparticle. A Gaussian linewidth broadening of standard deviation $\sigma_z = 8\,\mathrm{pm}$ is assumed, which represents the cavity stability during most of lifetime measurements presented later. The cavity FWHM is calculated as $\delta d = 14.5\,\mathrm{pm}$.

Secondly, the overlap between the transition dipole and the electric field vector is set to one for the maximum Purcell factor. However, in general it is random, due to a polycrystalline structure of the nanoparticles and three different possible transition dipole orientations of an europium ion at the C_2 site in yttria [186]. Thus an ensemble average over all possible orientations has to be taken. The Purcell factor is proportional to the squared dot product of both vectors, which is expressed in spherical coordinates,

$$F_P^\star(\theta,\varphi) = F_P\sin^2\theta\,\cos^2\varphi. \tag{6.5.4}$$

The ensemble averaging is done analytically by the integration over the 1st octant of the unit sphere, assuming a uniform distribution of orientations and an electric field vector lying on the x-axis, i.e. $\vec{e}_d \cdot \vec{e}_E = \sin\theta \cos\phi$:

$$\langle \xi_{dipole} \rangle = \frac{\langle |\vec{d} \cdot \vec{E}_{max}|^2 \rangle}{|\vec{d}|^2 |\vec{E}_{max}|^2} =$$
$$= \frac{1}{N(\theta,\phi)} \int_0^{\frac{\pi}{2}} \int_0^{\frac{\pi}{2}} \sin^2\theta \cos^2\phi \sin\theta \, \mathrm{d}\theta \, \mathrm{d}\phi = \frac{1}{N(\theta,\phi)} \frac{\pi}{6} = \frac{1}{3}, \tag{6.5.5}$$

with the normalization factor $N(\theta,\phi) = \int_0^{\frac{\pi}{2}} \int_0^{\frac{\pi}{2}} \sin\theta \, \mathrm{d}\theta \, \mathrm{d}\phi = \pi/2$.

Lastly, I am taking into account the random position of an europium ion inside the nanoparticle, which results in a random position in the standing wave field of the cavity mode. The lateral extent of the nanoparticle is much smaller than the cavity mode waist such that I assume every ion to be placed at the lateral field maximum of the Gaussian cavity mode. The DBR mirror coating has a spacer layer such that the field maximum is located $z_{max} = 40\,\mathrm{nm}$ above the mirror surface. The Purcell factor is hence reduced depending on the z-position of the emitter according to:

$$F_P^\star(z) = F_P \cos^2\left(\frac{2\pi}{\lambda}(z - z_{max})\right). \tag{6.5.6}$$

The field correction factor for a maximally coupling emitter is then defined as as,

$$\xi_{field}(d_{NP}) = \begin{cases} \cos^2\left(\frac{2\pi}{\lambda}(z - z_{max})\right) & \text{for } d_{NP} < z_{max}, \\ 1 & \text{for } d_{NP} \geq z_{max}. \end{cases} \tag{6.5.7}$$

The ensemble averaged field correction factor $\langle \xi_{field} \rangle$ is calculated by integration over all z positions within the nanoparticle, assuming a uniform density of ions, i.e. a cube-shaped nanoparticle for ease of calculation.

$$\langle \xi_{field}(d_{NP}) \rangle = \left(\frac{1}{d_{NP}} \int_{z=0}^{d_{NP}} \cos\left(\frac{2\pi}{\lambda}(z - z_{max})\right) \mathrm{d}\, z \right)^2 \tag{6.5.8}$$
$$= \left(\frac{\lambda}{2\pi d_{NP}} \left(\sin\left(\frac{\lambda}{2\pi}(d_{NP} - z_{max})\right) + \sin\left(\frac{\lambda}{2\pi} z_{max}\right) \right) \right)^2. \tag{6.5.9}$$

In principle, the effective Purcell factor can also be further reduced by the quantum efficiency, QE, of the emitter,

$$F_P^{eff} = QE \cdot \zeta \cdot F_P, \tag{6.5.10}$$

which is defined as the ratio $QE = \gamma_r/\gamma_{tot}$ of the radiative decay rate γ_r by the total decay rate $\gamma_{tot} = \gamma_r + \gamma_{nr}$, also including non-radiative decay channels e.g.

via phonons. However, according to measurements of Buijs et al. [69], non-radiative quenching of the $^5D_0$ state at impurities of the crystal lattice is negligible for doping concentrations below 10%. Thus, for our sample with 0.3% doping I can assume a near-unity quantum efficiency and thus neglect it in the following.

Finally, the maximum and ensemble averaged effective Purcell factors that are expected in our measurements can be plotted for the $^5D_0 \rightarrow {}^7F_0$ (Fig. 6.12 a)) and the $^5D_0 \rightarrow {}^7F_2$ (Fig. 6.12 b)) transition, respectively. The Purcell factors of about 1 (2.5) for the ensemble average (maximum) of the 580 nm transition are much lower than previously estimated [67]. Hence, I expect to measure a lifetime about half the free-space lifetime for the ensembles addressed here. The largest reduction between the Purcell factor of a perfectly coupling single ion and an ensemble stems from the dipole orientation correction factor. The 611 nm transition shows even lower Purcell enhancements of below 0.5 due to its broad homogeneous linewidth.

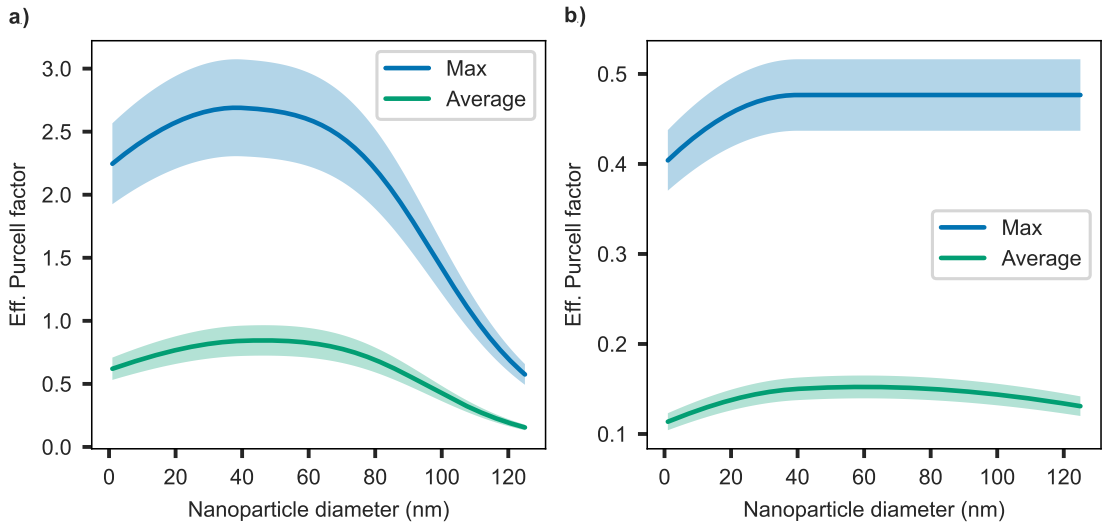

Figure 6.12: Estimation of the maximum (blue) and ensemble averaged (green) effective Purcell factors dependent on the nanoparticle diameter for a realistic cavity performance. The light blue and green areas depict the uncertainty of one standard deviation. Plot a) (b)) shows the calculation for the $^5D_0 \rightarrow {}^7F_0$ ($^5D_0 \rightarrow {}^7F_2$) transition.

Simulation of Decay Dynamics Similarly to the Monte Carlo simulation of the excited state decay dynamics presented in [187], I deduce an analytical description of the decay curve for an ensemble of emitters inside the cavity. In order to obtain a more precise description of the decay dynamics, I model the cavity length jitter by a time-dependent detuning about the peak of the Lorentzian cavity resonance

resulting in the reduced Purcell factor:

$$F_P^\star(t,\phi) = F_P^{eff}\frac{1}{1+\left(\frac{\delta z(t,\phi)}{\delta d}\right)^2}, \tag{6.5.11}$$
$$\text{with} \quad \delta z(t,\phi) = \sum_{i=0}^{2} a_i \sin(2\pi f_i t + \phi_i + \phi).$$

A sum of three sine functions is taken to represent the largest contributions in the spectrum of the cavity length jitter in Fig. 5.15, at frequencies $f_i = 100, 310$ and 1000 Hz with respective amplitudes $a_i = 5, 6$ and 3 pm giving a total cavity length jitter of $\sigma_z = 8.4$ pm, which resembles the value for most of the lifetime measurements. To avoid a fixed phase relation between the three sine functions, each gets a random phase offset ϕ_i in every run of the simulation. In total, the time-dependent, reduced Purcell factor can be written as:

$$F_P^\star(t,\phi,\theta,\varphi,z) = \frac{F_P^{eff}}{1+\left(\frac{\delta z(t,\phi)}{\delta d}\right)^2}\sin^2\theta\,\cos^2\varphi\,\cos^2\left(\frac{2\pi}{\lambda}(z-z_{max})\right). \tag{6.5.12}$$

The normalized, background-corrected histogram of the cavity-enhanced decay curve for an ensemble of emitters can finally be calculated as,

$$\langle I(t)\rangle = \frac{1}{N}\int_{z,\phi,\theta,\varphi=0}^{d_{NP},2\pi,\pi/2,\pi/2} \beta(t,\phi,\theta,\varphi,z)\, e^{-\frac{(F_P^\star(t,\phi,\theta,\varphi,z)+1)}{T_{1,fs}}t}\sin\theta\,\mathrm{d}z\,\mathrm{d}\phi\,\mathrm{d}\theta\,\mathrm{d}\varphi, \tag{6.5.13}$$

with the normalization factor,

$$N = \int_{z=0}^{d_{NP}}\int_{\phi=0}^{2\pi}\int_{\theta=0}^{\pi/2}\int_{\varphi=0}^{\pi/2}\sin\theta\,\mathrm{d}z\,\mathrm{d}\phi\,\mathrm{d}\theta\,\mathrm{d}\varphi = d_{NP}2\pi\frac{\pi}{2} = \pi^2 d_{NP}, \tag{6.5.14}$$

and the cavity collection efficiency $\beta = \frac{F_P^\star}{F_P^\star+1}$. The latter accounts for a higher probability to detect photons when the Purcell factor is higher and thus applies a weighting to the distribution. I also included an integration over the phase offset ϕ of the cavity length detuning to simulate different offsets for each trial of the pulsed measurement.

The integrals cannot be solved analytically, therefore a numerical integration is done to obtain the simulated histogram of a lifetime measurement for $F_P^{eff} = 2$ and $F_P^{eff} = 100$ for a free-space lifetime of $T_{1,fs} = 2$ ms shown in Fig. 6.13.

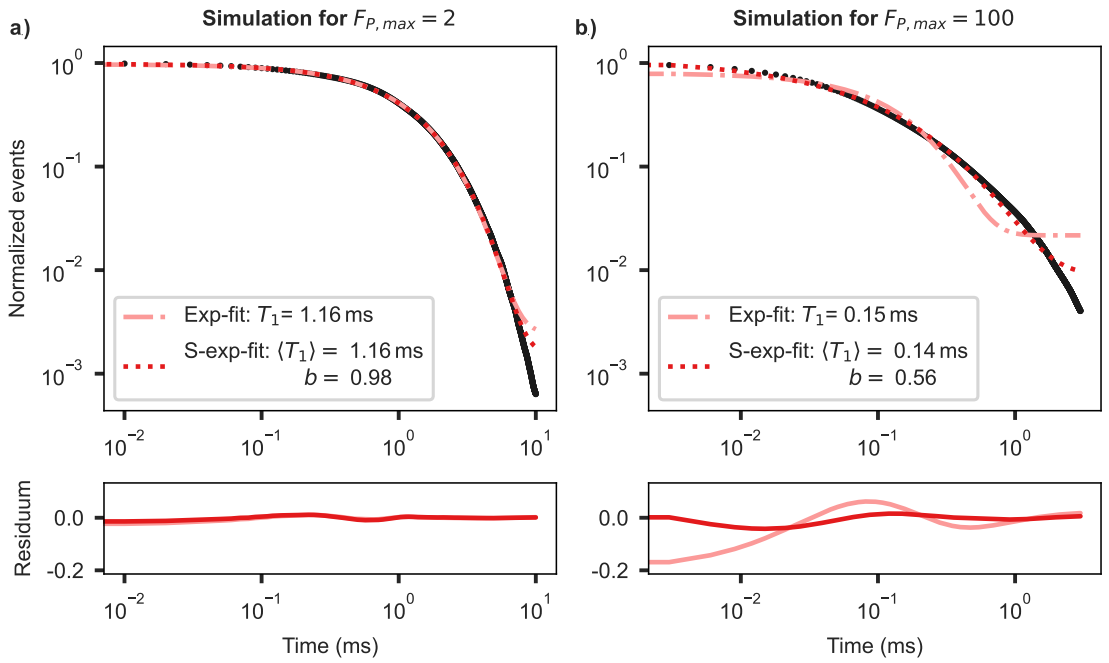

Figure 6.13: Numerical simulation (black) of the decay dynamics of an ensemble of emitters inside a realistic cavity for a free-space lifetime of $T_{1,fs} = 2\,\text{ms}$ and a maximum, effective Purcell factor of $F_P^{eff} = 2\,(100)$ in plot a) (b)). A mono-exponential decay function (Exp-fit, light red) as well as a stretched exponential function (S-exp-fit, dark red) is fitted to the data to extract the decay time constant T_1 as well as the stretching parameter b. Below the histograms the deviation of the fit curve from the data is shown.

In principle, for the ensemble lifetime histogram one would expect to see a stretched exponential decay of the form

$$I(t) = I_0\, e^{-\left(\frac{t}{T_{1,fs}}\right)^b}, \tag{6.5.15}$$

due to a distribution of Purcell factors leading to a superposition of exponential decays with different decay time constants [188]. However, since just a maximum, effective Purcell factor of around 2 is expected, the simulation in Fig. 6.13 a) indicates that a mono-exponential decay, i.e. $b = 1$, should fit the data quite well and the variation of Purcell factors for different emitters does not really come into play. In comparison to that, the simulation with a maximum effective Purcell factor of 100 in Fig. 6.13 b) gives a stretching parameter $b = 0.56$. This value is much smaller than the near-unity stretching for the case of a low Purcell factor. Although the decay time constant of both the exponential (light red) and stretched exponential (dark red) fits give a similar result, the residuum of the fit below the histogram is larger for the mono-exponential fit function. These results motivate to use a mono-exponential fitting function for the evaluation of the lifetime measurements in the following paragraph.

Cavity-enhanced Lifetime Measurements The cavity length tunability allows to selectively Purcell-enhance only the 580 nm transition, only the 611 nm transition or both simultaneously. By choosing any longitudinal mode order of the 580 nm laser except of the DR-condition, only the $^5D_0 \rightarrow {}^7F_0$ transition is enhanced by the cavity. It is also possible to enhance only the 611 nm transition by locking the cavity on a low setpoint of the 580 nm resonance of the DR mode order which should suppress the Purcell enhancement of the 580 nm transition. By keeping the cavity passively stable on the peak of the DR-condition, a twofold Purcell enhancement of both transitions simultaneously is achieved. Over the course of this project, I was using different techniques to stabilize the cavity on a certain setpoint while performing a pulsed measurement which also results in a pulsed error signal for the feedback loop. For most of the measurements presented here, I relied on the high passive stability of the cavity and only compensated for slow drifts by a slow feedback loop or a pulsed locking. Since these stabilization schemes were developed over the course of the investigation of the different nanoparticles, the datasets are incomplete with respect to the three different lifetime measurements.

The cavity-enhanced lifetime of the respective transition is extracted by first fitting a mono-exponential function $I(t) = I_0 \exp(-\frac{t}{T_1}) + I_{bgd}$ to a normalized histogram. From the fit result the background offset I_{bgd} is taken and subtracted from the data. In a second step a linear function is fitted to the normalized, background-corrected histogram on a log-linear scale and the decay time constant T_1 is extracted from the slope:

$$\ln(I(t)) = \ln(I_0) - \frac{1}{T_1}t. \tag{6.5.16}$$

The histograms and fit results for some selected lifetime measurements of the six nanoparticles can be seen in Fig. 6.14.

Free-space Lifetime Measurements In order to experimentally determine the Purcell factors according to Eq. 3.6.23, also the free-space lifetime has to be determined. In the following, I would like to render this term more precisely since an europium ion in "free-space" would have an infinitely long excited state lifetime due to the dipole forbidden nature of the transition. Europium ions doped into yttria bulk crystals typically exhibit a lifetime of 1 ms [68], however in nanoparticles the reduced density of states the ions can couple to, depending on the size of the nanoparticles, prolongs this bulk lifetime. Furthermore, placing the nanoparticle on the surface of a DBR mirror further modifies the density of states and can lead to a lifetime shortening (for details see [97]). A lifetime of $T_{1,substrate} = 2.1 \pm 0.1$ ms was measured for a nanoparticle residing on a glass substrate in a confocal microscope and only a slightly shorter lifetime of $T_{1,DBR} = 2.0 \pm 0.1$ ms was found for a nanoparticle on a DBR cavity mirror.

As the lifetime of individual particles vary, in order to quantify the Purcell effect, it is important to measure lifetimes of the same nanoparticle, both in free-space and in the cavity. Therefore, the free-space lifetime is understood as the lifetime measured on the DBR mirror either in the confocal microscope (NP5 & NP6 in Fig. 6.14 e) & f)) or inside the cavity under detuning from resonance (NP3 & NP4 in Fig. 6.14 c) & d)). The latter is achieved by locking the cavity on a low setpoint of 6 HWHM which amounts to only 3% of the peak Purcell effect and hence can be regarded as the free-space lifetime. To calculate the Purcell factors for NP1 and NP2, I use a free-space lifetime of $\bar{T}_{1,fs} = 2.0 \pm 0.1\,\mathrm{ms}$ which is an average value of confocal microscope measurements of four different nanoparticles on the same mirror.

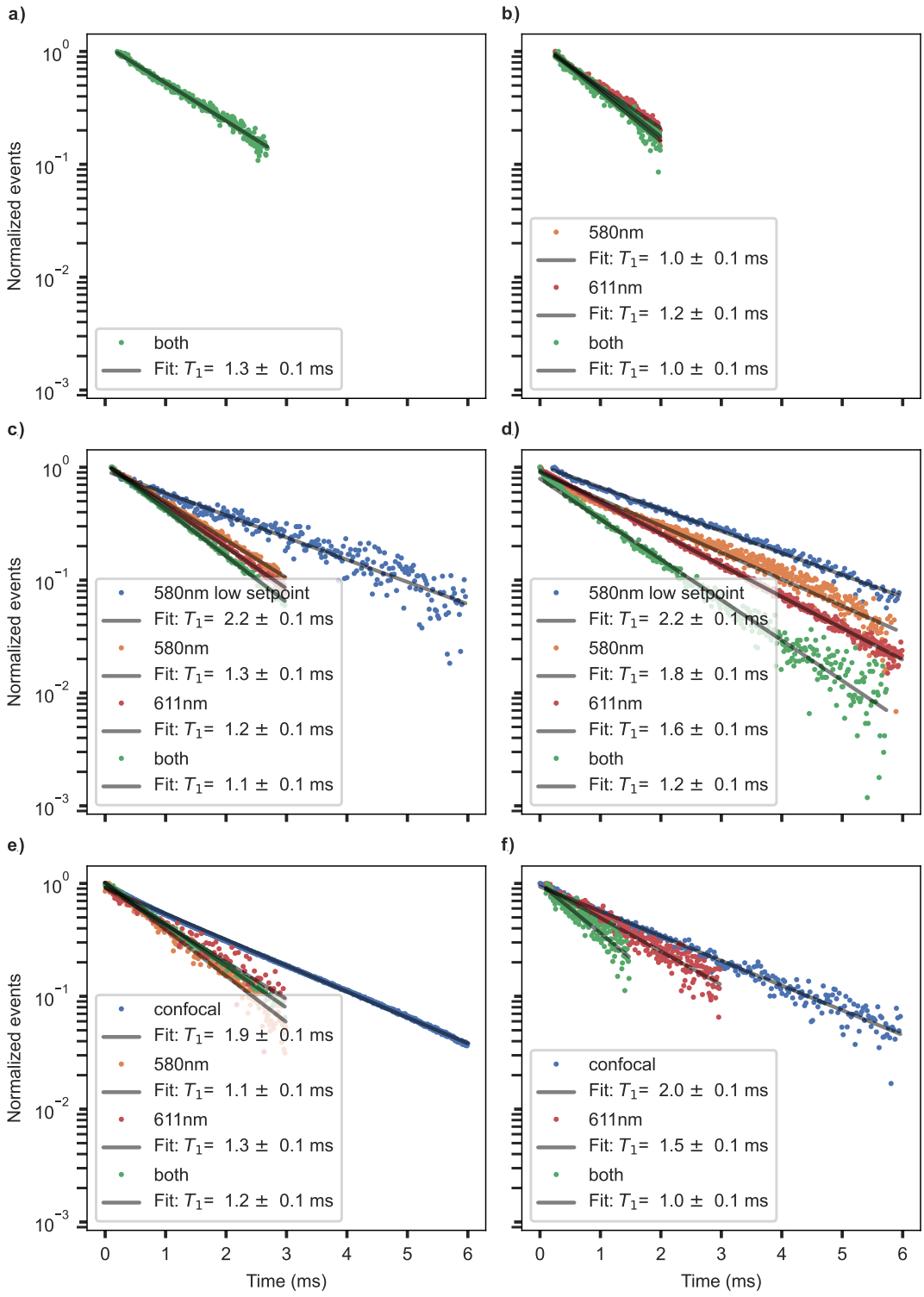

Figure 6.14: Cavity-enhanced (orange, red, green) and free-space (blue) lifetime measurements of NP1 (a) to NP6 (f) adapted from [56]. The different colors indicate the Purcell-enhanced transition(s): orange: only 580 nm transition, red: only 611 nm transition and green: both transitions are resonant simultaneously. The black lines are linear fits to the normalized and background-corrected data to extract the lifetime T_1.

Purcell Factors Using the lifetimes obtained from the data shown in Fig. 6.14, the effective, ensemble averaged Purcell factors for the different nanoparticles can be calculated as:

$$F_P^\star = \frac{T_{1,fs}}{T_{1,c}} - 1, \tag{6.5.17}$$

$$\sigma_{F_P^\star} = \sqrt{\left(\frac{1}{T_{1,c}}\right)^2 \sigma_{T_{1,fs}}^2 + \left(\frac{T_{1,fs}}{T_{1,c}^2}\right)^2 \sigma_{T_{1,c}}^2}, \tag{6.5.18}$$

with a fixed error of $\sigma_{T_{1,fs}} = \sigma_{T_{1,c}} = 0.1\,\text{ms}$ due to a larger influence of the background value that is subtracted from the linear fits than the error given by the fitting routine. The results, together with theoretical values of the maximum and ensemble Purcell factors obtained from Eq. 6.5.2, are plotted in Fig. 6.15. The Purcell factors of the 580 nm transition lie between 0.25 to 1.0 and fit approximately with the theoretical ensemble averaged result. The large spread could be explained by the fact that the theoretical calculation averages uniformely over all dipole orientations but for a distinct nanoparticle there could be a predominant orientation of the subensemble that is addressed in the lifetime measurement. The Purcell factors of the 611 nm transition are systematically too high, although I assumed zero detuning between the cavity and ${}^5D_0 \rightarrow {}^7F_2$ line. The exact spectral overlap between the cavity mode and one of the five ${}^5D_0 \rightarrow {}^7F_2$ transitions is hard to predict and should vary for each nanoparticle due differences in the dispersion. Furthermore, the suppression of the 580 nm transition by the detuned cavity, could be not strong enough for these measurements. The Purcell factors for the enhancement of both transitions fits quite well to the theoretical estimation within the errors. The sum of 580 nm and 611 nm Purcell factors does not match the Purcell factors of both transitions simultaneously, which should be the case according to the formula in Eq. 3.6.30. However, this would support the assumption that the 580 nm transition was not suppressed well enough and thus the 580 nm Purcell factor is partly added twice in the sum.

In Eq. 3.6.33 I showed that a calculation of the free-space lifetime is possible from the three different lifetimes measured in the cavity. Plugging in the three lifetimes for NP 3, 4 and 5 gives $T_{1,fs} = 1.4 \pm 0.2, 2.9 \pm 0.4$ and $1.2 \pm 0.2\,\text{ms}$. Within their statistical errors, these values don't match the free-space lifetimes measured by the other methods. This suggests additional systematical errors in this method. An unsufficient suppression of the 580 nm transition could again be an issue here and does not allow for the reliable determination of the free-space lifetime from a three-fold cavity lifetime measurement.

In summary, a maximum ensemble averaged Purcell factor of 1.0 ± 0.2 could be measured by enhancing only the 580 nm transition or both transitions. Due to the good agreement between the data and the numerical simulation, it is reasonable

to predict Purcell factors of up to 2.5 and 3.0, for the 580 nm transition and both transitions, respectively, for a single ion with the current experimental setting.

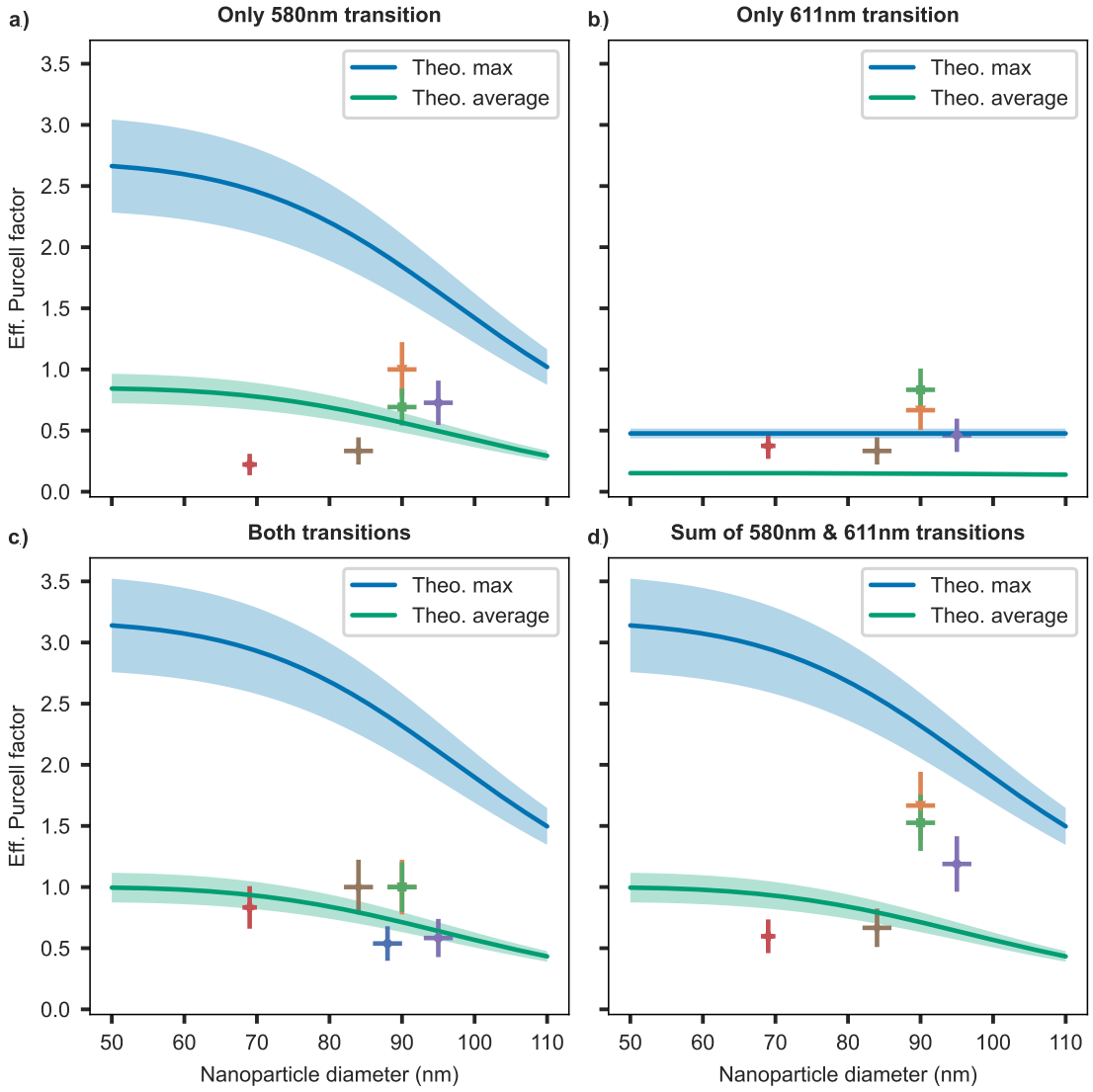

Figure 6.15: Measured effective Purcell factors of NP1 to NP6 (colors refer to the different NPs as defined in Fig. 6.7) together with the theoretical estimation of the maximum (blue) and ensemble averaged (green) effective Purcell factors adapted from [56]. In a) (b)) only the ${}^5D_0 \rightarrow {}^7F_0$ (${}^5D_0 \rightarrow {}^7F_2$) transition is enhanced by the cavity, whereas plot c) shows the measurements where both transitions are simultaneously resonant with the cavity. For comparison, the sum of the Purcell factors in a) and b) are depicted in d).

6.6. Addressing Hyperfine Levels

When exciting the europium ions with a single tone laser pulse, the decay into three possible ground state HF levels leads to optical pumping as soon as the nuclear spin lifetime becomes significantly longer than the optical lifetime. The lifetime of a spin state was measured by my colleagues Vishnu Unni Chorakkunnath and Evgenij Vasilenko by spectral hole burning (SHB) spectroscopy at 16 K in a powder of the same yttria nanoparticles used here. They evaluated the depth of the spectral hole for different time delays between the burn and probe pulses. The datapoints together with an exponential decay fit function can be seen in Fig. 6.16. It results in a spin state lifetime of $T_{1,spin} \approx 1.4\,\mathrm{s}$. Therefore, one can expect to get a depletion of the HF state that is addressed by the single laser frequency for temperatures below 20 K, which leads to a decrease of the fluorescence countrate in a laser scan measurement. Often, this property is used in SHB spectroscopy to get an upper bound of the optical coherence time as well as the splittings of the HF levels and their relative oscillator strengths [61], [189].

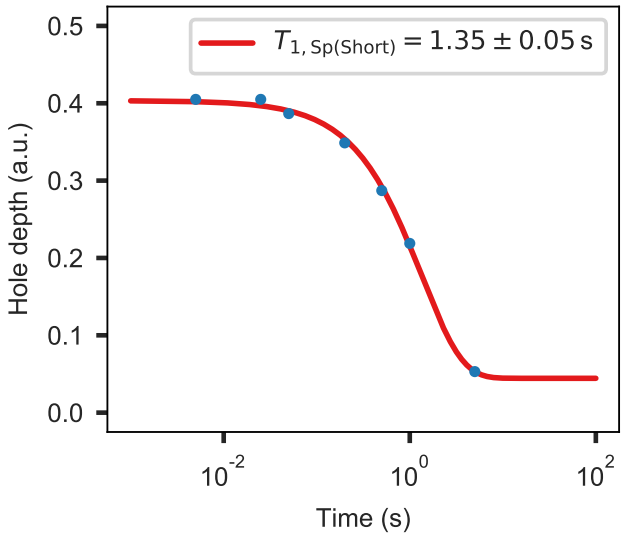

Figure 6.16: Depth of the spectral hole dependent on the burn - probe pulse time delay to evaluate the europium spin lifetime. The measurement was done at 16 K using a powder of europium-doped yttria nanoparticles inside a fiber-ferrule setup. It was carried out by my colleagues Vishnu Unni Chorakkunnath and Evgenij Vasilenko.

Another aspect is that the excitation probability of a single ion with a single tone pulse is only one third due to the three equally populated spin ground states of europium at zero magnetic field. Hence, in my case, the primary goal is not to perform spectral hole burning measurements, but rather the opposite, that is

an effective repumping of the holes in order to avoid the depletion of a HF state. In this Section, I will therefore give a qualitative verification of the correct pulse sequences to address the HF levels to achieve a higher excitation probability and that I am able to repump a spectral hole. The idea of the burn and repump pulse sequence used in the following is schematically shown in Fig. 6.17.

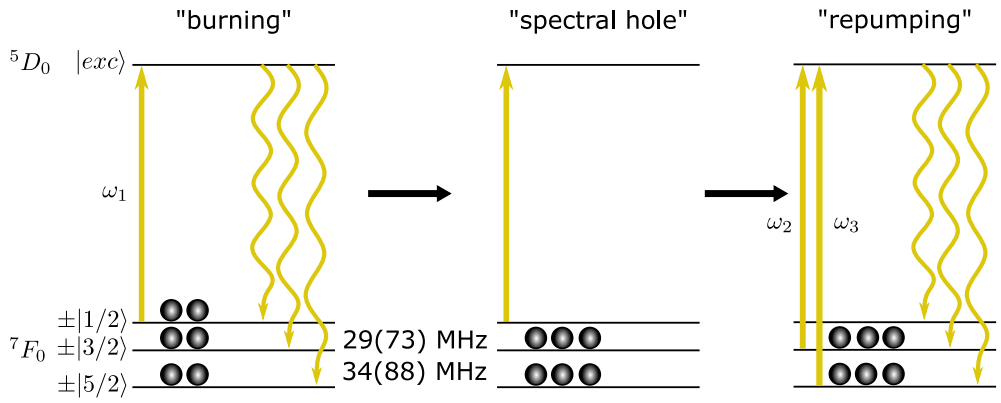

Figure 6.17: Scheme of the burn-repump-sequence used to optically address the three HF states. The frequency splittings are given for the ^{151}Eu (^{153}Eu) isotopes. In the first step (left), a single tone laser pulse of frequency ω_1 leads to a depletion of the upper spin state. This is called a persistent spectral hole (center). In the repumping step (right) I apply a two-tone laser pulse of frequencies ω_2 and ω_3 to deplete the lower two levels and ideally end up with a full population in the spin 1/2 state.

In a first "burning" step, a laser pulse of frequency ω_1 is applied and prepares a non-equilibrium state by optical spin pumping. This creates a persistent spectral hole with a decay time constant given by the spin state lifetime. The latter was measured by colleagues in the group to be on the order of seconds to minutes at temperatures between 20 K and 4 K. In the last step, the population is repumped into the depleted HF level by a two-tone laser pulse of frequencies ω_2 and ω_3.

The fluorescence during a burn-repump sequence in the cavity was measured utilizing the DR-scheme and stabilizing the cavity with a slow drift lock and a low setpoint of 4 HWHM detuning. The laser is locked to the reference cavity to address the same subset of ions over the course of the measurement, which takes several hours. A histogram of the 611 nm fluorescence is recorded over the time span of a full sequence which allows the observation of the burning and repump dynamics during the laser pulses which is usually not possible inside a cavity. The histogram of a measurement at 10 K on NP3 with and without a repumping pulse is shown in Fig. 6.18.

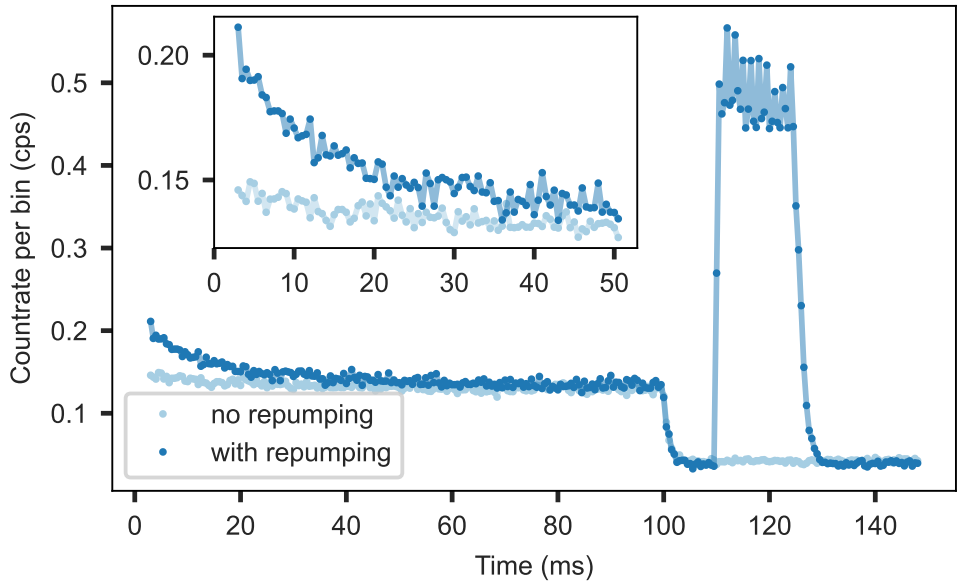

Figure 6.18: Histogram of the 611 nm fluorescence during a burn-repump sequence with (dark blue) and without repumping pulse (light blue) at 10 K on NP3. The frequencies of the burn and repump pulses match the hyperfine splitting of the ^{151}Eu isotope. The inset shows the first 50 ms of the histogram where a decaying countrate can be observed when a repump pulse is applied. The high countrate around 120 ms stems from the strong repump pulse.

For this measurement, after a 100 ms burn pulse of 300 nW intracavity power, the laser is switched off either for 50 ms (no repumping, light blue curve) or a 15 ms repumping sequence is switched on to repopulate the optically pumped levels (with repumping, dark blue curve). In this case the repumping sequence consists of ten sets of alternating 500 μs pulses with three frequencies matching the HF-splitting of the ^{151}Eu isotope. Applying this repumping sequence should mix the populations to the equilibrium state again. A difference in the initial excited state population at the beginning of the burn pulse can be seen in the inset of Fig. 6.18. This behaviour can be traced back to a higher population of the addressed HF level compared to the case without repumping and shows that spectral hole burning becomes an issue below 10 K.

To further characterize the burning and repumping behaviour, the above measurement is performed for three different intracavity power levels for the frequency splitting of the ^{153}Eu isotope (Fig. 6.19 a)). Just the burning time window is cut out and an exponential decay is fitted to the data. Increasing the burn power by two orders of magnitude leads to a factor of five faster pumping timescale. However, the burning contrast after 100 ms is significantly larger for the lowest power

and reaches about 50 %. It could decrease even further for longer burning times. The different burning contrasts can be explained by a different power-broadened linewidth, which, for higher powers, has a higher overlap also with the off-resonant HF-levels and thus leads to a repumping which reduces the depletion of population in the resonant HF-level. The same argument holds for the different contrast observed when repumping with the ^{151}Eu versus ^{153}Eu level splittings which can be seen in Fig. 6.19 b). Since the HF splittings are smaller for the ^{151}Eu isotope, burning with the same power of 3 μW in both cases, leads to less contrast.

In summary, these results show that spectral hole burning is an issue for intracavity powers below a few μW and temperatures below 10 K such that a repumping of population is necessary. Pulse sequences for repumping have been found, that proved to increase the burning contrast when applied for a time window of 15 ms. However, optical power and duration of the sequences are not yet optimized for maximal contrast.

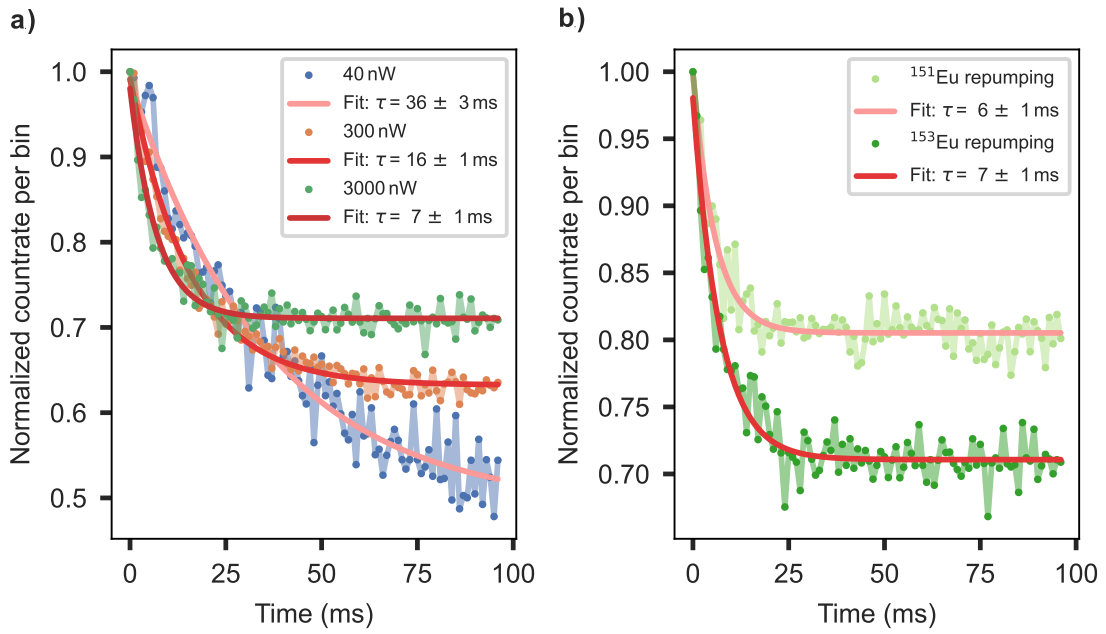

Figure 6.19: a): Histograms during the burn pulses at three different intracavity power levels using a repump sequence for the ^{153}Eu isotope. The different red lines show the result of an exponential fit from which I extract the burning time constant τ. b): Comparison between the frequency splittings for the ^{151}Eu (light green) and ^{153}Eu (dark green) isotopes used for repumping at the same power level of 3 μW.

A last measurement to verify the correct addressing of HF-levels, was to detune the frequency of the burn pulse while keeping the repump pulse frequencies ω_2 and ω_3 fixed to address the ^{151}Eu isotope. I performed such a series of measurements

on NP4 at 10 K with a power level of 1 μW and a shorter 40 ms burn and repump pulse lengths. Since each measurement takes several hours to acquire sufficient statistics, histograms for only six different detunings were measured. In Fig. 6.20 a drop in the burning decay time can be observed at zero detuning. This is expected since the burning frequency is in resonance with the optical transition ω_1 of a subclass of ions, which leads to a fast depletion of the HF-level. However, it should be mentioned that the uncertainties of these measurements are quite large and the reproducibility is limited. Fitting an inverted Lorentzian function to the datapoints results in a homogeneous linewidth of $\gamma_h = 9 \pm 5$ MHz. This value seems reasonable considering the elevated temperature of 10 K and the power-broadened linewidth due to a high excitation power.

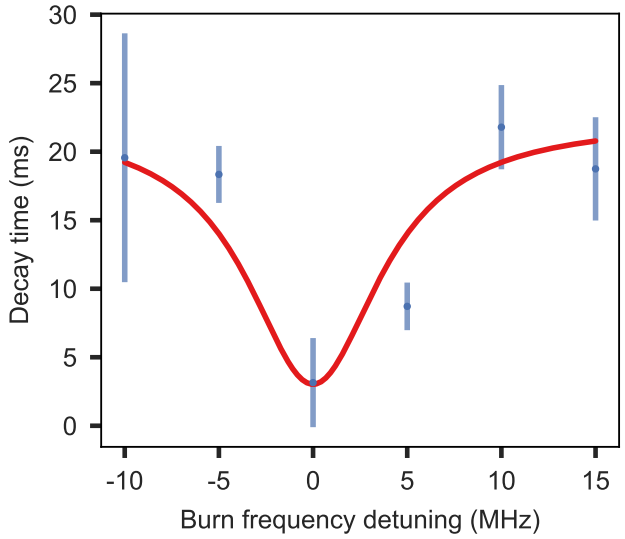

Figure 6.20: Optical pumping time constant obtained from exponential fits as shown in Fig. 6.19 versus the frequency detuning of the burn pulse with a fixed repump pulse matching the frequencies ω_2 and ω_3 of the ^{151}Eu isotope. The measurements were done in the center of the inhomogeneous line of NP4 at 10 K. The red curve displays the inverted Lorentzian fit function.

To sum up, the measurements presented here show the ability to address individual hyperfine levels of different europium isotopes and avoid persistent spectral hole burning by a suitable repumping pulse. These insights will become relevant when addressing single ions, where the low countrates will drop further if no repumping is applied.

6.7. Saturation and Optical Coherence

Another important property of the small sub-ensemble of ions within a nanoparticle is the optical coherence time T_2^*. Since it is not guaranteed that the spectral features described in Section 6.4 are homogeneous lines of individual ions, which is required to give us a precise measurement of the coherence time, I make use of a saturation spectroscopy method often called transient spectral hole burning (TSHB). Similar to spectral hole burning discussed in the previous section, TSHB can be used to obtain an upper bound of the homogeneous linewidth by measuring the width of a short-lived "transient" spectral hole [189]. Before going into the details of this technique, the cavity-enhanced saturation behaviour is measured first.

Saturation Measurement The DR excitation and detection scheme is used and the intracavity power is adjusted via the setpoint of the cavity lock. Here, the laser is tuned to 580.850 nm, the center of the inhomogeneous line of NP3 at 20 K. Using CW excitation, the 611 nm fluorescence countrate is measured for 25 s and the mean value is taken. The background countrate at the same powers is determined by tuning the laser wavelength to 580.175 nm to be off-resonant with the ions. The signal with background (blue) as well as the background-subtracted signal (orange) as a function of the laser power can be seen in Fig. 6.21. Varying the intracavity power over five orders of magnitude shows that the saturation law for a single two-level system (light red) [190],

$$I(P) = I^{\infty}\frac{P}{P + P_{sat}}, \tag{6.7.1}$$

does not fit very well to the background corrected signal (orange) in Fig. 6.21. Since an ensemble of emitters is addressed with their homogeneous lines distributed over an inhomogeneous linewidth, which is orders of magnitudes broader than the expected homogeneous linewidth, the saturation behaviour can not be described by the above equation 6.7.1. In this case, the strong resonant driving of an emitter leads to power broadening of its line and thus more emitters spectrally overlap and can be excited by the laser. Since the power broadening of the linewidth is proportional to the square root of the power [190], I expect to see an increase of the countrate according to $I(P) = I_0\sqrt{P}$. Fitting a power law $I(P) = I_0 P^b$ (dark red line in Fig. 6.21) results in $b = 0.38 \pm 0.01$ and a smaller value of the square root of the cumulative squared residuum (Fig. 6.21 bottom) than the TLS saturation law. It is therefore close to the expected square root behaviour. The argument for such a "stretched root" saturation behaviour is the same as for the stretched exponential decay in the lifetime measurements in Section 6.5. The ensemble of emitters addressed by this measurement varies in dipole orientation, position in

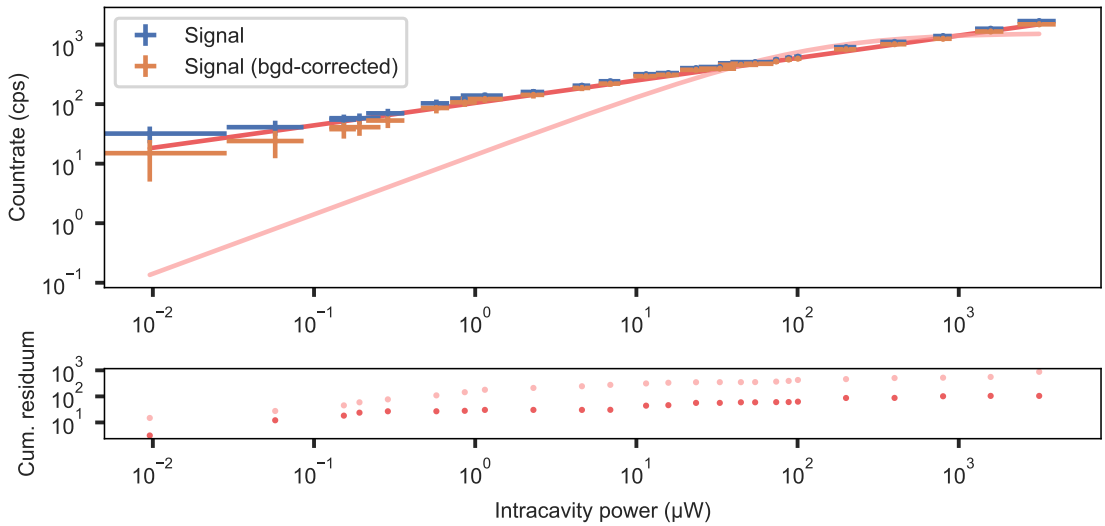

Figure 6.21: Saturation behaviour of NP3 at 20 K together with fits to the background-corrected data (orange) of a TLS saturation law given by Eq. 6.7.1 (light red) and a power law (dark red). The figure is adapted from [56]. The square root of the cumulative squared fit residuum for both saturation laws is depicted in the bottom panel. The blue datapoints show the measured 611 nm fluorescence countrate whereas the background countrate was subtracted for the orange datapoints.

the standing wave field maximum and potentially their homogeneous linewidths. Therefore, it is likely to observe a superposition of differently power broadenend linewidths.

Transient Spectral Hole Burning A TSHB measurement is a pump-probe laser spectroscopy experiment, where the first laser pulse saturates the optical transition and the second pulse probes the absorption or fluorescence. Sweeping the detuning of the probe pulse reveals a Lorentzian shape of the measured absorption or fluorescence and gives an upper bound of the homogeneous linewidth of the transition, $\gamma_h \leq 0.5\,\gamma_{hole} - \gamma_{laser}$ [189]. Here, γ_{laser} is the laser linewidth. In my case, I modify the TSHB technique to a CW measurement without distinct pump and probe pulses i.e. a standard saturation spectroscopy method. I use an electro-optic phase modulator[72] to generate a frequency comb structure from the 580 nm laser. By tuning the driving frequency of the modulator, the detuning between the comb teeth can be changed. At zero detuning, the full laser power is at the center wavelength and the 611 nm fluorescence signal is given as $I(P) = I_0\sqrt{N\,P_{tooth}}$, where N is the number of teeth in our comb. If a detuning $\Delta\omega_{comb} > \gamma_h$ is reached, each peak of the comb is saturating an independent sub-ensemble of ions and the total fluorescence signal sums up to $I(P) = I_0\,N\sqrt{P_{tooth}}$. Therefore, a contrast of $\sqrt{N}$

[72] *PM594*, Jenoptik

should be observed when sweeping the detuning from zero to several homogeneous linewidths and the countrate trace reveals the width of the transient hole γ_{hole}.

In order to detect a strong contrast in the countrate, N should be as high as possible. This can be achieved by concatenating several EOMs in a row as done by [191]. Since only a single EOM was available, it was driven with a sum of five tones to generate tens sidebands in addition to the carrier. The laser spectrum for a detuning of 5 MHz, recorded in transmission of our reference cavity, can be seen in Fig. 6.22. The laser spectrum reveals the disadvantage of this method, namely strongly varying intensities of the sidebands, despite optimizing the relative amplitudes and phases of the RF signal before.

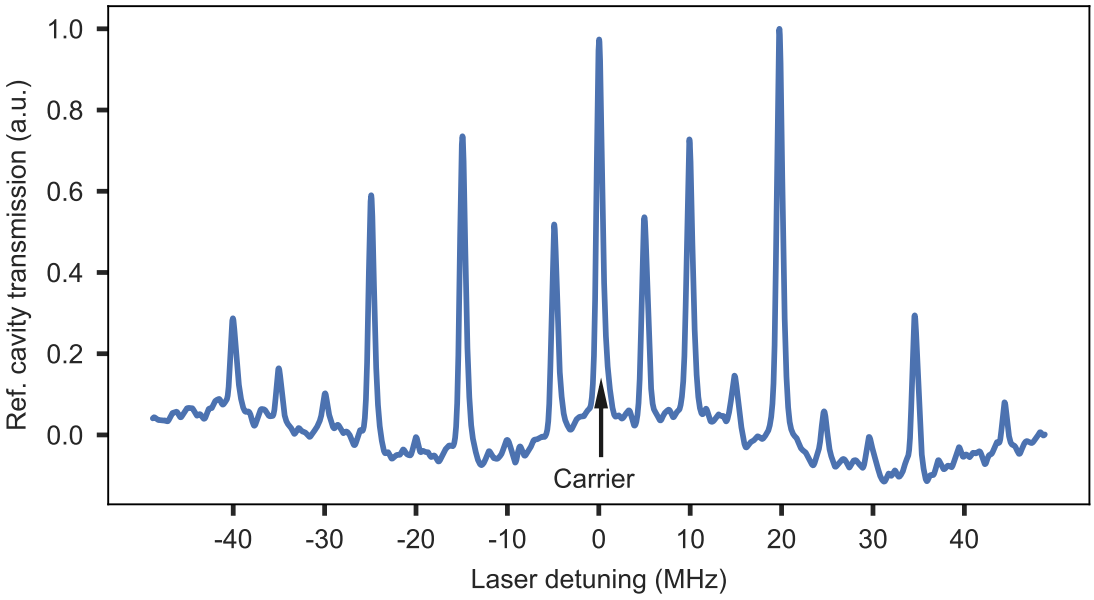

Figure 6.22: Laser spectrum of the frequency comb structure for the TSHB measurement generated by a phase EOM driven with a sum of five tones with 5 MHz detuning of each. The spectrum was recorded in transmission of the reference cavity with a resolution of 240 kHz limited by the cavity linewidth.

The transient spectral hole burning measurement for different power levels can be seen in Fig. 6.23. The measurements were done with the laser tuned to 580.854 nm at the inhomogeneous line center of NP3 at 4 K.

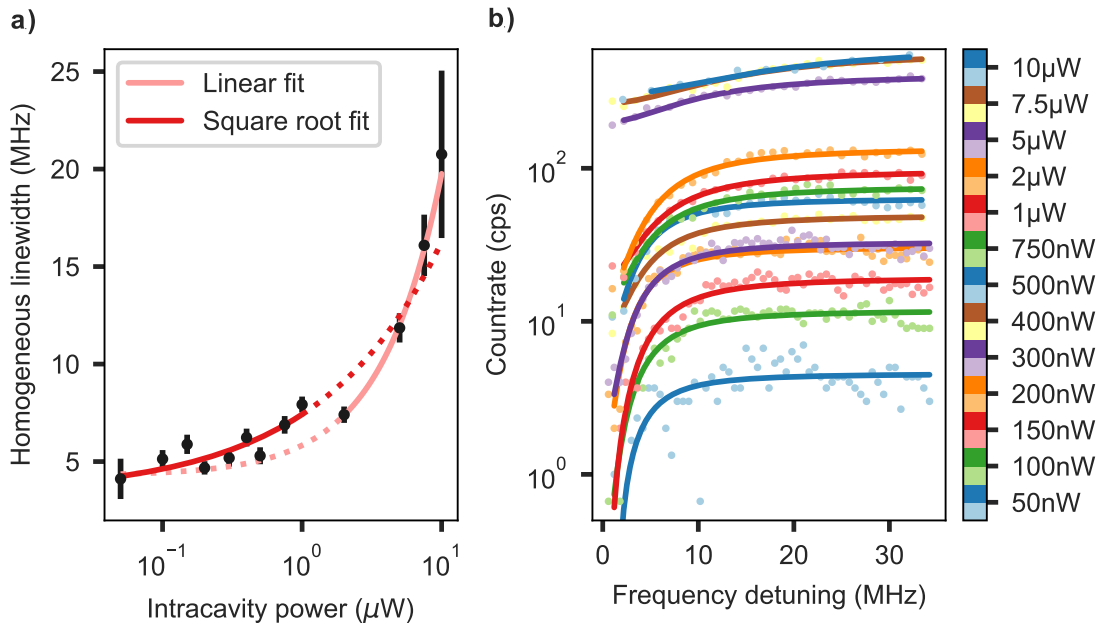

Figure 6.23: b): Transient spectral hole burning measurements at different intracavity power levels indicated by the respective colors together with inverted Lorentzian line fits (solid lines). The DR-scheme with collection of the 611 nm fluorescence was used. a): The widths obtained from the fits at each power in b) are then plotted against the intracavity power. The expected square root power broadening function is fitted to the datapoints (dark red) except of the four values for the highest powers. A linear function is fitted to the four datapoints of highest intracavity power (light red), where a temperature-broadening of the line is expected. The figure is adapted from [56].

An inverted Lorentzian line is fitted to the data for each power level and the hole width is extracted as the FWHM of the Lorentzian fit. The homogeneous linewidth is then calculated as $\gamma_h = 0.5\,\gamma_{hole} - \gamma_{laser} \approx 0.5\,\gamma_{hole}$, since the laser linewidth on the timescale of the transient hole is negligible, $\gamma_{laser} < 1\,\text{MHz}$. An upper bound for the homogeneous linewidth of the europium ions inside NP3 can be obtained from the offset parameter of the square root fit function $I_0\sqrt{P}+\Gamma_0$ in Fig. 6.23 a). A value of $\gamma_h = 3.3 \pm 0.6\,\text{MHz}$ or a coherence time of $T_2^* = 96 \pm 18\,\text{ns}$ is obtained. The linewidth is about an order of magnitude larger than the expected value of about $\gamma_h = 0.5\,\text{MHz}$ measured by [60]. The square root function does not fit to the datapoints of the four highest powers, so they were excluded for this fit. A linear fit matches the datapoints of the four highest powers quite well. This could hint to temperature broadening of the line caused by laser heating. For temperatures below 10 K the linewidth is approximately linear with temperature [60] and the relation between intracavity power and local temperature of the NP could be assumed to be linear in the first order.

However, in [155] strong differences in linewidths are reported for different Erbium-doped yttria nanoparticles. Therefore, it cannot be excluded that the broad linewidth is a property of just this particular nanoparticle. The precision and validity of this measurement is limited due to the inhomogeneous peak powers of the frequency comb and the low SNR for the lowest power levels and thus has to be improved in these respects in the future. To get a higher SNR a future measurement should use a $M \times N$ frequency comb to get a M-times higher overall countrate. This could be achieved by using two or more cascaded EOMs as it was done by [191].

6.8. cQED Parameters

The measurements described in the previous sections allow for the calculation of the most important cavity QED parameters of our cavity-emitter system. The lifetime measurements described in Sec. 6.5 allow for the determination of the rate $\gamma_{all} = 1/T_{1,fs}$ and the effective Purcell factors. The cavity linewidth κ can be determined using the finesse of 14,500 including the scattering losses from a 70 nm nanoparticle at the cavity length of $d_c = 5.8\,\mu$m of the DR-condition. The emitter dephasing rate γ_d is given by the upper bound on the homogeneous linewidth determined by TSHB in Sec. 6.7. Finally, the emitter-cavity coupling rate g, defined by Eq. 3.6.2, can be expressed in the following way using the expression for the mode volume of a Fabry-Pérot type cavity:

$$g = \sqrt{\zeta}\sqrt{\frac{3\,c\,\lambda^2}{2\pi^2\,w_0^2\,d_c T_{1,fs}}}. \tag{6.8.1}$$

I summarize the cQED parameters for the measured best case scenarios of the 580 nm and 611 nm transitions for a 70 nm nanoparticle and a free-space lifetime of $T_{1,fs} = 2.0$ ms in Tab. 6.2. The corresponding parameters for the bare cavity resonances at these two wavelengths can be found in Tab. C.1 in the appendix C.

In both cases cooperativities $C \ll 1$ are calculated and thus no coherent exchange of energy between the cavity mode and emitter is possible. For future

Parameter	g **(MHz)**	κ **(GHz)**	γ_{all} **(kHz)**	γ_d **(MHz)**	F_P^{eff}	C
$^5D_0 \rightarrow {}^7F_0$	$2\pi \cdot 0.4$	$2\pi \cdot 1.8$	$2\pi \cdot 0.08$	$2\pi \cdot 3.3$	3.4	$8 \cdot 10^{-5}$
$^5D_0 \rightarrow {}^7F_2$	$2\pi \cdot 2.4$	$2\pi \cdot 2.5$	$2\pi \cdot 0.08$	$2\pi \cdot 0.7 \cdot 10^6$	0.47	$5 \cdot 10^{-11}$

Table 6.2: Summary of the measured, best-case cavity QED parameters of a 70 nm nanoparticle and $T_{1,fs} = 2.0$ ms.

quantum information protocols it would be desirable to reach a cooperativity of $C \approx 1$. This allows e.g. to reflect a photon at the cavity dependent on the qubit state of the emitter and can be used to entangle qubits residing in different cavities as shown by Daiss et al. [125]. To reach this regime, several parameters would need to be improved in the following way: assuming a YSO crystal is used as host matrix showing twice the branching ratio of $\zeta_{YSO} = 0.016$ compared to yttria [67]. Then, it is supposed to find single emitters with good coherence and a linewidth of $\gamma_d = 50\,\mathrm{kHz}$ as measured in [64] at 2 K. Finally, fiber mirrors with a radius of curvature of $10\,\mu\mathrm{m}$ could be used and the cavity could be operated at the shortest possible length of around $2.5\,\mu\mathrm{m}$. Under these conditions $C \approx 1$ can be reached if the finesse could be increased to about $\mathcal{F} = 75,000$. Thus, if it would be possible to fabricate nanoparticles of around $40 - 50\,\mathrm{nm}$ diameter from YSO instead of yttria while preserving the good coherence properties, it should be feasible to reach a cooperativity of about one.

6.9. Single Ion Countrate Estimation

I close this chapter with an outlook on the single ion countrate, that can be expected with the current experimental setup. I am using the results on the cavity stability discussed in Chapter 5 and the results of cavity-enhanced spectroscopy of the previous sections to give a more accurate estimation of the signal from a single ion. I assume the best measured and therefore realistic parameters for the experiment as listed below:

- Cavity length jitter: $\sigma_z = 2.5\,\mathrm{pm}$
- Perfect dipole alignment: $\xi_{dipole} = 1$
- Ion at the standing wave field maximum $\xi_{field} = 1$ (for $d_{NP} \geq 40\,\mathrm{nm}$)
- Collection optics path transmission: $T_{path} = 0.8$
- Detector quantum efficiency: $\eta_{det} = 0.65$
- Excited state population of $p_{ex} = 50\%$ due to resonant but incoherent three-tone excitation pulse (independent of incomplete relaxation of excited state during detection window)
- Branching ratio: $\zeta_{580nm} = 0.007$ ($\zeta_{611nm} = 0.36$)
- Free-space lifetime: $T_{1,fs} = 2.0\,\mathrm{ms}$

Pulsed Measurement The detected fluorescence countrate for a pulsed experiment can be calculated as:

$$R_{det} = R_{pulsed}(d_{NP}) \cdot \eta_{out}(d_{NP}) \cdot T_{path} \cdot \eta_{det}, \tag{6.9.1}$$

with the outcoupling efficiency η_{out} defined in Tab. 3.1, which is dependent on the nanoparticle scattering losses, and the pulsed emission rate into the cavity mode given by:

$$R_{pulsed}(d_{NP}) = p_{ex} \cdot f_{rep} \cdot \frac{F_P^{eff}(d_{NP})}{F_P^{eff}(d_{NP}) + 1} \cdot \left(1 - e^{-\frac{F_P^{eff}(d_{NP})+1}{T_{1,fs}} t_{det}}\right). \tag{6.9.2}$$

Here, the repetition rate of the experiment is denoted as $f_{rep} = 1/(t_{ex}+t_{det})$ and the last term in the above equation takes into account the incomplete relaxation within the detection window t_{det}. In Fig. 6.24 the single ion countrate is calculated for a 70 nm nanoparticle when only the 580 nm fluorescence (blue) (611 nm (orange)) is collected and the sum of both rates if the cavity is kept at the double-resonance mode order. I assumed an excitation pulse duration of $t_{ex} = 1\,\mu$s and zero detuning between the cavity mode and the 611 nm transition, $\delta_{611nm} = 0$ GHz.

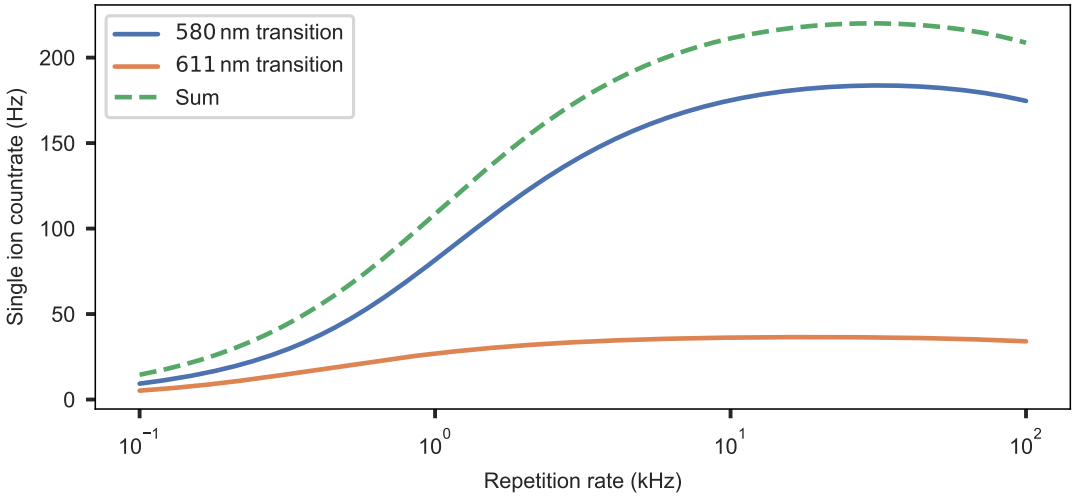

Figure 6.24: Estimation of the single ion countrate dependent on the repetition rate of a pulsed experiment adapted from [56]. Collecting only the 580 nm (611 nm) transition is depicted by the blue (orange) curve and the green curve shows the sum of both if the cavity is operated on the DR-condition.

The effective Purcell factor reached in this scenario is $F_P^{eff} = 3.2\,(0.46)$ for the 580 nm (611 nm) transition. Due to the weak Purcell effect on the 611 nm transition, not much signal is gained by additionally collecting the 611 nm fluorescence

in this pulsed experiment. Here, it would be more advantageous to perform this measurement with the fiber in contact with the mirror to reach a higher stability and shorter cavity length.

In Fig. 6.25 a) the pulsed 580 nm countrate is shown dependent on the repetition rate and additionally the nanoparticle diameter. For even smaller nanoparticles of diameter 40 nm a maximum effective Purcell factor of 3.7 is obtained and the repetition rate can be increased up to about 33 kHz. This could result in countrates up to 220 Hz. The detector has a dark countrate of 20 Hz, thus a standard deviation of $\sqrt{20}$ Hz $\approx$ 5 Hz assuming Poissonian statistics. The signal-to-noise ratio of such a measurement would then be about 40.

CW Measurement In Section 6.4 high resolution laser scans under CW excitation and collection of only the 611 nm fluorescence were presented. In Fig. 6.25 b) an estimation of the single ion countrate is depicted that can be expected from such a measurement. The CW countrate is calculated by replacing R_{pulsed} in Eq. 6.9.1 by:

$$R_{cw}(d_{NP}, \delta_{611nm}) = p_{ex} \cdot \frac{F_P^{eff}(d_{NP}, \delta_{611nm})}{T_{1,fs}}. \tag{6.9.3}$$

I assume again $p_{ex} = 0.5$ and a three-tone excitation sequence matching the HF-level splittings of one of the europium isotopes. The dependence of the countrate of the detuning between the cavity and 611 nm lines was taken into account since this can vary strongly between different nanoparticles due to a difference in the local mirror dispersion. In the best case, one gets an effective Purcell factor of 0.46 and a single ion countrate of up to 40 Hz i.e. a signal-to-noise ratio of 8. The background corrected countrates observed in the laser scans in Section 6.4 match the estimation performed here. Thus, from a signal-to-noise perspective it should be possible to detect single ion signals also with this method.

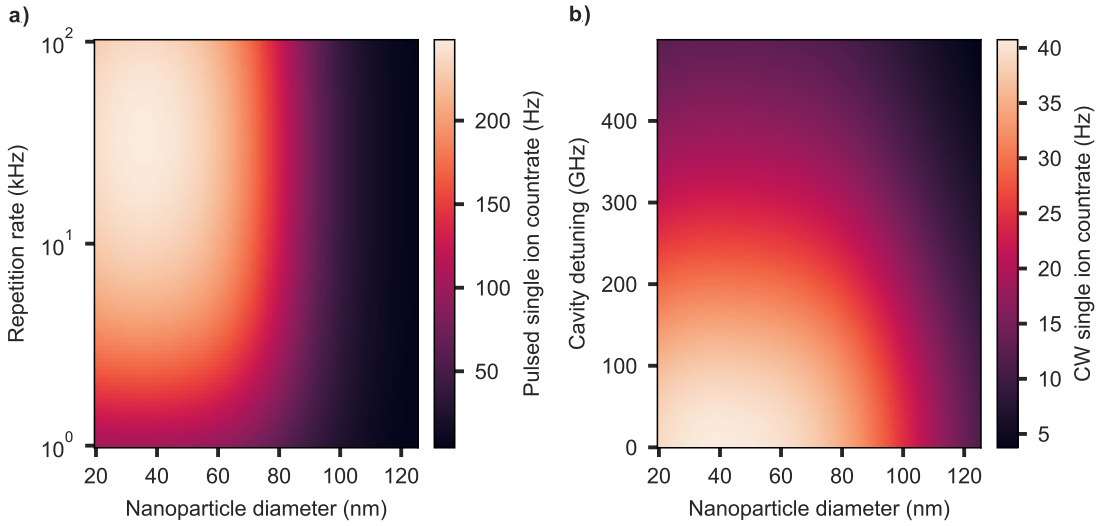

Figure 6.25: a): Estimation of single ion countrates for a pulsed measurement only collecting the 580 nm fluorescence dependent on the repetition rate of the experiment and the nanoparticle diameter. This figure is adapted from [56]. b): Countrate for a CW measurement collecting just the 611 nm fluorescence as a function of the detuning between the cavity mode and 611 nm transition and the diameter of the nanoparticle.

7. Conclusion and Outlook

The consortium of the European Union Quantum Flagship project SQUARE, which my work was part of, laid out the vision of using individual rare-earth ions doped into nanoscale solid-state hosts to build a quantum processor node [37]. Among the various REI species which were considered, europium ions play a key role due to their exceptional long spin coherence time [57], which could be harnessed as memory and gate qubit, whereas e.g. erbium ions could serve as communication and readout qubits due to their optical transition in the telecom band. In order to approach this goal, I incorporated europium-doped yttria nanoparticles inside a cryogenic, fiber-based Fabry-Pérot microcavity in order to enhance the low spontaneous emission rates and work towards optically detecting single ions.

Distributing Yttria Nanoparticles on Cavity Mirrors The first step towards cavity-enhanced spectroscopy, was to create a spatially homogeneous distribution of well-dispersed (in terms of the cavity mode size) individual nanoparticles on the surface of a cavity mirror. Spin-coating recipes used by my predecessor proved to be not reproducible to distribute the smaller 60 nm nanoparticles on the mirror. Therefore, I established a new method by aerosol printing a water-SDS-nanoparticle colloidal solution onto predefined regions on the cavity mirror. After optimizing the printing parameters, it was possible to obtain about 25% single, isolated nanoparticles, which was evaluated using SEM images. The printed cavity mirrors were characterized in terms of the spatial distribution and spectral properties of the nanoparticles using different techniques. A "free-space" optical excited lifetime of $T_{1,opt} = 2.0 \pm 0.1$ ms could be measured for nanoparticles residing on a cavity mirror.

Although proven successful in many respects, the method could be further refined in a future sample preparation run. Different surfactants could be tested to find a better stabilization of the colloidal solution taking into account measurements of the zeta potential. The origin of residuals on the mirror surface, which appear as cavity mode size limited dark spots on the scanning cavity images, should be found in order to avoid those and speed up the search for appropriate nanopar-

ticles. Another way of simplifying the search of nanoparticles inside the cavity would be to pick and place individual nanoparticles using the AFM cantilever. This method is very time consuming but a precise placement of arrays of well-separated nanoparticles on a planar cavity mirror would speed up the search in a later step.

Cavity Length Stability Under Cryogenic Conditions A new flow cryostat system was set up and its performance was tested. The flow cryostat design including an exchange gas sample chamber aims for low noise operation of the cavity stage while providing a good thermalization of the nanoparticles due to the helium exchange gas. Placing the cavity stage inside a flow cryostat, I achieved a RMS cavity length stability of 2.5(5) pm with (without) active stabilization leading to a finesse-limited cavity performance, a long-awaited goal. Bringing the fiber into contact with the planar mirror further increases the stability and a value of about 0.8 pm was measured even without active stabilization. In order to perform more sophisticated cavity-enhanced spectroscopy measurements, the software package PyRPL, controlling a fast FPGA hardware for digital signal processing, was adapted to our needs. It provides a sequenced, cascaded, closed-loop feedback mechanism tailored for our cavity stage design, which includes two piezo stacks to control the cavity length. The cavity control was then incorporated into a larger, flexible software architecture to control many devices needed for the measurement. This became necessary since data acquisiton should only take place when the cavity is on resonance, which requires a careful monitoring of the latter over long timescales in a noisy lab environment.

Although the cavity length stability suffices for first measurements, a vibration isolation platform could be incorporated to further reduce the noise from the cryostat cold plate. As done for the cavity setup inside the closed-cycle cryostat of the group [166], one could put the main frame of the cavity stage onto posts intercepted by steel springs. Furthermore, the high contact mode stability would permit to scale up the cavity finesse in the future to values of about 150,000, which would be at the limits of the coating properties. As can be seen in Fig. 7.1a) even at such high finesses, the cavity performance would not be limited by mechanical vibrations. The software automation of the measurement routine could be extended to provide a control over the locking status of the laser frequency stabilization as well as compensate for drifts of the cavity fiber due to piezo creep. A whole protocol of different types of measurements could be run autonomous to find single emitters by laser scans and characterize their properties such as the lifetime, homogeneous linewidth and autocorrelation function.

Cavity-enhanced Spectroscopy Over the course of this work, I investigated six different nanoparticles with sizes ranging from 70 nm to 95 nm. PLE laser scans of the inhomogeneous lines were recorded and FWHM linewidths in the range from 50 GHz to 150 GHz were observed. Some substructure within the inhomogeneous lines is visible but laser scans at lower powers and longer averaging times did not show reproducible spectral features. The optical lifetimes of small ensembles were determined for every particle and resulted in effective Purcell factors around 1 for the $^5D_0 \rightarrow {}^7F_0$ transition at 580 nm and about 0.5 for the spectrally broad $^5D_0 \rightarrow {}^7F_2$ transition at 611 nm. Both values, within their errors, are close to the theoretically predicted, ensemble-averaged Purcell factors which are approximately a factor of three lower than the maximal expected Purcell enhancement for a single ion with a good coupling to the cavity field. Further spectral properties were measured inside the cavity such as the presence of optical pumping for temperatures below 10 K and a pulse sequence to repump the population was demonstrated. These insights become important when addressing single ions since optical pumping must be avoided in this case. Using transient spectral hole burning, an upper bound of about 3.3 MHz of the homogeneous linewidth could be estimated. However, the TSHB measurement presented here is far from being optimized regarding the homogeneity of the excitation frequency comb as well as the signal-to-noise ratio. Nevertheless, these findings are important steps towards single ion spectroscopy since a better knowledge of spectral parameters facilitates the search for the right parameters to observe spectral lines of single ions. An estimation of the countrate for a single ion assuming the cavity parameters and performance presented in this thesis resulted in 240(80) Hz with (without) 3-pulse excitation of all HF-levels for a 70 nm nanoparticle.

This single ion countrate could be further improved by several measures, which result in countrates plotted in Fig. 7.1b) using Eq. 6.9.1:

- Using a fiber profile with only 10 µm radius of curvature leading to a mode waist of about 0.9 µm.
- Contact mode with a length stability of 0.8 pm as well as shortest possible cavity length of about 2.5 µm.
- Finding a smaller nanoparticle of 50 nm diameter, which should be within the size distribution of the currently used batch (leading to scattering losses of $S_{NP} = 10$ ppm for $w_0 = 0.9$).
- Annealing both mirror coatings to reduce the absorption losses to about 10 ppm.
- Deploy the 3-pulse excitation scheme to address all HF-levels and get a 50% excitation probability (incoherent excitation i.e. no π-pulse assumed).

Under these circumstances effective Purcell factors of up to 27 can be reached. However, optimizing the mirror coating for the best single ion countrate doesn't lead to this maximal Purcell-effect. This is due to the outcoupling efficiency which comes into play for the simulation of the countrate. A maximum countrate of about 600 Hz can be reached with a single-digit ppm transmission value for the fiber mirror and about 125 ppm transmission of the planar mirror. Then, a cavity finesse of only 25,000 and outcoupling efficiency of 51% is achieved, resulting in an effective Purcell factor of 14.

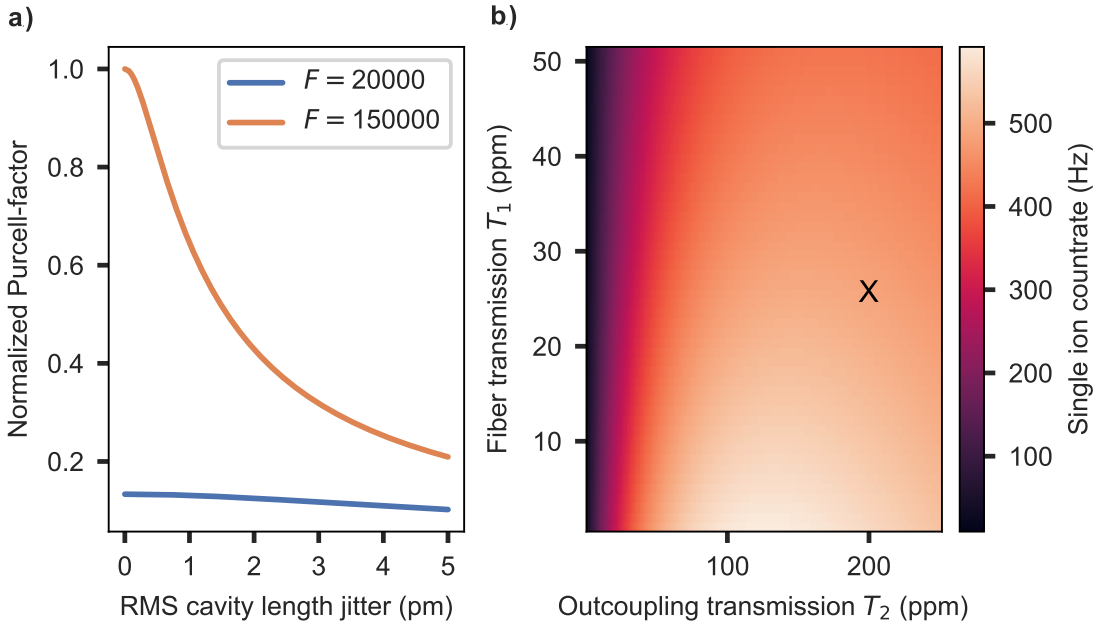

Figure 7.1: a): Normalized Purcell factor dependent on the RMS cavity length jitter for a finesse of 20,000 (blue) and 150,000 (orange). The contact mode stability of 0.8 pm reached within this work would still yield a finesse-limited cavity performance at highest possible finesses. b): Estimated single ion countrate for a pulsed spectroscopy of the 580 nm transition dependent on the mirror coating transmissions. The coatings are assumed to have reduced absorption losses of 10 ppm each due to annealing. The cavity geometry is defined by a fiber profile with 10 µm radius of curvature resulting in a mode waist of 0.9 µm at shortest possible cavity length of about 2.5 µm. Furthermore, a nanoparticle diameter of 50 nm as well as a 3-pulse excitation leading to 50% excitation propability per shot is considered. The black cross denotes the mirror transmissions of the coating used within this work.

Appendices

A. Pick and Place of a Single Nanoparticle

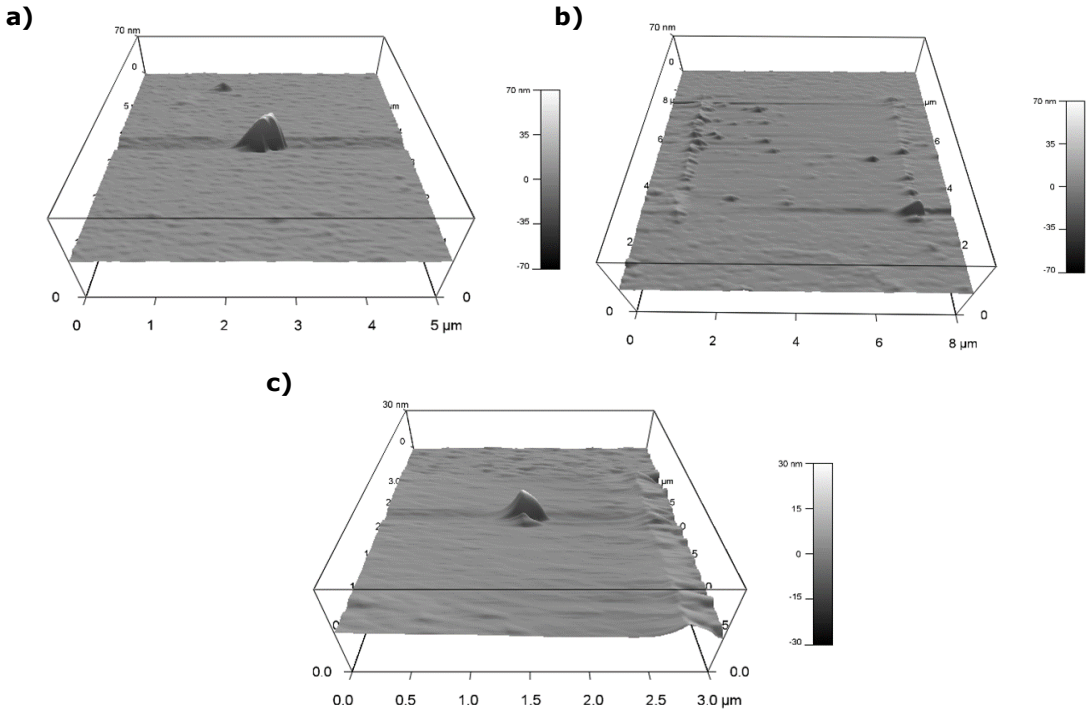

Figure A.1: Atomic force microscopy images of a single nanoparticle pick and place procedure using the AFM cantilever. Image a) shows an AFM tapping mode scan of a single nanoparticle on a cavity mirror. In b) the NP was picked up by the cantilever using the contact mode and a scan of a slightly larger area than in a) was performed in tapping mode with the NP being stuck on the cantilever. Scanning the cantilever again in contact mode over a small area of $100 \times 100\,\mathrm{nm}^2$ places the NP on the desired location on the mirror surface. This could be confirmed by a tapping mode scan of the nanoparticle shown in c). Note that the contact mode scan to pick up the nanoparticle cleared the scanning area from some molecular dirt on the mirror surface (likely stemming from a mirror annealing in a dirty oven) seen as little hills in b). The last scan in c) reveals a smaller height of the NP of only about 30 nm, which could be attributed to a different orientation of the NP after the pick and place procedure.

B. Inhomogeneous Line of NP5 During a Cooldown

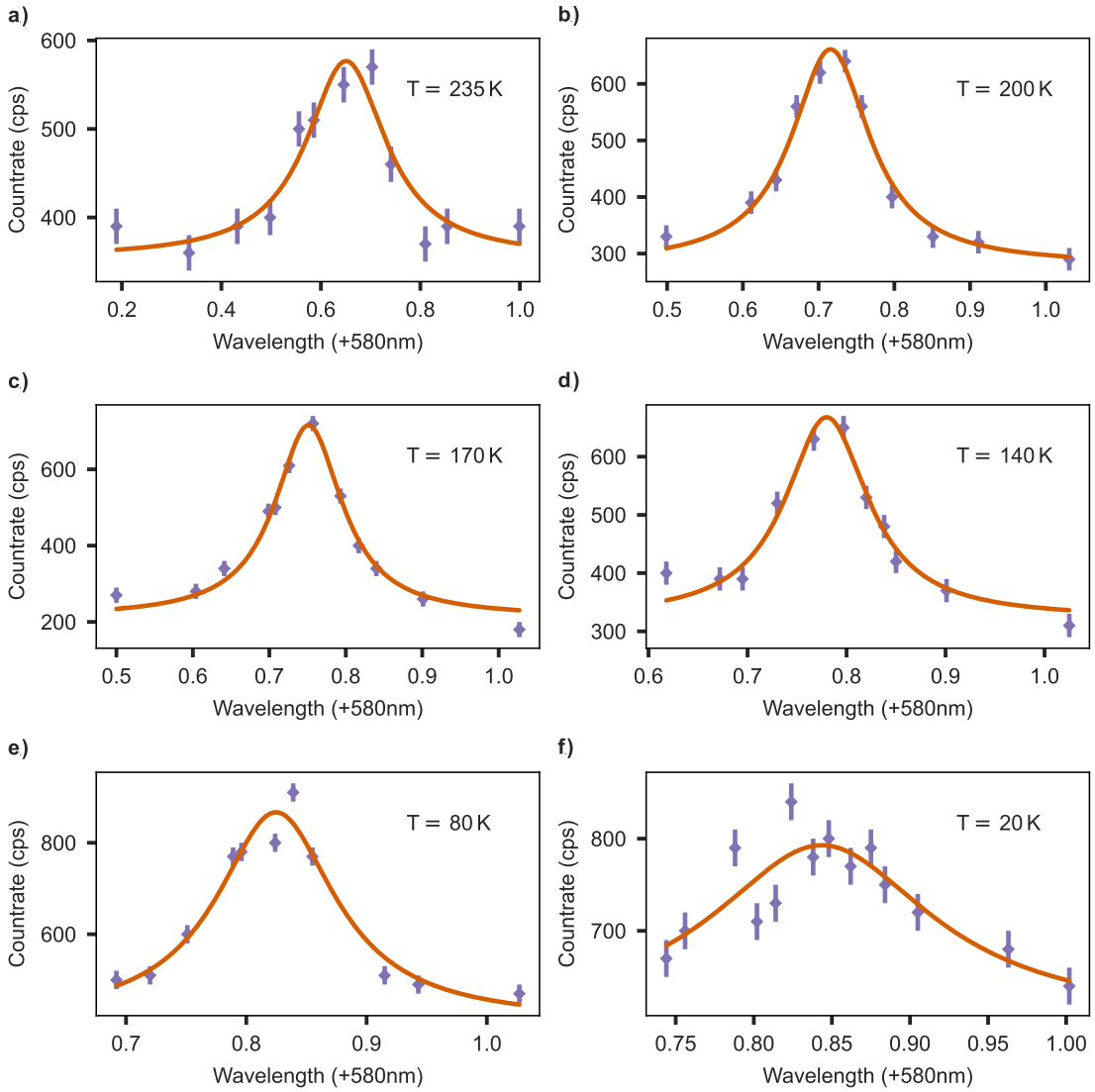

Figure B.2: Full set of the inhomogeneous line of NP5 during a cooldown from 235 K to 20 K. The red line depicts the fit of a Lorentzian line to the data to extract the FWHM and center position for the plots in Fig. 6.5.

C. Overview of the Cavity Parameters

Parameter	Symbol	580 nm Resonance	611 nm Resonance
Cavity finesse	$\mathcal{F}$	$17,500$	$9,500$
Optical cavity length	d	$5.8\,\mu m$	$5.8\,\mu m$
Cavity quality factor	Q	$350,000$	$180,500$
Cavity linewidth	$\delta\nu$	$1.5\,GHz$	$2.7\,GHz$
Cavity decay rate	κ	$9.3\,GHz$	$17.1\,GHz$
Cavity ringdown time	τ_c	$108\,ps$	$58\,ps$
Beam waist	w_0	$1.3\,\mu m$	$1.3\,\mu m$
Mode Volume	V_m	$7.7\,\mu m^3$	$7.7\,\mu m^3$
Purcell factor	F_P	675	406

Table C.1: Overview of the relevant cavity parameters for an empty cavity operated at the double-resonance of the wavelengths 580 nm and 611 nm used for the measurements presented in Chapter 6.

D. Publications and conference contributions

Publications

1. *A highly stable and fully tunable open microcavity platform at cryogenic temperatures*
   M. Pallmann, T. Eichhorn, J. Benedikter, B. Casabone, T. Hümmer, D. Hunger
   APL Photonics (2022) [166]

2. *Cavity-mediated collective emission from few emitters in a diamond membrane*
   M. Pallmann, K. Köster, Y. Zhang, J. Heupel, T. Eichhorn, C. Popov, K. Mølmer, D. Hunger
   Phys. Rev. X (2024) [192]

3. *Multimodal Purcell enhancement and optical coherence of Eu^{3+} ions in a single nanoparticle coupled to a microcavity*
   T. Eichhorn, N. L. Jobbitt, S. Bieling, S. Liu, T. Krom, D. Serrano, R. Huber, U. Lemmer, H. de Riedmatten, P. Goldner, D. Hunger
   arXiv (2024) [56], submitted to Nanophotonics

Conference Contributions

1. *Cavity-enhanced Spectroscopy of a Few-ion Ensemble in Eu^{3+} : Y_2O_3* (Poster)
   DPG Frühjahrstagung der Sektion AMOP
   Rostock, Germany, March 2019

2. *Towards Cavity-enhanced Spectroscopy of Single Europium Ions* (Talk)
   Summerschool SQUARE Project
   Karlsruhe, Germany, July 2019

3. *Towards Quantum Computing with Rare Earth Ions* (Talk)
   Optics & Photonics Seminar
   Karlsruhe, Germany, July 2019

4. *Towards Quantum Computing with Rare Earth Ions* (Talk)
   Quantum Futur Akademie
   Karlsruhe, Germany, August 2019

5. *Cavity-enhanced Spectroscopy of a Few-ion Ensemble in Eu^{3+} : Y_2O_3* (Poster)
   Karlsruher Days of Optics & Photonics (KDOP)
   Karlsruhe, Germany, September 2019

6. *Cavity-enhanced Spectroscopy of a Few-ion Ensemble in Eu^{3+} : Y_2O_3* (Poster)
   DPG Fall Meeting
   Freiburg, Germany, September 2019

7. *Cavity-enhanced Spectroscopy of a Few-ion Ensemble in Eu^{3+} : Y_2O_3* (Poster)
   Summerschool on Quantum Light Sources
   Erice, Italy, October 2019

8. *Cavity-enhanced Spectroscopy of a Few-ion Ensemble in Eu^{3+} : Y_2O_3* (Poster)
   Rare Earth Ion Doped Crystals for Quantum Information Workshop
   Grenoble, France, October 2019

9. *Die Quantenzitrone - ambigue Weltbilder in Physik und Kunst(pädagogik)* (Talk)
   Landau Lectures on Art
   Landau, Germany, June 2021

10. *Towards Cavity-enhanced Spectroscopy of Single Europium Ions* (Talk)
    Rare Earth Ion Doped Crystals for Quantum Information Workshop
    Bad Honnef, Germany, August 2021

11. *Cryogenic Fiber-based Fabry-Pérot Microcavities* (Talk)
    DPG Frühjahrstagung der Sektion AMOP

Erlangen (online), Germany, March 2022

12. *Cavity-enhanced Spectroscopy of Rare Earth Ion Doped Nanomaterials* (joined Talk with Jannis Hessenauer)
    Rare Earth Ion Doped Crystals for Quantum Information Workshop
    Edinburgh, United Kingdom, June 2022

13. *Towards Cavity-enhanced Spectroscopy of Single Europium Ions* (Invited talk)
    Seminar of the group of Prof. W. Tittel
    Geneva, Switzerland, September 2022

14. *Towards Cavity-enhanced Spectroscopy of Single Europium Ions* (Talk)
    APD March Meeting
    Las Vegas, United States of America, March 2023

15. *Spectroscopy and Cavity-enhanced Emission Europium-based Solid State and Molecular Systems* (joined Talk with Evgenij Vasilenko)
    Rare Earth Ion Doped Crystals for Quantum Information Workshop
    Lund, Sweden, September 2023

16. *Towards Cavity-enhanced Spectroscopy of Single Europium Ions in Yttria Nanocrystals* (Talk)
    DPG Frühjahrstagung der Sektion AMOP
    Freiburg, Germany, March 2024

References

[1] C. Monroe, D. M. Meekhof, B. E. King, W. M. Itano, and D. J. Wineland, "Demonstration of a Fundamental Quantum Logic Gate", *Physical Review Letters*, vol. 75, no. 25, pp. 4714–4717, 1995.

[2] C. Monroe, D. M. Meekhof, B. E. King, and D. J. Wineland, "A "Schrödinger Cat" Superposition State of an Atom", *Science*, vol. 272, no. 5265, pp. 1131–1136, 1996.

[3] J. Pii. "Chinese Quantum Companies and National Strategy 2023". TheQuantumInsider, Ed. (2023), [Online]. Available: `https://thequantuminsider.com/2023/04/13/chinese-quantum-companies-and-national-strategy-2023/` (visited on 08/31/2024).

[4] EuropeanUnion, Ed. "New Strategic Research Agenda on Quantum technologies". (2020), [Online]. Available: `https://digital-strategy.ec.europa.eu/en/news/new-strategic-research-agenda-quantum-technologies` (visited on 08/31/2024).

[5] M. A. Nielsen and L. Chuang, *Quantum Computation and Quantum Information*. Cambridge University Press, 2010.

[6] D. P. DiVincenzo, "Two-bit gates are universal for quantum computation", *Physical Review A*, vol. 51, no. 2, pp. 1015–1022, 1995.

[7] D. P. DiVincenzo, "The Physical Implementation of Quantum Computation", *Fortschritte der Physik*, vol. 48, no. 9-11, pp. 771–783, 2000.

[8] H. J. Kimble, "The quantum internet", *Nature*, vol. 453, no. 7198, pp. 1023–1030, 2008.

[9] EuropeanUnion, Ed. "The European Quantum Communication Infrastructure (EuroQCI) Initiative". (2024), [Online]. Available: `https://digital-strategy.ec.europa.eu/en/policies/european-quantum-communication-infrastructure-euroqci` (visited on 08/31/2024).

[10] P. Shor, "Algorithms for quantum computation: Discrete logarithms and factoring", in *Proceedings 35th Annual Symposium on Foundations of Computer Science*, Santa Fe, NM, USA: IEEE Comput. Soc. Press, 1994, pp. 124–134.

[11] L. K. Grover, "Quantum Mechanics Helps in Searching for a Needle in a Haystack", *Physical Review Letters*, vol. 79, no. 2, pp. 325–328, 1997.

[12] E. Grumbling and M. Horowitz, *Quantum Computing: Progress and Prospects*. National Academies Press, 2019.

[13] J. I. Cirac and P. Zoller, "Quantum Computations with Cold Trapped Ions", *Physical Review Letters*, vol. 74, no. 20, pp. 4091–4094, 1995.

[14] F. Schmidt-Kaler, H. Häffner, M. Riebe, *et al.*, "Realization of the Cirac–Zoller controlled-NOT quantum gate", *Nature*, vol. 422, no. 6930, pp. 408–411, 2003.

[15] N. A. Gershenfeld and I. L. Chuang, "Bulk Spin-Resonance Quantum Computation", *Science*, vol. 275, no. 5298, pp. 350–356, 1997.

[16] M. Kjaergaard, M. E. Schwartz, J. Braumüller, *et al.*, "Superconducting Qubits: Current State of Play", *Annual Review of Condensed Matter Physics*, vol. 11, no. 1, pp. 369–395, 2020.

[17] C. Monroe, "Quantum information processing with atoms and photons", *Nature*, vol. 416, no. 6877, pp. 238–246, 2002.

[18] J. Schmiedmayer, R. Folman, and T. Calarco, "Quantum information processing with neutral atoms on an atom chip", *Journal of Modern Optics*, vol. 49, no. 8, pp. 1375–1388, 2002.

[19] J. L. O'Brien, G. J. Pryde, A. G. White, T. C. Ralph, and D. Branning, "Demonstration of an all-optical quantum controlled-NOT gate", *Nature*, vol. 426, no. 6964, pp. 264–267, 2003.

[20] F. Flamini, N. Spagnolo, and F. Sciarrino, "Photonic quantum information processing: A review", *Reports on Progress in Physics*, vol. 82, no. 1, p. 016 001, 2019.

[21] C. Becher, W. Gao, S. Kar, *et al.*, "2023 roadmap for materials for quantum technologies", *Materials for Quantum Technology*, vol. 3, no. 1, p. 012 501, 2023.

[22] D. D. Awschalom, R. Hanson, J. Wrachtrup, and B. B. Zhou, "Quantum technologies with optically interfaced solid-state spins", *Nature Photonics*, vol. 12, no. 9, pp. 516–527, 2018.

[23] J. J. Pla, K. Y. Tan, J. P. Dehollain, *et al.*, "High-fidelity readout and control of a nuclear spin qubit in silicon", *Nature*, vol. 496, no. 7445, pp. 334–338, 2013.

[24] D. B. Higginbottom, A. T. K. Kurkjian, C. Chartrand, *et al.*, "Optical observation of single spins in silicon", *Nature*, vol. 607, no. 7918, pp. 266–270, 2022.

[25] T. Van Der Sar, T. H. Taminiau, and R. Hanson, "Diamond-based quantum technologies", *Photoniques*, no. 107, pp. 44–48, 2021.

[26] C. E. Bradley, J. Randall, M. H. Abobeih, *et al.*, "A Ten-Qubit Solid-State Spin Register with Quantum Memory up to One Minute", *Physical Review X*, vol. 9, no. 3, p. 031 045, 2019.

[27] M. H. Abobeih, Y. Wang, J. Randall, *et al.*, "Fault-tolerant operation of a logical qubit in a diamond quantum processor", *Nature*, vol. 606, no. 7916, pp. 884–889, 2022.

[28] C. Toninelli, I. Gerhardt, A. S. Clark, *et al.*, "Single organic molecules for photonic quantum technologies", *Nature Materials*, vol. 20, no. 12, pp. 1615–1628, 2021.

[29] S. L. Bayliss, D. W. Laorenza, P. J. Mintun, B. D. Kovos, D. E. Freedman, and D. D. Awschalom, "Optically addressable molecular spins for quantum information processing", *Science*, vol. 370, no. 6522, pp. 1309–1312, 2020.

[30] D. Loss and D. P. DiVincenzo, "Quantum computation with quantum dots", *Physical Review A*, vol. 57, no. 1, pp. 120–126, 1998.

[31] M. Veldhorst, C. H. Yang, J. C. C. Hwang, *et al.*, "A two-qubit logic gate in silicon", *Nature*, vol. 526, no. 7573, pp. 410–414, 2015.

[32] N. Ohlsson, R. Krishna Mohan, and S. Kröll, "Quantum computer hardware based on rare-earth-ion-doped inorganic crystals", *Optics Communications*, vol. 201, no. 1-3, pp. 71–77, 2002.

[33] J. H. Wesenberg, K. Mølmer, L. Rippe, and S. Kröll, "Scalable designs for quantum computing with rare-earth-ion-doped crystals", *Physical Review A*, vol. 75, no. 1, p. 012 304, 2007.

[34] L. Rippe, B. Julsgaard, A. Walther, Y. Ying, and S. Kröll, "Experimental quantum-state tomography of a solid-state qubit", *Physical Review A*, vol. 77, no. 2, p. 022 307, 2008.

[35] A. Walther, L. Rippe, Y. Yan, *et al.*, "High-fidelity readout scheme for rare-earth solid-state quantum computing", *Physical Review A*, vol. 92, no. 2, p. 022 319, 2015.

[36] R. L. Ahlefeldt, M. J. Pearce, M. R. Hush, and M. J. Sellars, "Quantum processing with ensembles of rare-earth ions in a stoichiometric crystal", *Physical Review A*, vol. 101, no. 1, p. 012 309, 2020.

[37] A. Kinos, D. Hunger, R. Kolesov, *et al.*, "Roadmap for Rare-earth Quantum Computing", *arXiv*, 2021.

[38] A. Kinos, L. Rippe, D. Serrano, A. Walther, and S. Kröll, "High-connectivity quantum processor nodes using single-ion qubits in rare-earth-ion-doped crystals", *Physical Review A*, vol. 105, no. 3, p. 032 603, 2022.

[39] R. Kolesov, K. Xia, R. Reuter, *et al.*, "Optical detection of a single rare-earth ion in a crystal", *Nature Communications*, vol. 3, no. 1, p. 1029, 2012.

[40] P. Siyushev, K. Xia, R. Reuter, *et al.*, "Coherent properties of single rare-earth spin qubits", *Nature Communications*, vol. 5, no. 1, p. 3895, 2014.

[41] T. Utikal, E. Eichhammer, L. Petersen, A. Renn, S. Götzinger, and V. Sandoghdar, "Spectroscopic detection and state preparation of a single praseodymium ion in a crystal", *Nature Communications*, vol. 5, no. 1, p. 3627, 2014.

[42] I. Nakamura, T. Yoshihiro, H. Inagawa, S. Fujiyoshi, and M. Matsushita, "Spectroscopy of single Pr3+ ion in LaF3 crystal at 1.5 K", *Scientific Reports*, vol. 4, no. 1, p. 7364, 2014.

[43] E. Eichhammer, T. Utikal, S. Götzinger, and V. Sandoghdar, "Spectroscopic detection of single Pr3+ ions on the 3H4-1D2 transition", *New Journal of Physics*, vol. 17, no. 8, p. 083 018, 2015.

[44] A. M. Dibos, M. Raha, C. M. Phenicie, and J. D. Thompson, "Atomic Source of Single Photons in the Telecom Band", *Physical Review Letters*, vol. 120, no. 24, p. 243 601, 2018.

[45] T. Zhong, J. M. Kindem, J. G. Bartholomew, *et al.*, "Optically Addressing Single Rare-Earth Ions in a Nanophotonic Cavity", *Physical Review Letters*, vol. 121, no. 18, p. 183 603, 2018.

[46] J. M. Kindem, A. Ruskuc, J. G. Bartholomew, J. Rochman, Y. Q. Huan, and A. Faraon, "Control and single-shot readout of an ion embedded in a nanophotonic cavity", *Nature*, vol. 580, no. 7802, pp. 201–204, 2020.

[47] T. Kornher, D.-W. Xiao, K. Xia, *et al.*, "Sensing Individual Nuclear Spins with a Single Rare-Earth Electron Spin", *Physical Review Letters*, vol. 124, no. 17, p. 170 402, 2020.

[48] K. Xia, F. Sardi, C. Sauerzapf, *et al.*, "Tunable microcavities coupled to rare-earth quantum emitters", *Optica*, vol. 9, no. 4, p. 445, 2022.

[49] A. Ulanowski, B. Merkel, and A. Reiserer, "Spectral multiplexing of telecom emitters with stable transition frequency", *Science Advances*, vol. 8, no. 43, 2022.

[50] C. Deshmukh, E. Beattie, B. Casabone, *et al.*, "Detection of single ions in a nanoparticle coupled to a fiber cavity", *Optica*, vol. 10, no. 10, p. 1339, 2023.

[51] M. Takezawa, R. Suzuki, J. Takahashi, *et al.*, "Room-temperature addressing of single rare-earth atoms in optical fiber", *Physical Review Applied*, vol. 20, no. 4, p. 044 038, 2023.

[52] K. Reinhardt, "Seltene Erden", *Chemie in unserer Zeit*, no. 18, pp. 24–34, 1984.

[53] E.-A. Demarcay, "Sur un nouvel élément l'europium.", *Comptes rendus hebdomadaires des séances de l'Académie des sciences*, no. 132, pp. 1484–1486, 1901.

[54] P. Goldner, A. Ferrier, and O. Guillot-Noël, *Rare Earth-Doped Crystals for Quantum Information Processing*. Elsevier, 2015, vol. 46, pp. 1–78.

[55] K. Binnemans, "Interpretation of europium(III) spectra", *Coordination Chemistry Reviews*, vol. 295, pp. 1–45, 2015.

[56] T. Eichhorn, N. Jobbitt, S. Bieling, *et al.*, "Multimodal Purcell enhancement and optical coherence of Eu^{3+} ions in a single nanoparticle coupled to a microcavity", *arXiv preprint arXiv:2412.06576*, 2024.

[57] M. Zhong, M. P. Hedges, R. L. Ahlefeldt, *et al.*, "Optically addressable nuclear spins in a solid with a six-hour coherence time", *Nature*, vol. 517, no. 7533, pp. 177–180, 2015.

[58] B. Merkel, A. Ulanowski, and A. Reiserer, "Coherent and Purcell-Enhanced Emission from Erbium Dopants in a Cryogenic High- Q Resonator", *Physical Review X*, vol. 10, no. 4, p. 041 025, 2020.

[59] A. Perrot, P. Goldner, D. Giaume, *et al.*, "Narrow Optical Homogeneous Linewidths in Rare Earth Doped Nanocrystals", *Physical Review Letters*, vol. 111, no. 20, p. 203 601, 2013.

[60] J. G. Bartholomew, K. De Oliveira Lima, A. Ferrier, and P. Goldner, "Optical Line Width Broadening Mechanisms at the 10 kHz Level in Eu^{3+} :Y_2O_3 Nanoparticles", *Nano Letters*, vol. 17, no. 2, pp. 778–787, 2017.

[61] D. Serrano, J. Karlsson, A. Fossati, A. Ferrier, and P. Goldner, "All-optical control of long-lived nuclear spins in rare-earth doped nanoparticles", *Nature Communications*, vol. 9, no. 1, p. 2127, 2018.

[62] S. Liu, D. Serrano, A. Fossati, A. Tallaire, A. Ferrier, and P. Goldner, "Controlled size reduction of rare earth doped nanoparticles for optical quantum technologies", *RSC Advances*, vol. 8, no. 65, pp. 37 098–37 104, 2018.

[63] S. Liu, A. Fossati, D. Serrano, A. Tallaire, A. Ferrier, and P. Goldner, "Defect Engineering for Quantum Grade Rare-Earth Nanocrystals", *ACS Nano*, vol. 14, no. 8, pp. 9953–9962, 2020.

[64] A. Fossati, D. Serrano, S. Liu, A. Tallaire, A. Ferrier, and P. Goldner, "Optical line broadening mechanisms in rare-earth doped oxide nanocrystals", *Journal of Luminescence*, vol. 263, p. 120 050, 2023.

[65] J. Karlsson, N. Kunkel, A. Ikesue, A. Ferrier, and P. Goldner, "Nuclear spin coherence properties of $^{151}Eu^{3+}$ and $^{153}Eu^{3+}$ in a Y_2O_3 transparent ceramic", *Journal of Physics: Condensed Matter*, vol. 29, no. 12, p. 125 501, 2017.

[66] A. Fossati, "Synthèse et spectroscopie cohérente de nanoparticules dopées terres rares pour les technologies optiques quantiques", Ph.D. dissertation, PSL Université Paris, Paris, 2019.

[67] B. Casabone, J. Benedikter, T. Hümmer, *et al.*, "Cavity-enhanced spectroscopy of a few-ion ensemble in Eu^{3+}:Y_2O_3", *New Journal of Physics*, vol. 20, no. 9, p. 095 006, 2018.

[68] H. Forest and G. Ban, "Evidence for Eu3+ Emission from Two Symmetry Sites in Y2O3 :Eu+3", *Journal of The Electrochemical Society*, vol. 116, no. 4, 1969.

[69] M. Buijs, A. Meyerink, and G. Blasse, "Energy transfer between Eu3+ ions in a lattice with two different crystallographic sites: Y2O3:Eu3+, Gd2O3:Eu3+ and Eu2O3", *Journal of Luminescence*, vol. 37, no. 1, pp. 9–20, 1987.

[70] T. Krom, "Fluoreszenzspektroskopie an Europium mit einem Konfokalmikroskop", Bachelor Thesis, Karlsruher Institut für Technologie, Karlsruhe, 2018.

[71] X. Caillet and C. Simon, "Precision of single-qubit gates based on Raman transitions", *The European Physical Journal D*, vol. 42, no. 2, pp. 341–348, 2007.

[72] I. Roos and K. Mølmer, "Quantum computing with an inhomogeneously broadened ensemble of ions: Suppression of errors from detuning variations by specially adapted pulses and coherent population trapping", *Physical Review A*, vol. 69, no. 2, p. 022 321, 2004.

[73] Z. Kis and F. Renzoni, "Qubit rotation by stimulated Raman adiabatic passage", *Physical Review A*, vol. 65, no. 3, p. 032 318, 2002.

[74] A. J. Meixner, C. M. Jefferson, and R. M. Macfarlane, "Measurement of the stark effect with subhomogeneous linewidth resolution in eu^{3+}:$yalo_3$ with the use of photon-echo modulation", *Physical Review B*, vol. 46, no. 10, pp. 5912–5916, 1992.

[75] R. M. Macfarlane, A. Arcangeli, A. Ferrier, and P. Goldner, "Optical Measurement of the Effect of Electric Fields on the Nuclear Spin Coherence of Rare-Earth Ions in Solids", *Physical Review Letters*, vol. 113, no. 15, p. 157 603, 2014.

[76] D. Jaksch, J. I. Cirac, P. Zoller, S. L. Rolston, R. Côté, and M. D. Lukin, "Fast Quantum Gates for Neutral Atoms", *Physical Review Letters*, vol. 85, no. 10, pp. 2208–2211, 2000.

[77] C. Rentschler, "Simulation of Single- and Two-Qubit Gates in Rare Earth Ions", M.S. thesis, Karlsruher Institut für Technologie, Karlsruhe, 2021.

[78] H.-P. Breuer and F. Petruccione, *The theory of open quantum systems*. Clarendon Press, 2010.

[79] A. Kinos, "Light-Matter Interaction and Quantum Computing in Rare-Earth-Ion-Doped Crystals", Ph.D. dissertation, Lund University, Lund, 2018.

[80] A. Kinos, L. Rippe, S. Kröll, and A. Walther, "Designing gate operations for single-ion quantum computing in rare-earth-ion-doped crystals", *Physical Review A*, vol. 104, no. 5, p. 052 624, 2021.

[81] A. Kinos, L. Rippe, A. Walther, and S. Kröll, "Microscopic treatment of instantaneous spectral diffusion and its effect on quantum gate fidelities in rare-earth-ion-doped crystals", *Physical Review A*, vol. 105, no. 3, p. 032 608, 2022.

[82] Fabry, "Theorie et applications d'une nouvelle methods de spectroscopie intereferentielle", *Ann. Chim. Ser. 7*, no. 16, pp. 115–144, 1899.

[83] C. Fabry and A. Pérot, "On a new form of interferometer", *Astrophysical Journal*, no. 13, pp. 265–272, 1901.

[84] E. M. Purcell, "Spontaneous emission probabilities at radio frequencies", *Physical Review*, vol. 69, no. 681, 1946.

[85] P. Goy, J. M. Raimond, M. Gross, and S. Haroche, "Observation of Cavity-Enhanced Single-Atom Spontaneous Emission", *Physical Review Letters*, vol. 50, no. 24, pp. 1903–1906, 1983.

[86] R. J. Thompson, G. Rempe, and H. J. Kimble, "Observation of normal-mode splitting for an atom in an optical cavity", *Physical Review Letters*, vol. 68, no. 8, pp. 1132–1135, 1992.

[87] A. Kuhn, M. Hennrich, and G. Rempe, "Deterministic Single-Photon Source for Distributed Quantum Networking", *Physical Review Letters*, vol. 89, no. 6, p. 067 901, 2002.

[88] J. W. Smith, J. C. Williams, J. S. Suelzer, N. G. Usechak, and H. Chandrahalim, "Three-dimensional Fabry–Pérot cavities sculpted on fiber tips using a multiphoton polymerization process", *Journal of Micromechanics and Microengineering*, vol. 30, no. 12, p. 125 007, 2020.

[89] A. A. P. Trichet, P. R. Dolan, D. M. Coles, G. M. Hughes, and J. M. Smith, "Topographic control of open-access microcavities at the nanometer scale", *Optics Express*, vol. 23, no. 13, p. 17 205, 2015.

[90] T. Zhong, J. M. Kindem, E. Miyazono, and A. Faraon, "Nanophotonic coherent light–matter interfaces based on rare-earth-doped crystals", *Nature Communications*, vol. 6, no. 1, p. 8206, 2015.

[91] P. Romagnoli, M. Maeda, J. M. Ward, V. G. Truong, and S. Nic Chormaic, "Fabrication of optical nanofibre-based cavities using focussed ion-beam milling: A review", *Applied Physics B*, vol. 126, no. 6, p. 111, 2020.

[92] D. Hunger, T. Steinmetz, Y. Colombe, C. Deutsch, T. W. Hänsch, and J. Reichel, "A fiber Fabry–Perot cavity with high finesse", *New Journal of Physics*, vol. 12, no. 6, p. 065 038, 2010.

[93] D. Hunger, C. Deutsch, R. J. Barbour, R. J. Warburton, and J. Reichel, "Laser micro-fabrication of concave, low-roughness features in silica", *AIP Advances*, vol. 2, no. 1, p. 012 119, 2012.

[94] A. Laliotis, M. Trupke, J. P. Cotter, G. Lewis, M. Kraft, and E. A. Hinds, "ICP polishing of silicon for high-quality optical resonators on a chip", *Journal of Micromechanics and Microengineering*, vol. 22, no. 12, p. 125 011, 2012.

[95] P. Qing, J. Gong, X. Lin, *et al.*, "A simple approach to fiber-based tunable microcavity with high coupling efficiency", *Applied Physics Letters*, vol. 114, no. 2, p. 021 106, 2019.

[96] C. T. Nguyen, D. D. Sukachev, M. K. Bhaskar, *et al.*, "An integrated nanophotonic quantum register based on silicon-vacancy spins in diamond", *Physical Review B*, vol. 100, no. 16, p. 165 428, 2019.

[97] J. M. H. Benedikter, "Microcavity Enhancement of Silicon Vacancy Centres in Diamond and Europium Ions in Yttria", Ph.D. dissertation, Ludwigs-Maximilian-Universität, München, 2019.

[98] A. Muller, E. B. Flagg, J. R. Lawall, and G. S. Solomon, "Ultrahigh-finesse, low-mode-volume Fabry–Perot microcavity", *Optics Letters*, vol. 35, no. 13, p. 2293, 2010.

[99] M. Mader, J. Reichel, T. W. Hänsch, and D. Hunger, "A scanning cavity microscope", *Nature Communications*, vol. 6, no. 1, p. 7249, 2015.

[100] T. Hümmer, J. Noe, M. S. Hofmann, T. W. Hänsch, A. Högele, and D. Hunger, "Cavity-enhanced Raman microscopy of individual carbon nanotubes", *Nature Communications*, vol. 7, no. 1, p. 12 155, 2016.

[101] Y. Colombe, T. Steinmetz, G. Dubois, F. Linke, D. Hunger, and J. Reichel, "Strong atom–field coupling for Bose–Einstein condensates in an optical cavity on a chip", *Nature*, vol. 450, no. 7167, pp. 272–276, 2007.

[102] L. Kohler, M. Mader, C. Kern, M. Wegener, and D. Hunger, "Tracking Brownian motion in three dimensions and characterization of individual nanoparticles using a fiber-based high-finesse microcavity", *Nature Communications*, vol. 12, no. 1, p. 6385, 2021.

[103] L. A.-M. Kohler, "Characterization and tracking of the three-dimensional translational motion and rotation of single nanoparticles using a ber-based microcavity with high nesse", Ph.D. dissertation, Karlsruher Institut für Technologie, Karlsruhe, 2021.

[104] H. S. Kaupp, "Coupling Nitrogen-Vacancy Centers in Diamond to Fiber-based Fabry-Pérot Microcavities", Ph.D. dissertation, Ludwigs-Maximilian-Universität, München, 2017.

[105] F. Rochau, I. Sánchez Arribas, A. Brieussel, S. Stapfner, D. Hunger, and E. M. Weig, "Dynamical Backaction in an Ultrahigh-Finesse Fiber-Based Microcavity", *Physical Review Applied*, vol. 16, no. 1, p. 014 013, 2021.

[106] H. Pfeifer, L. Ratschbacher, J. Gallego, *et al.*, "Achievements and perspectives of optical fiber Fabry–Perot cavities", *Applied Physics B*, vol. 128, no. 2, p. 29, 2022.

[107] T. Hümmer, "Cavity-enhanced hyperspectral Raman and Absorption Microscopy", Ph.D. dissertation, Ludwigs-Maximilian-Universität, München, 2019.

[108] M. Mader, "A Scanning Cavity Microscope", Ph.D. dissertation, Ludwigs-Maximilian-Universität, München, 2018.

[109] B. E. A. Saleh and M. C. Teich, *Fundamentals of photonics*. John Wiley &Sons, 2019.

[110] A. E. Siegman, *Lasers*. Univ. Science books, 1986.

[111] J. Benedikter, T. Moosmayer, M. Mader, T. Hümmer, and D. Hunger, "Transverse-mode coupling effects in scanning cavity microscopy", *New Journal of Physics*, vol. 21, no. 10, p. 103 029, 2019.

[112] M. Uphoff, M. Brekenfeld, G. Rempe, and S. Ritter, "Frequency splitting of polarization eigenmodes in microscopic Fabry–Perot cavities", *New Journal of Physics*, vol. 17, no. 1, p. 013 053, 2015.

[113] T. Krom, "Development of a low temperature all-fiber resonator platform with integrated Eu3+:Y2O3 nanocrystals", M.S. thesis, Karlsruher Institut für Technologie, Karlsruhe, 2021.

[114] S. A. Furman and A. V. Tikhonravov, *Basics of optics of multilayer systems*. Ed. Frontières, 1992.

[115] C. J. R. Sheppard, "Approximate calculation of the reflection coefficient from a stratified medium", *Pure and Applied Optics: Journal of the European Optical Society Part A*, vol. 4, no. 5, pp. 665–669, 1995.

[116] C. Koks and M. P. Van Exter, "Microcavity resonance condition, quality factor, and mode volume are determined by different penetration depths", *Optics Express*, vol. 29, no. 5, p. 6879, 2021.

[117] J. M. Bennett, "Recent developments in surface roughness characterization", *Measurement Science and Technology*, vol. 3, no. 12, pp. 1119–1127, 1992.

[118] G. Mie, "Beiträge zur Optik trüber Medien, speziell kolloidaler Metallösungen", *Annalen der Physik*, vol. 330, no. 3, pp. 377–445, 1908.

[119] M. Quinten, *Optical properties of nanoparticle systems: Mie and beyond*. Wiley-VCH, 2011.

[120] M. Wind, J. Vlieger, and D. Bedeaux, "The polarizability of a truncated sphere on a substrate I", *Physica A: Statistical Mechanics and its Applications*, vol. 141, no. 1, pp. 33–57, 1987.

[121] E. Jaynes and F. Cummings, "Comparison of quantum and semiclassical radiation theories with application to the beam maser", *Proceedings of the IEEE*, vol. 51, no. 1, pp. 89–109, 1963.

[122] A. Auffèves, J.-M. Gérard, and J.-P. Poizat, "Pure emitter dephasing: A resource for advanced solid-state single-photon sources", *Physical Review A*, vol. 79, no. 5, p. 053 838, 2009.

[123] A. Auffèves, D. Gerace, J.-M. Gérard, M. F. Santos, L. C. Andreani, and J.-P. Poizat, "Controlling the dynamics of a coupled atom-cavity system by pure dephasing", *Physical Review B*, vol. 81, no. 24, p. 245 419, 2010.

[124] M. Fox, *Quantum optics: an introduction*. Oxford University Press, 2006.

[125] S. Daiss, S. Langenfeld, S. Welte, *et al.*, "A quantum-logic gate between distant quantum-network modules", *Science*, vol. 371, no. 6529, pp. 614–617, 2021.

[126] S. Langenfeld, O. Morin, M. Körber, and G. Rempe, "A network-ready random-access qubits memory", *npj Quantum Information*, vol. 6, no. 1, p. 86, 2020.

[127] S. Langenfeld, S. Welte, L. Hartung, *et al.*, "Quantum Teleportation between Remote Qubit Memories with Only a Single Photon as a Resource", *Physical Review Letters*, vol. 126, no. 13, p. 130 502, 2021.

[128] D. Niemietz, P. Farrera, S. Langenfeld, and G. Rempe, "Nondestructive detection of photonic qubits", *Nature*, vol. 591, no. 7851, pp. 570–574, 2021.

[129] D. Meschede, H. Walther, and G. Müller, "One-Atom Maser", *Physical Review Letters*, vol. 54, no. 6, pp. 551–554, 1985.

[130] G. Rempe, H. Walther, and N. Klein, "Observation of quantum collapse and revival in a one-atom maser", *Physical Review Letters*, vol. 58, no. 4, pp. 353–356, 1987.

[131] M. G. Raizen, R. J. Thompson, R. J. Brecha, H. J. Kimble, and H. J. Carmichael, "Normal-mode splitting and linewidth averaging for two-state atoms in an optical cavity", *Physical Review Letters*, vol. 63, no. 3, pp. 240–243, 1989.

[132] T. Wilk, S. C. Webster, A. Kuhn, and G. Rempe, "Single-Atom Single-Photon Quantum Interface", *Science*, vol. 317, no. 5837, pp. 488–490, 2007.

[133] D. Wang, H. Kelkar, D. Martin-Cano, *et al.*, "Turning a molecule into a coherent two-level quantum system", *Nature Physics*, vol. 15, no. 5, pp. 483–489, 2019.

[134] D. Najer, I. Söllner, P. Sekatski, *et al.*, "A gated quantum dot strongly coupled to an optical microcavity", *Nature*, vol. 575, no. 7784, pp. 622–627, 2019.

[135] M. Förg, L. Colombier, R. K. Patel, *et al.*, "Cavity-control of interlayer excitons in van der Waals heterostructures", *Nature Communications*, vol. 10, no. 1, p. 3697, 2019.

[136] C. Gebhardt, M. Förg, H. Yamaguchi, *et al.*, "Polariton hyperspectral imaging of two-dimensional semiconductor crystals", *Scientific Reports*, vol. 9, no. 1, p. 13 756, 2019.

[137] C. T. Nguyen, D. D. Sukachev, M. K. Bhaskar, *et al.*, "Quantum Network Nodes Based on Diamond Qubits with an Efficient Nanophotonic Interface", *Physical Review Letters*, vol. 123, no. 18, p. 183 602, 2019.

[138] D. F. Walls and G. J. Milburn, *Quantum optics*, 2nd ed. Springer, 2008.

[139] P. A. M. Dirac, "The quantum theory of the emission and absorption of radiation", *Proceedings of the Royal Society of London. Series A, Containing Papers of a Mathematical and Physical Character*, vol. 114, no. 767, pp. 243–265, 1927.

[140] M. Motsch, M. Zeppenfeld, P. W. H. Pinkse, and G. Rempe, "Cavity-enhanced Rayleigh scattering", *New Journal of Physics*, vol. 12, no. 6, p. 063 022, 2010.

[141] A. Meldrum, P. Bianucci, and F. Marsiglio, "Modification of ensemble emission rates and luminescence spectra for inhomogeneously broadened distributions of quantum dots coupled to optical microcavities", *Optics Express*, vol. 18, no. 10, p. 10 230, 2010.

[142] E. Janitz, M. K. Bhaskar, and L. Childress, "Cavity quantum electrodynamics with color centers in diamond", *Optica*, vol. 7, no. 10, p. 1232, 2020.

[143] S. Chen, M. Raha, C. M. Phenicie, S. Ourari, and J. D. Thompson, "Parallel single-shot measurement and coherent control of solid-state spins below the diffraction limit", *Science*, vol. 370, no. 6516, pp. 592–595, 2020.

[144] T. Cosgrove, *Colloid science: principles, methods and applications*. Blackwell Pub., 2005.

[145] Y. Wang and W. Zhou, "A Review on Inorganic Nanostructure Self-Assembly", *Journal of Nanoscience and Nanotechnology*, vol. 10, no. 3, pp. 1563–1583, 2010.

[146] T. Graham, "Liquid diffusion applied to analysis", *Philosophical Transactions of the Royal Society*, vol. 151, pp. 183–224, 1861.

[147] H. Hamaker, "The London—van der Waals attraction between spherical particles", *Physica*, vol. 4, no. 10, pp. 1058–1072, 1937.

[148] Elcap. "Simplified illustration of the potential development in the area and in the further course of a Helmholtz double layer". (2013), [Online]. Available: `https://en.wikipedia.org/wiki/Double_layer_%28surface_science%29#/media/File:EDLC-Potentialdistribution.png` (visited on 05/17/2024).

[149] M. Smoluchowski, "Zur kinetischen Theorie der Brownschen Molekularbewegung und der Suspensionen", *Annalen der Physik*, vol. 21, pp. 756–780, 1906.

[150] S. P. Yeap, "Permanent agglomerates in powdered nanoparticles: Formation and future prospects", *Powder Technology*, vol. 323, pp. 51–59, 2018.

[151] B. Derjaguin and L. Landau, "Theory of the stability of strongly charged lyophobic sols and of the adhesion of strongly charged particles in solutions of electrolytes", *Progress in Surface Science*, vol. 43, no. 1-4, pp. 30–59, 1941.

[152] E. J. W. Verwey, "Theory of the Stability of Lyophobic Colloids.", *The Journal of Physical and Colloid Chemistry*, vol. 51, no. 3, pp. 631–636, 1947.

[153] R. Hogg, T. W. Healy, and D. W. Fuerstenau, "Mutual coagulation of colloidal dispersions", *Transactions of the Faraday Society*, vol. 62, p. 1638, 1966.

[154] C. Vautier-Giongo and B. L. Bales, "Estimate of the Ionization Degree of Ionic Micelles Based on Krafft Temperature Measurements", *The Journal of Physical Chemistry B*, vol. 107, no. 23, pp. 5398–5403, 2003.

[155] C. Deshmukh, "Detection of a single erbium ion in a nanoparticle", Ph.D. dissertation, Universitat Politècnica de Catalunya, Barcelona, 2022.

[156] R. Huber, "Gedruckte Temperatursensor-Arrays mit hoher räumlicher Auflösung", Ph.D. dissertation, Karlsruher Institut für Technologie, Karlsruhe, 2024.

[157] Optomec, *Aerosol Jet Flex System for Conformal Printed Electronics Applications*, Tech. Rep., 2023.

[158] J. C. Simon, O. A. Sapozhnikov, V. A. Khokhlova, L. A. Crum, and M. R. Bailey, "Ultrasonic atomization of liquids in drop-chain acoustic fountains", *Journal of Fluid Mechanics*, vol. 766, pp. 129–146, 2015.

[159] J. Grammel, "Optically detected magnetic resonance of Nitrogen-Vacancy centers in diamond observed in a scanning fiber cavity for quantum network applications", M.S. thesis, Karlsruher Institut für Technologie, Karlsruhe, 2020.

[160] M. Dortmund, "Resonator-enhanced Spectroscopy on Eu:Y2O3 nanocrystals", BA thesis, Karlsruher Institut für Technologie, Karlsruhe, 2020.

[161] Y. Fontana, R. Zifkin, E. Janitz, C. D. Rodríguez Rosenblueth, and L. Childress, "A mechanically stable and tunable cryogenic Fabry–Pérot microcavity", *Review of Scientific Instruments*, vol. 92, no. 5, p. 053 906, 2021.

[162] S. Vadia, J. Scherzer, H. Thierschmann, *et al.*, "Open-Cavity in Closed-Cycle Cryostat as a Quantum Optics Platform", *PRX Quantum*, vol. 2, no. 4, p. 040 318, 2021.

[163] M. Fisicaro, M. Witlox, H. Van Der Meer, and W. Löffler, "Active stabilization of an open-access optical microcavity for low-noise operation in a standard closed-cycle cryostat", *Review of Scientific Instruments*, vol. 95, no. 3, p. 033 101, 2024.

[164] M. Salz, Y. Herrmann, A. Nadarajah, *et al.*, "Cryogenic platform for coupling color centers in diamond membranes to a fiber-based microcavity", *Applied Physics B*, vol. 126, no. 8, p. 131, 2020.

[165] T. Ruelle, D. Jaeger, F. Fogliano, F. Braakman, and M. Poggio, "A tunable fiber Fabry–Perot cavity for hybrid optomechanics stabilized at 4 K", *Review of Scientific Instruments*, vol. 93, no. 9, p. 095 003, 2022.

[166] M. Pallmann, T. Eichhorn, J. Benedikter, B. Casabone, T. Hümmer, and D. Hunger, "A highly stable and fully tunable open microcavity platform at cryogenic temperatures", *APL Photonics*, vol. 8, no. 4, p. 046 107, 2023.

[167] M. B. Pallmann, "Purcell-enhanced emission and collective effects of nitrogen-vacancy centers in diamond coupled to a microcavity", Ph.D. dissertation, Karlsruher Institut für Technologie, Karlsruhe, 2023.

[168] PiezomechanikGmbH. "Piezoaction in Practice". (2024), [Online]. Available: `https://www.piezomechanik.com/fileadmin/content_files/catalogs/piezomechanik-piezoaction-in-practice.pdf` (visited on 08/05/2024).

[169] Lake Shore Cryotronics. "Cryogenic Reference Tables". (2024), [Online]. Available: `https://www.google.com/url?sa=t&source=web&rct=j&opi=89978449&url=https://www.lakeshore.com/docs/default-source/product-downloads/literature/lstc_appendixi_l.pdf%3Fsfvrsn%3D5f2ab85b_4&ved=2ahUKEwjV9ayW792HAxXhwQIHHbroFDIQFnoECBwQAQ&usg=AOvVaw0JF2v8bf80MbrHxl5WlgY-` (visited on 08/05/2024).

[170] J. R. Rumble, *CRC handbook of chemistry and physics*. CRC Press, Taylor & Francis Group, 2017.

[171] J. Bechhoefer, "Feedback for physicists: A tutorial essay on control", *Reviews of Modern Physics*, vol. 77, no. 3, pp. 783–836, 2005.

[172] L. Neuhaus, "Cooling a macroscopic mechanical oscillator close to its quantum ground state", Ph.D. dissertation, Université Pierre et Marie Curie - Paris VI, Paris, 2016.

[173] R. W. P. Drever, J. L. Hall, F. V. Kowalski, *et al.*, "Laser phase and frequency stabilization using an optical resonator", *Applied Physics B Photophysics and Laser Chemistry*, vol. 31, no. 2, pp. 97–105, 1983.

[174] E. D. Black, "An introduction to Pound–Drever–Hall laser frequency stabilization", *American Journal of Physics*, vol. 69, no. 1, pp. 79–87, 2001.

[175] L. Neuhaus. "PyRPL". (2014), [Online]. Available: `https://pyrpl.readthedocs.io/en/latest/#` (visited on 06/24/2024).

[176] L. Neuhaus, M. Croquette, R. Metzdorff, *et al.*, "Python Red Pitaya Lockbox (PyRPL): An open source software package for digital feedback control in quantum optics experiments", *Review of Scientific Instruments*, vol. 95, no. 3, p. 033 003, 2024.

[177] T. Filiba. "RPyC - Transparent, Symmetric Distributed Computing — RPyC". (2024), [Online]. Available: `https://rpyc.readthedocs.io/en/latest/index.html` (visited on 06/25/2024).

[178] Y. Nigara, "Measurement of the Optical Constants of Yttrium Oxide", *Japanese Journal of Applied Physics*, vol. 7, no. 4, p. 404, 1968.

[179] K. De Oliveira Lima, R. Rocha Gonçalves, D. Giaume, A. Ferrier, and P. Goldner, "Influence of defects on sub-å optical linewidths in Eu3+: Y2O3 particles", *Journal of Luminescence*, vol. 168, pp. 276–282, 2015.

[180] A. M. Stoneham, "Shapes of Inhomogeneously Broadened Resonance Lines in Solids", *Reviews of Modern Physics*, vol. 41, no. 1, pp. 82–108, 1969.

[181] T. Kushida, "Linewidths and Thermal Shifts of Spectral Lines in Neodymium-Doped Yttrium Aluminum Garnet and Calcium Fluorophosphate", *Physical Review*, vol. 185, no. 2, pp. 500–508, 1969.

[182] J. I. Thorpe, K. Numata, and J. Livas, "Laser frequency stabilization and control through offset sideband locking to optical cavities", *Optics Express*, vol. 16, no. 20, p. 15 980, 2008.

[183] J. F. S. Brachmann, "Towards 6Li - 40K Ground State Molecules", Ph.D. dissertation, Ludwig-Maximilians-Universität München, München, 2012.

[184] J. R. Klauder and P. W. Anderson, "Spectral Diffusion Decay in Spin Resonance Experiments", *Physical Review*, vol. 125, no. 3, pp. 912–932, 1962.

[185] C. W. Thiel, R. M. Macfarlane, Y. Sun, *et al.*, "Measuring and analyzing excitation-induced decoherence in rare-earth-doped optical materials", *Laser Physics*, vol. 24, no. 10, p. 106 002, 2014.

[186] A. Fossati, S. Liu, J. Karlsson, *et al.*, "A Frequency-Multiplexed Coherent Electro-optic Memory in Rare Earth Doped Nanoparticles", *Nano Letters*, vol. 20, no. 10, pp. 7087–7093, 2020.

[187] B. Casabone, C. Deshmukh, S. Liu, *et al.*, "Dynamic control of Purcell enhanced emission of erbium ions in nanoparticles", *Nature Communications*, vol. 12, no. 1, p. 3570, 2021.

[188] R. Kohlrausch, "Ueber das Dellmannsche Elektrometer", *Annalen der Physik*, vol. 148, no. 11, pp. 353–405, 1847.

[189] S. Völker, "Hole-Burning Spectroscopy", *Annual Review Physical Chemistry*, no. 40, pp. 499–530, 1989.

[190] W. Demtröder, *Laser Spectroscopy 1*. Springer Berlin Heidelberg, 2014.

[191] A. Gritsch, L. Weiss, J. Früh, S. Rinner, and A. Reiserer, "Narrow Optical Transitions in Erbium-Implanted Silicon Waveguides", *Physical Review X*, vol. 12, no. 4, p. 041 009, 2022.

[192] M. Pallmann, K. Köster, Y. Zhang, *et al.*, "Cavity-Mediated Collective Emission from Few Emitters in a Diamond Membrane", *Physical Review X*, vol. 14, no. 4, p. 041 055, 2024.

List of Figures

List of Tables

Danksagung

Eine Promotion in Experimentalphysik ist meiner Auffassung nach immer ein Teamwork-Projekt, welches der Doktorand nicht alleine stemmt. Sowohl im universitären Forschungsumfeld, aber besonders auch im privaten Umfeld, ist die Unterstützung verschiedenster Personen essenziell, um diese Arbeit über die vielen Jahre zu meistern. Daher begreife ich meine Promotion nicht als mein alleiniges Werk, sondern als ein gemeinsames meines Doktorvaters David Hunger, meiner Kollegen in der Arbeitsgruppe (aka die Hungerharken), meiner Frau Anna, meiner Familie und meiner engsten Freunde. Diesem für mich wichtigen Personenkreis möchte ich an dieser Stelle herzlichst danken!

David, dir als meinem Mentor, Betreuer und natürlich auch Chef bin ich super dankbar, dass du mich auf dieses spannende und ehrgeizige Projekt angesetzt hast. Ich rechne es dir hoch an, dass du mir den Vertrauensvorschuss gewährt hast, mich als "Theoretiker" auf meine Wunschstelle in der experimentellen Quantenoptik einzustellen. Du hast die nötige Ruhe und Geduld gehabt, mir eine lange Einarbeitungsphase zu geben und mich Stück für Stück an das Experiment heranzuführen. Wenn ich zurückdenke für welche ersten Erfolge beim Aufbau des Experiments ich mich abgefeiert habe, muss dir das aus deiner Sicht echt lächerlich vorgekommen sein. Du hast dich aber trotzdem mit mir gefreut und dich begeistert gezeigt. Das ist sicherlich eine deiner Stärken im Umgang mit uns Mitarbeitern und eine schöne Eigenschaft. Ich bin dir auch sehr dankbar, dass du mir im Laufe meiner Promotion die vielen Reisen auf eine Summerschool, Workshops und Konferenzen ermöglicht hast. Mein Highlight dabei war das APS March Meeting in Las Vegas 2023, auf das du mich hingewiesen hast. Auch wenn das Experiment oft zäh lief und nicht ganz die gewünschten Resultate erzielt hat, bin ich wirklich sehr froh darüber, dass du mir den Freiraum gelassen hast, verschiedene Dinge auszuprobieren und meinen Ideen freien Lauf zu lassen. Auch was deine Mitarbeiterführung und Betreuung angeht, kann ich dir eine 5-Sterne Bewertung geben.

Ein weiterer wichtiger Punkt, der zum Gelingen dieser Arbeit beigetragen hat, ist die Unterstützung, die ich von meiner Frau Anna bekommen habe. Ich kann dir wirklich nicht genug danken, Sweety, für deinen Support, deine Geduld und dein Interesse an meiner Arbeit. Ich weiß sehr wohl, wie sehr auch dich manchmal gefordert hat, wenn ich schlecht gelaunt, überarbeitet und fertig wieder mal zu

spät vom Labor nach Hause kam. Dass du dich dann trotzdem noch für inhaltliche Details meines Experiments interessiert hast und mir zugehört hast, wenn ich ausschweifend etwas erklärt habe, weiß ich wirklich sehr zu schätzen. Neben dem mentalen Support, der wichtig war, um diese Arbeit überhaupt zum Ende zu bringen, hast du auch an der ein oder anderen Stelle inhaltlich an meiner Promotion mitgewirkt. Du hast mich öfters mal auf eine Unlogik in meiner Argumentation oder Denkweise aufmerksam gemacht und mich so vor Fehlern bewahrt. Nachdem der Spuk jetzt aber bald vorbei sein dürfte, verspreche ich dir, dass ich mich wieder mehr unserer frisch-gegründeten Familie widmen und mehr Zeit mit dir und Louis als mit PAULA verbringen werde.

Einen großen und herzlichen Dank möchte ich natürlich auch meinen Kollegen in der Arbeitsgruppe aussprechen. Entgegen dem Klischee bin ich der Meinung, dass Physik ist ein sehr soziales Fach mit viel menschlicher Interaktion ist. Und wie wusste schon Stromberg:

> "Je größer das Büro, desto weniger Platz ist darin für das Menschliche."

Deshalb sitzen wir auch mit acht Leuten auf zehn Quadratmetern. Ganz nach dem Motto,

> "Ein Mitarbeiter mit schlechter Laune ist wie ne Schneeflocke, einer alleine ist harmlos. Ein paar Dutzend sind schon ein Schneeball. Und wenn du dann nicht aufpasst, hast du ratz-fatz ne Lawine in der Hütte.",

sind coole Kollegen sehr wichtig. Und dabei geht es nicht nur darum die langen Wartezeiten in der Mensa zu überbrücken ("Kinder, was dauert denn das hier wieder so lange? Als ich mich hier angestellt hab, hatt' ich noch volles Haar."), sondern sie sind auch sehr fürs fachliche Gelingen verantwortlich. So genug der Stromberg-Zitate, ich möchte neben einem generellen Dank an meine Promotionskollegen und die vielen Master- und Bacheloranden, die ich als "Oldie" in der Gruppe miterleben durfte, noch ein paar Kollegen ausdrücklich erwähnen.

Max hat quasi mit mir angefangen und wir waren die Hälfte der Zeit Experiment-Buddys. Ich habe die vielen Stunden im Labor und im Büro neben dir wirklich sehr genossen und schätze deine Pfälzer Frohnatur, durch die du uns oft herzlich zum Lachen gebracht hast. Legendäre Ideen wie das Nippel-Fluxi und die Verbreitung des Stromberg-Humors in der Gruppe sind wesentlich auf dich zurückzuführen. Ich finde es echt cool, dass wir über die Arbeit hinaus auch privat gute Freunde geworden sind und hoffe, diese Freundschaft besteht noch lange fort!

Larissa hat auch einen großen Anteil daran, dass ich überhaupt in dieser Gruppe gelandet bin, da sie als erste Doktorandin in Karlsruhe bei meinem Vorstellungsge-

spräch dabei war und mich mit ihrer fröhlich-gut-gelaunten Art davon überzeugt hat, dass ich mich in der Gruppe wohlfühlen werde. Das hat sich dann auch bewahrheitet und auch mit Larissa hat sich übers Bouldern, Mountainbiken und Kaffeespezialitäten Testen eine Freundschaft über den Job hinaus entwickelt, die ich sehr schätze.

Jannis möchte ich, neben unseren gemeinsamen sportlichen Aktivitäten, ausdrücklich für das gemeinsame Rätseln über Cavity-Effekte und Quantenoptik danken. Ich schätze deine klugen Argumentationen und Einschätzungen sehr und wir hätten an PAULA zusammen bestimmt ein gutes Team abgegeben :)

I also want to say a big thank you to my beloved "Nicky Nick"! It's really great that you joined us and brought so much fun and sweet cakes to the group ;). I really enjoyed working together with you on the experiment during the last half year and I know that PAULA is in good hands with you.

Weiterhin möchte ich Evgenij hier erwähnen, der auch ein Europium-Leidensgenosse der ersten Stunde ist (eigentlich sogar noch vor mir!). Neben unseren vielen Diskussionen als Labornachbarn schätze ich an dir besonders deine offene Art und deine emotionale Reaktion auf politische Themen (Die Grünen!). Das macht dich nahbar und du stichst hervor. Ich freue mich sehr, während meiner verbleibenden Zeit in der Gruppe weiter mit dir über Russland, Veganismus und die Grünen zu diskutieren! Du bist mir übrigens noch schuldig, Habecks Buch zu lesen und mir zurückzugeben =D.

Ein Dank sei an dieser Stelle auch noch Julia ausgesprochen, die mir in München im Oktober 2018 den seichten Einstieg in die experimentelle Quantenoptik ermöglicht hat und mir geduldig zum dritten Mal den Aufbau erklärt hat. Ihr habe ich zu verdanken, dass das meiste Equipment und eine funktionierende Cavity bereits da war, als ich in die Gruppe kam.

Neben den bereits erwähnten Hungerharken haben auch Kerim, Jonas, Shalom, Jeremias, Andras, Vishnu und Svenja einen großen Anteil daran, dass ich mich morgens ausnahmslos gefreut habe, in die Uni zu kommen und mit euch gleich morgens beim Frühstück, spätestens beim Mittagessen und auch oft außerhalb der Arbeit bei Gruppen-, Instituts- und sonstigen Events zu schnacken und zu lachen.

Last but not least haben meine Familien einen großen Anteil am Gelingen dieser Arbeit. Meinen Eltern, Feli und Wolfgang, bin ich super dankbar, dass ihr mir meine Technik- und Physikbegeisterung in die Wiege gelegt habt. Durch meine Schulausbildung unter Mamas Fittichen habt ihr die Grundlage für das erfolgreiche Physikstudium und die Freude am Lernen bereitet. Ich weiß sehr zu schätzen, dass ihr mich in meinen verschiedenen, teils schwierigen Lebenslagen immer be-

dingungslos unterstützt habt. Meiner Schwester (auch im Geiste) Tabea will ich an dieser Stelle speziell für die vielen Gespräche über Arbeitspsychologie und Managementaspekte danken. Ich nehme aus diesen Gesprächen immer viel für mich mit und werde auch in Zukunft von deinen Erfahrungen profitieren. An meine Schwiegerfamilie geht auch ein großes Dankeschön für die Unterstützung bei den vielen großen Ereignissen in Annas und meinem Leben in den letzten Jahren. Ich schätze sehr, dass ihr bei meinen experimentellen Auf und Abs mitgefiebert habt. Wie sagt man so schön: Geteiltes Leid ist halbes Leid. Und ich füge an: Geteilte Freude ist doppelte Freude!